Accuracy assessment of the SU2 flow solver

for

Non-Ideal Organic Vapor Supersonic Expansions using Experimental Data

Fabio Beltrame

POLITECNICO DI TORINO

TUDelft

Politecnico di Torino

Thesis for the Master of Science degree in Aerospace Engineering

Accuracy Assessment of the SU2 Flow Solver for Non-ideal Organic Vapor Supersonic Expansions using Experimental Data

Supervisor:
Prof. Giuliana Mattiazzo (Politecnico di Torino)

Academic tutor:
Ir Adam Head (TU Delft)

Author:
Fabio Beltrame
253615

M.Sc Thesis pursued at TECHNISCHE UNIVERSITEIT DELFT

Sept. 2019 - Mar. 2020

Abstract

Organic Rankine Cycle power systems are rapidly gaining attention as efficient, cost-effective decentralized solutions for thermal energy conversion. Waste heat, geothermal, solar or other renewable energy sources can be exploited for power generation using small high temperature ORC units expanding the high density and high temperature vapor in turbines. Efficient expanders for these devices are fundamental, but research in this field is still at its early stages. The flows characterizing these systems can be classified as highly non ideal and the fluid dynamics knowledge at the moment does not cover these flows. The objective of the most recent studies in the non ideal compressible fluid dynamics (NICFD) field is the validation of CFD software implementing complex thermodynamic models based on the flow non ideality. The present work collocates itself in the NICFD studies and aims to the characterization of supersonic organic vapor expansions in order to assess the accuracy of CFD flow solvers such as SU2 comparing different thermodynamic models in various operating conditions. This represents a first step towards the full validation of SU2 for non ideal flows in order to correctly predict the performance of ORC expanders and to optimize their design.

Numerical predictions using the Peng-Robinson equation of state coupled with polytropic and non-polytropic specific heat ratio models as well as the Ideal gas model implemented in SU2 have been evaluated running Euler simulations in different operating conditions in order to assess their accuracy using experimental data.
The steady state intervals for the three process runs have been identified using two different approaches: for the on design cases a standard approach was used, for the off design condition a new drift proof method capable of detecting steady state intervas in smaller time windows was developed. The Schlieren imaging technique has been used to characterize the expansion in the nozzle; the Hough transform, together with Canny edge detection algorithm has been used to develop an algorithm capable of detecting Mach lines. A Schlieren post processing method is proposed: four programs based on the algorithm for Mach line extraction have been developed. The first program is capable of detecting and quantifying the flow symmetry in a nozzle, the second one analyzes the dataset as a whole to verify that statistical convergence of the results is achieved and that the dataset is indeed in steady state. Then, the two other tools are capable of extracting Mach lines on the midplane of the nozzle and its walls to then evaluate the Mach number fields, together with its total uncertainty. It is shown that the Mach number at the exit of the nozzle has uncertainties that range from 0.03 to 0.1 depending on the quality of the dataset. The Mach number uncertinties calculated in a smaller field of view Schlieren dataset are smaller than 0.05 and, in the kernel region, smaller than 0.02 due to the fact that the uncertainty on the Mach depends on the value of the Mach number of the flow in that position.

Finally after having quantified all the uncertainties in the balance of plant, test section, Schlieren measurement chain and post processing tools affecting the experimental results, the SU2 accuracy assessment is presented. The Euler CFD simulations are compared to the experimental results using an accuracy parameter developed in this thesis. It is shown that the most complex model, the Peng-Robinson non polytropic, is capable of predicting with a good level of accuracy the midplane Mach number for the on design and close to on design conditions of the nozzle. Differences between

the predicted Mach number and the experimental average values are always below the experimental uncertainty, which ranges from 0.05 to 0.12 depending on the dataset and the axial position in the nozzle. Furthermore, the accuracy assessments in the three operating conditions of the nozzle shows different outcomes depending on the operating conditions. While the accuracy of the on design cases on the midplane was high, the off design experimental results on the midplane deviate from the simulation predictions as soon as the the flow approaches M=1.7; in the discussion of the results in Chapter 5 it is shown that in off design conditions Euler simulations may not be accurate in the predictions of the result thus cannot be used for a validation, no matter the equation of state used. The accuracy assessment using the extracted Mach number on the nozzle profiles, on the other hand, shows that 3D and boundary layer effects cannot be neglected when the Mach number is being evaluated in the wall proximities; even in operating conditions close to the design, the uncertainty bands do not always cross the simulation and the differences in the experimental Mach and the numerical predictions are often larger than 0.1.

- An expert is man who has made all the
mistakes which can be made,
in a narrow field. -

Niels Bohr

Acknowledgements

Contents

CONTENTS

List of Figures

List of Tables

Glossary

Acronyms

AC   Axisymmetric Contraction. 24
ADC   Analog-to-digital Converter. 42, 43
AIAA   American Institute For Aeronautics And Astronautics. 10
ASME   American Society Of Mechanical Engineers. 10, 12
BC   Boundary Conditions. 105, 126
BOP   Balance Of Plant. 17, 22, 32, 35, 44, 105, 106
CD   Converging–diverging. 7, 24, 107
CFD   Computational Fluid Dynamics. 1, 2, 10, 114
CFL   Courant–Friedrichs–Lewy. 107
CL   Confidence Level. 76
CLOWT   Closed Loop Organic Wind Tunnel. 2, 7
CNC   Computer Numerical Control. 46, 66
DAQ   Data Acquisition. 23
DNS   Direct Navier-Stokes. 116
EOS   Equation Of State. 2, 4, 6, 104
FOV   Field Of View. 87, 100, 102, 104, 125
GPRS   Global Pixel Reference System. 67, 69, 71, 84, 91, 125
HPCS   Hough Parameters Counting Space. 51, 52, 54
IG   Ideal Gas. 4, 109, 111, 114, 115, 124
IPRSV   Improved Stryjek-Vera Peng-Robinson. 6, 115, 116
LES   Large Eddy Simulation. 116
MM   Hexamethyldisiloane. 5, 9, 22, 24, 25, 27, 29, 31, 32, 34, 108, 109
MOC   Method Of Characteristics. 24, 25, 47, 60, 61, 106
MOV   Mechanically Operated Valve. 18
NH   Nozzle Housing. 24
NICFD   Non-ideal Compressible Fluid Dynamics. 1, 5
NRS   Nozzle Reference System. 67, 69, 84, 96, 125
NS   Navier-Stokes. 15
ORC   Organic Rankine Cycle. 17
ORCHID   Organic Rankine Cycle Hybrid Integrated Device. 2, 17, 23
PBA   Probability Bound Analysis. 10
PR   Peng Robinson. 2, 6, 109, 111, 112, 114, 115, 116, 117, 119
PR.0   Process Run Number. 32, 111
RANS   Reynolds-Averaged Navier-Stokes. 15, 116
SC   Settling Chamber. 20, 21, 24, 32, 44
SRQ   System Response Quantities. 86, 124, 125
SS   Steady State. 126, 127, 128
SSI   Steady-state Identification. 34, 35, 36, 40, 126, 127, 128
TC   Testing Channel. 24, 31, 33, 50, 125
TROVA   Test-Rig For Organic VApours. 2, 7, 8

Notation

Chapter 1

Introduction

The need for efficiency improvements in propulsion and power applications grows as the human impact on the enviroment is reaching non-reversible dangerous global warming effects that can endanger many species on the planet, including humans. Renewable energy sources are without a doubt valuable energy harvesting methods and electric motors can efficiently substitute combustion engines in many applications. Still, today electric systems cannot substitute combustion engines especially in high energy applications; thus the need to increase the efficiency of these system is growing by the day.

Organic rankine cycle (ORC) power systems are rapidly diffusing as an efficient, cost-effective decentralized technology for the conversion of thermal energy sources in the small-to-medium power range. Thermal energy sources can be either waste heat from combustion propulsion systems or renewable heat sources, e.g. solar, geothermal. The most critical component is arguably the expander, especially if the power capacity is small or very small (Power outut 3 - 50 kW$_e$), as it is the case for innovative high-potential applications such as waste heat recovery from engines, or conversion of concentrated solar radiation. In these so-called high-temperature applications, the expansion ratio is very high; therefore, turbines are the expanders of choice [Casati *et al.* (2014)].

Mini-ORC units find their application for waste heat recovery in the energy and propulsion field due to the high density and high internal energy of the fluids at relatively low temperatures. Efficient expanders for these organic vapors are the enabling components of such systems, and all the related developments are at the early research stage [Head *et al.* (2017)] especially because of the highly non-ideal flow conditions in which these turbines have to operate; the organic fluids behaviour,for mini-ORC applications, is still being experimentally characterized and the accuracy of complex fluid models implemented in Computational fluid dynamics (CFD) software is yet to be validated.

Working fluids involved are typically organic compounds (carbon based) such as aliphatic and aromatic hydrocarbons, halocarbons, and siloxanes, which feature high molecular complexity and high molecular mass [Spinelli *et al.* (2018)]. Expansions taking place within ORC turbine blade channels are of particular interest, since they occur in the close proximity of the critical point of the fluid, thus showing remarkable deviation from the ideal-gas behavior. Indeed, in these so-called non-ideal regions, Spinelli *et al.* (2018) shows that the behavior of isentropic expansions is dependent on the flow stagnation conditions and not only on the expander geometry, as it is the case of ideal gases.

The study of these non-ideal flows became a sub-field in the area of fluid dynamics, namely non-ideal compressible fluid dynamics (NICFD), which had its first dedicated seminar in 2016 [Journal of Physics: Conference Series (2017)]; it is also officially recognised by the European Research Community on Flow, Turbulence and Combustion (ERCOFTAC) as special interest group (SIG)49 [ERCOFTAC (2016)]. Non-Ideal Compressible Fluid Dynamics aims to the study and characterization of of highly non-ideal flows, defined by the irregular behaviour of fluids which are supercritical, very dense (high molecular complexity), or two phase. In these cases, more complicated equations of state , which are often based on empirical relations, are required to accurately calculate the

performance of NICFD flows. Examples of these are the Peng-Robinson equation of state (EoS), the improved Peng -Robinson equation of state with the Stryjek-Vera modification IiPRV) and the Helmholtz energy equation of state. There are only a few CFD softwares implementing these complex equations using external libraries, e.g. fluidprop, or internally coded equations of state, e.g. Peng Robinson (PR) in SU2, since most CFD tools rely on the assumption that most fluids obey the ideal gas law; nevertheless, a full validation of the CFD predicted results for classical NICFD applications has never been done; the reason being that experimental gas dynamics data concerning the fluids and the flow conditions of interest for ORC expanders is very limited limited. Experimental facilities capable of studying NICFD flows in mini-ORC fluid conditions (such as the ORCHID) are only recently starting to produce results; the difficulties in the realization of these type of wind tunnels are numerous and are mostly related to the high pressures and temperatures needed to study the expansions of these organic vapors in the ORC-expander conditions to then validate the numerical CFD predictions implementing complex fluid models. The state of the art ORC Wind tunnel (WT) facilities, which are discussed in the following sections, at the present day are the Closed Loop Organic Wind Tunnel (CLOWT) [Hasselmann *et al.* (2014)], Test-Rig for Organic VApours (TROVA) [Spinelli *et al.* (2010)] and the most recent one, the organic Rankine cycle hybrid integrated device (ORCHID) [Head (2020)]: the aim of these facilities is the experimental study and characterization of supersonic expansions of organic vapors in ORC turbine conditions, where the non ideal effects are significant and appropriate models in CFD tools have to be validated in order to correctly design efficient expanders for waste heat recovery systems using mini ORCs.

1.1   Scope of This Work

The need for a comprehensive validation of CFD software for NICFD is related to the realization of optimal designs for ORC expanders, which are efficient and cost-effective power generation systems from heat sources that can range from waste heat of combustion or renewable energies. The full validation of a CFD software is a very complicated and time consuming process, especially when many computational sub-models influence the solution like for the present applications. In this thesis, the first step of this long process is taken, performing an accuracy assessment of the SU2 flow solver for NICFD. The research questions that are addressed are the following:

- What are the predictive capabilities of the SU2 Fluid Dynamic Solver when simulating dense organic vapor flow expansions in highly non-ideal conditions?

- How can we determine the accuracy of a numerical prediction using experimental data? What experiment is more suited? Which SRQs can be used? How do we extract experimental data?

- What kind of simulations have to be performed? Can an Euler simulation be used for the Uncertainty Quantification (UQ) in the numerical framerwork or is viscosity influencing the results?

- Can we identify all of the error sources affecting the experimental results and quantify the uncertainties in the data extraction process and in the experimental campaign?

Now, these questions will gradually be answered throughout this thesis by completing a series of objectives:

1. identification of error sources and quantification of the uncertainties in the balance of plant of the experimental facility that influence the test section, thus the experimental data (Ch.2);

2. identification of error sources in the nozzle test section and Schlieren measurement chain in order to evaluate the impact of these errors on the uncertainty of the system response quantities used for the accuracy assessment (Ch.2);

3. identification of steady state conditions for the process runs and development of a drift proof method capable of identifying a steady state period in small intervals of time (Ch.2);

4. development of Schlieren data extration tools capable of detecting Mach lines in a nozzle's midplane and walls to compare the experimental Mach value to the numerical prediction using SU2;

5. quantification of all the uncertainties on the extracted Mach angles and Mach number (Ch.3-4);

6. comparison of Euler simulations and experimental results using different fluid models to compare the numerical predictions with the observed flow (Ch.5), and finally

7. explanation of the accuracy assessment results in order to set the basis for a solid future validation using valuable fluid models as well as correct flow assumtions depending on the boundary conditions of the expansion in the nozzle (Ch.5-6).

1.2   Classical Non-ideal Compressible Fluid Dynamics

Complementary equations, such as the equation of state, and the thermodynamic model of the fluid, are necessary to close the Navier-Stokes conservation equations system, whose solution characterizes entirely any flow of a given fluid. In most gas dynamics applications, the Ideal Gas (IG) EoS is capable of correctly relating the thermodynamic properties of the fluid such as pressure, density and temperature:

$$P = \rho RT.$$

The thermodynamic model often used with the Ideal Gas law is the constant specific heat, which is capable of simplifying equations without compromising the results when classical aerodynamic flows are considered. The range of non-ideal gas behaviour is characterized by the compressibility factor :

$$Z = \frac{P\,v}{R\,T}, \tag{1.1}$$

where $v = 1/\rho$ is the specific volume of the fluid and $R = \mathrm{R}/M_{mol}$ is the specific constant of the fluid. It follows that an ideal gas has $Z = 1$, thus it is possible to define a function which quantifies the departure of a non-ideal gas from the ideal case $1 - Z$. If this function tends to zero, the ideal gas equation can be used, while if $1 - Z < 1$ then different more complex fluid models need to be used to correctly predict the behaviour of the fluid. The compressibility factor is not the only parameter characterizing NICFD flows: when dealing with organic vapors, the complex molecular structure changes radically the thermodynamic behaviour of the fluid, especially when close to the critical point; if the molecular complexity of a fluid is large enough, the large specific heat of the molecule causes the speed of sound to increase over isentropic expansions to the point that expansion waves can coalesce into rarefaction shock waves. Conversely, compression fans in supersonic flows are possible if the molecularly complex fluid is in these non-ideal thermodynamic states [Duhem (1909), Becker (1922), Zel'dovich (1946)]. The non-ideal behaviour of fluids, related to the molecular complexity and critical point conditions, can be appreciated in the quantitative differences in the variation of the speed of sound with density

$$c = \sqrt{\left(\frac{\partial P}{\partial \rho}\right)_S},$$

which is the speed at which disturbances or waves propagate within the fluid. In an ideal gas, the speed of sound varies with temperature:

$$c = \sqrt{\gamma RT},$$

where the specific heat ratio $\gamma = C_P/C_V$ is usually considered constant with temperature with the most simple thermodynamic model. In reality, especially at high temperatures, γ varies with T, thus the non polytropic thermodynamic model needs to be implemented. The variation of the speed of sound with density, at constant entropy S, for non ideal flows has been investigated thoroughly ; the parameter

$$\left(\frac{\partial^2 P}{\partial v^2}\right)_S,$$

where the specific volume v is the inverse of the density, defines the non ideal behaviour of the fluid and its effects in terms of the phenomena that can be encountered in the expanding flow. In 1942, Landau (1942) introduced a non-dimensional parameter for the evaluation of the the curvature of isentropes in the P-v thermodynamic plane

$$\frac{v^3}{c^2}\left(\frac{\partial^2 P}{\partial v^2}\right)_S$$

which Hayes (1958) modified to define what we now call fundamental derivative of Gas Dynamics:

$$\Gamma = \frac{v^3}{2c^2} \left(\frac{\partial^2 P}{\partial v^2} \right)_S , \tag{1.2}$$

in which $c^2 = -v^2 (\partial P / \partial v)_S$. This parameters fundamentally defines the variation of the speed of sound in a fluid. For Ideal gasses, one can notice how

$$\Gamma_{IG} = \frac{\gamma + 1}{2} > 1$$

thus flows of perfect gases always exhibit so-called positive non linear behavior: the speed of sound c increases over isentropic compression and decreases over isentopric epxansion. As a consequence of this dependence of the speed of sound on density, in ideal gases, compressible shock waves are the only type physically admissible.

In conclusion, the Non-ideal compressible fluid dynamics branch refers to compressible flows of thermodynamically non-ideal fluids in which the variation of the speed of sound with density over isentropic flows is very different to that of an ideal gas, thus new equations of state need to be used. For example, in the MM supersonic flow studied in this thesis, the speed of sound incresases along the the expansion in the highly non ideal on-design conditions of the nozzle. When considering NICFD flows, depending on the molecular complexity of the fluid and the thermodynamic conditions of the vapor, one can distinguish flows that have qualitatively similar trends to the ideal gases and are classified as **classical non-ideal compressible flows**. On the other hand, flows that are predicted to be completely different from flows of ideal gases, are termed non-classical flows. In these cases, the speed of sound variation is opposite and strong enough to determine unconventional phenomena such as rarefaction waves; the sub-field of NICFD studying these flow is defined as non-classical compressible gas dynamics (Fig. 1.1)

Γ	Possible phenomena	Classification	Soundspeed variation	Substance state
$\Gamma > 1$	Compression shocks, expansion Fans	Classical Compressible Fluid Dynamics	$\left(\frac{\partial c}{\partial P} \right)_s > 0$	Perfect gas
$\Gamma = 1$	Flow with $c =$ const.*	Classical Non-ideal Compressible Fluid Dynamics	$\left(\frac{\partial c}{\partial P} \right)_s = 0$	Gas made of molecules in states featuring $c =$ const.
$0 < \Gamma < 1$	Compression shocks, Expansion fans		$\left(\frac{\partial c}{\partial P} \right)_s < 0$	Dense vapor
$\Gamma = 0$	Stationary acoustic wave*	Non-classical Non-ideal Compressible Fluid Dynamics	$\left(\frac{\partial c}{\partial P} \right)_s < 0$	Dense vapor of sufficiently complex molecules
$\Gamma < 0$	Rarefaction shocks, Compression fans		$\left(\frac{\partial c}{\partial P} \right)_s < 0$	

* Arguably, this type of flow is a limiting case and cannot occur in practice.

Figure 1.1: Classification of gas dynamics regimes - taken from Head (2020).

Peng-Robinson EoS

It is now clear that when dealing with non-ideal fluid dynamics, new equations of state need to be used and validated to correctly predict the flow behaviour. As previously mentioned, there are a few accurate semi-empirical fluid models available in literature, such as the Peng-Robinson, its improved vesion by Stryjek-Vera and the Helmhholtz energy EoS. This thesis focuses on the accuracy assessment of the Peng-Robinson fluid model implemented in SU2, coupled with a variable specific heat model to predict isentropic expansions in different thermodynamic conditions of an organic vapor, under the assumption of inviscid flow.

The **Peng-Robinson equation of state** is a semi-empirical fluid model based on the same analytical relation that was developed by van der Waals (1873), in which the pressure of the non ideal gas is the sum of a repulsion pressure and an attraction pressure, respectively:

$$P = \frac{RT}{v - b} - \frac{a}{v^2},$$

where b is the co-volume parameters modelng the repulsion pressure following the hard sphere assumption, and a is the molecular attraction parameter, modeling the attraction pressure. Van der Waals original approach was later improved by Soave(1972), presenting the the SRK (Soave, Redlich, Kwong), which quickly gained acceptance because of the accurate predictions of the equilibrium ratios in Vapor-Liquid equilibrium (VLE) calculations. The SRK equation always predicts specific volumes for the liquid which are greater than the literature values and the deviation increases from about 7% at reduced temperatures below 0.65 to about 27% when the critical point is approached; for these reasons, Peng & Robinson (1976) developed an improved equation of state by changing the modelization of the co-volume b and the entire attraction pressure using empirical coefficients and achieving a much better level of accuracy in the liquid density values as well as in the prediction of vapor pressures and equilibrium ratios. The equation proposed is

$$P = \frac{RT}{v - b(T_c)} - \frac{a(T)}{v(v + b(T_c)) + b(v - b(T_c))}, \tag{1.3}$$

where

$$a(T) = a(T_c)\alpha(T_r, \omega)$$

$$a(T_c) = 0.457235 \frac{R^2 T_c^2}{P_c}$$

$$b(T_c) = 0.077796 \frac{RT_c}{P_c}$$

in which the critical point pressure and temperature of the fluid P_c and T_c resectively, must be known. The function $\alpha(T_r, \omega)$ is the one proposed by Soave (1972), and depends on the parameter $T_r = T/T_c$, which is the reduced temperature, and ω, the acentric factor, whose value depends on the molecular complexity of the fluid:

$$\alpha^{1/2} = 1 + k(1 - \sqrt{T_r}).$$

The parameter k is a function of the acentric factor of the considered fluid ω:

$$k = 0.37464 + 1.54226\omega - 0.26992\omega^2.$$

The PR model with the above k parameter introduces discontinuities in the fluid properties prediction as the critical point is approached; the improved Stryjek-Vera Peng-Robinson (iPRSV) equation of state fixes these problems by changing the evaluation of the k as shown by van der Stelt *et al.* (2012).

1.3   Facilities for Fundamental Research on Non-ideal Fluids

Facilities capable of studying dense organic vapor expansions in highly non ideal conditions are still a very new concept nowadays. The main vapor tunnels that are now active in the field of NICFD research applied to ORC expanders are the following:

1. Closed Loop Organic Wind Tunnel , Muenster university of Applied Sciences, Germany;

2. Test Rig for Organic VApors, Politecnico di Milano, Italy , and

3. Organic Rankine Cycle Hybrid Integrated Device, Delft university of thechnology, the Netherlands.

Recently, White & Sayma (2018) presented the design of a closed-loop supersonic test facility intended for experimental characterisation of the flow of organic fluids under typical operating conditions experienced within an ORC turbine. The test section is part of a wider test facility, developed for the study of ORC expanders. The working fluid is R1233zd, and the test facility is sized to deliver test conditions up to 20 bar and 125°C with a mass-flow rate of 1 kg/s. White & Sayma (2018) presents an overview of the test facility as well as a detailed design of the Mach 2 CD nozzle, the contraction zone, the settling chamber and the diffuser. The facility is not operating yet, but the author explain the details of the envigased PIV experiments, the operating conditions, the constraints and the compatibility with the working fluid.

The CLOWT follows the concept of a closed loop continuous running wind tunnel - also known as a gas cycle WT- which is suitable for an organic fluid, to be driven at higher temperatures and higher internal pressures. Currently its working fluid is the Novec^{TM} 649, a harmless fluorketone, but Reinker *et al.* (2017) explains that the CLOWT is not restricted to this fluid, but other fluids would require detailed examinations in terms of material compatibility. Reinker *et al.* (2017) explains the operating principle of the facility and reports the maximum operating pressure of the facility to be 0.6 MPa and the maximum pressure 423K (160° C), which is relatively low with respect to the other state of the art facilities. The operation of the CLOWT is limited by the compressor capabilities to subsonic and transonic regimes, but its objectives are slightly different from the TROVA's and the ORCHID's: the CLOWT aims to study the flow of organic vapors through linear turbine cascades in order to develop reliable empirical loss correlations for the design and performance evaluation of ORC expanders.
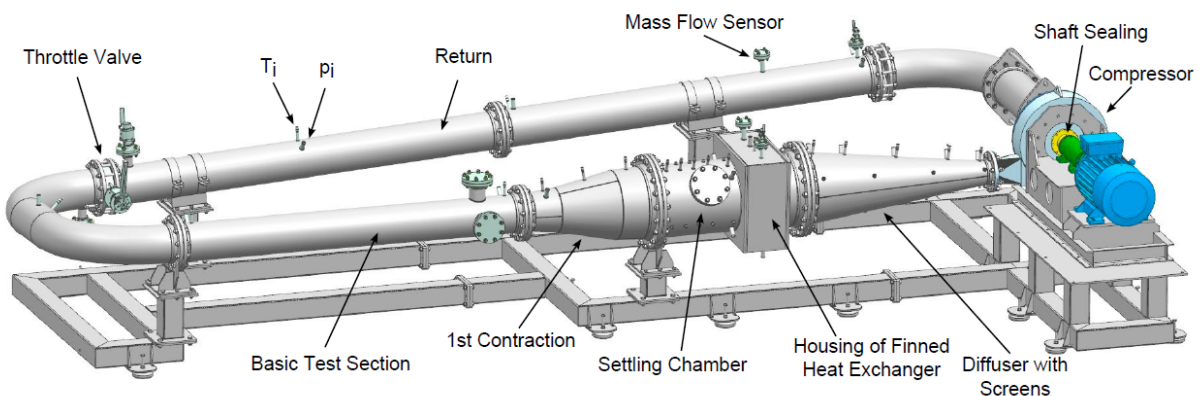
Figure 1.2:   Schematic representation of the CLOWT facility - taken from Reinker *et al.* (2017)

Spinelli *et al.* (2010) presents the TROVA (Fig. 1.3) as a blow down wind tunnel facility built to study nonideal fluids with the original motivation of ORC turbine research. A straight-axis planar convergent-divergent nozzle represents the test section for early tests, but the test rig can

also accommodate linear blade cascades. Due to high fluid density and operating temperature of the facility, the blow down operating scheme was implemented to reduce the necessary power input to about 30 kW$_{th}$; this prevents continuous operation which would require a much higher thermal power. Spinelli *et al.* (2013) shows that a wide variety of working fluids can be tested in the TROVA, with adjustable operating conditions up to maximum temperature and pressure of 400^oC and 50 bar, respectively. Despite the fact that the test rig operation is unsteady, the inlet nozzle pressure can be kept constant by a control valve. Design and simulations have been performed by Spinelli *et al.* (2013), with both lumped-parameter and 1D models, using siloxane MDM and hydrofluorocarbon R245fa as the reference working fluids, described by state-of-the-art thermodynamic models. Their calculations show how experiments may last from 12 seconds up to several minutes (depending on the fluid and test pressure). The facility records pressure, temperature, and the flow field in a nozzle test section with the design capability to implement Laser Doppler Velocimetry (LDV) [Spinelli *et al.* (2016)]. Schlieren imaging technique is used to visualise the flow based on density variations. Since the TROVA operates as a blow down facility, the working fluid is charged to the maximum design conditions and then the gas is released through the nozzle test section. Samples are recorded during transient flow but are considered steady state snapshots by Gori *et al.* (2020) since the timescale of thermodynamic variation is much larger than the molecule flow timescale, defined by the flow velocity.
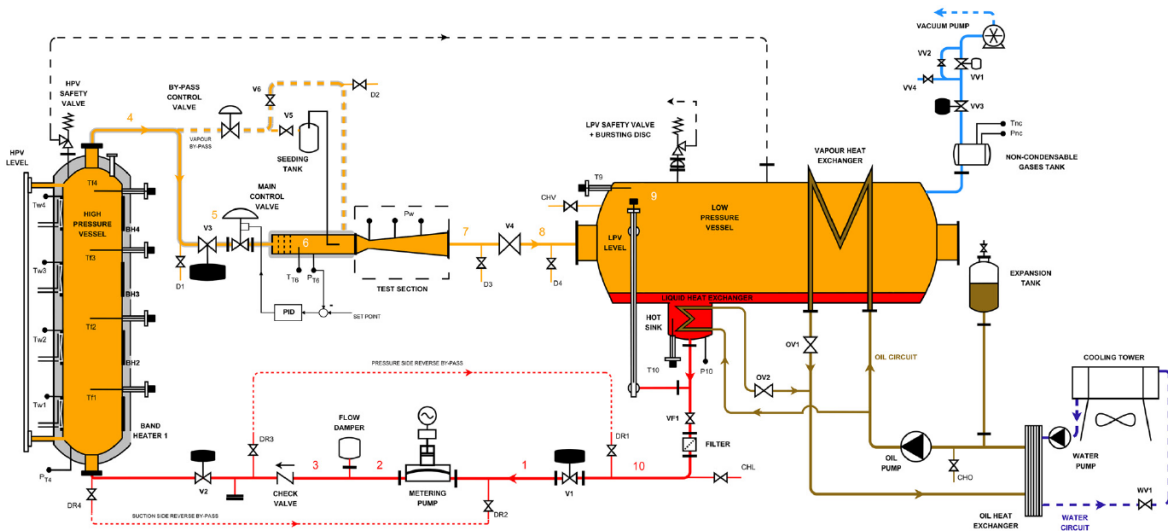
Figure 1.3: Final layout of the TROVA (Politecnico di Milano) - taken from Spinelli *et al.* (2013)

The research group of A. Guardone already useed the facility to characterize NICFD flows; Spinelli *et al.* (2016) characterized via pressure measurements and qualitative Schlieren images a MDM non ideal expansion, with total inlet conditions of 3.15 bar and 246^oC, producing a compressibility factor at the inlet of $Z = 0.884$ and $\Gamma = 0.885$. Gori *et al.* (2017) took a step foreward comparing SU2 CFD simulations for NICFD flows (with a low non ideality factor $1 - Z \approx 0.1 - 0.2$) with experimental data from the TROVA, consisting of pressure measurement and Schlieren images. Three different geometries were considered: an empty nozzle with $Z = 0.81$, a diamond shaped airfoil at zero angle of attack with $Z \approx 0.9$ and a backward facing step in the throat, with $Z \approx 0.89$. Complex equations of states, such as the iPRSV, were used in both deterministic Euler simulations and RANS and proven to be fairly accurate. No uncertainties were considered in the simulations, nor in the experiment; furthermore, only pressure measurements obtained from 9 static pressure taps were used as experimental data, while the Schlieren images were not considered. Spinelli *et al.* (2018) present the first attempt to extract data from the Schlieren images of a non ideal expansion of MDM for two nozzles ($M_1 = 1.5$ and $M_2 = 2$) and two inlet conditions; one at a higher pressure than the other. The compressibility factor at the inlet conditions range from 0.61 (for

higher pressures) to 0.81. The Mach angle was extracted on the nozzle's midplane using the Hough transform and compared to accurate CFD predictions using iPRSV and RefProp as fluid models; it is important to point out that no uncertainties other than the angular resolution on the Mach lines extracted were considered, the method was not presented and the comparison between Schlieren results and CFD simulation was done in the reflex and uniform region, where the fluid is in the almost ideal state. Gori *et al.* (2020) took one more step foreward, presenting an accuracy assessment of SU2 performing an UQ analysis to compute the variability of the numerical solution with respect to the uncertainties affecting the test-rig operating conditions. Pressure and Mach measurements were used, but again a rigorous uncetainty quantification in the experimental framework was not conducted. Furthermore the quality of the data acquisition is a possible area of improvement: the number of pressure taps is less than ten, thus the spatial resolution is limited, the Schlieren images have a low resolution and no uncertainty other than the angular resolution was addressed in the Schlieren data extraction. Finally the steady state condition of the flow is not quantified and the non-repeatability of the process due to the blow down configuration limits the overall result of the accuracy assessment.

The ORCHID is a regenerative hybrid ORC vapor tunne test-bed, with a BoP capable of feeding two different test sections for fundamental NICFD studies and for characterization and testing of ORC components, e.g. mini ORC expanders. It was designed by Head *et al.* (2016) and commissioned at the Aerospace Propulsion and Power laboratory of the Delft University of Technology in a period between mid 2018 and early 2019; its full capabilities and first results are presented in Head (2020). This high-temperature ORC vapor tunnel features a BoP implementing a high-temperature (up to 623 K) and pressure (up to 25 bar) regenerative organic Rankine cycle. At the moment, only a nozzle test section designed for fundamental NICFD studies is installed, but in the near future the design of the turbine test section will be realized and inserted in the setup. The ORCHID has been designed taking into consideration the possibility of using many different working fluids but currently MM has been selected for the first experimental tests: these consist of the characterization of highly non-ideal supersonic expansions in a two-dimensional converging-diverging nozzle. At the moment of writing, only Schlieren images and pressure measurements along the nozzle have been obtained and used to be compared to CFD simulations comparing different equations of state.

1.4   Validation of CFD Software

The CFD community, primarily through the American Institute for Aeronautics and Astronautics (AIAA), was the first engineering community to seriously begin developing concepts and procedures for V&V methodology. V&V stands for verification and validation, both concepts extremely important when dealing with numerical simulation of physical phenomena. Oberkampf & Roy (2010) reports the American Society of Mechanical Engineers (ASME) definition of verification as the process of determining that a computational model accurately represents the underlying mathematical model and its solution; in other words, a model is verified if you are solving the right equations. Validation, on the other hand, is a much more complicated concept and it has many different definitions, each one, on a certain level, has some degree of accuracy, but in reality this concept really depends on the context and the application in which a certain model has to be validated. Oberkampf & Trucano (2002) defines the validation process as a combination of three aspects:

- Quantification of the accuracy of the computational model results by comparing the computed system response quantities of interest with experimentally measured SRQs;

- Use of the computational model to make predictions, in the sense of interpolation or extrapolation of the model, for conditions corresponding to the model's domain of intended use, and

- Determination of whether the estimated accuracy of the computational model results satisfies the accuracy requirements specified for the SRQs of interest.

Although the definitions and details of model validations may vary depending on the point of view, all the most influencial pubblications reguarding software validation have common best practices and general outlines. Organisations such as the American Institute of Aeronautics and Astronautics (AIAA), American Society of Mechanical Engineers (ASME), and the Joint Army Navy Nasa Air Force (JANNAF) have also expressed an interest in validation standards and published documents for reference, usually based on a preferential approach of one of the main authors in the V&V field. The most influencial authors having discussed the concept of validation, such as Eça *et al.* (2010), Roache (2009), Coleman & Steele (2009) and Roy & Oberkampf (2010), have analyzed and criticised the competing approaches to code validation in academia and industry, but they all agree that validation has four principle criteria:

- Validation is done through comparison of software results with experimental data;

- Code verification and solution verification must precede the validation stage;

- Validation experiments are kept to the highest standard of rigour, with detailed records of geometry, conditions, and apparatus in order to identify all possible error sources and quantify the correlated uncertainties ;

- The Validation metrics must consider the uncertainties in the experiment as well as in simulation results.

Now, having defined what validation is and what are the criteria that a rigourus validation has to follow, the choice of an appropriate validation metric is necessary. In literature, many different software validation metrics have been discussed, but it is possible to identify the main detailed metrics which define, nowadays, the state of the art in validation applied to CFD software. The key validation metrics are the ASME [American Society of Mechanical Engineers (ASME) (2009)] standard, based on Coleman's work, Romero's real space validation methodology [Romero (2015), ?] and the Probability bound analysis (PBA) approach of Oberkampf and Roy [Roy & Oberkampf (2010)]. The following sub section briefly explain the first two key metrics, which seem to be capable of giving a more detailed feedback on the level of accuracy of a numerical prediction.

Coleman Approach(ASME standard)

The validation metrics presented by Coleman & Stern (1997) and Eça *et al.* (2010) are the validation standard uncertainty U_{val} ad the validation comparison error E. The validation uncertainty is defined as the square root sum of three independent uncertainties as follows:

$$U_{\text{val}} = \sqrt{U_{\text{num}}{}^2 + U_{\text{input}}^2 + U_{\text{D}}^2}. \tag{1.4}$$

The numerical uncertainty U_{num} is the uncertainty in the system response quantities (SRQ) predicted by the model, deriving from the *numerical* procedure adopted to solve the equations. This uncertainty is the square root sum of three different components: the round-off , iterative and discretisation error. The first two error sources can be considered negligible if double precision values are used together with sufficiently converged solutions, while the discretisation error can also be neglected when sufficiently fine meshes are used; grid convergence studies can be adopted to assess the influence of the discretization uncertainty: if the mesh is fine enough and the result of the grid refinement study present a small discretization uncertainty, this can also be neglected[(Roache, 2009), Celik *et al.* (2008)]. The uncertainty in the simulation input parameters U_{input} depends on the level of accuracy in the knowledge of the the code's inputs such as fluid properties, geometry and/or boundary conditions. Finally, U_{D} is the total uncertainty on the SRQ in the experimental results.

The validation comparison error is defined as the difference between the average numerical prediction S and the average experimental values D of the SRQs under consideration:

$$E = S - D = \delta_S - \delta_D. \tag{1.5}$$

Now, the error of the model is somewhere in the interval of the validation comparison error plus or minus the validation uncertainty:

$$\delta_{\text{model}} = E \pm U_{val}.$$

It follows that the goal of the procedure is to estimate the interval

$$[E - U_{\text{val}} \ , \ E + U_{\text{val}}]$$

that contains the modelling error, δ_{model}, with a 95% confidence level. The validity of the model is proportional to how much smaller the error E is with respect to the validation uncertainty, given that this one is not too large obviously. The model needs to be improved if $|E| > U_{\text{val}}$, however, if $|E| < U_{\text{val}}$ then the model is capable of predicting the physics of the problem under investigation. The magnitude of $|E|$ relative to U_{val} that confirms the level of validation is somewhat arbitrary and must be defined for each specific case study.

Romero Real Space Approach

The Real Space metric compares the error between prediction and experiment with separate experimental and simulation uncertainties to convey clear information of what the comparison error indicates. Romero (2015) presents the experimental results and the simulation results side by side, with net total uncertainty bars U_D on the experimental values and net uncertainty bar U_{sim} on the simulation. Again, the simulation uncertainty is the square root sum of the three main uncertainties of the simulation, namely the input, numerical and discretization uncertainties.

This metric, therefore, defines four cases of validity (reported in Fig. 1.4) for a point of validation:

1. Zero order validity: limits of the experimental value lie within the simulated uncertainty bounds;

2. Dubious validity A: the simulated uncertainty bounds lie within the larger experimental uncertainty bounds;

(a) Zero order validity

(c) Dubious validity B

(b) Dubious validity A
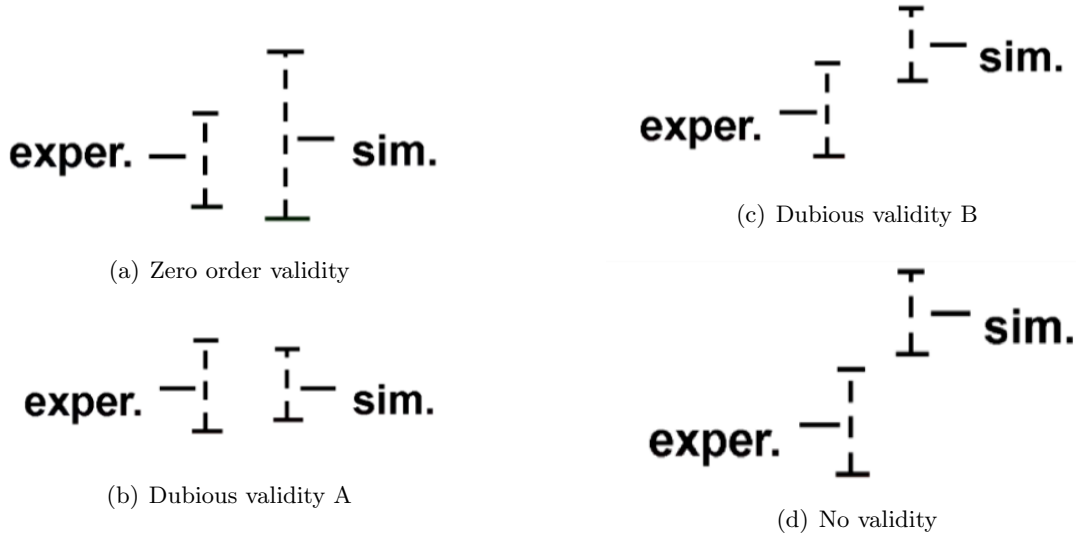
(d) No validity

Figure 1.4: Real space validation cases - taken from Romero (2011).

3. Dubious validity B: uncertainty bounds of the two results overlap;

4. No validity: the uncertainty bound do not overlap.

Bills (2020) shows how Romero validation method proposes the distinction between travelling uncertainties, which are propagated through the constitutive model (the model to be validated), and non-travelling uncertainties which are not. The experiment is designed to focus on the constitutive model (fluid sub-model in the case of the present thesis), but uncertainties related to the other models, often, cannot be completely removed (for example turbulence or viscosity in the present case). For this reason Romero proposes separation between these uncertainties because the travelling ones affect subsequent uses of the constitutive model beyond the single validation exercise. If the constitutive model will be used for a validation, the travelling uncertainties need to be propagated through, while the non-travelling uncertainties will not be propagated. In theory the experiment design should remove non-travelling uncertainties if possible. Bills (2020) explains how the metric then requires the distinction between uncertainties affecting the experiment, and uncertainties affecting the model. This division is fundamental for the final metric since the experimental and model uncertainties will never be reunited. The uncertainties should also be distinguished between aleatory and epistemic. This leads to many potential groups of uncertainties, which will each be calculated separately, then combined to form the net U_D and net U_{sim}. The details and mathematical manipulations of each uncertainty type of the method are presented by Eklund *et al.* (2016).

Evaluating the uncertainty with the Real Space method is procedurally different from Coleman ASME standard, but it provides equivalent results with more information. Both methods compare an experimental value and simulated values with full consideration of all uncertainties, however there is a clear difference in the final presentation of the uncertainties: Coleman & Steele (2009) puts all the uncertainties together, while Romero (2015) Real Space approach distinguishes the sources of uncertainty and focuses on their categorisation since evaluating and propagating uncertainties depends on their type and influence on the model to be validated. The Real Space method is suggested for complex validation exercises where few simulations can be done within the allotted time, such as the fire model validated as shown by Romero *et al.* (2010). The Real Space method conveys the most information about the level of validity of each component that influences the final comparison between simulation and experiment, but it is also the most complicated to produce due to the uncertainty categorization and propagation.

In conclusion, the division of experimental uncertainty, which describes how well true physics can be observed, and model uncertainty, indicating the precision of the software, conveys information about the solver to developers and users. It follows that the model should not provide a resolution

greater than that which we can observe in the experiments, otherwise the simulated answer could produce theoretical results that are not physical. Ideally, the uncertainty bars for the experiment and simulation would match completely. With the Real Space metric improving U_D can change the model assessment from a dubious validation to zero order validation given that the simulation results are accurate. Then, if zero order validation is achieved, the calculated U_{sim} can be interpreted as the uncertainty of the model for that case.

1.5   SU2 Flow Solver Overview

Pini *et al.* (2017) and extended the capabilities of the open-source SU2 software suite for the numerical simulation of NICFD viscous flows over unstructured grids. A built-in thermodynamic library implementing complex thermophysical laws has been developed by Vitale *et al.* (2015) and incorporated in SU2 to account for the non-ideal thermodynamic characteristics of fluid flows evolving in the close proximity of the liquid-vapour saturation curve and critical point. Pini *et al.* (2017) shows that the numerical methods, namely the Approximate Riemann Solvers (ARS), viscous fluxes and boundary conditions have been generalised to non-ideal fluid properties. Quantities of interest for turbomachinery cascades, as loss coefficients and flow angles, can be automatically determined and used for design optimization. The results obtained by Pini *et al.* (2017) demonstrate that SU2 is highly suited for the analysis and the automatic design of internal flow devices such as ORC expanders operating in the non-ideal compressible-fluid regime. Although SU2 is capable of implementing complex thermodynamic models and equations of state for NICFD flows [Economon *et al.* (2015)], its level of accuracy is yet to be quantified, since the software has never been validated for these flows. For this reason, the research question still stands today: *is the SU2 flow solver capable of accurately predicting classical NICFD flows for dense organic vapors? Which models need to be used to produce valid results depending on the thermodynamic state of the flow? How can these models be validated?*

In any modern scientific computing analysis there is a wide range of submodels that are combined to yield the complete physics model for the simulation [Oberkampf & Roy (2010)].For this reason it is important to critically examine each submodel to try and determine if the assumptions in the submodel are appropriate for the experiment of interest and, later, evaluate important modeling assumptions, for example in this case the inviscid flow or the neglection of the 3D effects, of the flowfield to determine their effect on the result. Understanding which equation of state is accurate depending on the non ideality of the expanding flow is fundamental to validate the entire software for efficient ORC expander design and optimization. SU2 is composed of different sub-models that are necessary to predict the behaviour of a flow. These sub models are presented in Fig. 1.5. The first
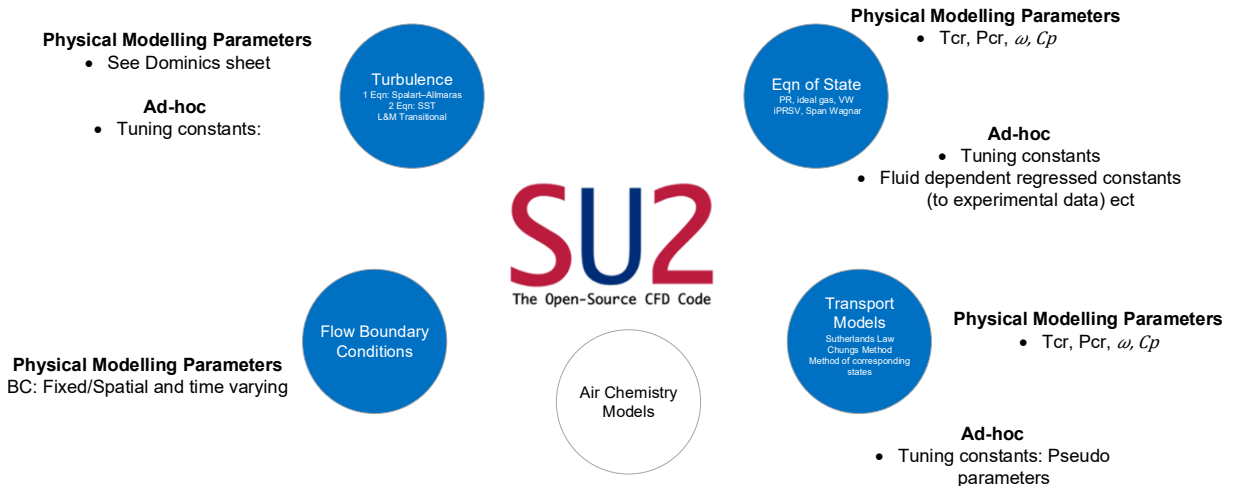
Figure 1.5:   Overview of the SU2 computational sub-models.

sub-model that needs validation is the equation of state of the fluid (also referred as fluid model): all the thermodynamic parameters such as temperature and pressure of the flow are evaluated by the equation of state. For this reason, this model is the most important one in the prediction of the fluid behaviour since all the other sub-models depend on it. For example, the specific heat, which is represented by a polynomial equation with fluid-tuned parameters, depends on the local

temperature of the flow, which is calculated with the equaiton of state. The turbulence sub-model as well depends on the values of the viscosity of the fluid as well as on the density, both variables that depend on local thermodynamic properties of the fluid.

For this reason, the NICFD fundamental research currently focuses on assessing which model is more appropriate to simulate non ideal organic vapor flows depending on the operating conditions of the flow, in other words, depeding on the non ideality of the flow represente by the compressibility factor Z and the fundamental derivative Γ.

SU2 main governing equations and sub-models

The Navier-Stokes (NS) and the Euler governing equations are implemented in SU2; both equation systems are specialized for the compressible and incompressible cases. The compressible NS conservation equations are capable of describing the behaviour of any flow, given that additional equations are coupled to the Navier-Stokes system to close it. By assuming constant density, one can derive the incompressible Navier Stokes equation; on the other hand, by neglecting heat transfer and viscosity the Euler equations can be easily obtained.

The NS conservation equations, namely mass, momentum and energy, can be written in the convective or conservative forms, but also integral or differential forms; switching from one definition to another is very simple. The differential conservative form of the conservation equations simply relates the change over time of the considered variable in a fixed point to the derivative of the flux of that variable through a control volume and to a source term S. For brevity, one can define the vector made of the first terms of the conservaion equations

$$\mathrm{U} = \begin{pmatrix} \rho \\ \rho\vec{q} \\ \rho E \end{pmatrix}$$

where ρ is the density of the fluid, $\vec{q} = (u, v, w)$ is the 3D velocity vector of the flow and E is the total energy per unit mass. Similarly, the fluxes can be summarized in two vectors, the convective fluxes and the viscous fluxes:

$$\mathrm{F}^{\mathrm{c}} = \begin{pmatrix} \rho\vec{q} \\ \rho\vec{q} \times \vec{q} + \bar{\bar{I}}P \\ \rho E\vec{q} + P\vec{q} \end{pmatrix}$$

$$\mathrm{F}^{\mathrm{v}} = \begin{pmatrix} \cdot \\ -\bar{\bar{\tau}} \\ -\bar{\bar{\tau}}\vec{q} - k\nabla T + \end{pmatrix};$$

where P is the static pressure, T the temperature, k the thermal conductivity and $\bar{\bar{\tau}}$ is the viscous stress tensor. Considering Newtonian fluids, for which one can express the viscous stress as a function of the dynamic viscosity μ and the velocity gradients, and Stokes hypothesys neglecting the bulk viscosity thus implying that $\lambda = 2/3\mu$, one can express the viscous tensor as

$$\bar{\bar{\tau}} = \mu(\nabla\vec{q} + \nabla\vec{q}^T) - \frac{2\mu}{3}(\nabla \cdot \vec{q})\bar{\bar{I}}.$$

It is now possible to express the NS equations in the compact conservative form:

$$\frac{\partial \mathrm{U}}{\partial t} + \nabla \cdot (F^c + F^v) - S = 0. \tag{1.6}$$

The system is close by using either the simple ideal gas equation of state or more complex models available. When turbulent flow are considered, Reynolds-Averaged Navier-Stokes (RANS) are solve in accord with the standard approach to turbulence modeling based upon the Boussinesq hypothesis,

which states that the effect of turbulence can be represented as an increased viscosity. Thus, the effective viscosity is now the sum of the dynamic and turbulent components:

$$\mu = \mu_d + \mu_t;$$

as a consequence the thermal conductivity in the energy equation becomes an effective thermal conductivity written as

$$k = \frac{\mu_d C_P}{Pr_d} + \frac{\mu_t C_P}{Pr_t},$$

where the turbulent parameters μ_t and Pr_t are obtained from a chosen turbulence model involving the mean flow state variables $\overline{U}$ and a series of other parameters which depends on the model used. The Shear Stress Transport (SST) model of Menter and the Spalart-Allmaras (S-A) model are two of the most common and widely used turbulence models; the S-A and SST standard models, along with several variants, are implemented in SU2.

Choice of the Simulaiton

As mentioned before, the validation of a software is a very complicated and long process. Each sub-model has to be validated separately otherwise it is not possible to identify where the model error lies; but even the validation of the sub-models is a very challenging process. Not only valuable experimental data for the chosen SRQs has to be gathered, but the correct design of experiments and conditions requires time, furthermore all the uncertainties affecting the experimental result must be quantified. When complicated phenomena are being studied, it is recommended to isolate as much as possible each single influence on the final result. For this reason, the first complete accuracy assessment of the deterministic SU2 simulations using Schlieren data was performed isolating the influence of the equation of state. For this reason, Euler simulations had to be performed in order not to introduce errors in the turbulence model used. The Equations of state used are the Peng-Robinson and the Ideal gas, both implemented in SU2, coupled with the polytropic (constant specific heat ratio) or non politropic (specific heat variable with the temperature) assumptions.

Chapter 2

The ORCHID

The Organic Rankine Cycle Hybrid Integrated Device (ORCHID) is a research facility resembling a state-of-the-art high-temperature organic Rankine cycle (ORC) system capable of continuous operation with different working fluids that has been designed by Head *et al.* (2016) and built at Delft University of Technology, the Netherlands. It consists of a single balance of plant (BoP) realizing an ORC which provides a continuous steady state flow in different operating conditions that can feed two different test sections, alternatively. The first TS consists of a nozzle with optical access to perform fundamental experiments, whose research objectives are the verification of NICFD theoretical fundamentals [Guardone *et al.* (2014)] and the validations of the related thermodynamic models and CFD codes[Vitale *et al.* (2015)]. The second TS is a test-bench for mini-ORC expanders, e.g. turbines, up to a power output of 100 kWe, whose aim is to provide data to validate or develop semi-empirical correlations for fluid dynamic losses, to assess design methodologies, and to evaluate the accuracy of CFD flow solvers for ORC turbomachinery [Casati *et al.* (2014)].

2.1   Overview

The ORCHID setup can be operated with a variety of working fluids as shown by Head (2020). The maximum achievable WF temperature and pressure are specified to be around 300° C and 25 bar allowing for the realization of a wide range of thermodynamic regimes of interest for NICFD studies and ORC applications. As previously mentioned, the ORCHID setup is conceived for both fundamental studies on NICFD flows and for testing and characterizing efficiency parameters of ORC components, most notably expanders. It features a BoP implementing a high-temperature regenerative ORC system configuration, as this is deemed the best solution for small (power output $3-50$ kW$_e$), cost-effective decentralized systems for waste heat recovery .

The innovative BoP configuration allows continuous measurements campaigns for highly supersonic flow regimes with a wide range of conditions typically encountered in supersonic ORC turbines. The exit Mach number for the designed nozzle is $M \approx 2$ while the thermodynamic conditions of the flow can span in a wide range of interest for present and currently envisaged mini ORC applications, having a maximum working fluid temperature $T_{\max} \approx 300^o$ C and pressure $P_{\max} \approx 25$ bar, allowing measurements, in both the test sections, in steady state liquid-vapor two phase, sub-, and super-critical regimes.

2.2   Balance of Plant (BoP)

The ORCHID facility is subdivided into three different closed loops; namely, the heating loop, the WF loop and the cooling loop. The TS is isolated from the WF loop by two pneumatically actu-
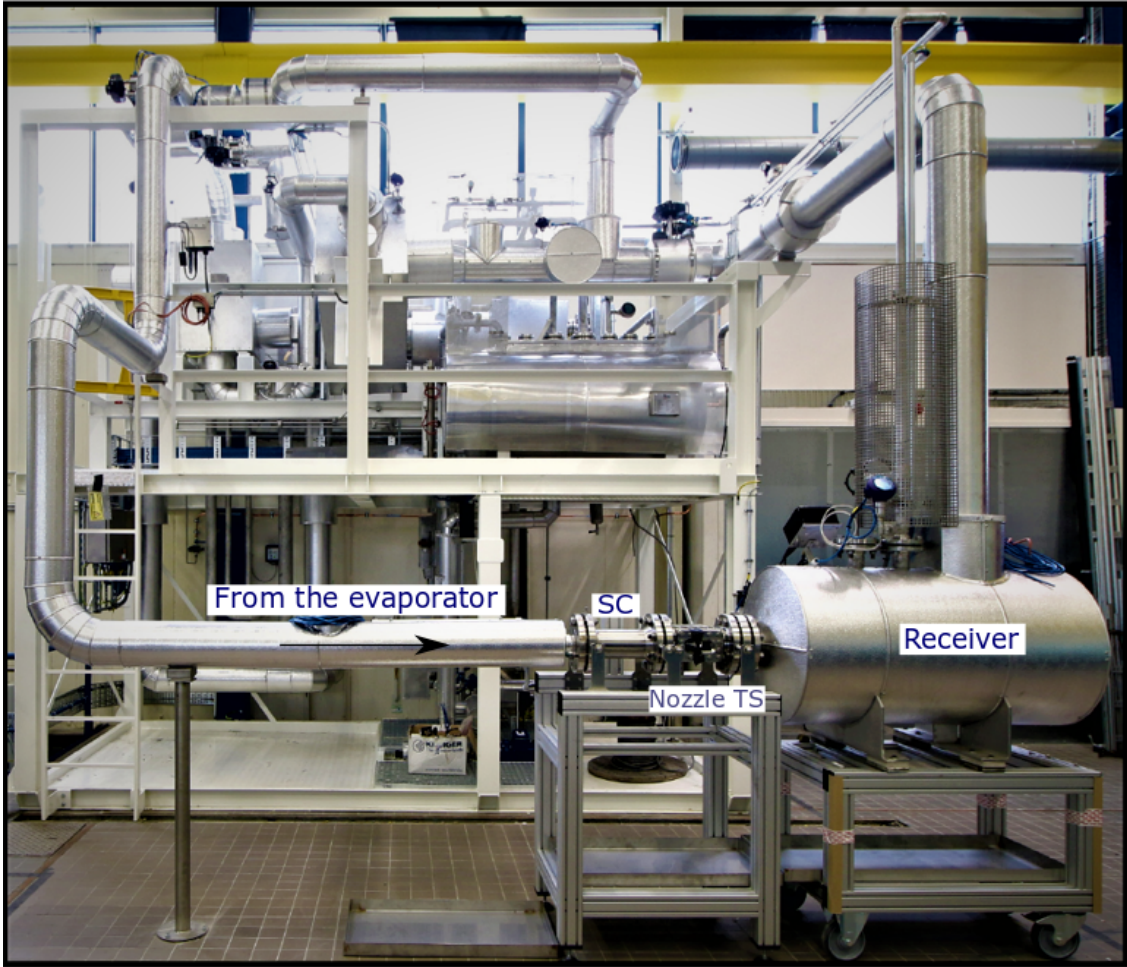
Figure 2.1: Frontal view of the ORCHID; the nozzle test section can be seen in the foregrownd next to the receiver - adapted from Head (2020).

ated equal percentage gate valves [1]; namely, MOV002a and PCV003. These valves can be opened depending on the required operational modes, e.g., operation over the bypass, as is the case during start-up, or over the TS. The setup can be equipped with two different test sections, however, the current configuration adopts the nozzle TS while a radial turbine will follow in the near future. The WF loop is further divided into to a high and low pressure section. The high pressure section ($P_{\mathrm{WF,max}} = 23.5$ barg) is the part of the setup between the primary pump and the TS, or before the bypass line. The low pressure section ($P_{\mathrm{WF,max}} = 4.5$ barg) is located after PCV003 or after OR01. The orifice OR01 of the bypass line has a circular conical hole of 16.5 mm and is designed to achieve a pressure drop similar to the one on design achieved in the nozzle in order to protect the heat exchangers from pressure shocks when the operational mode is changed from the bypass to the TS and vice versa.

The primary positive displacement (volumetric) pump requires a rather large NPSH, thus a ROTOS single stage magnetically driven centrifugal booster pump is placed in series right before the primary pump in order to obtain the required maximum pressure of the WF designed for the facility. A pulsation damper was also necessary since the primary pump Wanner Hydra Cell G35 15 has the drawback of creating a pulsating flow and vibrations. The Alfa Laval heat exchagers were sized based on a conservative estimates of heat transfer properties on the hot and cold sides

---

[1]The equal percentage mechanically operated valve (MOV) are not completely leak tight, so vapor can condense forming pools of liquid in the nozzle.

(a) Isometric View of the ORCHID.
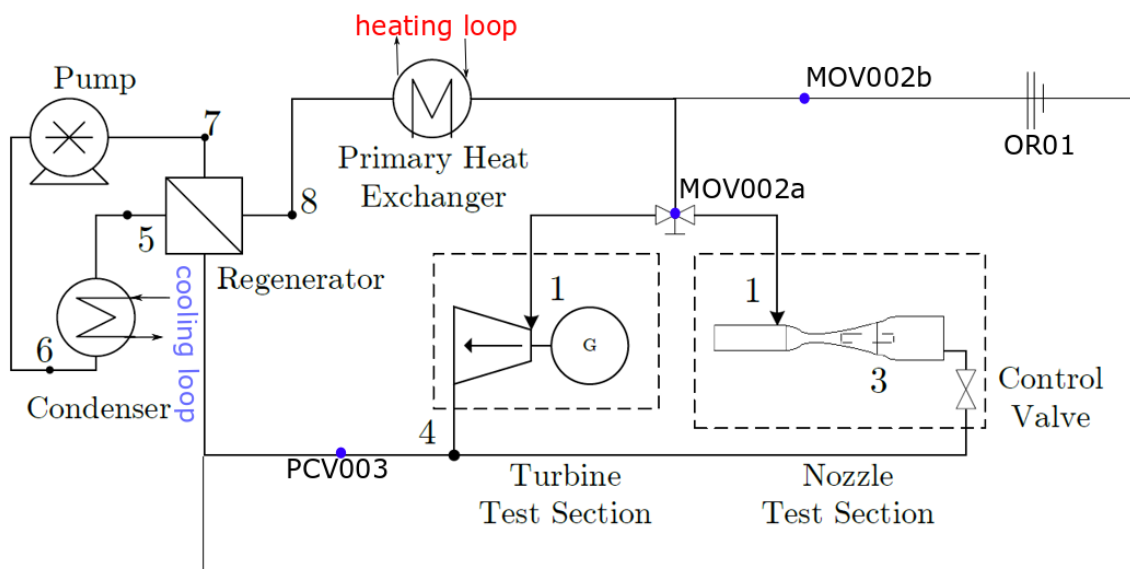
(b) Simplified PFD of the ORCHID. Adapted from Head *et al.* (2016).

Figure 2.2: The Organic Rankine Cycle Hybrid Integrated Device (ORCHID) is located in the Propulsion and Power (PP) Lab of the Aerospace faculty at the TU Delft.

respectively. The regenerator is a shell and plate heat exchanger with a thermal load of 317 kW$_{\text{th}}$. After the fluid leaves the pulsation damper and the regenerator, the prewarmed WF then travels to the evaporator (primary heat exchanger) where the fluid changes to the vapor state. The evaporator is also a shell and plate heat exchanger with a thermal load of 317 kW$_{\text{th}}$.

The nozzle TS requires a thermal power input of 400 kW$_{\text{th}}$ on design conditions, while the turbine test section will be operated at 1/7th of this power. The WF mass flow during the on design nozzle experiments is 4122 kg/h while for turbine testing will vary between 300 and 600 kg/h. After the test section, the hot vapor enters the regenerator preheating the cold liquid on the other side. Once the vapor enters the condensor is changed back to the liquid state. The condenser is a plate heat exchanger with a thermal load of 377.5 $kWth$, connected to the cooling loop, which is a separate loop operating with a glycol water mixture. The cooling water pump is a cast iron monoblock centrifugal pump and the speed is controlled up to a maximum motor speed and a flow rate. The heat transferred is dissipated by a tube and fin aircooler. The heating loop is also a separate loop operating with Therminol VP1 whereby the thermal source is an electric heater from HTT. The HTT pump is a magnetically driven centrifugal pump with a design speed of 2900 rpm.

2.2.1   Pressure Losses from the Evaporator to the Nozzle Inlet

During the Schlieren acquisition process runs presented in this thesis, direct measurements of the inlet pressure of the nozzle have not been aquired. The measurements of the evaporator pressure PZA003 therefore need to be processed to estimate the nozzle inlet total pressure and its uncertainty. The system connecting the evaporator, where PZA003 is measured, to the inlet of the nozzle is well known and has a fixed configuration. The flow exiting the evaporator has to travel in a pipeline, a equal percentage configuration gate valve (MOV002a) and in the settling chamber (SC), at very low speeds. Before getting into the details of how the losses can be calculated and how the uncertainty is propagated through the components, a few important consideration on the three components in the connection beteen the evaporator and the nozzle are presented.

MOV002a   : A mechanically operated valve is positioned after the evaporator to control the flow and for safety reasons in case a quick reduction in the mass flow in the test section is needed. The valve introduces a pressure drop ΔP_1 which is a function of the valve opening parameter, the mass flow rate and the fluid under consideration. There are characteristic curves and parameters provided by the supplier of the valve which can be used to evaluate coefficients that can be used in semi-empirical formulas to evaluate the presure drop across the valve as a function of the opening of the valve ϕ, type and state of the fluid, mass flow rate $\dot{m}$ and the flow thermodynamic parameters such as γ.

Pipeline   : The pipeline that connects the evaporator to the nozzle's settling chamber details, e.g. length, geometry, surface roughness, are known. The pressure drop ΔP_2 in a pipeline depends on the friction coefficient λ, the geometric parameters of the pipe such as the length over diameter ratio and the surface roughness inside the pipes, the geometry of the line itself such as the curvature and the type of corners, which defines the value of experimental coefficients, and mostly on the velocity of the flow. The relation of a general pipline total pressure losses a can be expressed as

$$\Delta P_2 = \lambda \left(1 + \sum_{i=1}^{N_{corner}} k_i \right) \frac{l_i}{D} \frac{V^2}{2g} \tag{2.1}$$

where $l - i$ are the length of the segments, D is the diameter of the pipe, V the velocity of the flow, and λ is the friction coefficient that can be evaluated by solving Colebrook-White equation

$$\frac{1}{\sqrt{\lambda}} = -2 \log_{10} \left(\frac{\epsilon_r}{3.7D} + \frac{2.51}{Re\sqrt{\lambda}} \right)$$

which correlates the friction coefficients to itself and two other adimensional coefficients, namely the Reynolds number and the adimensional rugosity of the pipe line ϵ_r/D.

Settling Chamber : The honeycombs and screens installed in the settling chamber minimize 3D effects, non uniformities in the flow and turbulence such that the quality of the flow in the test section is as high as possible. These settling chamber installations before the nozzle test section introduce another pressure drop ΔP_{sc}. Each Screen is characterized by a pressure drop coefficient k_j:

$$k_j = \frac{\Delta P_j}{q} = f_1(Re, \sigma, \theta)$$

and a deflection coefficient

$$\alpha_j = f_2(\sigma, k_j, \theta),$$

where Re is the Reynolds number Re, σ is the open area ratio, $q = 1/2\rho V^2$ is the dynamic pressure and θ is the flow incidence angle. The total pressure drop in the settling chamber is obviously the sum of all the pressure drops across the installed screens:

$$\Delta P_{sc} = \frac{1}{2}\rho V^2 \sum k_j \tag{2.2}$$

An estimation of the total pressure losses from the evaporator to the inlet of the nozzle combining the evaluation (via semi-empirical formulas and coefficients) of the three elements single losses

$$\Delta P_{\text{loss}} = \Delta P_1 + \Delta P_2 + \Delta P_{sc},$$

does not provide an accurate prediction. Furthermore the propagation of the uncertainties cannot be quantified accurately since the characteristic curves, coefficients and formula used to evaluate pressure losses rarely take into account the uncertainty of the coefficients or the fitted curves. It is also important to notice that if any of the equations evaluating the pressure drop from the evaporator to the inlet of the nozzle have a dependancy on the pressure value itself, then the original uncertainty on the evaporator pressure must be propagated through all the equations containing the pressure. In conclusion, not only it is very inaccurate to evaluate each component losses singularly using coefficients and curves with no related uncertainty, it is also a very long process if uncertainty propagation has to be taken into account.

Wind tunnel calibration procedures have been proven to be the most reliable method to evaluate characteristic parameters of the experimental set up as a whole. Plenty of literature is available for many classical wind tunnel layouts and operating regimes, such as subsonic, transonic, supersonic and hypersonic [Pope (1961), AGARD (1994)]. When calibrating a wind tunnel, many parameters can be adjusted or experimentally evaluated in order to correct the measurements and results of the experimental campaing taking into account all possible error sources such as boundary layer effects on the TS geometry, flow angularity, unwanted pressure gradients, losses, and more. The ORCHID acquistion instruments, have been correctly calibrated and aligned to minimize bias errors. The error source analysis will be discussed in detail in Sec. 2.6. During the first data acquisition campaigns of the ORCHID, the inlet pressure measurements were not available: in this case appropriate calbration curves are fundamental to correctly transform the evaporator pressure mean and uncertainty in the nozzle inlet pressure and uncertainty. These calibration curves are the most accurate method to evaluate the pressure losses and the uncertainty change due to the pipeline, valve and settling chamber components. These curves can be easily obtained with a few dedicated experimental runs in different typical operating conditions. Now, the geometry and details of the pipeline, MOV002a and the SC are fixed; thus the diameter of the pipes, the geometric parameters of the settling chamber as well as the valve are constant and do not influence the pressure losses when the operating conditions of the facility change. The valve opening parameter ϕ will always be fixed at 100% since this will obviously minimize the losses across the valve at any operating conditions of the fluid. The
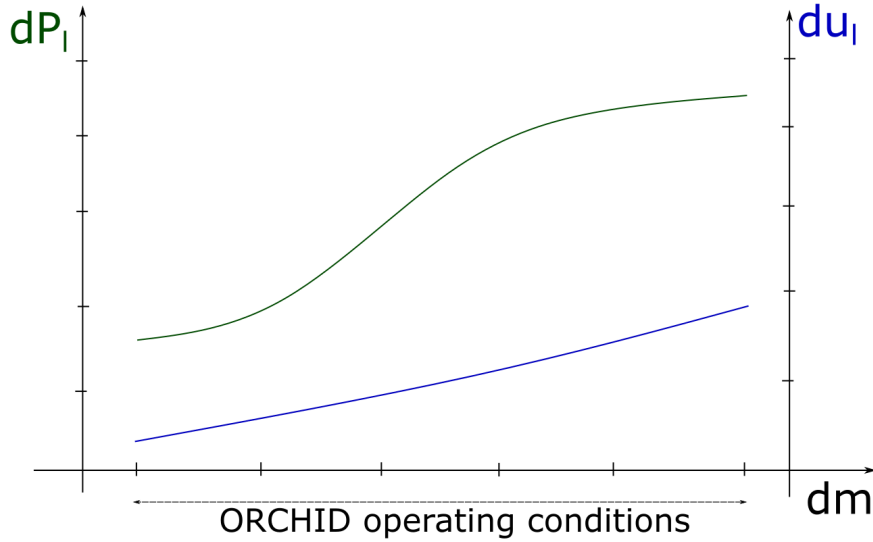
Figure 2.3: Example of the calibration curve results for the pressure losses and uncertainty correction coefficeints.

characteristic curves of the pressure loss and standard uncertainty change before the inlet of the nozzle, can therefore be obtained for a given working fluid (MM for example), and the fixed design of the ORCHID. Before proceeding to the regression of data to obtain the calibration curves, the following correction coefficients need to be defined:

$$dP_l = \frac{\text{mean}(PZA003) - \text{mean}(P_{in})}{PZA003}$$

$$du_l = \frac{\sigma_{PZA003} - \sigma_{P_in}}{\sigma_{PZA003}}$$

$$dm = \frac{\dot{m}}{\rho_{PZA003}VD^2},$$

where σ is the standard deviation of the acquired variable, V is the velocity of the flow in the pipe and ρ is the density of the fluid. The procedure suggested is very simple: firstly, keeping the opening parameter of the valve at 100%, different operating conditions for the ORCHID BoP need to be chosen, from lower mass flow rates, determined by almost ideal gas conditions not useful for the NICFD results, to the maximum operating conditions allowed by the facility. The velocity and density in the pipes right after the evaporator can be fixed to an on-design value, and must be kept constant. For each of the chosen operating conditions, mass flow rate, evaporator pressure and nozzle inlet pressure are acquired in a minimum 10 min. interval of steady operating conditions. The adimensional parameters can then be calculated for each operating condition then, a least square method regression can be performed on the experimental data to obtain the two curves needed. An qualitative example of the expeted results is reported in Fig. 2.3.

For the ORCHID, these calibration curves have not been developed yet due to the very recent construction of the facility, but are expected to be available in the future. In the present work, the pressure losses evaluation has been measured for operating conditions similar to PR.022 and PR.024: direct measurements at the inlet of the nozzle show a total pressure loss of

$$\Delta P_{\text{loss}} \approx 0.7 bar$$

across the pipeline, valve and settling chamber (PR.027 shown by Head (2020)). From preliminary analysis of the uncertainties it was possible to notice a reduction in the fluctuations of the pressure: this was an expected result since the SC has the main functionality of reducing turbulence and fluctuations, increasing the overall quality of the flow entering the nozzle. In the present work, the

total expanded uncertiainty on the inlet total pressure is assumed to be equal to the total expanded uncertainty evaluated for the evaporator pressure; when calibration curves are available, a correction factor can then be easily applied to obtin the final correct uncertainty on the nozzle inlet pressure.

$$
\begin{cases}
P_{in}^0 = PZA003 - \Delta P_{\text{loss}} = PZA003 - 0.7 \\
U_{PTin} \leq U_{PZA003}
\end{cases}
\tag{2.3}
$$

2.2.2 The Data Acquisition System

Data acquisition is the process of measuring an electrical or physical phenomenon such as voltage, current, temperature, pressure, or sound with a computer. A data acquisition (DAQ) system consists of sensors, DAQ measurement hardware, and a computer with programmable software. Compared to traditional measurement systems, PC-based DAQ systems exploit the processing power, productivity, display, and connectivity capabilities of industry-standard computers providing a more powerful, flexible, and cost-effective measurement solution.

The ORCHID is equipped with a national instruments (NI) data acquisition and control system. The DAQ contains 35 sensors which records data and monitors the ORCHID's operation as shown by Head (2020). Industrially certified sensors such as pressure and temperature transmitters, a Coriolis mass flow meter and a turbine flow meter are used throughout the facility. The input and output signals measured and controlled by the DAQ system include analogue signals of the sensors and hardware in the range of 4 – 20 mA and 0 – 10 V at a 16-bit resolution. The ORCHID has several types of sensors from WIKA which are used for the acquisition of the thermodynamic variables in the ORCHID; in the following paragraphs, pressure and temperature sensor details are reported as presented by (Head, 2020, Ch.5):

Pressure measurements   There are five 232.50 pressure indicators, a CPG1500 precision digital pressure gauge, and ten UPT 20 type pressure transmitters which have been installed in the low and high pressure side of the WF as well as in the cooling loop. The transmitters are divided into ranges of 0 — 16 barg, -1 – 5 barg and 0 — 40 barg, and their electrical output is a 4 – 20 mA current signal. They are directly connected to a 24-bit A/D input module (NI 9208) in the NI cRIO[2]. All sensors are matched and calibrated to their respective operating range.

Temperature measurements   There are three S5550 temperature indicators and fourteen TR10-C temperature transmitters. All sensors are equipped with a 4-wire input connection, so the influence of the connecting cable on the measuring result is completely eliminated since any possible asymmetries in the connecting cable's lead resistance are also compensated. The temperature transmitters are divided into ranges of $0 - 150^oC$, $-10 - 400^oC$, $0 - 300^oC$, $-20 - 200^oC$ and $0 - 350^oC$; their corresponding electrical output is a 4 – 20mA current signal as it was for the pressure transmitters. They are directly connected to a second 24 - bit A/D input module (NI 9208) in theNI cRIO.

2.3   Nozzle TS

2.3.1   Overview of the Structure and Components

The test section of a wind tunnel facility allows flow measurements for fundamental gas dynamic experiments like the validations equations of state, thermodynamic models, CFD software and much more. Head (2020) splits the ORCHID TS into three compartments: the settling chamber, nozzle

---

[2]CompactRIO is a real-time embedded industrial controller made by National Instruments for industrial control systems.
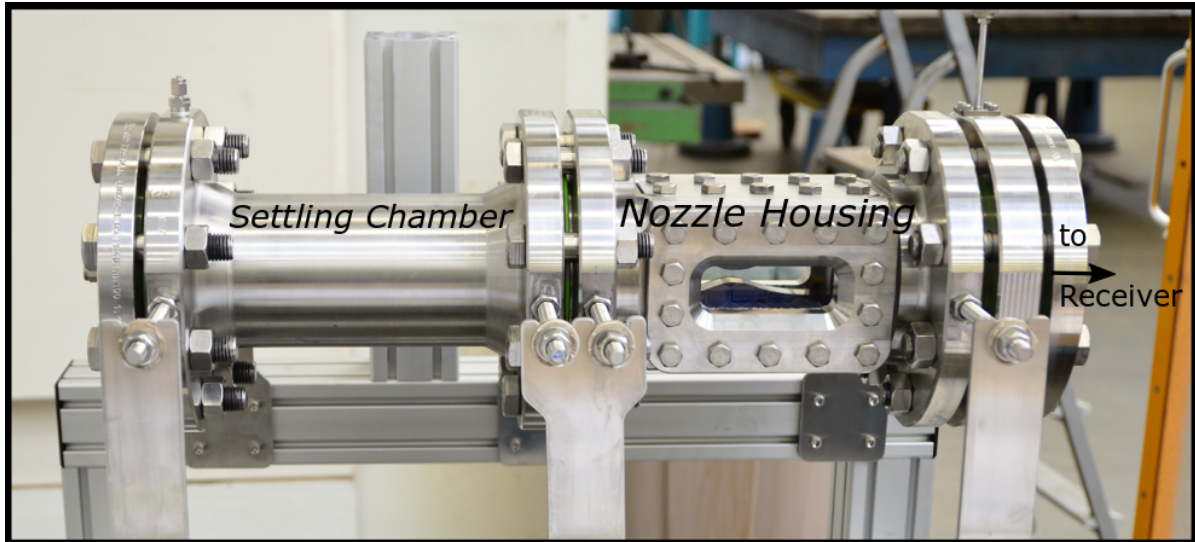
Figure 2.4: The nozzle test section is inside a nozzle housing with windos allowing access for optical flow measurements techiques - adapted from Head (2020).

housing, and the receiver. The first compartment, the SC, contains installations and flow conditioning devices such as honeycombs and screens; these devices are used to lower the turbulence intensity of the flow and uniform the velocity field to an ideally 1D flow, before entering the nozzle housing (NH). Measurements in wind tunnels are influenced by the intensity and scale of the turbulence in the test section: the boundary layer characteristics, as well as the transition, strongly depend on the turbulence level in the test chamber, as a result pressure measurements can be influenced as well as the velocity of the flow and many other derived parameters.

Wind tunnel turbulence should be as low as possible such that optimal measurements can be achieved; this is done by optimizing the honeycombs and screens geometric parameters and placing nets to achieve the decay of the turbulence breaking the large vortices in smaller ones to then be dissipated by the viscosity of the fluid on smaller scales. Head (2020) splits the design of the NH in three different components: the Axisymmetric Contraction (AC), CD nozzle and the Testing Channel (TC). He shows how the AC allows a geometrical transition between the SC to the planar de Laval nozzle and further reduces the turbulence intensity by substantially accelerating the flow axially before reaching the CD nozzle. After this section, the testing channel can be used to study shocks generated by different objects mounted on an appropriate support system. Finally the receiver dissipates most of the kinetic energy of the flow exiting the nozzle by allowing a free jet expansion.

2.3.2   Design of the Nozzle

In order to minimize losses, the nozzle is designed using the method of characteristics together with the Helmholtz energy equation of state following the approach of Guardone *et al.* (2013). A nozzle designed with the MoC ensures that the local flow turning angle, defined by the fluid properties during the expansion, is equal to the local turning angle of the nozzle profiles, thus, ideally, the flow does not perceive the precence of the walls and an isentropic expansion is achieved. The CD nozzle and TC are made from two equal and removable profiles which are made leak tight with Viton seals. This allows to easily reshape the channel geometry, in case a different fluid needs to be tested, thus another nozzle designed since the results of the design using the MoC strongly depends on the fluid properties and thermodynamic conditions.

The ORCHID CD nozzle, presented in Fig. 2.5, has been designed by Head (2020) for MM with

inlet total conditions of $T_{in}^0 = 252^o$ C, $P_{in}^0 = 18.4$ bar, an on design pressure ratio of $P_{in}^0/P_{out}^0 = 8.8$ which fixes the back pressure at $P_{out}^0 = 2.1$ bar, and a design exit Mach number $M_{\text{exit}} = 2$.
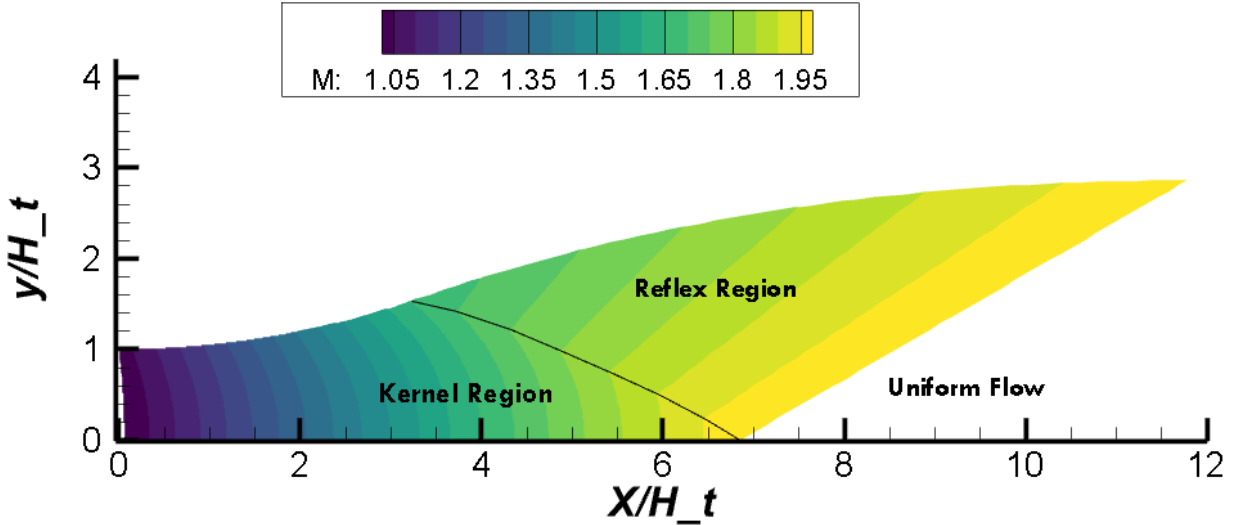
Figure 2.5: The ORCHID nozzle diverging profile designed for the MM with the MoC. The Sauer line is where the io-Mach contours start, the reflex to uniform line is where the contours end.

The geometrical throat, in a real nozzle, does not correspond to the sonic condition: the $M = 1$ line in usually very hard to locate precisely. The MoC requires a supersonic flow condition in order to be performed, thus the nozzle design has to start where the flow has a Mach number greater or equal to one; this starting point can be identified as a line, where the initial value problem is produced. The Sauer line, which can be easily identified as the line from which the solution field (the contour) starts, approximates the sonic line, which in a real nozzle is never a straight vertical line at the geometrical throat, but rather a wide parabola, indicating that the sonic condition on the midplane is reached slighty downstream of the geometrical throat. The Sauer line depends on the upstream section of the throat, the width of the throat as well as on the gas properties. The solution of the MoC, thus the final shape of the nozzle, is largely dependent on the prediction of the Sauer line [Thompson (1988), Zucrow & Hoffman (1976), Anand (2016)]. The Kernel area is bounded by the initial value problem line, the initial expansion curve and the Kernel to Reflex regions line. In this section the flow is expanding because of the expansion waves generated at the wall. As the flow crosses each expansion wave, the fluid expands and its velocity increases. The end of Kernel region implies that the flow on the midplane is fully expanded, thus the uniform flow region begins on the midplane. The Kernel to reflex line is the last characteristic line of the Kernel region: after this line, which starts from the inflection point of the nozzle profile, the flow expands in the reflex region, characterized by straight lines. Note that the reflex region only expands the flow which is not on the midplane. Once the entire flow field is fully expanded the uniform flow section can easily be identified by straight parallel Mach waves; in this section, ideally, the flow has constant properties.

2.4   Schlieren Technique

2.4.1   Optical Theory

Schlieren imaging is a well established experimental technique used to visualize flow fields using the refraction of light caused by the change in the refractive index of the fluid as a function of the local density. For many years it has been fundamental in order to study shockwaves, where the change in pressure and density of the fluid is very sudden and large in magnitude; but when it comes to Mach waves the relative change of the refractive index for conventional fluid is extremely low and this makes the study of mach lines in supersonic flows very hard in conventional wind tunnels. When Organic dense vapours with high molecular complexity are used, the change in the refractive index associated with a change in the density of the fluid is several times larger. Using state of the art facilities like the ORCHID it is possible to capture Schlieren images with clear Mach lines for supersonic expansions of dense organic vapours. It is for this reason that a tool capable to acquire as much data as possible from thousands of Schlieren images was needed.

The speed of light in a given medium c is related to the speed of light in a vacuum $c_0 = 3 \times 10^8$ [m/s] through the refractive index

$$n = \frac{c_0}{c}.$$

It must be noted that the fluid under consideration is sufficiently tranparent such that the absorption of the transmitted light, described by the imaginary part of the refractive index, can be neglected; thus, only the real component of the refractive index is considered.

The refraction of light $\alpha_2 - \alpha_1$ between two mediums having a different refractive index is described by Snell's law:

$$n_1 \sin \alpha_1 = n_2 \sin \alpha_2,$$

where $\alpha_{1,2}$ is the incidence angle of the light beams. In a fluid, there is no clear separation between two different refractive index areas: the refractive index of the fluid, instead, changes gradually with the density

$$n(x) = f(\rho(x)).$$

It follows that the light rays are bent in proportion to the gradient of the refractive index in a plane ∇n which depends on the density gradients in the flow [Goldstein & Kuehn (1983) and Settles (2001)]. The resulting ray curvature by is given in equation 2.4 .

$$\frac{\partial^2 x}{\partial z^2} = \frac{1}{n}\frac{\partial n}{\partial x} \quad ; \quad \frac{\partial^2 y}{\partial z^2} = \frac{1}{n}\frac{\partial n}{\partial y} \tag{2.4}$$

The components of the angular light ray deflection can be obtained by integrating equation 2.4:

$$\epsilon_x = \frac{1}{n}\int \frac{\partial n}{\partial x}\partial z \quad ; \quad \epsilon_y = \frac{1}{n}\int \frac{\partial n}{\partial y}\partial z.$$

For two-dimensional Schlieren images in the test section of depth $z_{in} - z_{out} = L$ along the optical axis, given that n_0 is the refractive index of the surrounding medium, the components of the angular light ray deflection are given in equation 2.5.

$$\epsilon_x = \frac{L}{n_0}\frac{\partial n}{\partial x} \quad ; \quad \epsilon_y = \frac{L}{n_0}\frac{\partial n}{\partial y} \tag{2.5}$$

In order to quantify the refraction of light, the refractive index n as a function of the fluid and its density must be evaluated. There are several mathematical and empirical models in literature which describe the relationship between the refractive index and density in both liquids and gases. A very common one is the Clausius–Mossotti equation, which is expressed in terms of molecular constants, properties of the fluid and the wavelength λ of the illumiation source used [Merzkirch (1987)]. The Lorentz–Lorenz relation together with its various linearised forms [Born & Wolf (2003)], also

expresses the refractivity index in terms of molecular constants, the properties of the fluid and molecular polarizability. A well known simplification of the Clausius–Mossotti equation is the empirical Gladstone–Dale equation, often used for air in the simple linear form

$$n = 1 + K\rho, \tag{2.6}$$

where K is the Gladstone-Dale coefficient which is determined experimentally; for air in standard conditions, $K \approx 0.23$ [cm^3/g] given a visible light source. When air is considered, Eqn. 2.6 shows that n is only weakly dependent upon ρ: a large change in air density would cause a very small change in n, thus Schlieren techique for air is mainly used for the Shock visualization since small density gradient would require extremely sensitive and precise equipment. Unfortunately, the K constant of organic fluids, such as siloxanes, is not known a priori from experiments since it has not been recorded in the literature and its value cannot be estimated theoretically; thus a new approach must be followed.

Head (2020) shows how the refractive index can also be determined from molar refractivity measurements that exist in literature or, if unavailable, by theoretical methods where A is estimated by the concept of additivity of bond refractions together with simplified methods given by Warrick (1946). The molar refractivity A is dependent on n, the pressure P, and the temperature T of the fluid and is defined as

$$A = \frac{4\pi\alpha N_A}{3},$$

where N_A is the Avogadro number and α is the mean polarizability evluated using the Lorents-Lorentz equation by knowing the number of molecules per unit of volume N:

$$\alpha = \frac{3}{4\pi N}\frac{n^2 - 1}{n^2 + 2}. \tag{2.7}$$

By knwoing the molar mass M_{mol} and the density ρ of the fluid one can express the molar volume as

$$\frac{N_A}{N} = \frac{M}{\rho},$$

thus the molar refractivity becomes

$$A = \frac{M}{\rho}\frac{n^2 - 1}{n^2 + 2}, \tag{2.8}$$

where the density ρ must be evaluated with an appropriate complex equation of state for organic vapors. Equation 2.8 can be manipulated to extract the refractive index n as a function of the molar refractivity, molar mass M and density of the fluid as follows:

$$n = \sqrt{\frac{1 + 2A\rho/M}{1 - A\rho/M}}. \tag{2.9}$$

The theoretical evaluation of the molar refractivity A for MM was done by Head (2020). In table 2.1 values of A for MM, D$_4$ (Octamethylcyclotetrasiloxane) and air are compared. From Fig. 2.6

Table 2.1: Molar refractivity value comparison between two organic fluids, namely MM and D$_4$, and one simple mixture gas such as air.

	molar refractivity[cm^3/mol]	reference
MM	48.94	(Head, 2020, Ch.6)
D$_4$	74.6	Warrick (1946)
air	6.66	Merzkirch (1987)

it is easy to notice how the molar refractivity, and thus the refractive index, significantly increases as the complexity of the molecule increases. Consequently, the refractive index change with density for dense organic fluids is substantially larger than the refractive index change for simple mistures such as air due to the much larger value of molar refractivity.
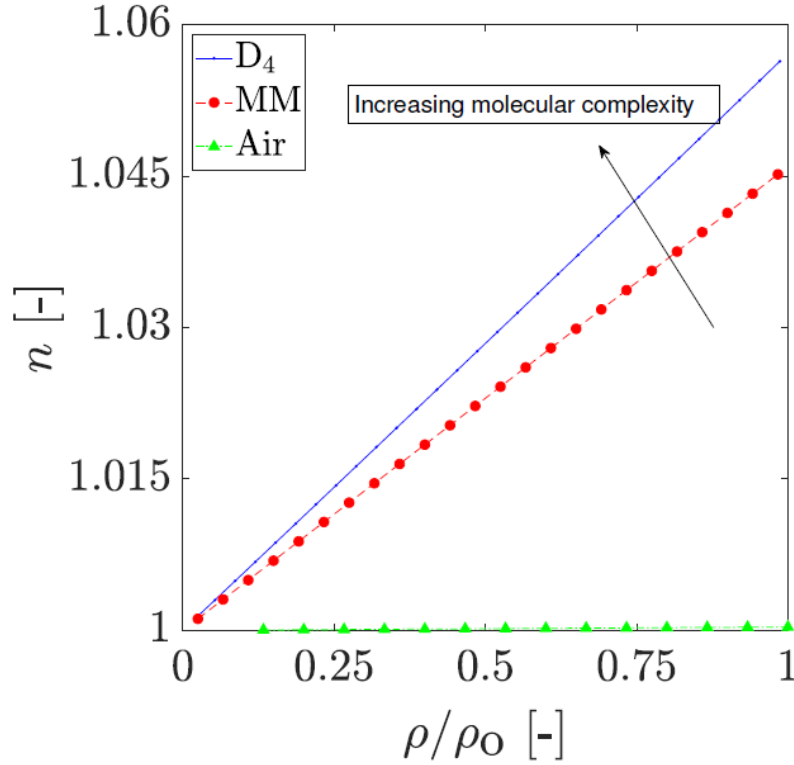
Figure 2.6: Variation of the refractive index n with nondimensionalised density, where ρ_0 is the stagnation density for isentropic expansions for the three fluids with an exit Mach number of approximately 2. Taken from (Head, 2020, Ch.6).

2.4.2   Measurement Chain

The adopted configuration is a flat mirror z-type layout and is shown in Fig. 2.7 and discussed in detail in (Head, 2020, Ch.6). All of the hardware elements, such as the light source (cold white LED from Thorlabs), lenses, mirrors and camera, are mounted on three separate rigid structures which ensure the correct alignment of all components. In all experimental runs the continuous light source was used at the maximum possible intensity. This ensured that measurements could be taken at the highest possible acquisition rates and shutter speeds.

The 2700mW light source from the LED is focused onto the pinhole and then redirected through the nozzle TS by mirror A. The two flat mirrors A and B are used to finely adjust the direction of the light beam towards lens C. The light from lens C is refocused to form an inverted image of the source at the knife-edge, which is a sharp opaque object mounted on an adjustable stand. The knife-edge adjusts the system sensitivity to density gradients in the vertical and horizontal direction by regulating the amount of light that reaches the camera, showing clear bright and dark region depending on how much the light is scattered and how the knife edge is positioned. A horizontal knife edge configuration would be sensitive to the vertical gradients in the flow while a vertical knife edge configuration would be sensitive to the horizontal gradients in the flow [Settles (2001)].

Two different cameras are used to acquire the Schlieren images: one high speed camera was used to mostly study the start up and shut down of the flow field as well as to record possible unsteady behaviour of the flow. For longer acquisition times, a low acquisition frequency camera was used to reduce the amount of data given a specified acquisition time. The first camera used is an Imager ProHS4M High speed camera from LaVision, with a maximum resolution of 2016×2016 pixels delivering up to a maximum frame rate of $1279\ fps$. The second camera used is a mono 16bit CCD camera (Model: BOBCAT IGV-B1610) with an image resolution of 1628×1236 pixels delivering up to maximum frame rate of $25 fps$. The pixel size is $4.4\ \mu m$ and it has a shutter speed/exposure time
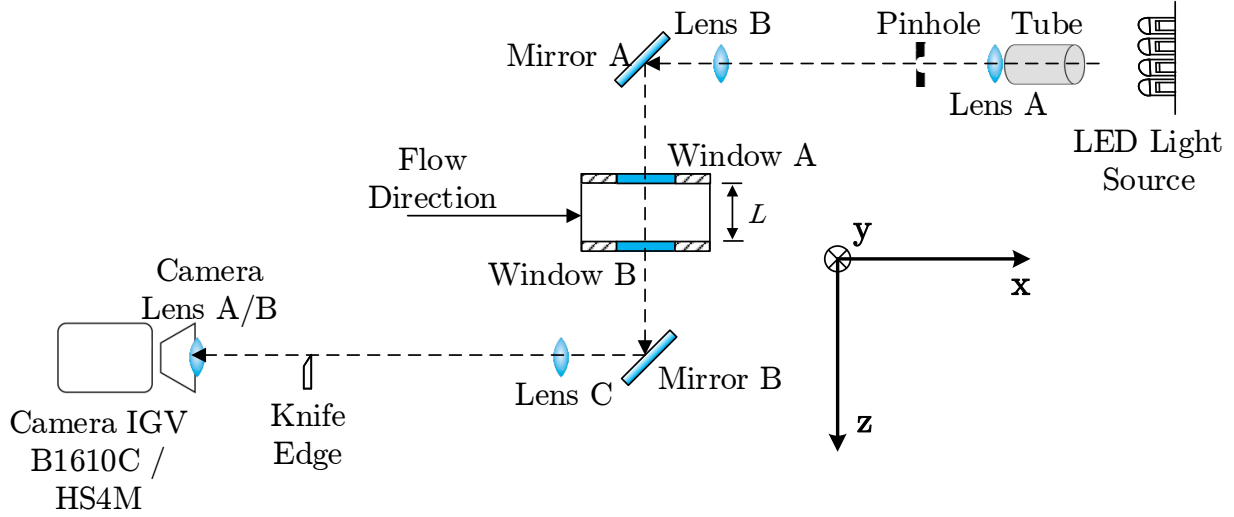
Figure 2.7: Top view of the optical lay-out used for visualising the flow. This is a simple lens-type setup with two flat mirrors. Taken from (Head, 2020, Ch.6).

ranging between $5\mu s$ to $59ms$ (nominal). An overview of the two camera specifications is presented in Tab. 2.2.

Table 2.2: Characteristics of the camera equipment - taken from Head (2020).

Model	HS4M	IGV-B1610C (Bobcat)	
	Value	Value	Unit
Maxiumum Resolution	2016×2016	1628×1236	pixel
Pixel Size	11×11	4.4×4.4	μm
Frame Rate	1279 (2240)[+]	25[*]	fps/Hz
Shutter Speed/ Exposure Time	1.5/1,000,000 to 4/100	1/200,000 to 1/17	sec

[+] Overclocked at full resolution.
[*] At full resolution.

2.4.3 Acquisition Procedure

The ORCHID must be started and the target nozzle boundary conditions achieved before a detailed measurement campaign can be conducted in the nozzle TS. During this period of time, the TS is empty and the flow circulates in the bypass over valve MOV002b and orifice plate OR01. Once the ORCHID BoP has reached steady state conditions (constant evaporator pressure and temperature for one hour or more), the vapor can be redirected over the nozzle TS.

Figure 2.8 shows the typical phases of the flow behaviour of every nozzle experiment on organic vapors at the first opening of the TS (NT.001); in particular the Schlieren images of figure 2.8 are taken from the process run PR.024-NT001. It must be kept in mind that the Schlieren measurement chain acquires the images flipped, thus the flow velocity in the images is directed always from right to left; since the post processing tools are designed to extract data from this Schlieren set up, which is the most common one, in the entire thesis the Schlieren images will be kept in the original orientation from right to left for consistency.

Figure 2.8(a) shows the empty nozzle test section before the opening of MOV002a; MM condensation on the TS windows can be seen due to the non-perfect sealing of the gate valves against the flow, thus since during start up liquid is present in the receiver, condensation is formed in the TS. During the opening of MOV002a, vapor is redirected from the bypass over the nozzle and the total
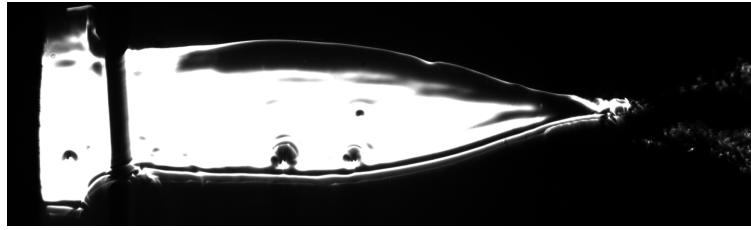
(a) No flow.
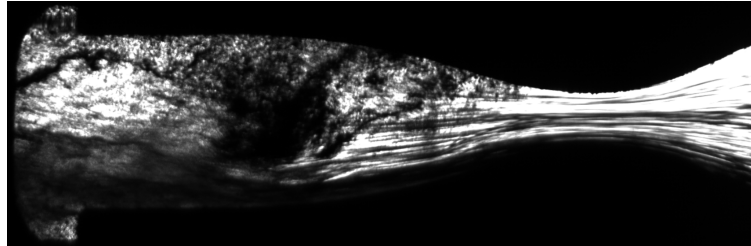
(b) Condensation in the flow during the starting process.
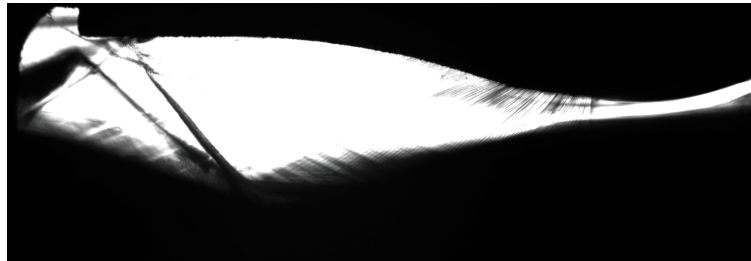
(c) Shock train quickly propagating downstream.
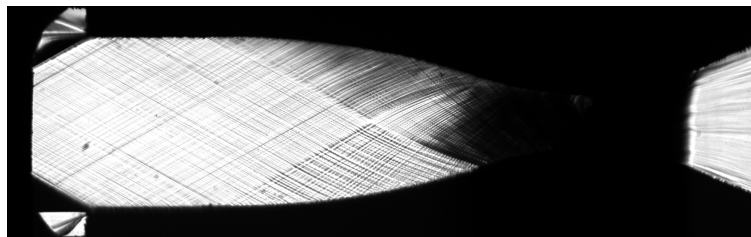
(d) Steady state condition of the flow in the nozzle(over expanded).
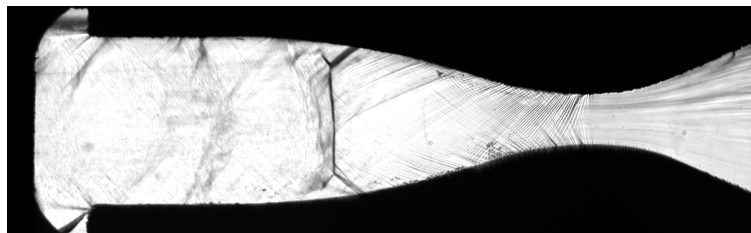
(e) Lambda shocks propagating upstream when the flow in the TS is being shut down.

(f) Calibration image taken after the first start.

Figure 2.8: Main phases in the first opening of the nozzle TS for experiments on organic vapor supersonic expansions. Schlieren images of PR.024-NT001.

pressure in the settling chamber begins to increase. Figure 2.8(b) shows a stream of liquid MM being transported downstream in the diverging section of the nozzle. This is a result of the temperature difference of the core vapor flow and the pipe temperature of the nozzle circuit. Fig.2.8(c) shows a series of very weak oblique shocks inside the nozzle rapidly moving towards the exit (left): condensation is still present in the test section and strongly influences the symmetry of the flow in these initial stages. In Fig. 2.8(d) the nozzle flow has reached steady state supersonic conditions. MOV002a is now fully opened and, after the temperature field stabilized, the back pressure PT004 of the nozzle is controlled to reach the desired value. After the flow reaches the boundary conditions indicated by Tab. 2.4 and the BoP is in steady state operating conditions, Schlieren images pressure can be recorded at the desired camera settings specified in table 2.3. At the exit of the nozzle, two recompression shocks can be seen, and the reason for this is explained in detail in Sec. 4.1. Below the bottom shock a dark line can be identified: that is not a density gradient, since it is also present in the calibration image (f). The graphite based gasket used to seal the test section was slightly eroded and graphite depositated in ricirculation zones right after the steps connecting the TC to the larger channel. These graphite impurities can be observed after both the top and bottom steps. Once the data acquisition has been completed, MOV002a is slowly close, decreasing the flow rate in the test section all the way to zero. During this process (shut down), the high pressure in the receiver pushes a normal shock connected to two labda shock structures inside the nozzle, upstream towards the throat (Fig.2.8(e)) until it fades away when the two lambda shocks and the normal shock reach the throat. Finally an individual calibration image is then taken (Fig. 2.8(f)) for post-processing purposes.

Table 2.3: General characteristics of the Schlieren measurement chain.

	PR.022	PR.024	PR.026
Knife edge orientation	Horizontal	Horizontal	Horizontal
FOV	Entire Flowfield	Entire Flowfield	Zoom on Throat
Type of camera	HS4M	Bobcat	Bobcat
Frame rate (fps) [Hz]	60	24.75	24.75
Exposure Time [μs]	600	-[*]	-[*]

[*] The camera automatically selects the exposure time from the frame rate: the value of the exposure time is in the interval specified in Tab. 2.2 with the upper limit not greater than $1/fps$.

2.5   Steady State Operation

The identification of the steady state time intervals during the data acquisition in the test section using the Schlieren measurement chain is a fundamental step in the accuracy assessment of computational models. As a matter of fact, the estimate of the steady state condition of the entire BoP which signals the beginning of the Schlieren acquisition period does not imply that the flow in the TS is actually in steady state conditions. It follows that the estimation of the steady state condition of the ORCHID is only a rough estimate of a wide interval in which the actual steady state flow is achieved in the nozzle.

For this reason, it is important to keep the ORCHID in the target conditions for a long time and possibly acquire the pressures, temperatures and the flow rate characterizing the flow in the nozzle at a higher sampling rate whenever the facility has reached a steady state operation condition. The sampling rate of the flow parameters has been kept constant at 1 Hz, even during the steady state operation; if the flow uring this time does not keep the steady state conditions for a long time, the number of samples taken will not be enought to analyze shorter intervals of time in which the flow could have been considered to be in steady state. The ideal frequency of acquisition during this steady state operation would be the same acquisition frequency of the Schlieren images

$$f_{\mathrm{acq,SS}} \approx (fps)_{\mathrm{Schlieren}}.$$

This way, an accurate steady state analysis can be performed by analyzing the nozzle's flow acquired variables thus identifying a steady state interval having the same sample size as the Schlieren data; this way the unfortunate condition in which enough Schlieren data for convergence of data can be achieved in a few seconds but minutes are needed for a steady state analysis. It is also extremely important that the Schlieren acquisition goes on for the wide identified interval such that, once the steady state interval has been identified, Schlieren images in such intervals are available.

In the three ORCHID experimental campaigns under considerations, pressures, temperatures and flow rate measurements are taken for the entire process runs at a constant sampling frequency of 1 Hz. The entire process run can last between 5 and 8 hours, in which the nozzle test section is usually opened only once or twice; the first or second opening of the nozzle TS is defined by the codes NT001 and NT002 respectively.

2.5.1   Operating conditions

Several experiments were designed to investigate the flowfield of a high speed expansion of the organic fluid MM. Each experiment, defined as Process Run number (PR.0)<IDnumber>, is characterized by different thermodynamic states and expansion ratios and , of course, same geometry. The target conditions of the three process runs are reported in table 2.4. The parameters identifying each of the three operating condition of the nozzle are the evaporator pressure PZA003, which will determine the inlet pressure of the nozzle, the inlet temperature measured in the SC TT0015, the WF flow rate FT001 and the back pressure measured in the receiver PT004. These operating conditions were selected since they represent the typical operating conditions of an ORC turbine [Head *et al.* (2016)]: on desing operation of an expander is as important as the off design and the correct prediction of the losses and, more in general flow behaviour, is extremely important for the realization of highly efficeint systems. The off design condition in PR.026 was set to much lower pressure in order to allow safer initial tests (important for the commissioning of the test rig and measuring devices), better evaluate the extent of the accuracy of the SU2 solution and gather more information on the behaviour of the fluid in more ideal conditions in order to compare it with the simulations. Furthermore, if the camera has no filter, the line extraction methods are much more accurate when the brightness in the image is more constant, ergo when density gradients are not too large.

Details about the runs are summarized in the following list:

Table 2.4: Run target coonditions

Experiment Run	Target BoP Process Conditions						
	TT0015	Units	FT001	Units	PT004	PZA003	Units
PR.022	252	C	4450	kg/h	1.1	18.4	barg
PR.024	252	C	4170	kg/h	0.5	17	barg
PR.026	252	C	2245	kg/h	-0.3	8.4	barg

- PR.022 is very close to the on-design conditions of the nozzle (run PR.025 shown by Head (2020)), has the highest inlet pressure and lowest expansion ratio. The images are taken with the High speed camera HS4M at 60 fps, the entire flow field was captured and no filter was applied to the camera, thus the density gradient is very large and the throat area is too dark to be detected. The nozzle test section was opened once (NT001). During this experiment, the polymer based gasket used to seal the TS melted as soon as the nozzle reached steady state: this can be noticed in the Schlieren images, where the top wall is completely hidden by an irregular dark area. It must be noted that most of the melted polymer leaked outside the test section thus obstructing the full visualization of the flow via Schlieren, but it did not affect the flow in the TC of the nozzle significantly.

- PR.024 is slightly off design, the inlet pressure is 17 barg and thu 1.4 bar lower than PR.022; furthermore the expansion ratio i 11.53, hich is slightly larger than the on deign one of 8.9. The entire flow field was captured with the Bobcat IGV B1610C camera at 24.75 fps; the density gradients are still very large and the throat area is again too dark to be seen or detected. The nozzle test section was opened once (NT001).

- PR.026 is far from the on design conditions of the ORCHID nozzle: the inlet pressure is 10 bar lower than the on design case and the expansion ratio is the highest between all three runs. The throat area was captured with the Bobcat camera, the density gradient is smaller thus the the flow in the throat can be appreciated and detected. The nozzle TS was opened twice, but the second opening (NT002) does not reach steady state, thus the data from the first opening is used instead (NT001).

The differences between the three process runs is not limited to temperatures and pressures; the non ideality of the organic vapor in the three process runs as well as all the fluid properties, e.g. fundamental derivative of Gas Dynamics, specific heat, speed of sound, γ, change; these differences in the non ideal fluid behaviour can be represented by the compressibility factor. In figure 2.9 the isentropic expansions are plotted on a $T - S$ diagram with the complement of the iso-Z ($1 - Z$) curves together with the value of the fundamental derivative Γ to fully understand the differences between the three PRs.

(a) T-S diagram for PR.022 andPR.024

(b) T-S diagram for PR.026
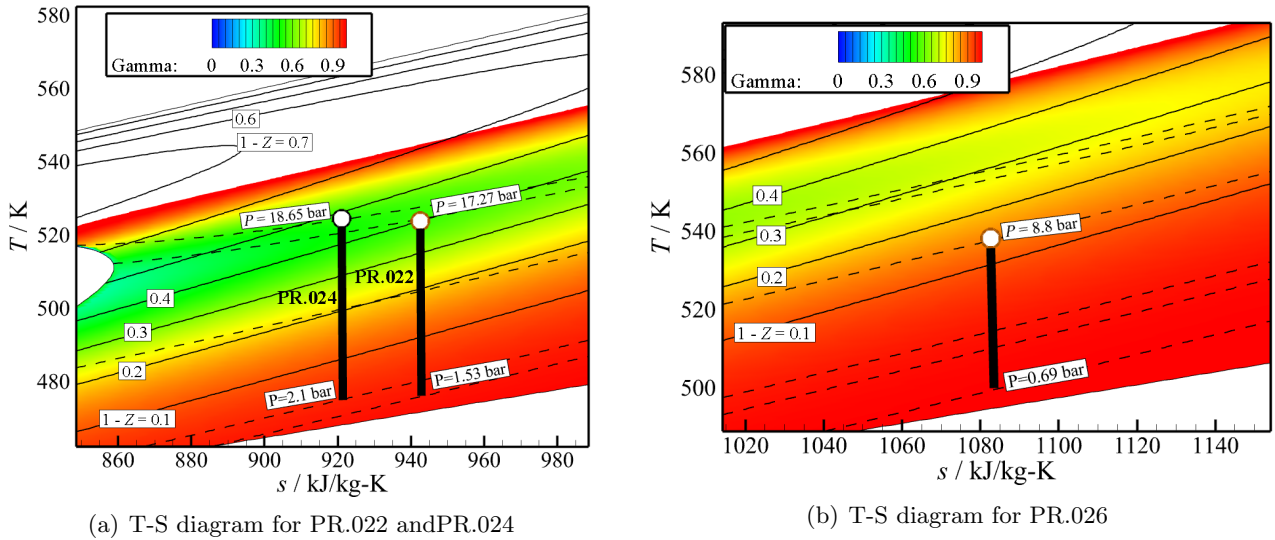
Figure 2.9: Isentropic expansions realized in the TS of the ORCHID nozzle. The dashed lines are constant pressure curves, the color contur is the value of Γ in the MM T-S diagram and the continuous curves are the complement to one of the compressibility factor Z.

2.5.2   Steady Steate Identification

It is extremely important to identify the steady state condition of the flow in the nozzle in order to extract the Mach number using the Schlieren technique and to compare it against the numerical predictions of the SU2 flow solver. Since the flow in the supersonic nozzle is defined by the geometry, which is obviously fixed, and the boundary conditions (inlet total pressure and temperature as well as back pressure), the measurements used to identify the steady state condition of the flow are:

- Evaporator pressure PZA003;

- Inlet total temperature TT0015;

- Back pressure PT004, and

- WF mass flow rate FT001.

When it comes to Steady state detection methods, there are various techniques available and most of these are based on selecting data windows, computing either averages, variances, or regressions on the data window, and comparing the results with previous window or larger intervals using appropriate statistical tests as shown by Rhinehart (2013). Kim *et al.* (2008), for example, proposed a steady state identification technique based on calculating the standard deviation over a time moving window. A Steady-state interval is then declared when the moving deviation lies under an established threshold. Another similar method is the one proposed by proposed by Cao & Rhinehart (1995), called the R-test, in which the data are treated sequentially for steady-state identification (SSI) without the need to select the time window. The ratio is calculated by two different methods in the same data window. During steady-state, this ratio will tend to one plus a user specified threshold, depending on the how accurate the steady state needs to be. Jiang *et al.* (2003) proposed a SSI method using wavelet-based multi-scale data processing. The process status at each time point is analyzed according to the wavelet transform of the extracted process trends. This method appears to be reliable for detecting rate of change in variables and estimating the measurement status at a point in time given that random errors are mainly present. Experience with the process is essential to determine key parameters and, as explained by the autors, more studies are needed for the applications of this method. Given that ORC vapor tunnel tests are just now developing, there are not many guidelines on steady state identification for these applications.

Woodland *et al.* (2012) proposed a standard for detecting steady-state periods in the measurements made within a simple Rankine cycle configuration. He states that steady state can be achieved when key process variables in two considered intervals, separated by ten minutes, have a relative change in average lessss than a sspecified threhold.

In this chapter two different approaches are followed for the identification of the steady state interval: for PR.022 and PR.024, the nozzle TS was kept open for a longer time than PR.026, thus the nozzle reached an equilibrium which lasted more than ten minutes: plenty of measurements are thus available. For this reason, Head (2020) used the simple the steady-state detection method of Kim *et al.* (2008), together with Woodland *et al.* (2012) criteria, to process measurements data of the ORCHID, in order to obtain steady-state intervals and evaluate the system performance off-line. When the PR.026 data was analyzed, it became clear that the nozzle TS was kept open for a shorter amount of time, as a result the flow did not have much time to reach a long enough steady state condition to apply the above mentioned SSI method. For this reason, a new detailed approach to the problem was developed.

The off-line steady state identification method developed in this Thesis derives from the concepts of SSI presented by Cao & Rhinehart (1995), Flehmig & Marquardt (2006) and Crow *et al.* (1955). The method identifies a steady state interval by firstly finding an interval where the least squares polynomial fit of the filtered data has a neglegible slope for all the variables under consideration. Then a ratio of variances G_v between the value and the mean and two consecutive values is evaluated with a foreward type statystic in moving windows identifying the interval where this ratio is smaller or equal to one. Finally the identified interval is split into two sub-intervals where means and standard deviations are computed and a maximum variance comparsion between the two windows is performed. This is done to verify that the steady state interval selected, which has no drift thanks to the G_v test, does not have large oscillations or outliers. An interval verifying the constraints of this analysis verifies strict steady state condition, furthermore this developed method ensures that no drift is present in the steady state, meanwhile other conventional approaches such as the one used for PR.022 and PR.024 does not verifiy the presence of drift. It must be pointed out that the validity of this analysis still relies on statistical quantities such as averages and variances, thus it is recommended to ensure that the number of samples in each considered sub-interval, is not too small thus valid statistical quantities can be calculated. If the sub-intervals have only a few samples, then the average of that sub interval will have a non neglegible uncertainty on the calculated mean, which is the standard deviation devided by the square root of the samples. The details of the implemented method are presented in appendix A.

The subplots of Fig. 2.10, 2.11 and 2.12 show the behaviour over time of a few key process variables of the ORCHID. The thermal oil termperature of the heater HTT PV is used to supply the necessary heat to the ORCHID BoP; this temperature is clearly is more steady than the others since it is regulated by a well tuned PID controller. It is also clear that the condensing temperature TT009 takes the longest to reach steady-state, as it is controlled by the last control loop activated in the ORCHID. By observing the evaporator pressure PZA003 trend one can notice when the nozzle TS was opened: as a matter of fact, a quick drop in the PZA003 pressure followed by a rapid increase, is the sign of the opening of the valve MOV002a; the pressure drop is caused by the immediate request for a high mass flow rate in the WF line, the steep increase iss due to the rapid stabilization of the conditions when the flow has completed a cycle in the BoP. Furthermore, by observing the mass flow rate of the working fluid and the cooling loop, it is possible to notice how the cooling loop flow is much more constant than the WF's as the second one has a longer and more complex cycle.

Process Run Details :

- PR.022: Figure 2.10(a) shows the entire process run which consists of start up, operation and shutdown of the ORCHID, for a total duration time of about 7h and 30 minutes. The test section of the nozzle was open from 17:00 to 18:12 (orange + blue intervals) but the steady state only starts around 17:45 , so about 45 minutes were necessary to stabilize the process variables. The steady state interval was identified using the analysis of Head (2020) combining Woodland *et al.* (2012) and Kim *et al.* (2008) and is presented in Fig. 2.10(b) in blue . The small fluctuations in the back pressure PT004 do not influence the supersonic expansion in the nozzle. A total of more than 10000 images were taken during steady state since the acquisition frequency of the HS4M used was set to 60 fps. It is possible to notice how the top wall is completely hidden by the melted PTE seal; the flow inside the nozzle was not significantly influenced by this since the gasked leaked on the outside of the TS.

- PR.024: Figure 2.11(a) shows the entire process run which consists of start up, operation and shutdown of the ORCHID, for a total duration time of about 5h and 30 minutes. The start-up began at 10:00 and the shutdown was completed at 15:30. The nozzle TS was opened once from 12:14 to 12:45; during this interval, after 15 minutes from the opening, the steady state was achieved and it lasted from 12:29 to 12:33 as is shown in Fig. 2.11(b). In steady state, a total of about 800 Schlieren image were taken with the Bobcat, but about 100 had to be removed due to strong changes in brightness caused by the regulation of the Schlieren measurement chain mid-experiment. A total of 700 raw Schlieren images are then available for pre processing.

- PR.026: The total duration time of the process run was about 4h and 30 minutes for PR.026. The nozzle TS was opened twice as it is possible to notice from the 4 small bumps in the evaporator pressure. The first opening was from 13:30 to 13:38, while the second opening was from 13:59 to 14:00 which is obviously too short to contain a steady state interval. At first glance, in the first opening the flow in the nozzle does not seem to have reached steady state as it is possible to notice from Fig. 2.12(b). The original steady state approach used for the first two cases cannot be applied to this case because its SSI resolution is limited by Woodland *et al.* (2012) time constraints, in other words it is not capable of identifying small steady state intervals and it requires longer test section opening times. For this reason another steady state approach was developed and used, capable of looking at the data much more in detail in order to identify one small steady state interval. The details of the newly developed *hybrid steady state analysis* are presented in Appendix A, while the results are presented in Fig. 2.13.
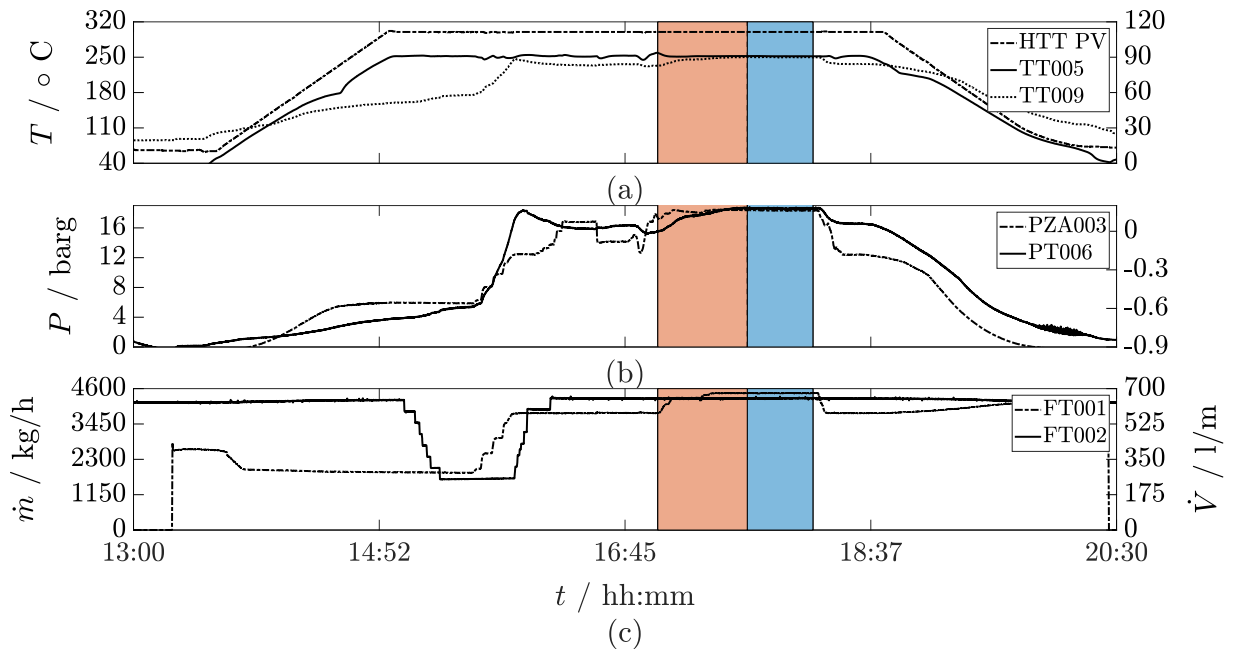
(a) Entire process run.
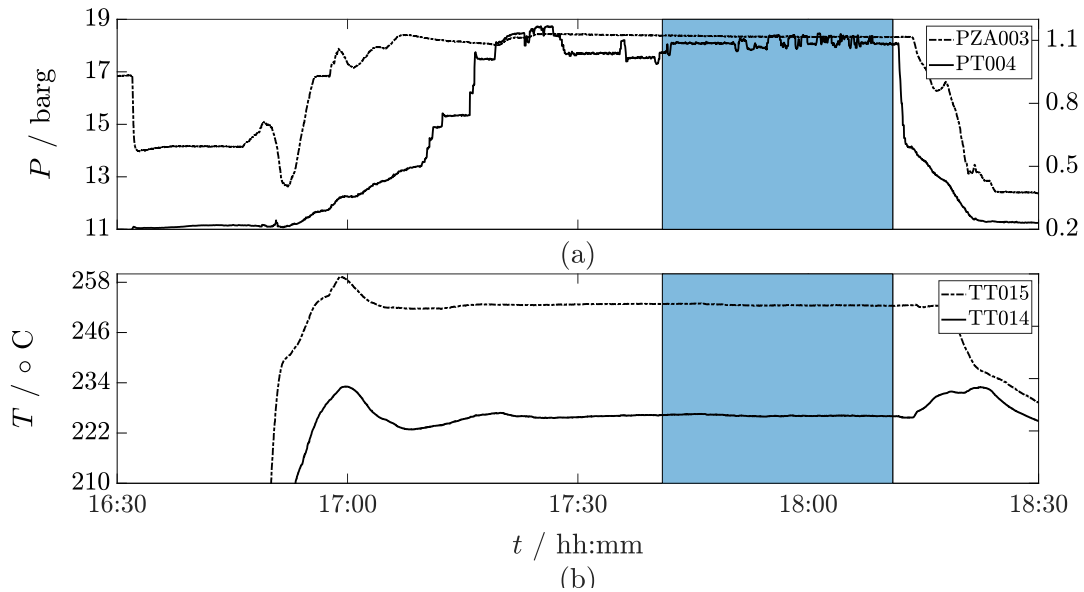
(b) Focus on the TS opening interval

Figure 2.10: Time series data of selected process variables for run PR.022-NT.001: Thermal oil electric heater temperature (HTT PV) and evaporator (TT005) — left axis; condensor (TT009) — right axis; evaporator pressure (PZA003) — left axis; condensor pressure (PT006) — right axis; WF flow rate (FT001) — left axis; cooling loop flow rate (FT002) — right axis; receiver pressure (PT004) — right axis; nozzle inlet temperature (TT015); receiver temperature (TT004). - datasets retrieved from Head (2020).
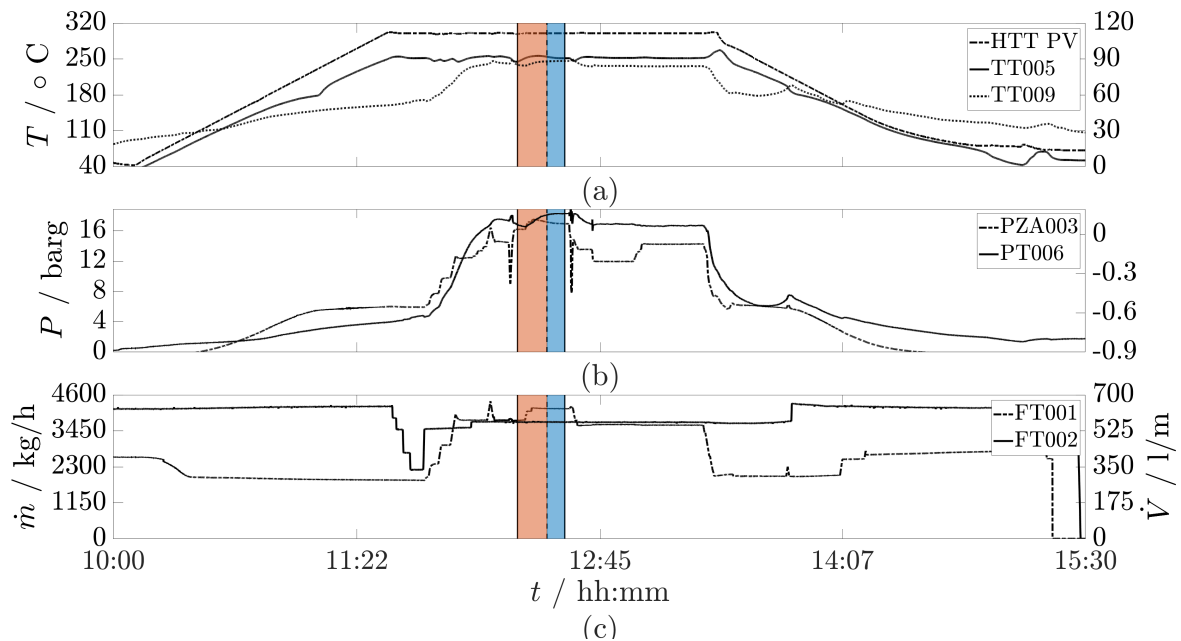
(a) Entire process run.
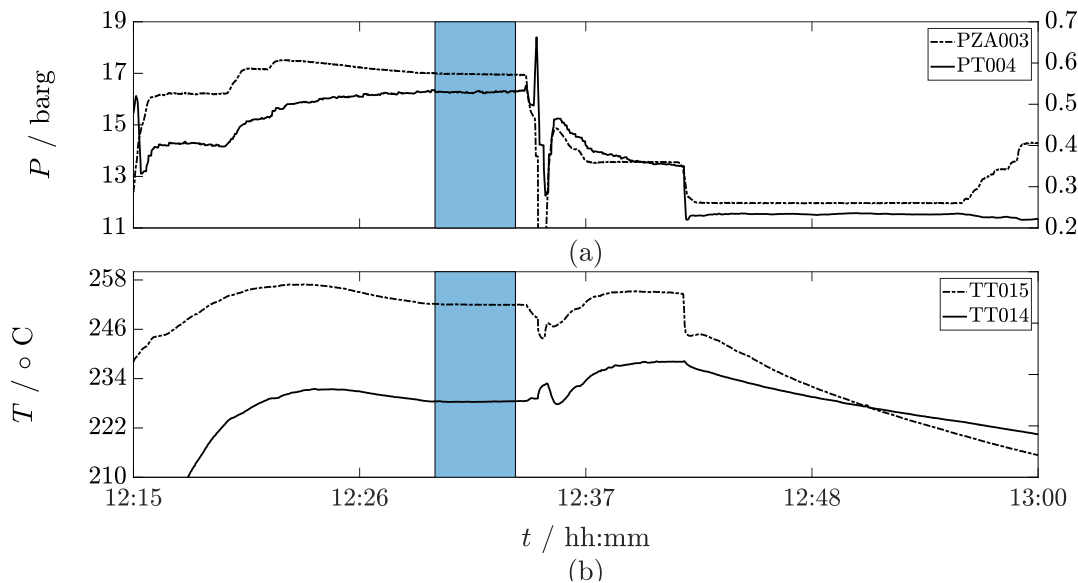
(b) Focus on the TS opening interval

Figure 2.11: Time series data of selected process variables for run PR.024-NT.001: Thermal oil electric heater temperature (HTT PV) and evaporator (TT005) — left axis; condensor (TT009) — right axis; evaporator pressure (PZA003) — left axis; condensor pressure (PT006) — right axis; WF flow rate (FT001) — left axis; cooling loop flow rate (FT002) — right axis; receiver pressure (PT004) — right axis; nozzle inlet temperature (TT015); receiver temperature (TT004). - datasets retrieved from Head (2020).
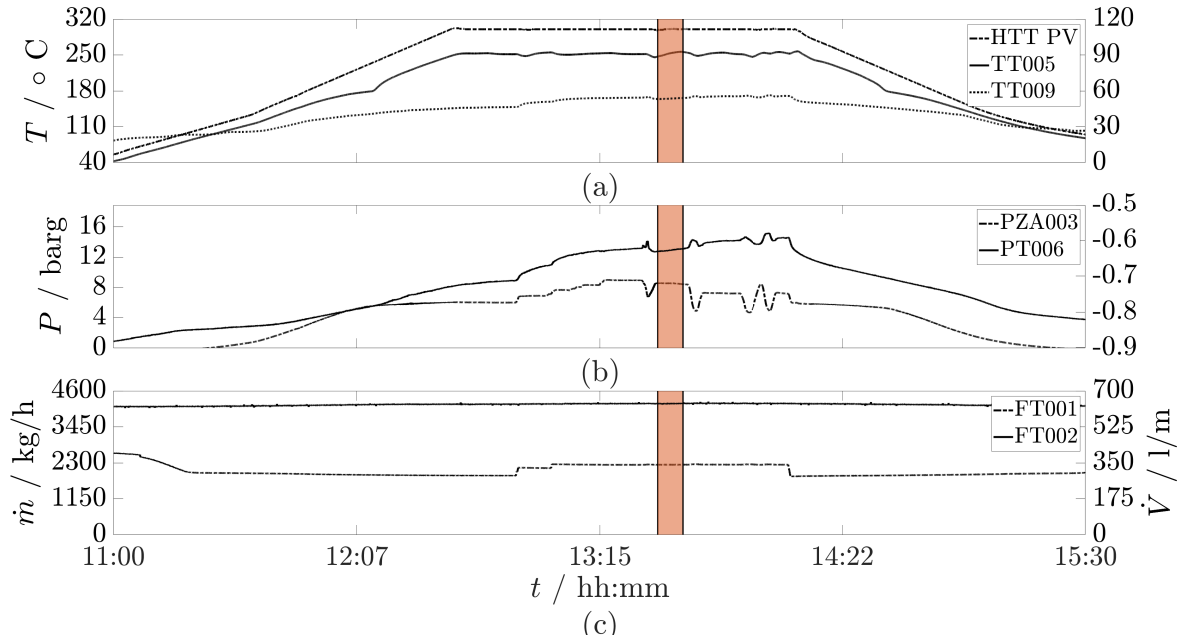
(a) Entire process run.
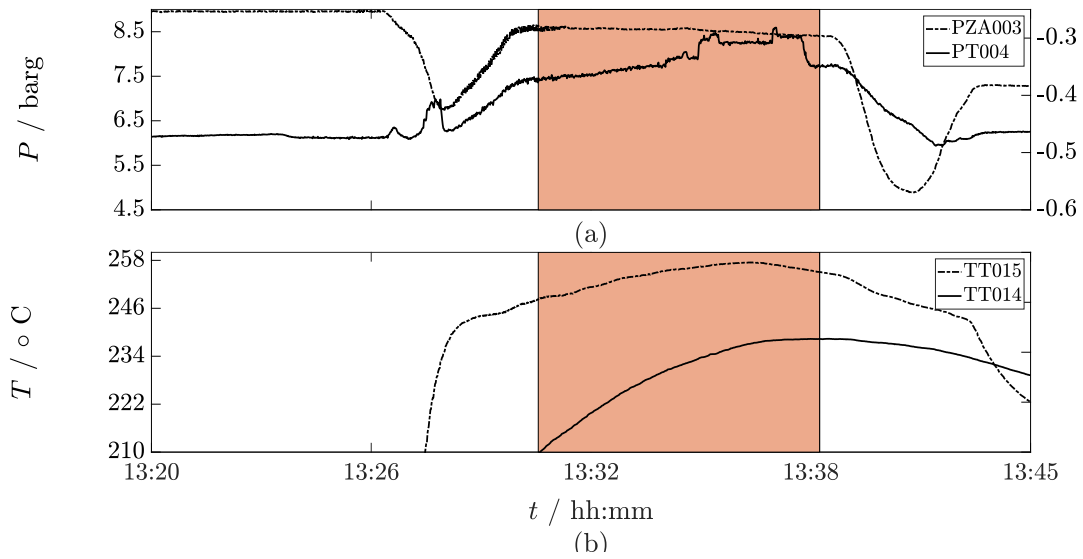
(b) Focus on the TS opening interval

Figure 2.12: Time series data of selected process variables for run PR.026-NT.001: Thermal oil electric heater temperature (HTT PV) and evaporator (TT005) — left axis; condensor (TT009) — right axis; evaporator pressure (PZA003) — left axis; condensor pressure (PT006) — right axis; WF flow rate (FT001) — left axis; cooling loop flow rate (FT002) — right axis; receiver pressure (PT004) — right axis; nozzle inlet temperature (TT015); receiver temperature (TT004). - datasets retrieved from Head (2020).
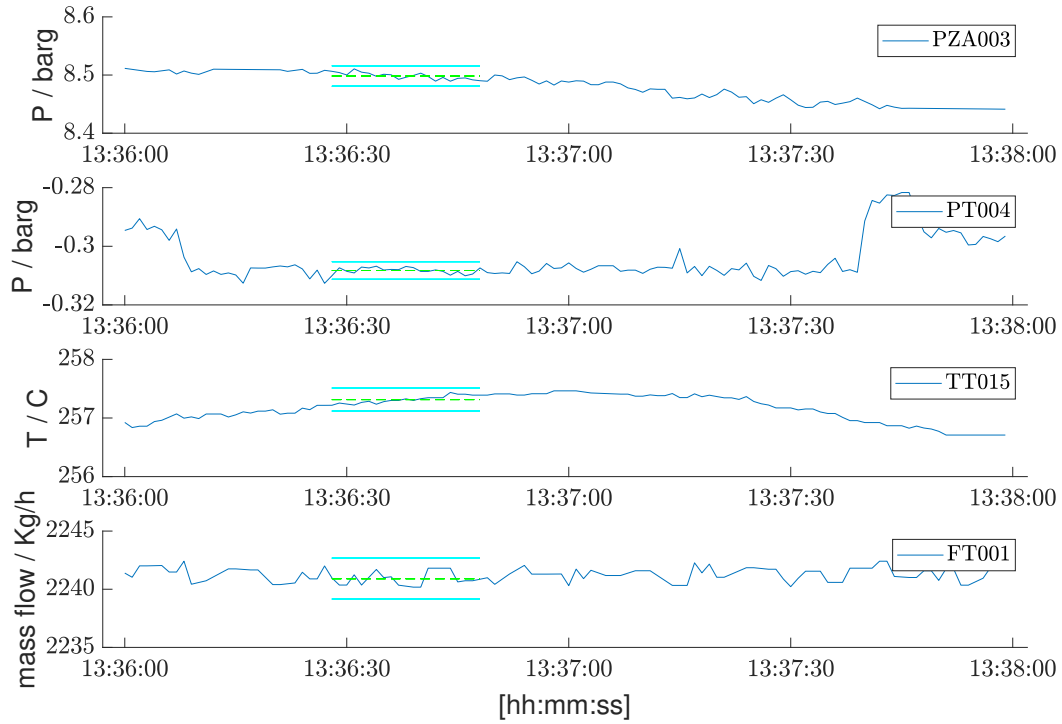
Figure 2.13: Identified steady state interval for PR.026 nozzle boundary conditions using the *Hybrid steady state analysis*: the solid cyan lines represent the three sigma limits of the average in the steady state interval, which is the green dashed line. The steady state interval is from 13:36:28 to 13:36:48.

Conclusions on the Steady State Intervals

A standard SSI method was used for the first two process runs since the test section was opened for a sufficiently long period of time such that the key process variables were able to stabilize for a time interval long enough to apply the steady state analysis of Head (2020). On the other hand, a new hybrid SSI method was used for the PR.026 since the nozzle test section was opened for a shorter interval of time, thus it was not possible to find a steady state interval long enough to apply the above mentioned criteria. For this reason, a more detailed steady state analysis was necessary to identify shorter steady state time intervals. Once each steady state interval is identified for each process run, to each process variable under evaluation, especially the nozzle's boundary conditions, an average value can be computed and its Type A (random) uncertainties can be assessed by evaluating the standard deviation of the acquired data. The results are summarized in table 2.5.

Table 2.5: BoP steady state measurements

TS variables	PR.022		PR.024		PR.026	
	mean	std. dev.	mean	std. dev.	mean	std. dev.
PTZ003A [barg]	18.35	±0.018	16.97	±0.017	8.50	±0.0047
PT004 [barg]	1.09	±0.023	0.53	±0.0045	-0.308	±0.0009
TT0015 [^{o}C]	252.6	±0.161	252.0	±0.058	257.27	±0.0380
TT0014 [^{o}C]	226.2	±0.164	228.4	±0.055	236.16	±0.1561
FT001 [Kg/h]	4450	± 4.880	4159	±4.666	2241	±0.4665

2.6 Error Source Identification and Uncertainty Quantification

Following the guidelines for error source identification and uncertainty quantification in ISO (1993), all the error sources concerning the ORCHID BoP, nozzle TS and the Schlieren measurement chain are analyzed and discussed. Uncertainties must be then quantified and associated with the identified error source in order to have a clear overview of the problem when conducting an accuracy assessment and setting the basis for a full validation.

2.6.1 Combining Uncertainties

When the uncertainty in a measurement quantity x is a combination of two uncertainties u_1 and u_2, the combined uncertainty on the variable x is:

$$u_{\mathrm{x}} = \sqrt{u_1{}^2 + u_2{}^2 + 2\rho_{1,2}u_1u_2},$$

where $\rho_{1,2}$ is the correlation coefficient of the two error sources and can range in value from -1 to +1. The correlation coefficient is defined in terms of the covariance of the two uncertainties adimensionalized with the product of the two terms :

$$\rho_{1,2} = \frac{\mathrm{cov}(u_1u_2)}{u_1u_2}$$

and it represents how much the to error sources affect one another. If the two error sources are statistically independent, then $\rho_{1,2} = 0$ and

$$u_{\mathrm{x}} = \sqrt{u_1{}^2 + u_2{}^2},$$

while if the correlation coefficient $\rho_{1,2} = 1$ then the two uncertainties are simply added on top of each other meaning that the two uncertainties never overlap, so the second uncertainty always amplifies the effect of the first one.

Each time a constant uncertainty, such as a resolution, is added to another uncertainty of any kind, the correlation factor is zero thus the uncertainties can be square root summed. For example, the uncertainties in the A/D conversion are square root summed and not added because they are independent from one another; the A/D uncertainty is also square root summed to the acquisition system uncertainty for the same reason. On the other hand, in the post processing tool uncertainties, the μ angle extraction uncertainty can't be simply added to the Type A uncertainty in the Mach angle because the correlation coefficient is not neglegible. The extraction uncertainty depends, among other factors, from the length of the extracted lines and this is correlated to the μ angle random uncertainty.

2.6.2 ORCHID Balance of Plant

When considering the Balance of Plant sources of error influencing directly the expansion in the nozzle, it is fundamental to keep in mind the layout of the facility (Fig. 2.14) in order to correctly evaluate the uncertainty contributes coming from fluctuations in the boundary conditions (Type A) and calibration of instruments, resolution and conversion. In the present work, all the measurements not directly correlated to the flow in the nozzle's test section are not considered; as a result the measures of interest are the evaporator pressure PTZ003A, the pressure PT004 and temperature TT0014 in the receiver , the settling chamber total temperature TT0015 and the flow rate measured after the pumps FT001.

The sources of error that must be considered when evaluating the uncertainties in the steady state operating conditions of the ORCHID are the following:

1. fluctuations of the pressure after the evaporator;
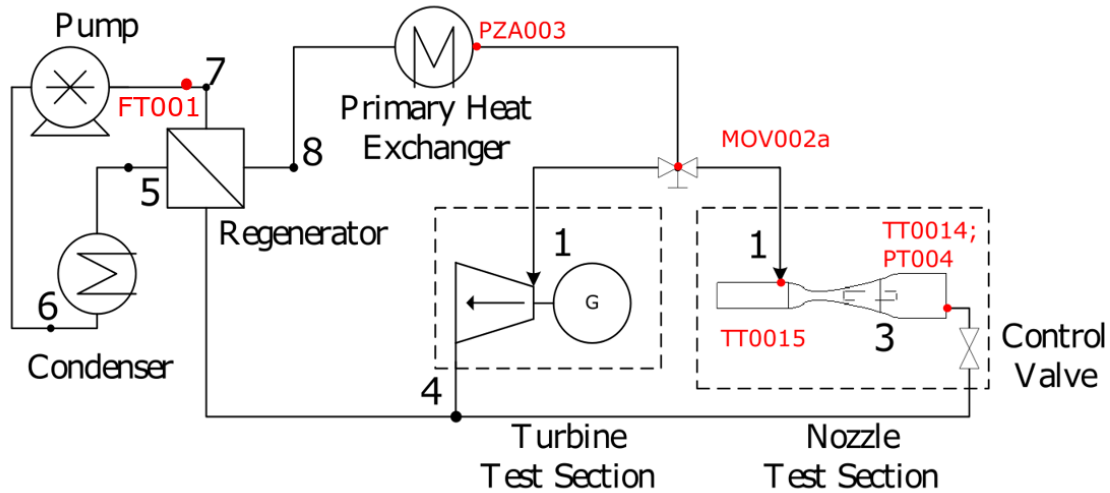
Figure 2.14: Simplified Scheme of the ORCHID BoP

2. fluctuations of the inlet total temperature;

3. fluctuations of the total temperature in the receriver;

4. evaluation of the pressure drop (losses) and uncertainty correction coefficient from the evaporator to the inlet of the nozzle across the pipes, MOV002a and the settling chamber through calibration curves;

5. fluctuations in the mass flow rate;

6. A/D conversion;

7. Sensors accuracy.

All the uncertainties deriving from fluctuations of parameters are estimated via statystical means. In Tab. 2.5, Type A uncertainties for the nozzle steady state conditions are shown for all the process runs under evaluation.

A/D conversion

Each sensor reading must be transformed from an analog singal to a digital one in order to be acquired by the acquisition computer. When the analog-digital conversion is performed on a singal, the uncertainty coming from this step must be calculated. The conversion uncertainty for the 24 bit NI 9208 analog-to-digital converter (ADC) module is calculated in the following since this is the module used for pressure, temperature and mass flow singals. The individual uncertainties of the module are calculated by retrieving the gain, offset and noise errors within the range of the device which can be obtained from the NI-9208 specification sheet's accuracy table.

- $\epsilon_{\text{gain}} = \pm 0.76\%$ of the reading;

- $\epsilon_{\text{offset}} = \pm 0.04\%$ of range;

- $\epsilon_{\text{noise,rms}} = 50 \ nArms$, at high resolution.

Since all the contributions of the module are independent, the total uncertainty is the root sum square of the gain, noise and offset uncertainties:

$$u_{A/D} = \sqrt{u_{\text{gain}}^2 + u_{\text{offset}}^2 + u_{\text{noise}}^2}.$$

Standard uncertainties are a good parameter to indicate the quality of a measurement, whereas expanded uncertainties are suited to prove the validity of a measure at a specified confidence level. All the errors ϵ are given with a coverage factor $K = 2$ to reach the 95% confidence level; as a result all the uncertainties evaluated in the following are expanded uncertanties.

The estimation of the A/D conversion uncertainty is performed following the guidelines of Instruments (2013). The gain uncertainty U_{gain} depends on the value that the sensor is reading; as a result this uncertainty may vary during the operation of the ORCHID. Due to the relatively small influence of this uncertainty on the total uncertainty on pressure, temperatures and flow rate it is assumed a constant value for U_{gain} using the maximum measured reading in output from the instrumentations connected to this ADC. Considering the maximum measured signal $r_{max} = 20mA$ and the relative error given by the supplier $\epsilon_{\text{gain}} = 0.76\%$ one can obtain:

$$U_{\text{gain}} = \epsilon_{\text{gain}} r_{max} = 0.152 \ mA$$

The offset uncertainty U_{offset} depends on the relative offset error and the maximum singal range of the module, so:

$$U_{\text{offset}} = \epsilon_{\text{offset}} \text{Range} = \frac{0.04}{100} 22 \ mA = 0.0088 \ mA$$

The noise error for the A/D module is given in root mean square Ampere, and has to be transformed into a peak value before calculating its uncertainty:

$$\epsilon_{\text{noise}} = \sqrt{2}(\epsilon_{\text{noise}}) = 70.7 \times 10^{-9} \ A = 70.7 \ nA.$$

Now the uncertainty associated with the noise, which is already small, decreases as the number of sample N_s increases since this uncertainty has a statistically converged mean of zero and must be considered only if one or a few samples are taken:

$$U_{\text{noise}} = \frac{\epsilon_{\text{noise}} K}{\sqrt{N_s}},$$

thus can be clearly neglected.

In conclusion, the total A/D expanded uncertainty for the NI9208 A/D module, used for all measurements under consideration for the three process runs, is:

$$U_{A/D} = \pm 152.3 \ \mu A,$$

which can be transformed into a relative uncertainty by dividing the value by the considered maximum reading used to calculate it:

$$U_{A/D\%} = \pm 0.7309\%.$$

DAQ Instrumentation

The ORCHID is equipped with several different types of pressure and temperature sensors from WIKA. The accuracy of the sensors are necessary in order to evaluate the total uncertainties on the total inlet pressure and temperature, exit temperature and mass flow that influence directly the supersonic expansion in the nozzle.

The full scale accuracy of the instrument corresponds to the expanded relative uncertainty of the measure $U_{\text{inst}}[\%]$; this includes the following factors: the intrinsic performance of the instrument, the measurement uncertainty of the reference instrument, long-term stability, influence of ambient

conditions, drift and temperature effects over the compensated range during a periodic zero point adjustment.

The total relative expanded uncertainty of the acquisition system is the root sum square of the relative uncertainties of the A/D module and the accuracy of the sensor.

$$U_{\mathrm{acq,sys}}\% = \sqrt{U_{A/D}^2 + U_{\mathrm{inst}}^2}$$

It must be noticed that while the relative uncertainties are constant for a given sensor, the instrument absolute uncertainties will depend on the average measured value.

$$U_{\mathrm{acq,sys}} = \overline{\mathrm{Value}} * U_{\mathrm{acq,sys}}\%$$

Table 2.6: Instrumentation and associated acquisition system uncertainties

Instrument	Acquired variable	Measuring range@	FS accuracy $U_{\mathrm{inst}}[\pm\%]$	System uncertainty[i] $U_{\mathrm{acq,sys}}[\pm\%]$
Temperature trans.	TT014 , TT015	$0 - 300$ [^oC]	0.29*	0.786%
Pressure trans.	PZA003 , PT004	$0 - 40$ [barg]	0.1	0.738%
Mass flow trans.	FT001	$0 - 5580$ [kg/h]	0.1	0.738%

*: valid for $150 - 300\ ^oC$ interval. The general relative FS accuracy formula at a given x temperature in the measuring range for these class A transmitters is: $FS(x) = 0.15/x + 0.002$.
i: Calculated for max measured value of 20 mA (includes the A/D converter and sensor). Coverage factor of k = 2.
@: Corresponding output signal is (4 - 20) mA or (0 - 10) V.

Evaporator, Inlet and Back Pressures

Once the steady state time interval has been identified (Sec. 2.5.2) fluctuations in pressure and temperature are below the 2% threshold but still present due to the dynamism of the physical problem under evaluation. The evaporator pressure PZA003, after having evaluated the valve, pipeline and SC losses, becomes the nozzle total inlet pressure P_{in}, which it will influence the expansion in the nozzle. Given that the PZA003 data are available, is possible to evaluate the means and standard deviations u_{PZA003} for the three process runs to evaluate the means and standard uncertainties on the inlet total pressure This is done by using the calibration curves of the OCHID BoP. Since these datasets are the first ever datasets of the ORCHID, the calibration curves are not availablke yet, but for the three cases under consideration, Sec. 2.2.1 shows that a total loss of 0.7 is an accurate estimation based on two experiments in similar operating conditions of the facility. Furthermore, it is assumed that the uncertainties are not afected, but this is known to be a very conservative estimation since the fluctuations are significantly reduced by the SC, thus the nozzle inlet pressure will have a smaller uncertainty.

In conclusion, the evaporator standard uncertainty is multiplied by a coverage factor $K = 2$ to extend the confidence level of the Type A uncertainty on the inlet pressure to 95% . At this point the Type A extended random uncertainty must be added to the Type B extended uncertainty of the acquisition system, which is the square root sum of the instrumentation accuracy and the A/D converter:

$$U_{PZA003} = \sqrt{(Ku_{PZA003})^2 + \sqrt{U_{inst}^2 + U_{A/D}^2}} = U_{P,in}.$$

The same procedure can be applied for the pressure in the receiver PT004, which is the back pressure of the nozzle: the standard deviation and the system uncertainty are known, thus the total expanded uncertainty can be calculated as well. It must be noted that the back pressure uncertainty does not have a significant impact on the expansion in the nozzle. In table 2.7 it is possible to find the results of the total expanded system uncertainty on the evaporator and back pressures for the three process runs.

Table 2.7: Total expanded uncertainties on the evaporator pressure

	PR.022	PR.024	PR.026
U_{PZA003} [bar]	0.147	0.137	0.070
U_{PT004} [bar]	0.048	0.014	0.0005

Inlet and Outlet Total Temperatures

The total inlet temperautre of the nozzle $TT0015$ is acquired in the settling chamber of the test section where the flow velocity is so small that the static and total temperature can be considered equal. The same applies for the outlet total temperature $TT0014$, measured in the receiver after the nozzle. In the steady state identification chapter has been verified that the fluctuations in temperature are below the steady state threshold; it is possible to associate an uncertainty to the total temperatures by calculating the standard deviations of the temperature acquisitions for a sufficiently large dataset. As a result, $95\%CL$ uncertainties are associated to the temperatures using a coverage factor $K = 2$.

To evaluate the total expanded uncertainties on the temperature measurements, the total Type B extended uncertainty coming from the temperature acquisition system must be square root summed to the standard deviation times the coverage factor K:

$$U_{TT015} = \sqrt{(Ku_{TT015})^2 + \sqrt{U_{inst}^2 + U_{A/D}^2}}$$

$$U_{TT014} = \sqrt{(Ku_{TT014})^2 + \sqrt{U_{inst}^2 + U_{A/D}^2}}.$$

Table 2.8: Total expanded uncertainties on the inlet and outlet temperatures

	PR.022	PR.024	PR.026
U_{TT015} [C]	1.986	1.984	2.020
U_{TT014} [C]	1.806	1.795	1.881

Working Fluid Mass Flow Rate

The uncertainty on the mass flow rate is caused by both fluctuations in the value (Type A) and the uncertainty in the acquisition system which is the square root sum of the A/D conversion and the instrument uncertainty:

$$U_{FT001} = \sqrt{(Ku_{FT001})^2 + U_{\text{acq,sys}}^2}.$$

Table 2.9: Total expanded uncertainties on the WF flow rate

	PR.022	PR.024	PR.026
U_{FT001} [Kg/h]	34.26	32.04	16.56

2.6.3   Nozzle Test Section

The nozzle TS facilitates the gas dynamic experiments where measurements of temperature, pressure, wave geometry and velocity take place. It has been long recognized that flowfield nonuniformity, or flowfield quality, is a significant contributor to uncertainty in wind tunnel measurements, but there has been only limited success to quantify this contributor (AGARD (1994) , AIAA (1999)). Flowfield nonuniformity in the test section of any type of wind tunnel can be caused by many sources. In the following, a few sources that are primarily associated with supersonic wind tunnels are listed:

1. poorly designed wall contours ahead of the test section, including the contraction section ahead of the nozzle throat, the nozzle expansion region, and the test section region;

2. velocity field asymmetry caused by inlet conditions and settling chamber imperfections;

3. machine errors in the milling process of the profiles;

4. imperfect alignment and sealing of the nozzle walls;

5. operation of a fixed nozzle wall wind tunnel at a Reynolds number different from the design condition;

6. boundary layer effects changing the area distribution of the nozzle causing the geomerty to slightly differ from the ond design case;

7. bias error on the measure of the effective throat height of the nozzle.

All the above are possible error sources that must be taken into account when the experimental campaign is being set up. The uncertainties deriving from the possible error sources are analyzed in the following.

Nozzle Profile Alignment

The 2D convergent-divergent nozzle and test chamber are made from two equal and removable profiles. This allows to reshape the channel geometry, e.g., in case a different fluid needs to be tested and thus another nozzle designed.
When profiles are sealed to form the 2D nozzle, two possible alignment errors can be introduced.

- The first error is caused by the axial shift between the two walls: it must be kept in mind that if the two walls are even sleightly misaligned, the flow in the nozzle will be non symmetric, and will severely compromise the quality of the experimental results. If the sealing is made correctly, then the geometry or alignment uncertainty does not need to be taken into account.

- The second error is caused by the deviation of the sealed nozzle actual throat height compared to the design throat height which was determined with the method of characteristics. When the distance between the two walls deviates from the one estimated on design, the expanding flow in the nozzle is influenced by the presence of the walls.

Nozzle Walls Geometry Accuracy

The Computer numerical control (CNC) milling process used to realise the nozzle profiles is extremely precise; it follows that the uncertainty in the geometry of the profiles can be neglected. This assumption will be later validated by checking the flow symmetry in the expanded flow when 2D effects become neglegible and the flow can be considered 1D. Furthermore, the surface finish on the walls is smooth enough to not introduce any significant disturbances in the flow and this can be easily seen in the raw Schlieren images, where no anomalies in the flow can be observed.

Flow Symmetry Imperfections

Flow symmetry is not only influenced by the imperfections in the profile geometry and the misalignment between the two nozzle halves. The design of the settling chamber, selection of flow conditioners and stability of the boundary conditions also affect the quality of the flow.

Since the Mach extraction is performed in a steady state time interval where all the thermodynamic variables (total inlet pressure and temperature, and exit temperature) have fluctuations under the steady state threshold. It is also assumed that the settling chamber is designed well enough such that the the flow entering the convergent part of the nozzle is symmetric.

Again, the flow symmetry assumption will be validated through experimental data extracting Mach line angles above and below the midplane of the nozzle and proving that they are close enough to each other.

Boundary Layer Effects

The influence of the boundary layer in the nozzle expansion is the reduction in the area distribution within the CD nozzle with the implication of slightly changing the expansion ratio of the nozzle. Furthermore, the presence of boundary layer is neglected when Euler simulations are performed: this introduces an error proportional to the viscosity of the flow as well as the Reynolds number, which determines the thickness of the boundary layer. When considering dense organic vapors, the viscosity of this fluids is much lower than the one of common gasses. Organic vapor expansions, especially in on-design conditions in a nozzle designed with the MoC, are characterized by neglegible boundary layer effects: both the thickness and the influence on the velocity fields are extremely small for these flows as shown by Dijkshoorn (2020).

Operator Measurement Bias

When sealing the profiles, the effective throat area could be different than the one predicted by the design using the method of characteristics because of the uncertainty on the stiffness of the polymeric gasket. When the nozzle has been sealed, the throat height is measured with a caliber and as a result the throat height has an uncertainty whose containment limits are given by the instrument accuracy:

$$U_{th,bias} = \frac{\text{Caliper, res}}{2} = 0.05 \; [mm]$$

2.6.4 Schlieren Measurement Chain

The Schlieren measurement chain is used to provide the flow visualisation of the wave geometries. There are several sources of error which influence the characterization of the flow and these include:

1. alignment of the optics;

2. camera resolution and settings (shutter speed, ISO, focal length).

Optical Hardware Alignment

When considering the Schlieren acquisition set up already discussed in Sec. 2.4.2, it must be noted that the alingment of the optics is extremely important to obtain clear Schlieren images; the set up of the Z-type schleiren measurement chain has been carried out following the standard procedures and in the most careful way possible. The error due to the misalignment of the optics can be neglected since the raw Schlieren images are well in focus as a result no significant misalignment is present.

Camera Resolution and Settings

The camera resolution is an error source that strongly and inderectly influences the extraction of the mach angles in the post processing phase by the pixel per mm ratio pix/mm. Higher resolution corresponds to a larger number of pixels and, considering a constant field of view, this translates to a higher pixel per mm ratio which improves the angular resolution of the detected angles and the spatial resolution of the post processing methods. It is also important to notice that given a fixed resolution it is possible to increase the pixel per mm parameter just by reducing the field of view, thus acquiring zoomed images. The pixel per mm parameter is not the only important parameter to consider to maximise the accuracy of the post processing methods. The focus and brightness of the image must be kept as constant as possible; when dealing with supersonic expansions, density gradients in the flow can get quite large and as a result the schlieren images will be very dark in the high density region and very bright in the lower density region. In order to optimize the brightness level and keep it constant in the image, filters can be applied to reduce the Type A random uncertainty in the μ and $Mach$ casued by the higher sensitivity to the binarization in too bright or too dark areas. If a filter is not available, it is suggested to increase the zoom of the camera and further reduce the field of view such that the density gradient in the image is reduced and the pixel per mm ratio is further increased.

In conclusion, when setting up the Schlieren measurement chain, the camera settings like the ISO, shutter speed and aperture of the camera must be be adjusted to have an ideal brightness level in the image at a fixed zoom and with a chosen filter.

2.7   Conclusions

In this Chapter, the ORCHID facility was introduced. The details and the purpose of the experiments were presented; having selected three process runs, the steady state condition of the flow in the nozzle test section was identified. All the error sources in the BoP, Schlieren measurement chain and test section were identified and the uncertainties quantified. Now that steady state measurements and Schlieren images are available for the three process runs under evaluation, the tools necessary to extract the data from the images are needed.

Chapter 3

Line Detection Algorithms for Schlieren Data

3.1   Overview of Line Detection Methods

There are not many options available when the objective is the detection of particular curves in Schlieren grayscale images. When the problem is reduced to detecting straight lines in the field of experimental fluid dynamics, more in particular the detection of shocks or Mach waves in Schlieren images, the first distinction that can be made in the methods available in literature is between traditional scanning methods and mathematical transform-based methods.

The first method, which can only be applied to simple shocks, is based on a pixel by pixel scan, following rows or columns, to identify points where the gradient of the black and white image is larger than a set threshold. Using the coordinates of the identified points for a polynomial fit, it is possible to estimate the shock angle and shape with uncertainties coming from the calibration phase and the fit itself. Using the extracted geometry of the shock together with the flow conditions before the shock, the flow field after the shock can be computed. This method has obvious limitations: when noisy images are analyzed, the shock detection becomes very inaccurate because the brightness gradient can vary along the shock. Another obvious limitation is when images with more than one or two lines are analyzed: when increasing the number of shocks, and more in general the complexity of the Schlieren image, the scanning method obviously fails to recognize the shock patterns and it would require too much user input in the domain and threshold specifications. Furthermore, one can conclude that this method is definetly not suited to analyze images where Mach lines are present.

While scanning methods can mostly detect lines or low order polynomials, classical mathematical transform-based methods are perfect for the detection in images of simple curves such as lines, parabolas, ellipses and circles; furthermore they can be applied directly on the whole images and require very little computational time.

The most valuable transforms for line detection available in literature are the **Hough transform** and the **Radon integral transform**. Both of these methods are fundamentally based on the same mathematical procedure: the goal is the construction of an accumulation matrix where each peak represents a set of parameters used to describe the desired curve to detect in an appropriate parameter space. Thus the output of the transforms is simply the projection data obtained from a tomographic scan of the window of interest in the image. In other words, the transform methods look at the image from all the specified angles of interest and place in the accumulation matrix how many points were detected in the projection. The accumulation matrix dimension and peculiarities are defined by the chosen curve to detect and, therefore, the appropriate parameter space.

The Radon transform is most suited for thick line detection or, more in general, is a method that works well when one wants to detect the line that separates two areas with different intensity in a binarized image. The Hough transform, on the other hand, requires an edge detection of the

binarized image and is very effective when thin lines must be detected. The edge detection algorithm used can strongly influence the results of the transform, thus an appropriate edge detection algorithm must be chosen.

When the recognition of shapes is addressed, deep learning methods must be considered and analyzed to understant their applicability to the field of fluid dynamics. The use of deep learning methods for flow feature identification is still a very immature research field: as outlined by Liu *et al.* (2019), its most promising application is the prediction and identification of flow features such as shocks and vortical structures given an approximate flow field solution from a preliminary CFD simulation and the geometry of the problem. As a result, they propose a solution using Convolutional Neural Networks (CNN) for the prediction of vortical structures and steady flow field around bluff objects; a significant computational time reduction has been proven since an accurate large scale CFD analysis is not needed.

At the moment (early 2020), however, the use of deep learning in Schlieren feature extraction is almost non present and the main reason is that there are several drawbacks in using machine learning based methods for experimental data extraction: firstly, the algorithms are usually very specific and a specific network can not be used if the data scale changes [Liu *et al.* (2019)]; furthermore a large number of training sets are required: the data used for the training process, which can be time consuming, can come from experimental results or numerical simulations. In the first case, a reliable data extraction tool is needed, in the second case the CFD tool must be valid for the case in consideration, and when considering NICFD applications the problem is complicated since a full validation in this field is missing at the time of writing.

In the present work, the Canny edge detection algorithm was used to detect the edges of the individual lines in the Schlieren images, then the Hough transform was applied to the binarized image to detect the lines. After testing the Canny, Sonny, Prewitt and Roberts edge detection algorithms, the Canny algorithm was chosen as the most suitable edge detection algorithm for complex images; furthermore Maini & Aggarwal (2009) prove that the Canny method for edge detection is the optimal edge detector at the moment for its accuracy and the possibility to deal with noisy images applying a Gausian noise filter.

The developed tools are able to extract useful information from Schlieren images and can be used for validation of numerical simulation as well as training sets for deep learning algorithms that are now emerging in the field of fluid dynamics.

The Hough transform together with the above mentioned edge detection algorithms was also used in the development of a flexible Shock detection program, capable of following oblique or parabolic shocks in the image plane and recording the average angles that form the shock. The Shock program was not used to validate the thermodynamic models yet because the first experiments in the ORCHID, which are reported in this thesis as well as in Head (2020), aim at the characterization of the simplest NICFD flows first; then a wedge will be placed in the TC to study shock structures for non-ideal organic vapor flows.

3.2 The Hough Transform

The Hough transform is a well established method for detecting and locating straight lines or curves in images. The purpose of the technique is to find the paramters defining a specified curve in an image by a voting procedure. This voting procedure is carried out in a parameter space, from which object candidates are obtained as local maxima in a so-called accumulator space that is explicitly constructed by the algorithm for computing the Hough transform.
The Classical or conventional Hough transform (CHT) is concerned with the identification of lines in an image; the technique has been later extended to identify arbitrary shapes, most commonly circles or ellipses, and it is now known as Generalized Hough Transform.

This technique transforms a binary image into a Hough parameters counting space (HPCS) which consisits in a n-dimensional matrix of accumulation cells. The dimensions of the matrix are given by the number of parameters necessary to identify the analytic curve; in the case of lines, the HPCS is a 2-D matrix. When collinear points are found in the binarized image, the set of parameters describing the line will fall into the closest accumulation cell. At the end of the process, local maximum values in the HPCS correspond to lines (or curves). The identification of curves is then simplified to the identification of local peaks in the HPCS.
This technique is very robust to noise and discontinuities in the image and in most cases it is not computational intensive. In spite of these advantages, the Hough transform requires pre processing steps of threshold binarization and edge detection (or thinning) for an image to become a point pattern with lines or curves of 1-pixel width.
In the following paragraphs, the **Classical Hough Transform (CHT)** implementation is analyzed in detail.

3.2.1 CHT Space Parametrization

The number of parameters that describe any given straight line in the picture plane is $n = 2$.

$$y = ax + b$$

It is then possible to represent any given line in the image plane with a specific set of parameters (a, b) in the parameter space however vertical lines pose a problem because the a parameter has no upper limit. For this reason it is much easier to switch to polar coordinates and use a so called *normal parametrization*:

$$\begin{cases} \rho = \sqrt{x^2 + y^2} \\ \theta = \arctan 2(y/x) \end{cases}$$

In the normal parametric space, a given line is defined by two parameters:

- ρ: algebric distance from the origin of the local reference system

- θ: angle of ρ with respect to an horizontal line, also called Hough angle .

Restricting the Hough angle $\theta = [-\pi/2, \pi/2]$ implies that the normal parameters describing any line are unique. Every line in the image plane now correspond to a unique point in the normal parametric space (ρ, θ). Let us consider n points in the image plane $(x_i, y_i), ...(x_n, y_n)$. When applying the normal parametrization, all these points become curves in the parameter space:

$$\rho = x_i \cos(\theta) + y_i \sin(\theta)$$

One can instantly notice how the sinusoidal curves corresponding to collinear points have a common point of intersection in the parameter space (ρ_0, θ_0), which defines the line passing through the collienar points.
In order to fully understand the CHT technique, four important properties of the point-curve transformation must be addressed and kept in mind:

1. A point in the image plane (x_i, y_i) corresponds to a sinusoidal curve in the parameter space $\rho = x_i \cos(\theta) + y_i \sin(\theta)$.

2. A point in the parameter space (ρ_i, θ_i) corresponds to a straight line in the image plane $y = -\frac{\cos(\theta_i)}{\sin(\theta_i)} x + \frac{\rho_i}{\sin(\theta_i)}$

3. Points lying on the same curve in the image plane correspond to to curves through a common point in the parameter space

4. Points lying on the same curve in the parameter space correspond to lines through the same point in the image plane.

3.2.2   Accumulation Matrix

Once the parametrization is complete, each point in the image plane (x_i, y_i) can be mapped to a sinusoidal curve $A(\rho, \theta)$. It must be mentioned that when the number of pixels in the image is large, this technique becomes computationally expensive since the number of different sinusoidal curves can be extremely large. The computational burden can be reduced defining an acceptable uncertainty on the normal parameters ρ and θ thus quantizing the parameters plane into a grid.

$$\theta \in [-\pi/2, n\mathrm{d}\theta, \pi/2]$$

$$\rho \in [-R, m\mathrm{d}\rho, R]$$

The HPCS, also called accumulation matrix, is now a 2-D matrix with n rows and m columns, where each cell is an accumulation cell and represents a point in the parameter space, thus a line in the image plane.
Each cell $A(\rho_i, \theta_i)$ is defined by a set of quantized parameters and when each point in the image plane is transformed into a sinusoidal curve, the closest corresponding cell counts are increased to form a discretized sinusoidal function.
When the HPCS is completed, accumulation cells with the highest count, which are the intersection oints of the sinusoidal curves, represent a line in the image plane, thus the problem of line detection is reduced to finding local peaks in the HPCS.
Since the angle is limited to 180 degrees, when the ρ vector is negative (left side of the reference system) the angle θ associated to it is always calculated in the right side using the anti-symmetric ρ vector with respect to the origin system.

In figure 3.1 a very simplificative example is shown: the black lines are the edges of the binarized 3D figure, the red arrows represent the origin of the reference system, the green arrows and blue angles are respectively the ρ and θ parameters representing that line in the parameter space. The accumulation matrix resulting from applying the Hough transform to the binarized image is reported in figure 3.2.

3.2.3   Line Extraction Process and Limitations

Once the peaks in the HPCS are identified, various sets of polar parameters (ρ, θ) representing lines are found. In order to extract the line information in the image plane, the parametric line must be anti-trasformed simply using the inverted equation for the normal parametrization. In doing so, it is extremely important to always keep in mind the reference system position and its orientation in both the image plane and the parametric plane.
To extract the angle that the detected lines form with the horizontal axis γ one has to add or subtract $\pi/2$ from the Hough angle depending on the reference system orientation and the sign of the extracted θ:

$$\gamma = \pi/2 \mp \theta$$
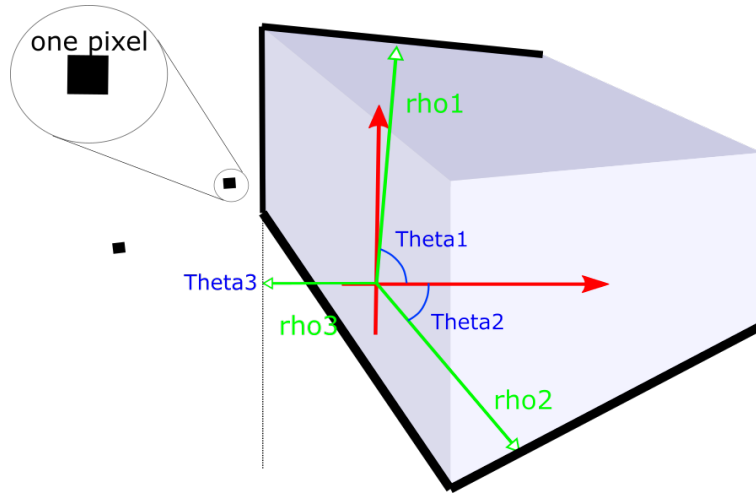
Figure 3.1: Visualization of the parametric representation of a line in the image plane. All the 4 lines are visible in the HPCS (Yellow)

theta[deg]	rho[pixels]				
	-40	-20	0	20	40
-90	0	0	0	0	0
-60	0	0	0	0	28
-30	0	0	0	1	0
0	0	29	0	0	0
30	0	35	0	0	0
60	0	0	0	0	0
90	0	0	0	0	30

Figure 3.2: Example of a HPCS for a simple problem; vectors quantization is extremely coarse to simplify visualization of the problem

There are a few limitations for the CHT that must be addressed in order to avoid results that do not make sense. Firstly, line results are sensitive to the quantization of the parameters ρ and θ: finer quantization gives better resolution but increases the computation time and exposes the problem of clustering high count accumulators corresponding to nearly collinear point. Secondly, this technique finds collinear point without reguard of continuity: as a result, a good line in the image plane can be distorted by the presence of unrelatd figure points in another part of the image that happen to be in the same accumulator cell. A related problem is that meaningless groups of nearly colinear points can be mistaken for a line. This problems are strictly correlated to the binarization threshold of the image, so it is necessary to find the optimal binarization before performing the Hough Transform.

When extracting lines with high resolution in noisy images, the clustering problem becomes severe and the extraction of data is not as immediate. The first useful procedure to reduce this problem is the reduction of the considered image: it is best to detect lines in small image sections called windows, where not too many lines are present, so the HPCS will not be too chaotic. Another important parameter is the minimum length of the line (in pixels) that must be detected: choosing the right value will avoid the detection of fake lines due to random collinear points in the image; the length of the line is the number of points in a specific accumulator cell $A(\rho_i, \theta_i)$. Even after applying a gaussian filter to the binarization and a good threshold, the HPCS will more often than not still have clustering and the peaks are not defined by one cell. This happens because the lines are usually not perfectly straight; this is very common and it does not pose a problem as long as there is one predominant local peak above the threshold.

In figure 3.3 a Schlieren image taken in the Shock Wave Boundary Layer Interaction study wind tunnel in Delft is presented as an example. This time, the Hough angular resolution is $0.5deg$ and the Schlieren image resolution is $2016 \times 2016[pixels]$. The image has been cropped to reduce the number of lines to detect and reduce the chances of detecting fake lines. A gaussian filter of 4 has been applied to the binarized image (3.4) to reduce the noise. In figure 3.5 the associated adimensionalized HPCS is presented: the counter for each accumulator is measured in "heat", so black means a count of approximately zero. From a quick analysis of the HPCS in fig 3.5 it is possible to notice how in proximity of $\theta \approx -45^o$ and $\theta \approx -45^o$ there are two very strong peaks which clearly represent the two lines across the shock. The first line at 45° is clearly the shock angle. The Hough angle θ sign is inverse due to the fact that the origin of the reference system of the matrix, in MATLAB, is the top left corner. By looking at the other smaller peaks it becomes clear that the peak around $\theta \approx -70^o$ represents the wedge angle (rightfully approximately 20 degrees) while the peak at $\theta \approx 55^o$ represents the weak shock line at the bottom of the picture. It is easy to now associate the other peaks to lines in figure 3.4.
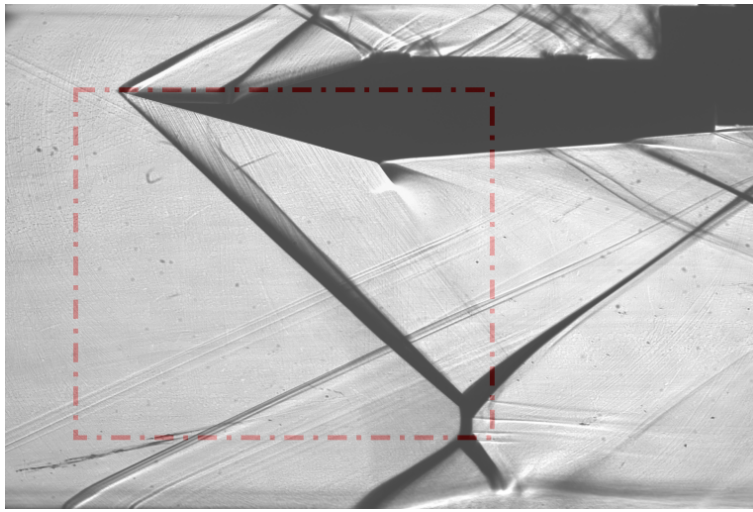
Figure 3.3:   Schlieren Image of a Shockwave (in Air) interacting with the boundary layer

When the CHT is performed, information about the actual segment in the image plane is lost unless an additional procedure is carried out while creating the accumulation matrix. In order to verify that the detected line is actually a real line and that the detection has had a succesfull outcome in terms of accuracy, it's extremely useful to superimpose the detected lines on the original image. In order to do so, each time a point in the image plane (x_i, y_i) is transformed into a curve in the parameter space, its coordinates must be saved and associated to all the cells in the matrix. Once the HPCS is complete, in a given cell $A(\rho_i, \theta_i)$ there will be a sequence of k points with image plane coordinates $[(x_1, y_1), (x_2, y_2), (x_k, y_k)]$, where k is the length of the line in pixels. When the collinear points are known, a segment is formed by the sequence of pixel coordinates with an allowed number of pixels to be skipped ($PixelSkip$) to still be considered the same segment.
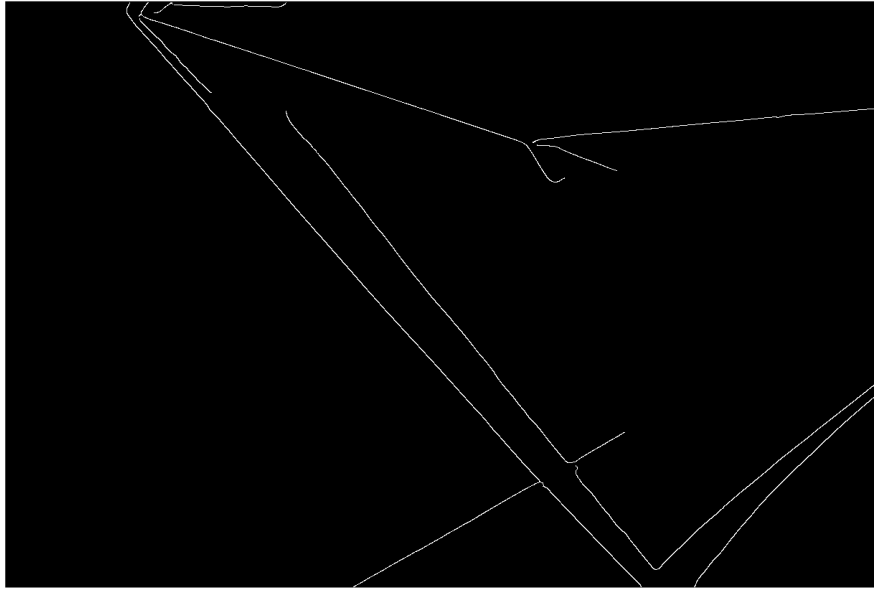
Figure 3.4: Binarized zoomed filtered image of the shock
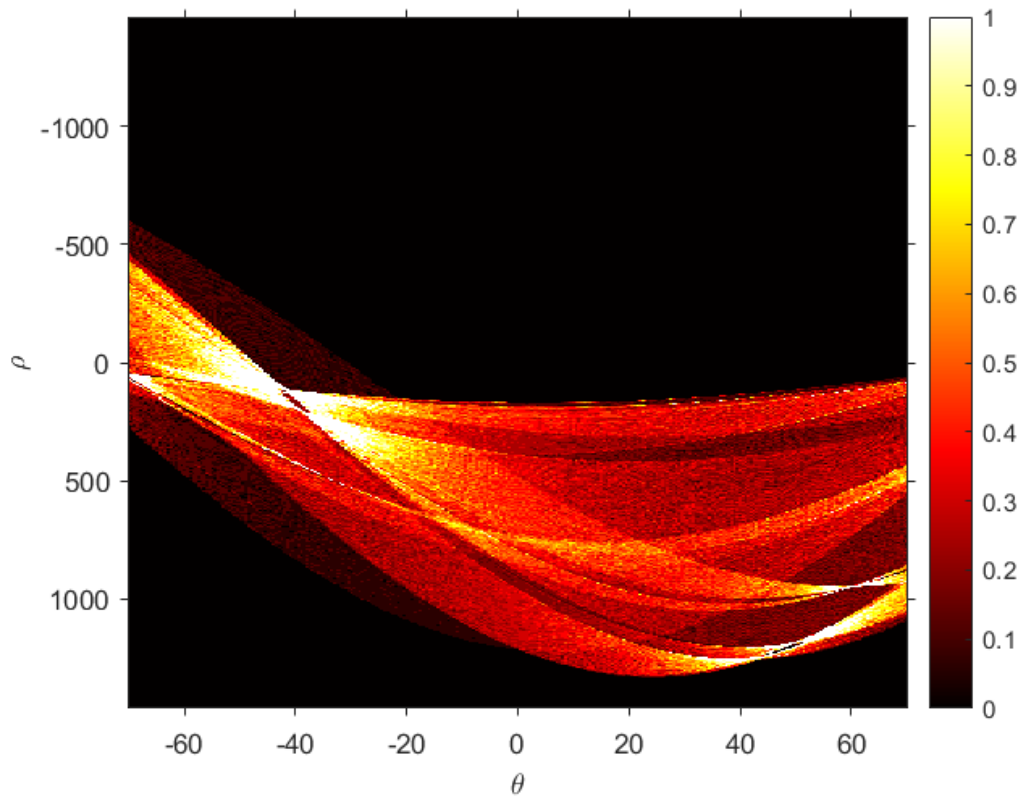
Figure 3.5: Accumulation matrix (HPCS) for the binarized image ($-70^o \leq \theta \leq 70^o$)

3.3 Implemented Line Extraction Tools for Schlieren Data

Schlieren imaging has been used to visualize flow patterns for many years. It is mainly used to study supersonic flows, more in particular shockwave behaviour because of the relative simplicity

in the visualization due to the strong density gradient. In recent times, with the technological advancements is now possible to visualize weak shocks and even Mach lines. When considering organic fluids, due to their properties given by the molecuralr complexity, the clarity of the Mach lines in a Schlieren image becomes good enough to make line extraction possible with a good degree of accuracy since the refractive index changes much more when density gradients are present in the flow, as it is possible to see from figure 2.6. Spinelli *et al.* (2018) used the approach to the Hough transform presented by Lo & Tsai (1995) and Duda & Hart (1972) to extract Mach angles from Schlieren images of an expansion of Siloxane MDM in the nozzle test section of the TROVA facility in Politecnico di Milano, Italy [Spinelli *et al.* (2010)]. The implemented algorithm, which is not presented or explained in the paper, extracts Mach lines in the reflex and uniform flow regions, considering the angular resolution of the pixel discretized domain as the only uncertainty on the Mach value. Furthermore, the TROVA experiments do not consider any Type A uncertainty on the extraction of the Schlieren results since non repeatability of the experiments due to the quasi-steady state measurements that can be taken due to the blow down operating conditions of the facility .

The following chapter presents a robust line extraction method capable of extracting lines on the midplane of a nozzle (or any other flow) as well as on the nozzle's profiles, quantifying all sources of uncertainty in the process. The programs are capable of detecting flow symmetry, verify the statistical convergence of the steady state data acquired in the Schlieren images, then finally extract the midplane and wall Mach angles and Mach numbers quantifying all the uncertainties on the final value as well as the uncertainty in the position to which that value is assigned.

3.3.1   Fundamental Parameters

In this section, the few key parameters that all the implemented line extraction tools share are explained.

In the following list are presented parameters which control the Hough transform extraction algorithm at the very core of the line detection programs, hence their influence on the solution is the same in all the developed tools.

- **Interrogation window**: small part of the Schlieren image where the Hough transform is applied. The interrogation windows discretized domain is defined by the windows pixel dimensions, its center pixel position and the step between two consecutive windows. Reducing the interrogation windows sizes will increase the spatial resolution of the overall line extraction tool while reducing the chances of detecting good lines and increasing the angular uncertainty of the extracted line.

- **Minimum line's length**: minimum number of collinear pixels in a window that can be considered as a line to be extracted. Higher values will increase the quality of the extracted lines, decrease the uncertainty on the angle but increase the chances of not detecting any line in a window.

- **Pixel skip factor**: maximum number of pixels that can be skipped between collinear pixels of a detected line; the skipped pixels will not count in the evaluation of the detected line length. Higher values will ensure the detection of lines even if the window is very noisy or if the lines are not well defined but will also increase the chances of detecting fake lines.

- **Peaks number**: maximum number of peaks that can be extracted from the Hough parameter counting space, which translates to the maximum number of lines that can be detected in the considered interrogation window. This value doesn't affect much the method and its influence is discussed further in the appendix B.

All line detection tools have the same binarization and thinning procedure, thus the same parameters. This step is implemented using MATLAB *edge* function with the **Canny** algorithm for the edging after adjusting the image brightness to optimize the binarizatoin results. The fundamental parameters in the binarization step are:

- **Edge threshold**: two element vector defining the neglegible value for brightness gradient to avoid detecting edges and the minimum value for considering the brightness gradient an edge

- **Gaussian noise filter**: Scalar value specifying the standard deviation of the gaussian filter

- **Adjust threshold**: single or double element vector specifying the parameters for the MAT-LAB *imadjust* function; this step can increase the effectiveness of the edge function thus increasing the quality of the lines in the binarized image.

3.3.2 Mach Line Detection Tools

Schlieren images have been used for decades in the field of fluid dynamics to visualize density gradients in flows, in most cases shock waves due to the high density gradient and thus the high change in the refractive index of the fluid which makes the visualization of the shock relatively easy. When it comes to the visualization of Mach lines, instead, the change of the refractive index for conventional fluids caused by the infinitesimal change in density on the Mach line is too small to be detected. When dense organic vapors are used, instead, this change in the refrective index across a Mach wave can be appreciated and thus visualized with the Schlieren technique. The Schlieren images that can be obtained for organic vapors expansions are thus filled with a net of Mach waves that must be detected.

The detection of many semi-parallel lines that cross each other in a net-like pattern is nowadays still a challenge. Conventional scanning methods are obviously impossible to apply to these datasets, as the Hough transform due to its limitations outlined in Sec. 3.2.3. In order to be able to accurately detect lines using the CHT, the conventional algorithm must be modified and a correct discretization of the domain and must be applied beforehand.
When analyzing a steady state condition of the flow in the nozzle, many Schlieren images must be processed in order to obtain the statystical quantities which can then be compared to the prediction of numerical simulations after a full error source identification (EI) and uncertainty quatification (UQ) have been performed. It must be kept in mind that the dataset must be pre processed in order to align and rotate the dataset to perfectly match the calibration image; furthermore the calibration image itself must be analyzed to verify that the midplane is perfectly horizontal.

Four new programs have been developed to extract useful information in Schlieren images of Supersonic expansions in nozzles. The *flow symmetry detection* tool can extract opposite Mach lines above and below the midplane at any given axial coordinate to verify that the slopes are equal within their uncertainty uncertainty, furthermore if the flow is 1D and fully expanded the Mach number of the flow can be computed at any x and y coordinate in the channel. The *Line Detection Program Stat. Conv.* is fundamental to evaluate the quality of the dataset and to verify that is large enough to achieve statistical convergence of the results. The *Line Detection Program* and *Wall line detection program* extract the angles of the Mach lines respectively on the midplane of the nozzle and the walls to evaluate the Mach values on the midplane and nozzle's profile axial coordinates. The total expanded uncertainties on each computed variable are also calculated, as well as the spatial uncertainty of the results.

The Schlieren images of the nozzle that can be fed into the tools, do not have to meet any particular requirement in order to be processed: in this work different fields of view are analyzed proving the robustness of the methods. It must be mentioned that the quality of the results strongly depend on the quality of the Schlieren images.
In depth details and results of the Mach line detection tools will be presented in chapter 4.

Overview of the structure

Each Mach line detection code has a similar backbone; in the following list, a few key steps that the midplane line detection and the wall line detection tool share are summarized:

1. INPUT SECTIONS: these sections give information about the Schlieren images type and dimensions, what lines have to be identified, what type of analysis must be carried out. The Folder and root name of the Schlieren sequence, rotation adjustments, filter and binarization parameters are also specified. Finally, the working space parameters such as the domain of acquisition, midplane estimation, walls identification parameters must be chosen;

2. CALIBRATION SECTIONS: The walls in the calibration image in the specified domain are detected, then the throat height and position are identified to then calculate the scale factor. Secondly, the walls in the Schlieren dataset are also acquired, to then superimpose the calibration and data walls in order to verify that they match. At this point it is possible to translate results from the global pixel reference system to the nozzle reference system;

3. DISCRETIZATION INPUT: the domain meshing specification and line extraction parameters are defined;

4. CALCULATION: extraction of lines from the dataset

5. RESULTS ANALYSIS AND STATYSTICS: filtering the outliers, evaluation of the statystical quantities, uncertainties and final results

6. REFERENCE SYSTEM CHANGE AND ITS UNCERTAINTY: results are translated to the nozzle reference system in order to be compared to the simulation

7. PLOTS: final plots and checking purposes plots can be shown and saved.

Reference Systems   Each time an image is read it becomes a matrix with its first element (pixel) in the top left corner; this matrix can be seen as a discrete cartesian space with the origin placed in the same spot as the first acquired pixel, the x axis going from left to right and the y axis from top to bottom. This reference system will be from now on called Global Pixel Reference System (**GpRS**). The scale factor and the localization of the throat are fundamental steps to change reference system and place the new origin in the throat, with the x axis following the expanding flow in the nozzle, defining the Nozzle Reference System (**NRS**) in which is possible to compare the CFD simulation results with the experimental data (figure 3.6. A fundamental step in the present work is the identification and quantification of all the possible error sources in each step of the post processing as well as in the experimental set up in order to correctly assess the accuracy of the SU2 flow solver with the Peng-Robinson equation of state together with variable specific heats.

Meshing   The meshing of the domain in interrogation windows depends on which tool is being considered: in figure 3.6 a simplistic overview of the meshing process for the tools is presented. In the flow symmetry tool the vertical axis is discretized in windows with specified height and width above and below the midplane, the step is half of their height and the meshing continues until a stopping criteria is met (automated walls stop method or user-input stop limit). In the midplane line detection tool, the windows step and size is variable along the expansion of the nozzle, aiming to achieve smaller windows closer to the throat (Kernel region) where the lines are much more curved and the Mach number changes quickly. In the wall line detection program, windows sizes can be defined at first and then the tool will mesh the domain following the detected walls of the Schlieren images until the entire user specified domain is meshed.
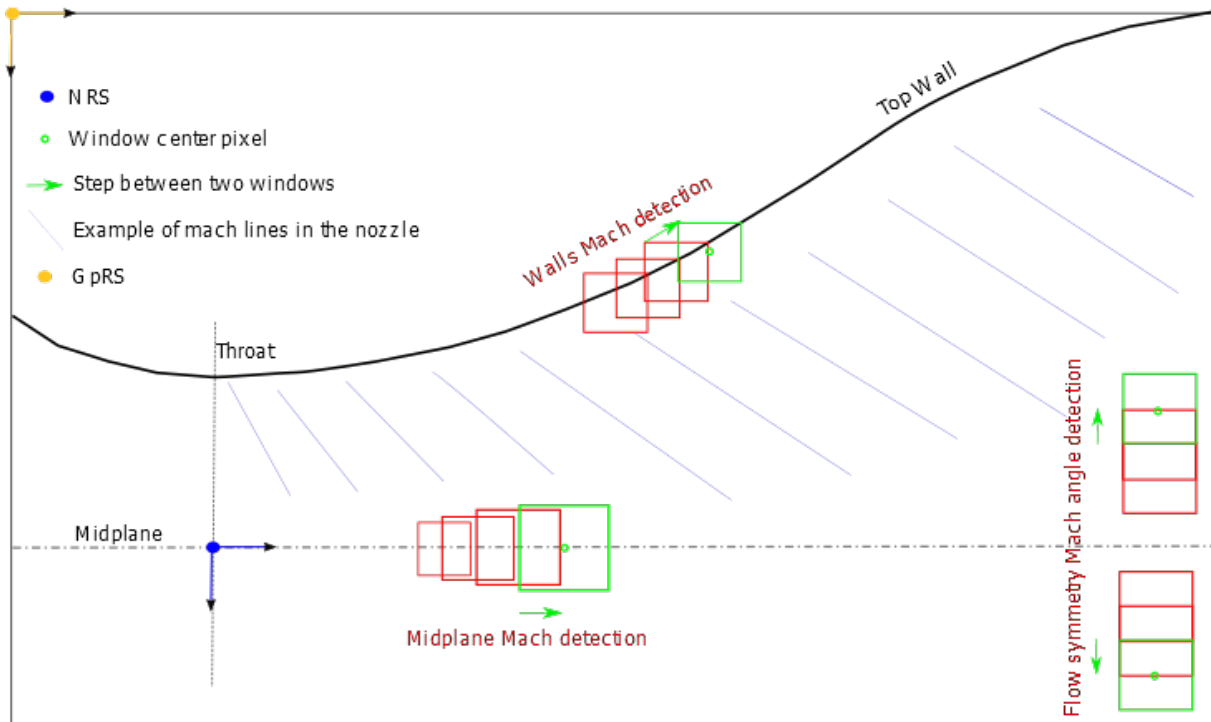
Figure 3.6: Overview of the discretization for the line detection tools

Wall detection   The detection of the walls, both in the calibration image and in the dataset, is performed by interpolating the points where a set threshold of brightness gradient is met. The image is scanned column by column looking for a change in brightness that represents the walls of the image. Once all the wall points are acquired, a polynomial fit is performed and with it an uncertainty in the fitted wall is associated to each coordinate.

Chapter 4

Mach line detection in a Supersonic Nozzle

4.1 Overview of the Schlieren data

In Sec. 2.5.1, three operating conditions of the ORCHID facility have been selected for the accuracy assessment. For all these process runs steady state conditions of the process variables have been identified and are reported in Tab. 2.5 hence all three cases will be analyzed using the developed tools and following the method outlined in this chapter. In Tab. 5.1 the steady state boundary conditions of the nozzle are reported.
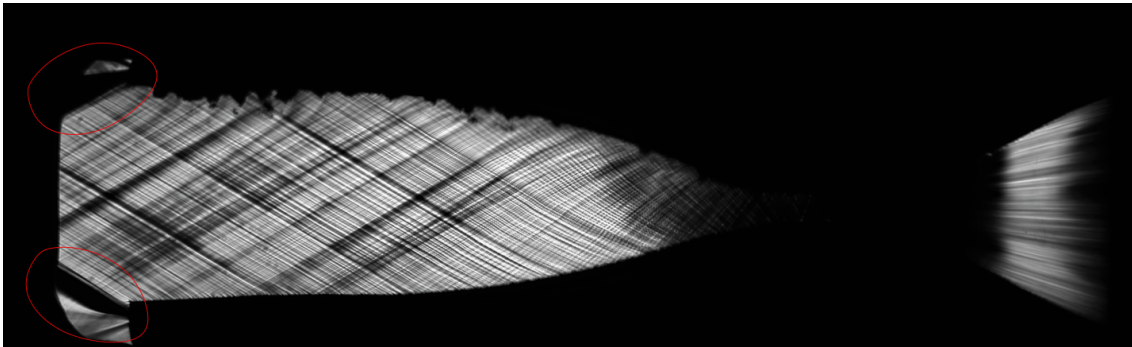
Figure 4.1: Highlight of the recompression shocks at the end of the nozzle where the over expanded flow meets a higher pressure in the receiver. (PR.022)

All the Schlieren images acquired have Mach lines in the entire flow region, even after the reflex region, where the flow is fully expanded and, theoretically, no Mach line should be present. Let us consider for a moment a nozzle, designed with the MoC, operating in perfectly on design conditions and having perfectly smooth walls, following the flow turining angle at an infinitesimal precision. In this case, no Mach line would be present: the Prandtl-Meyer expansion fans would produce infinite expansion waves, thus a continuous expansion, without discontinuities like Mach lines are, even if they are very weak (isentropic). Now in reality things are quite different. The MoC has obviously a finite reslution, the maximum number of points on the wall where the characteristics were propagated used on desing was 100: thus the spline interpolating those points to create the nozzle profiles will never follow the ideal curve of the flow. Secondly, and more importantly, even if the nozzle walls were polished, surface roughness plays a very important role in Mach waves generation. For these reasons, surface roughness and imperfect geometry, the Prandtl meyer expansion fan is discretized into many expansion waves. The effect of these geometric imperfections can also be observed in the two zoomed out photographs: it is possible to notice two slightly stronger Mach waves generated right at the end of the reflex regions on the walls; in this point the diverging curvature of the nozzle
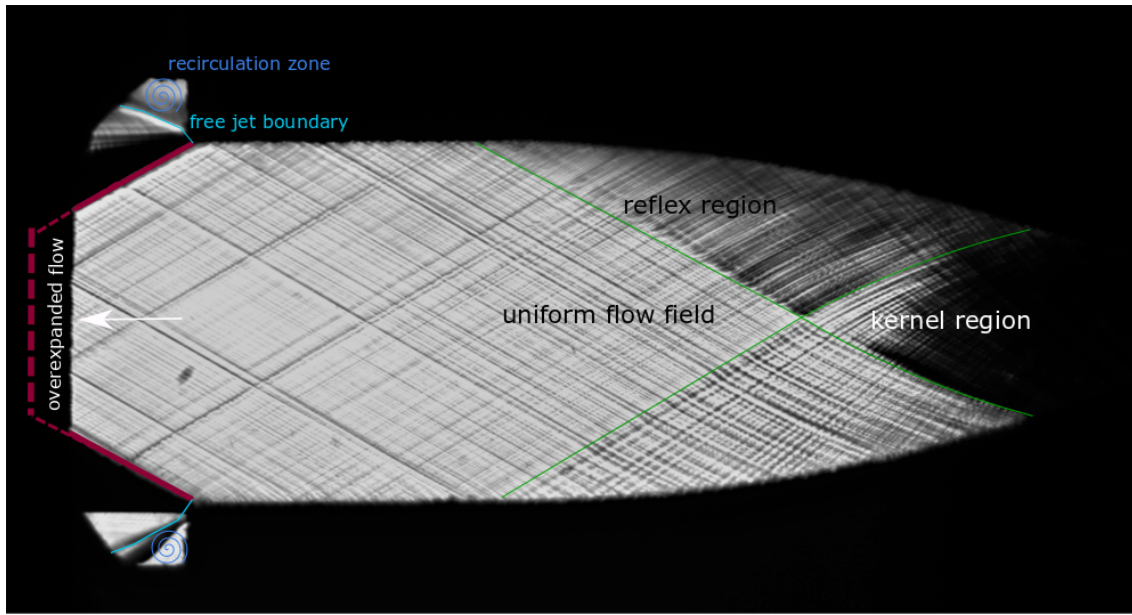
Figure 4.2: The overexpanded of PR.024 flow meets the higher pressure receiver, shocks can be seen together with the recirculation zones, free jet boundary and an hypothetical position of the Mach disk (shock diamond).

meets the constant section channel. Even if the geometry of the diverging part of the nozzle wass designed to have an horizontal tangent at the exit, an extremely small discontinuity can be observed in the flow. As a matter of fact, two slightly stronger (darker) mach waves generate in these points for both datasets (see Figs. 4.1 and 4.2).

There is another effect that can be appreciated just by looking at the raw Schlieren images: the significant overexpansion of the flow, even in the theoretical on design case. The cause for this is that the test section nozzle, in reality, is different from the nozzle designed with the MoC: when the two profiles were tightened together, the gasket allowed a larger displacement than what was calculated, thus the two walls are closer to each other than they were supposed to be. As a result, the throat of the ORCHID nozzle is smaller, thus the area ratio A_t/A_e of the nozzle is increased. Due to this area ratio increase, the nozzle expands more than the original on design case, but the back pressure was fixed at the original on design case. As a result, the flow exiting the nozzle is overexpanded and recompression shocks can be observed at the exit of the constant channel right after the diverging part of the nozzle for PR.022, which has the original on design expansion ratio of a little over 8.8. (4.1).

When considering PR.024, the expansion ration set by the BoP was increased to about 11.3 (4.1), but the recompression shocks at the end are still present, meaning that the fow is still over expanded and the new on-design expansion ratio for the effective ORCHID nozzle is larger than 11.3. In Fig. 4.2, the main flow features for the overexpanded flow of PR.024 are highlighted. The dotted dark red line is an indication of where the diamond shock could be, while the thin cyan lines indicate the beginning of the free jet boundary. When a jet overexpands in an ambient with a static pressure higher than the exit pressure of the flow, the flow starts a series of expansion and recompression cycles due to Mach waves and shocks reflecting on the free jet boundary, creating the well known phenomena of Mach disks untill most of the kinetic energy is dissipated by the viscosity of the fluid and shokcs.

The pressure ratio imposed for PR.026 is even higher than the one for PR.024, but the only results available are zoomed-in, so it is not possible to establish how far the pressure ratio set for PR.026 was from the effective design pressure ratio of the ORCHID nozzle.

Table 4.1: Imposed expansion ratio for the three Process Runs in steady state conditions

PR.0	22	24	26
ORCHID P_{in}^0/P_{out}^0	8.92	11.29	12.71
observed result	over expanded	over expanded	not observable
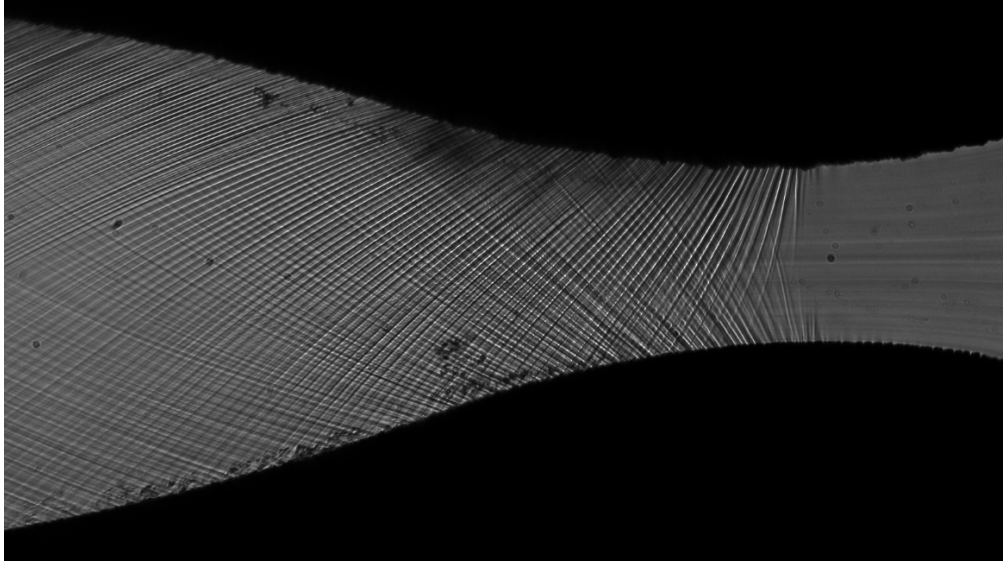
Figure 4.3:   Zoomed in raw Schlieren image - PR.26

As anticipated, the acquired Schlieren images have two different fields of view as it is shown in figure 4.3 and 4.4. The image with a smaller field of view will be from now on referred as *Zoomed-In* while the other one will be referred as *Zoomed-out*. The zoomed-in Schlieren images are fundamental to characterize the Mach field in the proximity of the throat where non ideal effects are more prominent. The zoomed out images, on the other hand, are useful to assess the flow symmetry once the expansion is complete and the flow is one-dimensional and to study the behaviour of the flow during the last part of the expansion and in the constant section duct, where the boundary layer effects should be more prominent, to verify that the euler simulation is accurate enough in predicting the flow field.
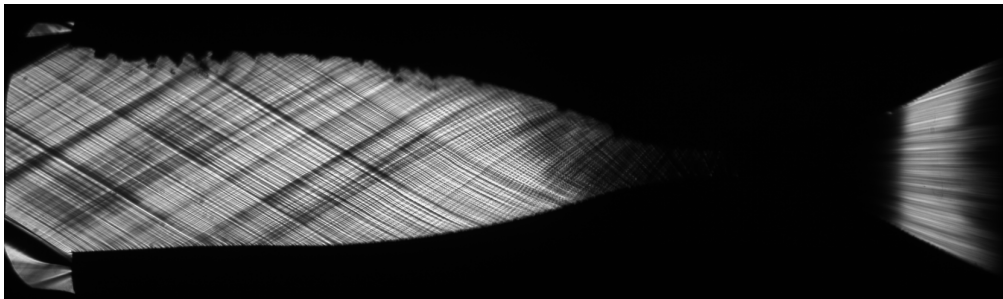
Figure 4.4:   Zoomed-out raw Schlieren image - PR.22 - The top wall is hidden by the melted polymer gasket

4.2 Schlieren Processing Method

The general procedure and method developed in this thesis can be applied to the processing of any kind of Schlieren data; furthermore, the statistical convergence tool is also be able to give valuable information about the steady state condition of the phenomena. Using this tool it is possible to analyze the results of the angle distribution along the midplane with respect to the number of images analyzed. It is also possible to specify different sub intervals in the dataset in which to perform the analysis and if the dataset is not in steady state the average angles will oscillate as well as the standard deviations.

Verifying the statistical convergence of data and the steady state condition is a fundamental step if the user's goal is to compare experimental results with a numerical simulation because the developed codes are able to capture the effect of the change over time of the boundary conditions on the flow field. In other words, it is possible to appreciate changes in the Mach field whenever the inlet conditions averages change over time. It must be always kept in mind that high frequency fluctuations will not be captured unless the acquisition frequency of the Schlieren measurement chain is high enough to have a sufficient number of samples (at least two according to the Nyquist-Shannon theorem) inside the period of the oscillatory behaviour of the fluctuation. For this reason, if steady state is not achieved the Mach line detection tool will give time time dependent results with a non converged average if the number of samples is not high enough.

The Schlieren images acquired in the experiment are usually not all in the steady state condition of the flow. The first step that must be followed is the identification of the steady state condition in the raw Schlieren dataset. Once the steady state time interval $\Delta t_{ss} = [t_0, t_1]$ has been identified by analyzing the stability of the key process variables in the ORCHID (Chapter 2), the steady state sequence of Schlieren images can be extracted from the complete data set of the process run. In order to do so, it is necessary to scan the entire data set looking at the image time stamp so that only the images acquired in an interval $dt_i \in \Delta t_{ss}$ are extracted, representing only the steady state condition of the flow in the test section.

4.2.1 Pre-processing stage
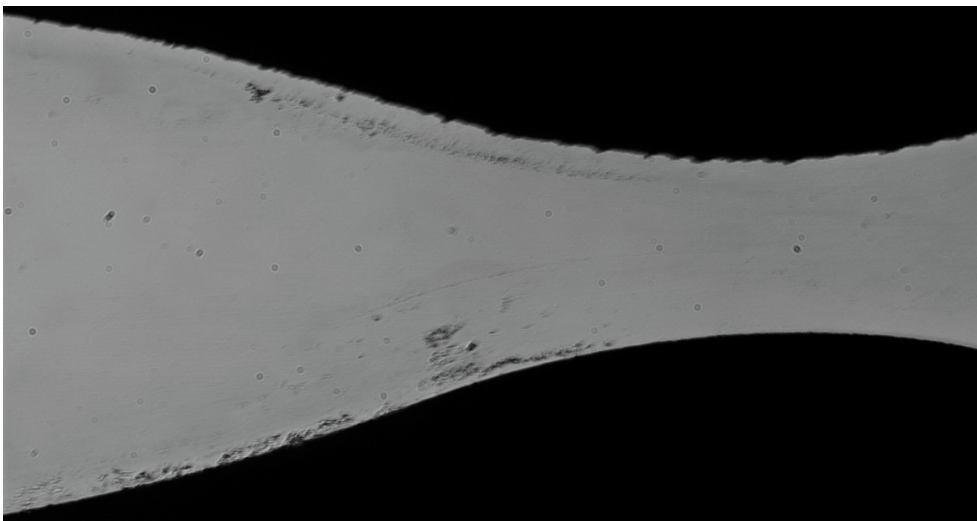
Figure 4.5: A typical calibration image of a zoomed-in dataset - PR.026 .

For each dataset of each run of the facility, a calibration image must be acquired. The codes will use the calibration image to translate the results from the pixel plane to an adimenional plane;

in order to do so, a scale factor and a reference point will be identified in the calibration image and they will be used in the post processing of the Schlieren images. The calibration image must obviously have the same FOV, scale factor and posssibly alignment of the Schlieren images. It is important to point out that the calibration image doesn't necessary have to be an image taken before the start up of the facility, but can also be a Schlierern image taken during the operating conditions of the facility as long as the image itself is very clear and well defined, with a limited brightness contrast throughout the full length of the photographed nozzle.

Once the calibration image has been identified, it is important to verify that the nozzle's axis is horizontal. While having an horizontal calibration image can be very helpful, the codes give the user the possibility to rotate both the Schlieren calibration and the data images freely; furthermore, the tools calculate the rotation misalignment of the images giving the user feedback on how horizontal the images are. It must be noted that the program allows the rotation of the calibration image and the entire dataset as a whole; as a result it is fundamental to correct the shift and rotation of all the dataset images in the steady state sequence so that the entire sequence does not change position or alignment in time. The cross-correlation analysis of the image-pairs to correct shift and rotation differences with respect to the first image of the dataset was done with the LaVision Davis software version 8.3.0.

Once the dataset is aligned to the calibration, it is possible to ssubtract the background to remove impurities and crop useless parts of the images using another external program called ImageJ . Finally image enhancements are optional as well, depending on the quality of the Schlieren images, and can be done both in ImageJ or inside the developed codes. It is also recommended to use 16 bit tif images, for better quality. The programs are able to handle bmp, 8 and 6 bit tif datasets, but if bmp are used, the conversion from RGB to grayscale must be uncommented from the codes.

4.2.2   Processing Stage

Now that a steady-state aligned sequence of Schlieren images is available, the data processing using the line detection programs will follow the flowchart presented in figure 4.6.

Firstly, the symmetry of the flow in the steady state dataset is verified; if the results prove the symmetry then the next step is the definition of a minimum required number of images for statistical convergence, if the symmetry can't be proven then it is important to understand if this is caused by the misalignment of the dataset, its quality or the physics of the problem. If the images are not properly aligned, the pre processing step must be optimized; if the problem is not in the alignment then either the quality of the dataset is not good enough or the flow is not symmetric. In this case it is mandatory to change dataset and start the procedure from the beginning. Once the symmetry has been proven and an appropriate number of images has been established, it is possible to proceed to the midplane and walls Mach field extraction.

Flow symmetry detection

First of all, in order to extract the Mach number from the Schlieren images using the Mach line angle μ, the direction of the flow velocity must be known since by definition μ is the angle between $\vec{V}$ and the Mach line.

$$\vec{V} \sin \mu = c$$

$$\frac{\vec{V}}{c} = \frac{1}{\sin \mu}$$

$$M = \frac{1}{\sin \mu}$$
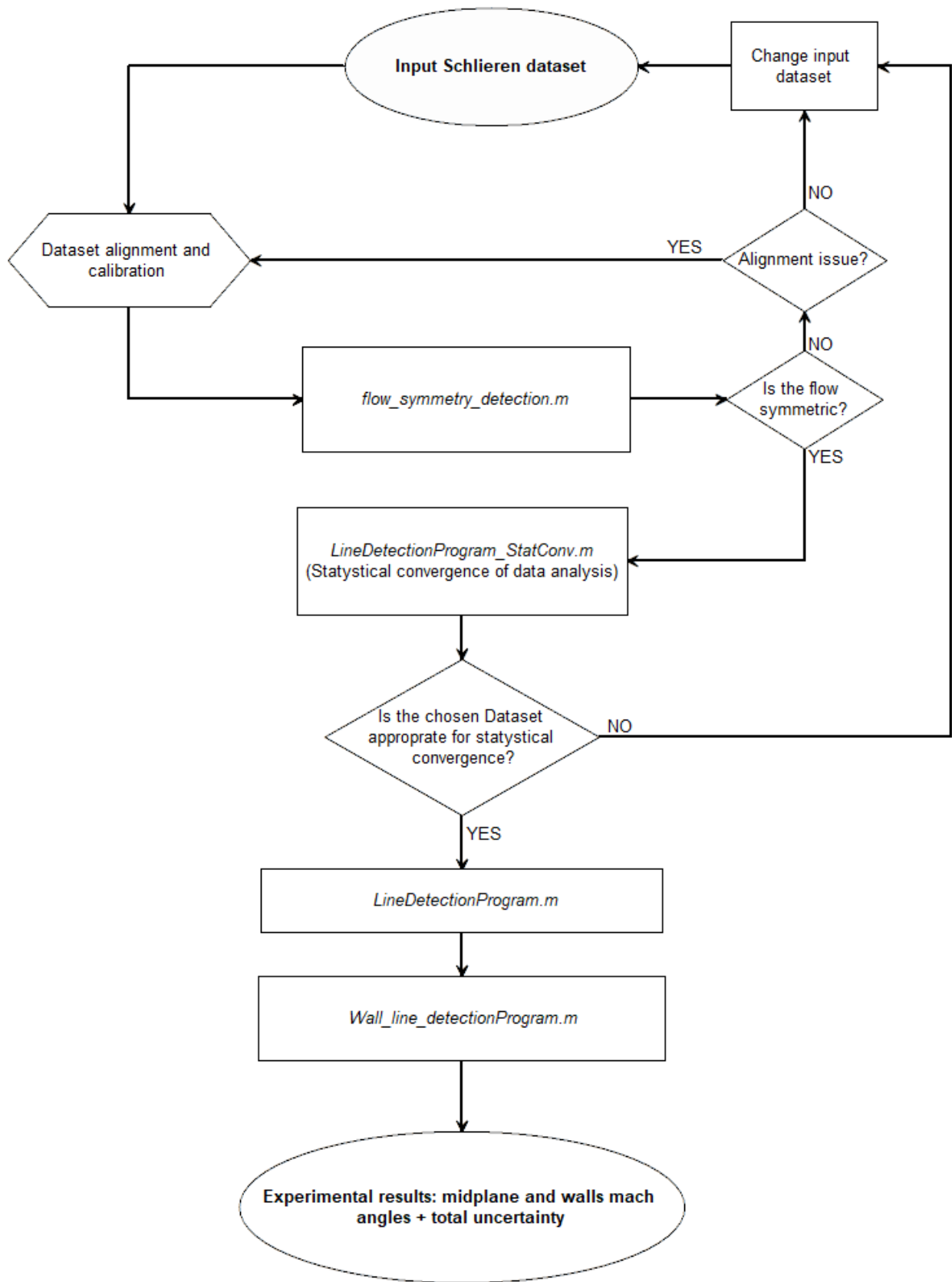
Figure 4.6: Flow chart of the post processing procedure.

Considering that the top and bottom walls of the Nozzle have been realized with extremely precise CNC machines and that the Schlieren sequence is in steady state, it is reasonable to assume that the flow is symmetric and that the axis of symmetry is the midplane.

In order to experimentally validate this assumption, the aligned dataset will be fed into the *flow symmetry detection* program. This tool will let the user select an axial coordinate in which opposite Mach lines above and below the midplane will be detected, so opposite μ angles will be compared to validate the assumption of symmetric flow.

The flow symmetry tool is able to detect straight lines above and below the midplane and then to compare them: for this reason, it is recommended to check the flow symmetry where the 2D (or 3D) effects in the expanding region become neglegible; this is achieved once the flow is fully expanded and, as a consequence, the Mach lines should be all straight, the flow one dimensional and the Mach number constant. The *flow symmetry detection* tool will read a sequence of aligned Schlieren images, will check if there is any rotation in the calibration and the dataset, and finally extract lines at a user-specified axial coordinate above and below the calculated midplane. When a supersonic flow is studied, two Mach lines are present: in order to compare the Mach value, the velocity direction must be known in each location where the line is extracted. Since this is the main assumption that the tool must verify, line angles are compared instead of Mach values or μ angles. As a consequence, this program will output the pairs of line angles with their relative uncertainties to assist the user in the validation of the assumption of symmetric flow. Furthermore, the average Mach will be computed anyways and that result is only meaningful if the flow field is one dimensional and the velocity horizontal.

If the symmetric flow assumption is proven to be valid, it is is possible to proceed in the calculation of the Mach field on the midplane since the velocity direction is known to be exactly horizontal. There are only two reasons for *flow symmetry detection* to output non-symmetric flow results: the first reason is that the flow is actually non symmetric, the second and most common reason is that the program inputs and settings are not properly chosen. In App. B , an in depth explanation on how the programs work and how to properly operate them is presented. In the following list, a few common mistakes that can cause a non symmetric flow result as an output from the *flow symmetry detection* tool are presented:

1. binarization parameters not optimized for the axial location in which lines must be extracted;

2. the chosen axial location is too close to the Kernel region, thus 2D effects can introduce a large error in the symmetry assessment;

3. poor image quality or large brightness gradients;

4. the ratio between interrogation window height and local nozzle height is not small enough;

5. the minimum extracted line length is too small and/or the pixel skip factor is too large.

If the symmetry of the flow is verified, it is possible to proceed to the next step; if not, then the dataset must be checked in order to understand if there was an issue in the pre processing alignment of the dataset or if the dataset is corrupted thus not good enough to be post processed.

Statistical Convergence of Data

Now that the flow symmetry has been proven the midplane velocity direction is known to be horizontal; as a consequence the Mach number in a given midplane position can be simply evaluated by calculating the angle between the extracted midplane Mach line and the horizontal axis. It is now necessary to verify that the number of Schlieren images in the chosen steady state interval is sufficiently large to verify the convergence of the means and the standard deviations. The *Line Detection Program StatConv* tool has the capability of receiving as an input the entire Schlieren dataset and analyzing the extracted lines results with respect to how many images are considered. Considering

that a dataset has N_{img} Schlieren images, the user can define how many iterations changing the number of processed images wants to perform. The variable parameter s in the program represents the number of images of the entire dataset in which the line extraction and results will be evaluated; in order to perform a statistical convergence analysis, s will increase gradually until $s = N_{img}$.

In order to establish the minimum sufficient number of images to achieve a satisfactory statistical convergence of data, the procedure presented in ISO (1993) was followed. The mean and standard deviations of a dataset can be influenced by the dataset size, this is why statistical convergence is achieved when the standard deviation in the mean value $\overline{\sigma}$ becomes neglegible and when the calculated means are constant with respect to the increase in the sample size. The standard deviation in the mean value

$$\overline{\sigma} = \frac{\sigma}{\sqrt{s}}$$

is evaluated by dividing the standard deviation of the images in the sub-set by the square root of the sample size s; increasing s from a minimum chosen number N_{min} to the entire dataset N_{img}, $\overline{\sigma}$ will tend to zero and the evaluated average values

$$\overline{x}_s = \frac{1}{s} \sum_{i=1}^{s} x_i \quad \text{with} \;\; s = [N_{min}, ..., N_{img}]$$

will be constant.
Thus, the sufficient number of images in steady state for each dataset is chosen once the standard deviation in the means becomes neglegible by analyzing the averages and the standard deviations of the SRQs with respect to the considered number of images of the dataset. When these values are constant, convergence is achieved.

The sample number for convergence is based on the characteristics of the measurement chain, the input parameters of the line extraction tools, the boundary conditions of the TS and the characteristics of the expansion, such as the its state and its molecular complexity. By considering datasets significantly larger than the estimated number of samples to achieve convergence, the computational time is increased without any improvements in the results.

Midplane Line detection

Now that a sufficiently large steady state dataset has been selected, it is possible to characterize the midplane axial mach distribution along the nozzle. The *Line Detection Program* has a couple of fundamental roles in the Schlieren data extraction method: firslty the tool will calculate the parameters necessary to translate results from the Global pixel reference system (GpRS) to the adimensional Nozzle reference system (NRS) or even the physical NRS in millimeters. This is achieved in the first section of the program by evaluating the scale factor SF [pixel/mm] , the throat position (or any other specified reference position), the walls polynomial fits, any misalignment issue in the calibration and the dataset and all the uncertainties connected to every mentioned procedure. Secondly the tool will extract the μ angles and thus the Mach number in the nozzle's midplane along the expansion of the flow and will evaluate all the uncertainties on the extracted value as well as the uncertainties associated with the new NRS positions and the discretization error.

The midplane line detection tool structure is the most complete one of all the tools, thus all the other programs have similar implementations, with usually less steps, with just a few key differences in the meshing procedure and the uncertainties calculation. In the following list, a detailed explanation of what each section does and how is presented.

- **INPUT 0**: an estimation of the Mach angle μ along the x-axis is performed automatically by giving the program three μ values along the expansion of the nozzle. The user can also

decide if a full analysis has to be performed or if previous data has to be loaded instead, and if the results have to be saved or not.

- **INPUT 1**: all the Schlieren images are read and binarized; the user has the option to choose if this task will be done in parallel, which requires a larger amount of RAM memory, or in series, which will take usually a lot longer. The calibration image is read, then the user has the possibility to rotate and adjust the dimensions of the entire dataset and/or the calibration image.

- **INPUT 2**: the edged binarized image can be cut and re-centered, an initial estimation of the midplane position Y_0 is required, then the user has to estimate the interval in which lines have to be extracted.

- **CALIBRATION 1**: the user can choose to use the automatic throat identification procedure to get the scale factor or another specified position. In this section, after giving the program the throat height in millimeters and its uncertainty, the polynomial fits of the walls in the calibration image are evluated using a binarized image with a specified threshold to correctly identify the walls. Knowing the walls, the throat location is identified by minimizing the distance between the two fitted walls, and the scale factor is then calculated dividing the throat height in pixel by the specified height in mm. Once the walls are evaluated the actual midplane position and possible rotation are calculated. In this section, the user can also use another method to get the calibration phase results: the exit height and position can be used, the program is also able handle both images that have been cut right at the exit or not; if the image is not cut at the exit, the program will identify the exit of the nozzle automatically. The result of the calibration can be appreciated in Fig. B.2 in the appendix.

- **CALIBRATION 2**: the walls of the Schlieren dataset are identified and superimposed to the calibration image walls to determine if they are matching. Misalignment and rotation information are given, and if the walls match as is shown in Fig. B.4, then all the calibration data can be used for the Schlieren images.

- **INPUT 3**: the meshing of the domain of interest is performed; the user can input how many windows must be created in the domain, the maximum and minimum sizes and then the program will mesh the midplane with windows that linearly decreease in size, from the exit towards the throat. In this section the user must also input the minimum and maximum allowed pixel skip factor and the minimum angle that one is expecting to extract $\mu_{min}(x)$. The minimum angle will be used to compute the minimum length factor C_{min} of the line that can be extracted to have neglegible misalignment error. The line length factor C is defined as

$$C = \frac{LL}{h_w}$$

where LL is the length of a line in pixels, and h_w the height of the interrogation window in pixels.

Following a simple geometric reasoning it is possible to choose a value that ensures that the extracted line will cross the midplane:

$$C_m = \frac{1}{2\sin(\mu_{min}(x))}.$$

This value can be reduced to increase the chances of detecting lines in the interrogation windows if the maximum sizes of the interrogation windows (at the exit of the nozzle) are sufficiently small compared to the nozzle height (see section 4.3 misalignment error). If the height ratio $r = h_w/H$, where $H(x)$ is the distance between two walls at a given coordinate, is always less than 0.2 then the minimum length factor can be reduced to:

$$C_{min} = \frac{1}{2\sqrt{2}\sin(\mu_{min}(x))}.$$

Using this value it is easy to prove that the maximum distance between the extracted line in the window and the midplane is less than 5% of the height of the nozzle: this value is small enough so that the velocity direction is still perfectly horizontal if one moves less than 5% of the nozzle's height above and below the midplane.

- **CALCULATION**: lines are extracted and saved in a structure; μ angle and Mach values are saved for each interrogation window location k and each frame f. The program will avoid detecting lines if the length of the line is under the minimum value, thus the extracted data in each window may vary. The variable *information lost* will keep count of how many lines were not extracted and where so that the user is able to verify that the extracted results are sufficiently large in every window to ensure statystical convergence of the data. As long as a sufficiently large dataset is used and not too many lines are skipped, the results will be valid.

- **RESULTS ANALYSIS AND STATISTICS**: the outliers are filtered first, then the standard deviations and averages over time f of the Mach values and angles are performed to evaluate the Type A uncertainties. The average over time of the detected lines length is computed to determine an average angular resolution, then the standard deviation on the length of the lines is propagated through the angular resolution equation to derive the extended uncertainty on the angular resolution which is then added to the average value to represent 95% of the cases. The Type A uncertainties on the Mach angle is added to the extraction uncertainty which is the square root sum of the hough resolution and the angular resolution. The extraction uncertainty on the μ angle is also propagated through the $M = f(\mu)$ equation. For both the μ angle and the Mach number, correlation coefficeints ρ_{ij} between the random uncertainties and the extraction uncertainties are evaluated and are found to be non neglegible; thus the total uncertainty is calculated as

$$u_{tot} = \sqrt{u_{rand}^2 + u_{extr}^2 + 2u_{rand}u_{extr}\rho_{12}}.$$

- **RESULTS 2**: the translation of all the results from the GpRS to the adimensional and dimensional nozzle reference systems is performed. The spacial uncertainties $u_{\Delta x}$ and $u_{X,NRS}$ are evaluated following the steps presented in 4.3.

- **SAVE / LOAD**: the user can set two flags at the beginning of the program that will determine whether the results of tha analysis will be saved or not, or if no analysis has to be performed so that the user can load previous data for plotting purposes.

- **PLOTS**: in this section all the trends are presented and it is possible to superimpose the average detected lines on a Schlieren image of the dataset for visualization purposes.

Wall Line detection

The *wall line detection program* relies in part on the results of the calibration section and spatial uncertainty evaluation of the midplane line detection program, thus it has to be run last. This tool is able to extract Mach lines in an automatically discretized space in proximity of the nozzle's walls in interrogation windows of a specified size. From the extracted lines and detected walls the program extracts the μ angle and thus the Mach number assuming the slip condition at the wall: considering small interrogation windows, the wall curve can be approximated to a line, thus the velocity direction is parallel to the slope of the line in that window.

The developed tool receives calibration data necessary to translate results to the adimensional NRS from the midplane line detection program; the user can also choose to load the calibration image fit of the walls in the *wall line detection program* in order to use the calibration walls instead of the automatic choice of using the automatically detected walls in the Schlieren data images. The choice of using either the caliration or the Schlieren walls to evaluate the wall angle that has to be subtracted to the detected line angle is up to the user which is assisted by the extended uncertainty

values for both fits of the walls.

In the following, the program section details and tasks are presented.

- **INPUT 1**: the Schlieren images are read and binarized; the user has the choice to do this in parallel or in series. The calibration image is read and the user has the possibility to rotate and adjust both the calibration image and the dataset.

- **INPUT 2**: in this section the wall parameters are specified: wall line extraction interval, initial guess of the midplane Y_0, binarization threshold for the wall detection. The user has the choice to evaluate the Mach number distribution on only the lower, upper or both walls.

- **CALIBRATION 1**: Schlieren walls are detected and the polynomial fit uncertainties calculated.

- **INPUT 3**: after loading the calibration data from the midplane line detection program, the user will choose which walls are going to be used to evaluate the local wall angle in the windows. The Hough transform angular resolution θ_{min} is chosen as well as the pixel skip factors and the windows dimensions. The minimum lines length factor choice is more complex than the case of the midplane: the thermal boundary layer of the nozzle can blur the image in the proximity of the walls, thus reducing the visibility of the Mach lines and increasing chances of not detecting lines. For this reason detecting lines that exactly touch the wall is counter productive; it is better to detect lines in any position inside the window and to assign the detected value to its center pixel: the distance between the wall and the center pixel is extremely small if the height ratio r is small enough, thus the misalignment error becomes neglegible. Once a sufficiently small height ratio is established, the minimum lines length factor can be choosen trying to make a compromise between finding as many lines as possible and not increasing the uncertainty coming from the angular resolution, which increases substantially as shorter lines are detected.

- **CALCULATION**: in this section the discretization of the domain and the calculations are performed together step by step, frame by frame. The discretization of the image along the walls is performed by achoring the corner pixel of each window to the wall polynomial equation and from there the window is defined by moving inside the nozzle (up or down depending on which wall is considered) of the window height in pixels h_w. Once the windows on top and/or bottom walls are defined, lines are extracted before moving to the next position. After the line extraction, the wall angle and its uncertainty must be evaluated. As mentioned earlier, the nozzle profile can be approximated to a line inside an interrogation window small enough that the approximation has a neglegible error. Now the wall angle at a certain axial coordinate corresponding to the center pixel of the window is

$$\alpha_w = \arctan\left(\frac{\text{wall}(x) + \text{wall}(x + b_w)}{b_w}\right)$$

where b_w is the base of the window, x is the axial coordinate at the beginning of the window and wall(x) is the polynomial equation of the wall. The uncertainty associated with the wall angle α_w, for both the upper and lower walls respectively, comes from the standard deviations $\sigma_w = [\sigma_u, \sigma_l]$ of the polynomial fits of the walls, at the beginning x and at the end $x + b_w$ of each window. In order to correctly quantify the uncertainty on the calculated wall angle it is necessary to firstly evaluate the maximum angular uncertainty at the two extremes of the window x_k and $x_k + b_w$, then finding the minimum between the two values:

$$u_{\alpha,w} = \min\left[\max[u_{\alpha,w1,2}(x_k)] , \ \max[u_{\alpha,w1,2}(x_k + b_w)]\right] \qquad (4.1)$$

The derivation of the uncertainty equation above is shown in section 4.3. Once the wall angle is evaluated the Mach line angle μ is calculated by adding or subtracting the 90 degrees of

the polar coordinates of the Hough transform and the wall angle; the choice of adding or subtracting depends on which wall is considered, the orientation of the reference system and the sign of the extracted angle. Once the actual Mach angle is known it is possible to calculate the instantaneous Mach number assigned to each k-th window:

$$M(k) = \frac{1}{\sin(\frac{pi}{2} \pm \theta_{\text{detected}} \pm \alpha_w)}.$$

Once the local istantaneous Mach number is computed, the program takes a step from the window k to $k+1$ of half of the window base; it follows that the next window's corner will be anchored to the wall when being still part of the previous window (as shown in figure3.6). At the end of this section all extracted lines are saved in a structure and the Mach angle and number are known for each location k and each frame of the dataset f. Two *information lost* parameters will keep track of all the lines that have not been found so that the user can verify that the results are still above the statistical convergence threshold previously assessed.

- **RESULTS**: after filtering outliers, the program calculates the averages and standard deviations over time for the Mach angle and Mach number in all the interrogation windows locations k. The procedure here is the same as the one for the midplane line detection program, the only difference is that the total uncertainty on the results are larger due to the uncertainty in the evaluated wall angle.

- **RESULTS 2**: the center pixels coordinates of each interrogation window in the GpRS are shifted inverted and adimensionalized with the throat height to be translated in NRS coordinates in order to be compared with the simulation.

- **SAVE / LOAD**: the user can set two flags at the beginning of the program that will determine whether the results of tha analysis will be saved or not, or if no analysis has to be performed so that the user can load previous data for plotting purposes.

- **PLOTS**: in this section all the trends are presented; it is also possible to load the results from the midplane *Line Detection Program* and superimpose the average calculated lines on the midplane and walls on a Schlieren image.

4.3 Error source identification and Uncertainty quantification in the Post Processing Tools

It is extremely important to identify all the sources of error resulting from the post-processing stage of the experimental data in order to accurately quantify the uncertainties on the analyzed system response quantities to correctly assess the accuracy of numerical simulations.

When trying to identify error sources in complex systems one can easily get lost in the large number of factors that could affect experimental results. For this reason, it is fundamental to identify all the error sources that could have a potentially appreciable effect on the measured variables.

The post processing most influential error sources are listed in the following, together with their origin and dependancy, explaining what are the factors influencing these errors:

- Hough transform resolution - caused by the user-specified discretization of the glsHough angle θ;

- Variation of the detected line length - the quasi-random detection of lines inside the interrogation windows determines a variable length of the lines caused by the slightly different binarization of the image as the brightness gradients can change from rame to frame;

- Random distribution on the μ angle associated with repeated measurements in the flow - associated with the detection of different lines in each window due to the brightness change during frames;

- Variation of the angular resolution in the local windows - caused by the variability in length of the detected lines;

- Angular resolution of a detected line - due to the pixel-discretized domain;

- Misalignment between the considered flow velocity direction in a window and the effective velocity direction associated with a detected line - depending on the size of the window discretized domain;

- Fitting of the detected walls from the calibration or Schlieren data images - whose accuracy depends on the quality of either the Schlieren or calibration image walls;

- Local wall angle approximation - depending on the size of the windows, the curvature of the nozzle and the clarity of the walls in the Schlieren or calibration images;

- Detection of the throat height in pixels - depending on the image clarity, binarization parameters and polynomial fit order;

- Throat localization in the GpRS - caused by the asymmetry of the polynomial fit of the walls;

- Discretization of the domain in windows - strongly influenced by the scale factor of the Schlieren images; if the scale factor increases then the window can decrease in size with respect to the nozzle in the Schlieren, thus increasing spatial resolution .

Once the sources of error have been clearly identified, the uncertainties in the post processing tools must be quantified. When dealing with error sources and uncertainties it is important to keep in mind that the number of uncertainties that can be evaluated can differ from the error sources; usually one can estimate more uncertainties than error sources since these can combine and propagate through equations.

In the following, all the most influential uncertainties in the post processing method are analyzed and quantified, one by one. The results are summarized in table 4.2, where a quick overview of the uncertainties is presented. Next to the uncertainty, the type can be found: this can be type A, type B, A-derived - which means that only type A uncertainties are used to calculate this uncertainty - and combined, which obviously means that the uncertainty is a combination of

statistically-calculated uncertainties, resolutions, propagation formulas etc. At the right of the Type, the Correlation/propagation box gives quick information on what the uncertainty is correlated to or to what other uncertainty is propagated. Keep in mind that much more information is available in the single analysis of the uncertainties down below. The origin column show if the uncertainty is a source uncertainty, or if the uncertainty derives from other uncertainties contributes. The the last column, gives a simplificative explanation of what the error sources of the uncertainties are.

Table 4.2: Overview of all the quantified uncertainties in the post processing.

Uncertainty	Type	Correlation/Propagation	Origin	Error Sources
$U_{\text{Hough,res}}$	B	-	source	θ discr.
U_{LL}	A	propag. to U_{AR}	source	line variability
$U_{data,\mu}$	A	corr. with $U_{\mu,ext}$	source	line variability
U_{AR}	A	propag. to AR_{95}	U_{LL}	LL variability
AR_{95}	combined	corr. with $U_{\text{data},\mu}$	derived	LL variability; pix. discr.
$U_{\text{poly,wallfit}}$	A	propag. to U_{SF}	source	wall fit
$U_{\alpha,w}$	combined	propag. to $U_{\mu,ext}$	derived	wall fit
U_{SF}	combined	propag. to $U_{X,NRS}$	derived	wall fit; throat bias
$U_{th,loc}$	A-derived	propag. to $U_{X,NRS}$	$U_{\text{poly,wallfit}}$	wall fit
$U_{\Delta x}$	B	-	source	domain discr.
$U_{X,NRS}$	combined	-	derived	wall fit; throat bias; throat loc.
$U_{data,M}$	A	corr. with $U_{M,ext}$	source	line variability
$U_{\mu,ext}$	combined	corr. with $U_{data,\mu}$	derived	θ discr.; pix. discr.; wall fit
$U_{M,ext}$	combined	corr. with $U_{data,M}$	$U_{\mu,ext}$	θ discr.; pix. discr.; wall fit

Hough Transform Angular Resolution $u_{\text{Hough,res}}$

The Hough transform can detect angles with a user-specified resolution θ_{min} for the lines polar coordinate θ in the image plane: this introduces an uncertainty in the line angles that are possible to detect and is defined as:

$$\theta_{true} = \theta_{\text{detected}} \pm \frac{\theta_{min}}{2}.$$

A uniform probability distribution inside the containment level $[-\theta_{min}, +\theta_{min}]$ of the real θ angles is assumed following the recommendations in ISO (1993) ; as a result the 100% CL uncertainty associated to the Hough transform resolution is

$$U_{\text{Hough,res}} = \frac{\theta_{min}}{2}.$$

Line Length u_{LL}

When a line is detected in a particular position, its length in pixels must calculated. It is important to notice that this length may vary between different frames in a fixed position due to the dynamism of the physical phenomena. For every spatial position, a local angular resolution must be evaluated: in the present thesis this is achieved using the average length of the detected lines and propagating their uncertainty through the equation of the angular resolution to determine a final angular resolution at a desired confidence level. For this reason, an uncertainty on the length of the lines u_{LL} in a location is introduced and can be easily evaluated computing the standard deviation of the various detected lines through all the frames. Once again, when the standard uncertainty is evaluated a coverage factor $K = 2$ is applied in order to extend the confidence level to 95%.
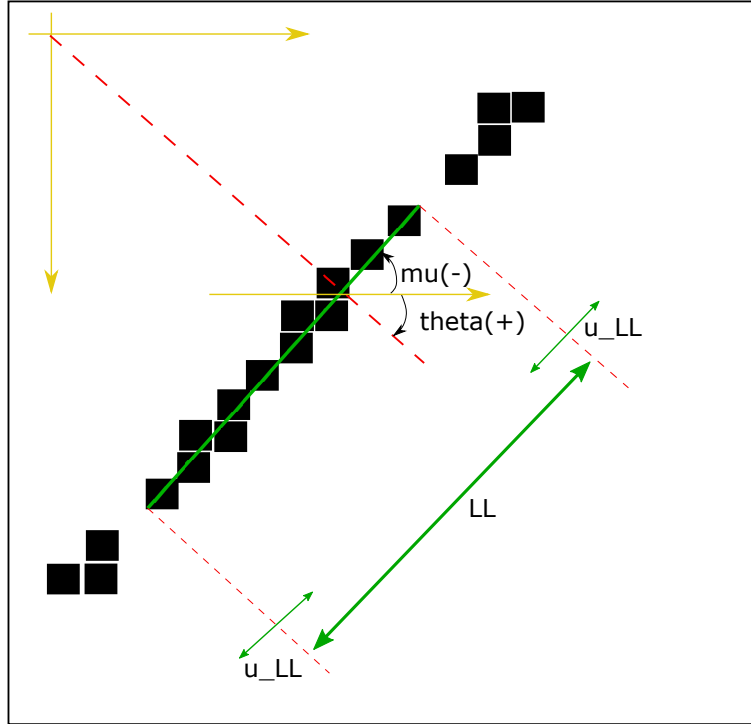
Figure 4.7: The uncertainty in the length of the line at a fixed position comes from the variability of the pixel distribution during time (frames)

Random Uncertainty on the Mach angle $u_{\text{data},\mu}$

When extracting lines in a section of the Schlieren image sequence, the implemented Hough transform selects the best line in that particular location and at that time stamp; the intrinsic variability of the physical phenomena and the data acquisition chain will cause a variance in the acquired line, hence a random distribution of angles around a mean is found. Once the statystical convergence of the Schlieren data has been verified for each data extraction location, the mean through time (for every frame) of the extracted Mach angle values that are found are representative of the true mean to which a standard deviation is associated. The first source of uncertainty that has to be considered is the classical Type A statistical uncertainty coming from the randomness of the binarized Schlieren images. This standard uncertainty (68% CL) is then expanded with a coverage factor $K = 2$ to a 95% CL.

Uncertainty of the Angular Resolution u_{AR}

The average length of the detected lines is fundamental to determine the average angular resolution $\overline{AR}$ on the Mach angles μ in a particular spatial coordinate. The average angular resolution associated to a particular position in space is evaluated in equation 4.2 using a simple trigonometry relation between the average length of the line in pixels $\overline{LL}$ in that position and the minimum possible distance in the image plane (one pixel). In figure 4.8 a simplistic case is presented: the average detected line (green) could also be the yellow line since both cross the pixels. The two lines have a maximum angular variation of $\overline{AR}$ (red).

$$\overline{AR} = \arctan(\frac{0.5}{\overline{LL}/2}) \tag{4.2}$$

It is now necessary to obtain a local angular resolution capable of representing most of the angular resolution in that position for all the frames; in the present work, a confidence level on the angular resolution of 95% has been chosen. In order to achieve this, the 95% CL uncertainty U_{AR} on the
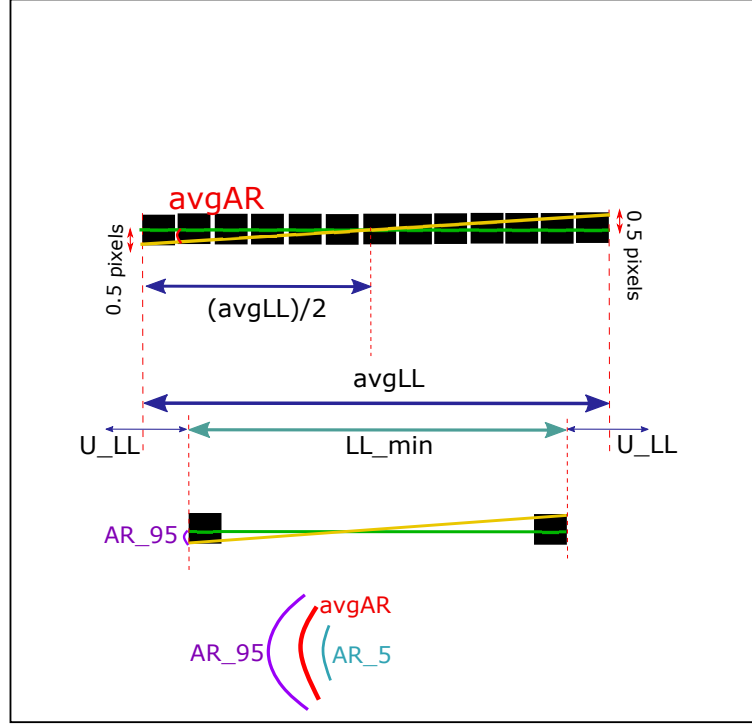
Figure 4.8: The average angular resolution at a fixed position depends on how many minimum distances (pixels) are present in the average line in that window during time

angular resolution must be calulated propagating the extended uncertainty on the length of the lines Ku_{LL} (with $K = 2$) through the equation 4.2 using a sensitivity coefficient.

$$u_{AR} = \frac{\mathrm{d}f(LL)}{\mathrm{d}LL} u_{LL}$$

Since the angular resolution is a function of the length of the lines, the angular resolution sensitivity to the line length can be easily obtained:

$$AR = f(LL)$$

$$\frac{\mathrm{d}AR}{\mathrm{d}LL} = \frac{\mathrm{d}}{\mathrm{d}LL} \arctan(\frac{1}{LL})$$

$$|\frac{\mathrm{d}AR}{\mathrm{d}LL}| = \frac{1}{LL^2 + 1}$$

Finally the uncertainty in the length of the lines can be propagated to the uncertainty in the angular resolution:

$$U_{AR} = \frac{1}{LL^2 + 1} K \ u_{LL}.$$

Now, keeping in mind that with this definition of angular resolution higher values of AR correspond to worse conditions, it is possible to obtain the local angular resolution capable of representing 95% of the extracted lines resolution. The uncertainty in the length of the lines derives from the fact that not all lines have the same length: some lines can be shorter than the average thus increasing the uncertainty in the angle. This uncertainty has been propagated to the angular resolution thus increasing its value and reducing the capability of distinguishing two lines: if the angular difference between two lines is smaller than the angular resolution, the lines are identified as the same. This step can be tricky since by definition an uncertainty is a value to add and subtract to an average to obtain an interval of confidence but in this case the situation is slightly different: the uncertainty on the angular resolution is an uncertainty on an uncertainty. It follows that depending on our decision

to add or subtract the uncertainty to the average, the confidence level of the uncertainty evaluated will change. In this case in order to obtain an angular resolution, which is an uncertainty in the angle of the line, capable of representing 95% of the cases, the uncertainty on the angular resolution had to be added. If the uncertainty on the angular resolution was subtracted to the average angular resolution, a confidence level of only 5% could be achieved since the lower value for the 95% interval would have been used (keep in mind Fig. 4.8).

In this analysis, a uniform probability distribution of the lines inside the angular resolution uncertainty has been assumed.

Extended Angular Resolution AR_{95}

Due to the complex relations between the numerous uncertainties in this analysis, it must be kept in mind that in the present work the word **resolution** represents the minimum distance measurable between two points; as a result, the Angular Resolution in this work is the minimum angle that can be detected, thus higher values of AR correspond to worse results.

The average angular resolution previously evaluated, has a probability of 100% to contain all the lines, given that average line length. Before adding a 95% confidence level (CL) uncertainty to it, one can lower the confidence level of the average angular resolution to 95%:

$$\overline{AR_{95}} = 0.95\overline{AR}.$$

Once the average angular resolution $\overline{AR_{95}}$ and its extended uncertainty U_{AR} are known, the local angular resolution capable of representing 95% of the data can be computed just by adding the extended uncertainty previously evaluated to the average value:

$$AR_{95} = \overline{AR_{95}} + U_{AR}$$

The angular resolution is a function of the Schlieren measurement chain: both the alignment and the camera settings(lenses, focal distance, shutter speed) strongly influence the length in pixels of the detected line and, as a result, the local angular resolution available.

Misalignment of the velocity direction $u_{\text{mis.},\mu}$

This source of error simply comes from the uncertainty in the velocity direction associated to a detected line. When detecting Mach lines along the expansion in the nozzle, the image must be discretized in sub-images called interrogation windows in which the Hough transform is applied. Taking as an example the midplane *Line Detection Program*, the Mach angle is extracted by knowing that the velocity is perfectly horizontal, so once the Hough angle θ is known, the μ angle (thus the Mach number as well) is simply derived by adding or subtracting $\pi/2$. This procedure is valid as long as the extracted lines are crossing the midplane where the velocity has been proven to be exactly horizontal.

Due to the imperfections in the images of the dataset, to increase the chances of detecting lines in the interrogation windows the minimum line length coefficient could be lowered but this could result in the detection of lines in the window that do not cross the midplane, so the velocity direction could be not exactly horizontal thus introducing an error on the value of the detected μ angle and , as a consequence, the Mach number.

This error is also present in the *Wall Line Detection Program*: the velocity direction in each window' center pixels is assumed to be tangent to the wall since the viscous boundary layer is too small to be identified with the Schlieren technique; thus it is reasonable to assume that the velocity, which is tangent to the boundary layer, is also tangent to the wall because the boundary layer has very little influence on the velocity field. Furthermore, due to the thermal boundary layer bluriness effect on the walls and the possible local condensation droplets, it is not always possible to extract lines touching the wall; instead lines can be better detected at a small distance from it, which must be the center pixel of each interrogation windows. The wall line detection program meshing process

will ensure that if the windows height is chosen such that the height ratio $r < 0.15$ in each k location, the center pixel of each window will be close enough to the wall such that the velocity direction in the window's center pixel can be considered to be parallel to the average tangent of the wall. This maximum acceptable height ratio depends on the nozzle's shape since it is evaluated by observing that the velocity change in the walls proximity is neglegible if the relative change of the adimensional coordinate $\delta y/H_t$ in the wall's proximity is less than 6%:

$$r = \frac{h_w}{H_t} = 0.15$$

$$\frac{r}{2} = \frac{h_w}{2H_t} = \frac{\delta y}{H_t} + \frac{b_w}{2H_t}\tan(\alpha_w),$$

at this point considering the worst situation which is closer to the throat where the wall angle is about $\alpha_w \approx 15^o$ and assuming that $b_w \approx h_w$, it is proven that the adimensional distance between the wall inclined midplane of the window and the wall itself is less than 6% of the throat height of the nozzle:

$$\frac{\delta y}{H_t} = \frac{r}{2}\left(1 - \tan(\alpha_w)\right) \leq 6\%.$$

Choosing a correct height ratio will not ensure the absence of the misalignment error: again it is necessary to establish a correct minimum line length factor value to ensure that all the lines will cross, or almost cross, the midplane of the window.

It follows that in order to neglect this uncertainty, a few constraints have to be respected. When considering all the implemented line detection tool, the general constraint that must always be respected is that the velocity change in both direction and intensity inside the all the interrogation windows in the mesh is not more than 2%. In order to verify this constraint the interrogation windows dimensions must be small enough: the optimal window size is the maximum size which respects this constraint. Optimal window sizing can be done by first estimating the velocity field inside the nozzle with the method of characteristics or with a preliminary Euler CFD simulation, then studying the velocity change along the adimensional vertical axis, which is the ratio of the vertial coordinate and local distance between the nozzle walls $y/H(x)$, at different axial coordinates x.

The tools that produce the final results for the accuracy assesment have further specific constraints that must be respected. In the *Line Detection Program* these are:

1. Verify that the velocity on the midplane of the nozzle is parallel to its axis by validating the assumption of symmetric flow;

2. Impose that the minimum length of the lines is such that if a line inside a window is detected, it will have to touch or cross its midplane. This constraint is already implemented and is shown in 4.3. The upper boundary of the length of the detected line LL can be arbitrary chosen keeping in mind that higher values will require higher computational time, while the lower value is derived by estimating the minimum angle that can be detected, which is the worst condition for the midplane crossing constraint, and imposing that the line touches the midplane.

$$\frac{h_w}{2\sin(\mu_{min})} \leq LL \leq \sqrt{2}h_w$$

Since the program takes as input the adimensional minimum line length parameter $C_{min} = \frac{LL_{min}}{h_w}$, the constraint becomes:

$$C_{min} = \frac{1}{2\sin(\mu_{min})} \leq \frac{LL}{h_w} \leq \sqrt{2} \tag{4.3}$$

,where h_w is the height of the interrogation window and μ_{min} is the minimum mach angle detectable.
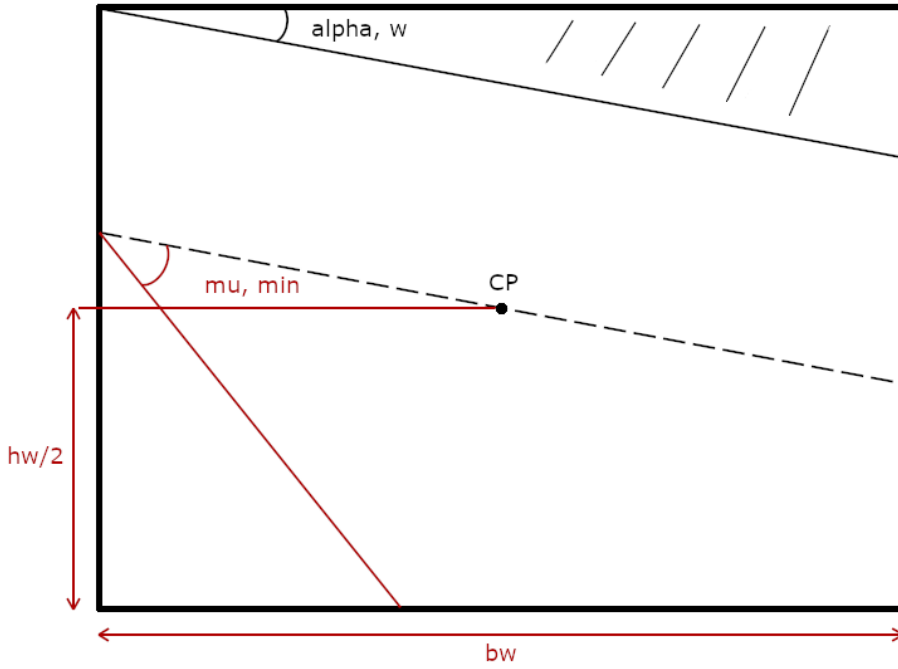
Figure 4.9: Sketch of the minimum length line that is still able to cross the wall-inclined midplane of the interrogation window.

For the **Wall line detection program**, the specific constraints that ensure a neglegible misalignment error are:

1. The interrogation windows base b_w must be chosen small enough such that the curvature of the wall inside the window is small enough so that the camber height is at most one pixel; this ensures that the tangent to the wall in the window is constant due to the discretization of the image in pixels, thus the velocity direction in the window can be considered constant along the line parallel to the wall and crossing the center pixel, so no velocity misalignment is present;

2. Impose that the minimum length of the lines is such that if a line inside a window is detected, it will have to touch or cross the line parallel to the wall and crossing the center pixel.

   Considering a generic window in the discretized wall domain (Fig. 4.9), one can easily write the following trigonometric equation:

$$LL_{min} \sin(\mu_{min} + \alpha_w) = \frac{h_w}{2} + \frac{b_w}{2} \tan(\alpha_w)$$

   to then express the minimum length of the detected line to verify the constraint in the worst case scenario

$$LL_{min} = \frac{1}{2} \frac{h_w + b_w \tan(\alpha_w)}{\sin(\mu_{min} + \alpha_w)}.$$

   The minimum lines length coefficient is then simply obtained by deviding the minimum detectable length which verifies the constraint:

$$C_{min} = \frac{LL_{min}}{h_w} = \frac{1}{2} \left(\frac{1 + \frac{b_w}{h_w} \tan(\alpha_w)}{\sin(\mu_{min} + \alpha_w)} \right) \tag{4.4}$$

This constraint is extremely conservative since it guarantees that 100% of the times the line detected will cross the center pixel crossing line parallel to the local wall. This would not be a problem if the images are of extremely good quality and with an optimal binarization, which is rarely the case. In order to substantially increase the chances of detecting lines in the windows, the recommended coefficient's value is halved, thus the contraint verification probability is reduced to 85% assuming a Gaussian random distribution of lines inside the window.

Detection of the Walls $u_{\mathrm{poly,wallfit}}$

The detection of the nozzle wall profiles is very important for two main applications: the first one is the image calibration phase, where walls are necessary in order to translate the results from a global system of reference in pixels to an adimensional SR with the origin located in the throat, calculating a scale factor using the throat height and identifying the throat position in the global pixels system of reference. The second application is the wall angle detection phase where the walls are needed to evaluate the direction of the flow velocity in their proximity to then derive the mach angle μ in the Schlieren data.

The wall detection procedure is the same in every line detection program implemented: the first step is binarizing the image using a very low threshold in order to increase the contrast between light gray and dark gray areas; the ideal result of the binarization is a black and white image where the nozzle is entirely white and everything around the walls is black. It is now possible to scan every pixel column of the image and obtain two different vectors representing the point coordinates of the walls $y_w = [y_u, y_l]$ for the upper and lower wall respectively along the pixel x coordinate. To the polynomial fit of the walls it is now associated a standard deviation of the fit $\sigma_w(x) = [\sigma_u, \sigma_l]$ which is a descrete function of the pixel domain x. Using a coverage factor $K = 2$ it is possible to extend the uncertainty in the position in pixels of the wall to a confidence level of 95%. It follows that the detected height of the throat in pixels H_{pix} has an uncertainty σ_H deriving from the extended uncertainties of the polynomial fits of the profiles:

$$U_{\mathrm{poly,wallfit}} = 2\sigma_H = 2(\sigma_u + \sigma_l)$$

Wall Angle $u_{\alpha,w}$

The wall angle α_w is a fundamental parameter to evaluate the Mach number on the wall, since the velocity direction, under the assuption of small boundary layer, can be assumed to be parallel to the wall in each window of the domain. Defining the raw Mach angle μ^* as the angle between mach line and the horizontal axis, the Mach on the wall can be evaluated as follows:

$$M_w = \frac{1}{\sin(\mu^* \pm \alpha_w)}. \tag{4.5}$$

It becomes clear how in order to estimate the uncertainty in the Mach angle $\mu = \mu^* \pm \alpha_w$ the uncertainty in the wall angle is required. Once the pixel uncertainty of the polynomial fit of the detected walls is assessed, the angular uncertainty of the walls must be calculated and added to the other uncertainties on the wall mach angles μ_w along the supersonic expansion in the nozzle. The extraction of the mach lines on the walls requires a discretization of the pixel domain in small windows; the local wall angle is evaluated by linearizing the wall curvature using the wall coordinate y_w at the beginning $x_w(i)$ and end of the window $x_w(i+1)$ to evaluate the inclination of the line that locally represents the wall. If the constraints outlined in the misalignment subsection are verified, the linearization of the wall does not introduce any additional significant uncertainty. Now, since the coordinates of the walls y_w have an uncertainty in pixels $\sigma_w(x)$ with a $68\% CL$ deriving from the fit, it possible to derive the equation to evaluate the angular uncertainty of the wall anle and later applying the coverage factor $K = 2$ to extend the confidence level to 95%.
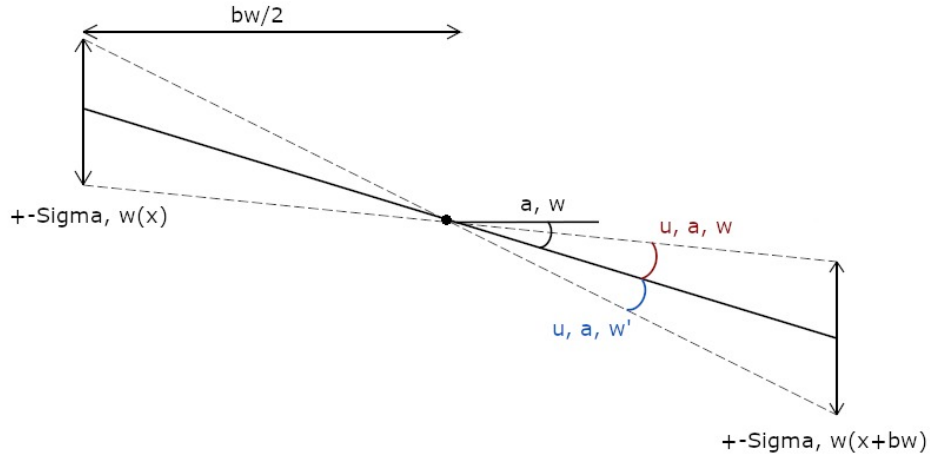
Figure 4.10: Sketch of the two possible angular uncertainties of the wall angle α_w due to the uncertainty of the walls at the two limits of an interrogation window $\sigma_w(x)$, $\sigma_w(x + b_w)$.

Keeping in mind Fig. 4.10 , it is possible to notice that the angular uncertainty produced by $\sigma_{u,l}$ of the walls is not constant: there are two possible uncertainties and for this reason the larger one must be chosen as the uncertainty on the wall angle. Using Fig. 4.11 as a reference, the uncertainty on the wall actual position $\sigma_w(x + b_w)$ will now be called D for simplicity. Now, the first step in evaluating the wall angular uncertainty is expressing the tangents of the wall angular uncertainties as the ratio of two segments:

$$\begin{cases} \tan(u_{\alpha,w}) = A/B \\ \tan(u'_{\alpha,w}) = A'/B' \end{cases} \tag{4.6}$$

where

$$\begin{cases} A = D\cos(\alpha_w - u_{\alpha,w}) \\ B = \frac{B_0}{\cos(u_{\alpha,w})} - D\sin(\alpha_w - u_{\alpha,w}) \\ A' = D\cos(\alpha_w + u'_{\alpha,w}) \\ B' = B_0\cos(u'_{\alpha,w}) + D\sin(\alpha_w + u'_{\alpha,w}) \end{cases}$$

and

$$B_0 = \frac{b_w}{2\cos(\alpha_w)}.$$

It is clear by substituting the segments in Eqn. 4.6 that the higher uncertainty value is the first one $u_{\alpha,w}$ where the cosine value is larger and the segment smaller; as a consequence this is the configuration from which the uncertainty equation is derived:

$$\tan(u_{\alpha,w}) = \frac{D\cos(\alpha_w - u_{\alpha,w})}{\frac{B_0}{\cos(u_{\alpha,w})} - D\sin(\alpha_w - u_{\alpha,w})}.$$
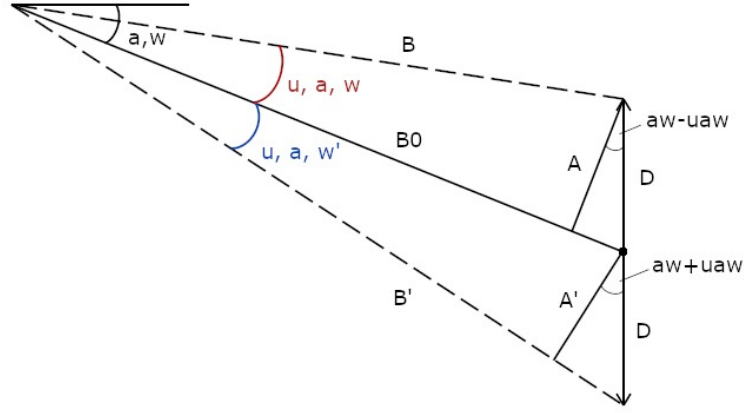
Figure 4.11: Sketch of the angular uncertainties considering half of an interrogation window: the other half is anti-symmetric. Thus, the values obtained for one half, are the same that can be obtained from the other.

Considering that the sine or cosine of a difference in angle can be expressed as

$$\begin{cases} \cos(\alpha_w - u_{\alpha,w}) = \cos(\alpha_w)\cos(u_{\alpha,w}) + \sin(\alpha_w)\sin(u_{\alpha,w}) \\ \sin(\alpha_w - u_{\alpha,w}) = \sin(\alpha_w)\cos(u_{\alpha,w}) - \cos(\alpha_w)\sin(u_{\alpha,w}) \end{cases},$$

using the first order Taylor expansions on the trigonometric functions for the small angular uncertainty $u_{\alpha,w} \to 0$ one can obtain:

$$u_{\alpha,w} = \frac{D(\cos(\alpha_w) + \sin(\alpha_w)u_{\alpha,w})}{B_0 - D(\sin(\alpha_w) - \cos(\alpha_w)u_{\alpha,w})}.$$

Keeping in mind that D is the uncertainty on the wall fit σ_w, a very small value, it is possible to neglect the second order uncertainty at the denominator $D\cos(\alpha_w)u_{\alpha,w}$. Now substituting B_0 in the equation

$$u_{\alpha,w} = \frac{D\cos(\alpha_w) + D\sin(\alpha_w)u_{\alpha,w}}{\frac{b_w}{2\cos(\alpha_w)} - D(\sin(\alpha_w))}$$

which can be re-written as

$$u_{\alpha,w}\left(1 - \frac{D\sin(\alpha_w)}{\frac{b_w}{2\cos(\alpha_w)} - D\sin(\alpha_w)}\right) = D\cos(\alpha_w)$$

it is possible to obtain the uncertainty on the wall angle as a function of the uncertainty in the fit of the wall D.

$$u_{\alpha,w} = \frac{2D\cos^2(\alpha_w)}{b_w - 4D\sin(\alpha_w)\cos(\alpha_w)} \tag{4.7}$$

Finally, knowing the equation of the worst case angular uncertainty, it is possible to estimate the actual wall angle uncertainty in each window which will be determined by the smaller uncertainty

on the wall fit D since a line is determined by two points; in this case the center of the window O in figure (...) and the point at the maximum distance of the smaller uncertainty at either side of the interrogation window. It follows that the wall angular uncertainty must be found for each window k using equation 4.7 at the start and end axial coordinates x_k and $x_k + b_w$ of each window and finding the minimum value between the two results, which is the one that determines the linearized wall.

By defining $D = K\sigma_w$ with $K = 2$, the resulting uncertainty on the wall angle will have a 95% confidence level:

$$U_{\alpha,w} = \min \left[\frac{2K\sigma_w(x) \cos^2(\alpha_w)}{b_w - 4K\sigma_w(x) \cos(\alpha_w) \sin(\alpha_w)} \, , \, \frac{2K\sigma_w(x + b_w) \cos^2(\alpha_w)}{b_w - 4K\sigma_w(x + b_w) \cos(\alpha_w) \sin(\alpha_w)} \right] \qquad (4.8)$$

Scale Factor u_{SF}

As mentioned earlier, in the image calbration phase detected walls are used to calculate the scale factor using the detected calibration walls to evaluate the throat height in pixels H_{pix}, and the user input throat height in SI units H_{mm}. The Scale factor is the ratio the two throat heights:

$$SF = \frac{H_{pixels}}{H_{mm}}$$

In order to find the throat, the distance between the two walls is minimized and a result a throat pixel height and position in the global pixels system of reference is found. The height in pixels H_{pix} of the detected throat has an uncertainty deriving from the standard deviations of the upper and lower walls; as a consequence the total uncertainty on the height of the throat in pixels is the sum of the two uncertaintites of the polynomial fit of the walls in the identified throat axial coordinate x_t:

$$\sigma_H(x_t) = \sigma_u(x_t) + \sigma_l(x_t).$$

The physical throat height in mm has an uncertainty coming from the resolution of the caliper used to measure it once the nozzle has been sealed. This uncertainty has 100% CL since the limits represent a containment interval. The resulting total uncertainty on the scale factor is evaluated by square root summing the two fractional uncertainties, after extending the standard uncertainty to a 95% CL, and then multiplying by the scale factor.

$$U_{SF} = SF \sqrt{\left(\frac{2\sigma_H}{H_{pixels}} \right)^2 + \left(\frac{U_{Hmm}}{H_{mm}} \right)^2}$$

Throat Location $u_{\text{th,loc}}$

The throat position is identified by identifying the axial coordinate at which the distance between the polynomial fits of the walls is minimum. Assuming that the CNC machine precision is so high that the walls can be considered perfectly equal, the detected walls will still not be perfectly symmetric due to imperfections in the Schlieren images. The identified throat position has, as a consequence, an uncertainty deriving from the shape of the detected walls, which strongly depends on the original quality of the image and the binarization threshold. This uncertainty is estimated by evaluating the maximum axial displacement between the zero derivative points of the two detected walls, which correspond to the local maximum and minimum depending on which wall is considered, and adding to it the round off error coming from the pixel discretized domain, which is equal to half of a pixel. The result is a 100%CL uncertainty in the throat position in the global pixels system of reference, which is the matrix containing the pixels of the image.

$$U_{th,loc} = 0.5 + |x_w(\min(y_u)) - x_w(\max(y_l))|$$

The throat location x_t will obviously be in the middle of the axial displacement interval.

$$x_t = \frac{x_w(\min(y_u)) + x_w(\max(y_l))}{2}$$

Discretistaion Error $u_{\Delta x}$

The implemented detection algorithm will always choose the best line in the selected window; the Mach lines will not only fluctuate around an axial coordinate, but will also vary in definition, contrast and brightness in each frame of the dataset. It follows that the line detection tools, for every frame, will detect lines that will cross the assumed velocity plane in different axial coordinates inside that given window. The assumed velocity plane for the midplane detection program is the midplane of the window, which correspond to the nozzle midplane as well, while for the wall detecion program is the line parallel to the wall angle that passes through the interrogation window's center pixel.

Since the implemented detection programs work on large datasets where statistical convergence is achieved, it has been observed that recording each extracted line axial position in each frame of the dataset, to then evaluate the mean position and the standard deviation with a confidence level greater or equal to 95%, has a neglegible reduction on the spatial resolution of the programs and a noticeable increase in computational time. For this reason a slightly more conservative approach has been followed, reducing the computation load and RAM usage: the spatial resolution of the programs, therefore the spatial uncertainty with $100\% CL$ is the step between two consecutive windows:

$$dx(x) = x_{cp}(k+1) - x_{cp}(k)$$

where $x_{cp}(k)$ is the center pixel of the k-th window. In the midplane *Line Detection Program* the step decreases as the throat is approached to better resolve the changes in velocity in the expansion of the nozzle. As for the step, the windows sizes, base and height, also decrease linearly approaching the throat; the linearly finer discretization of the specified domain $[x_{\text{start}}, x_{\text{end}}]$ is controlled by the following parameters:

- *Int*: total number of windows to generate

- dx_m: twice the minimum step between two windows allowed in the mesh

- *bws*: ratio between the window's base and the distance between the windows k and $k+1$; a value of 2 has been found to be the optimal value

- $[upp_{max}, low_{max}]$: maximum allowed half height of the windows; these values are always equal to each other in order to generate a mesh with the windows center pixels lying on the nozzle's midplane. When these two values are not equal, the meshing will be performed either slightly above or below the nozzle's midplane.

Once these parameters are defined, the windows dimensions can be calculated. The maximum window width that will be generated is:

$$b_{wmax} = 2\left(\frac{bws(x_{\text{end}} - x_{\text{start}})}{Int}\right) - dx_m$$

so the equation defining the bases of the windows is expressed as

$$b_w(k) = b_{wmax} - \left(\frac{b_{wmax} - dx_m}{Int}\right)k \qquad \text{with} \quad k = [1, ..., Int]$$

while the heights are

$$h_w(k) = NU(k) - NL(k)$$

where

$$NL(k) = Y_0 - low_{max}\frac{b_w(k)}{b_{wmax}}$$

$$NL(k) = Y_0 + upp_{max}\frac{b_w(k)}{b_{wmax}}.$$

In conclusion, the discretization error is equal to the non constant step:

$$dx(x) = b_w(x)/2.$$

In the *Wall line detection program* the window size is kept constant and equal to the optimal value closer to the throat; again the step is half of the window base, and it will be obviously constant

$$dx = b_w/2.$$

NRS Position $u_{X,NRS}$

This uncertainty can be calculated after the calibration and discretization phases. The global pixel reference system (**GpRS**) of the Schlieren image has the origin of the pixel matrix in the top left corner which sadly doesn't correspond to any relatable point in the physical plane, therefore its physical position is unknown. It is then necessary, in order to compare experimental results with the simulations, to translate results to the **NRS (nozzle reference system)**, with the origin located at the intersection between the midplane of the nozzle and the throat, and the positive x-axis following the expansion of the flow from the throat towards the exit to the end of the Schlieren image. It is important to keep in mind that two different NRS exist: the most useful one is the adimensional NRS, which is directly calculated by shifting the origin, inverting the x-axis and dividing the coordinates x_i by the throat height in pixels H_{pix}. It is also possible to translate results to the physical NRS, which is the same as the adimensional with the only difference being that the coodinates are then multiplied by the throat height in millimeters, thus introducing another small uncertainty. In the present work, every time the NRS subscription is used it is referring to the adimensional NRS, unless differently specified.

Translating the center pixels coordinates from the GpRS to the adimensional NRS is very simple: firstly the axial shift of the origin is performed, moving from the left corner of the image to the axial coordinate of the detected throat x_t; this introduces the first source of error in the adimensional NRS total uncertainty. Secondly the axis must be flipped and the origin moved to the midplane of the nozzle; these operations do not add any uncertainty. Lastly the coordinates of each point must be adimensionalized with the throat height in pixels H_{pix} which has an uncertainty , thus another source of error is introduced. This operations can be translated into a single equation:

$$X_{NRS}(i) = \frac{(x_t - X_{GpRS}(i))}{H_{pix}}$$

It must be noted that the variables that introduce the uncertainties in the new coordinate systems are one at the numerator and one at the denominator and that both uncertainties are independent, which means that there is no correlation between the two. In this case, in order to compute the resulting uncertainty on the NRS coordinates $u_{X,NRS}$, the fractional uncertainties of the two variables must be added in quadrature [ISO (1993)] ; then, as shown in equation 4.9, the resulting fractional uncertainty can be multiplied by the value of the coordinate to obtain the absolute resulting uncertainty.

$$U_{X,NRS} = X_{NRS}\sqrt{\left(\frac{2\sigma_H}{H_{pix}}\right)^2 + \left(\frac{U_{th,loc}}{x_t}\right)^2} \tag{4.9}$$

Extraction Uncertainty on the Mach angle $u_{\mu,ext}$

The extraction uncertainty on the Mach angle can be seen as a comprehensive resolution, or accuracy, of the detected μ angle. It is simply calculated by square root summing the Hough resolution, which is constant, the extended angular resolution, which changes with the interrogation window locations k, and, for the wall line detection only, the wall angle uncertainty.

$$U_{\mu,ext} = \sqrt{AR_{95}^2 + U_{Hough,res}^2 + U_{\alpha,w}^2}$$

It is also important to notice that if the velocity direction on the midplane of the nozzle has an uncertainty due to the fact that flow symmetry has not been verified, that must be taken into account and it will behave exactly like the uncertainty on the wall angle, since both have the same origin: the uncertainty on the velocity direction.

Random Uncertainty on the Mach Number $u_{data,M}$

As discussed for the error source $\epsilon_{data,\mu}$ the intrinsic randomness of the lines acquired in a location through time will also cause a Type A random error on the local Mach number, evaluated at each time frame based on the extracted line. As a result, for each interrogation window an average value of Mach and a standard deviation is associated. As for the μ angle, the random standard uncertainty on the local Mach is extended to a confidence level of 95% using the coverage factor $K = 2$.

$$U_{data,M} = K u_{data,M}$$

Propagation of the Extracted μ Angle Uncertainty on the Mach $u_{M,ext}$

Each time the Mach number is computed in a location and at a certain time frame using the extracted μ angle, the combined angle extraction uncertainty $u_{\mu,ext}$ on the angle μ itself must be considered and propagated through the equation $M = 1/\sin(\mu)$ to evaluate the uncertainty in the Mach number deriving from the uncertainty of the extracted line $U_{M,ext}$. The extraction uncetainty on the Mach is then added to the Type A random uncertainty $U_{data,M}$ to evaluate the total expanded uncertainty on the Mach.

Once the extraction uncertainty has ben assessed, the propagation of the uncertainty through the $M = f(\mu)$ equation is achieved after evaluating the sensitivity coefficient:

$$\delta M = \frac{\mathrm{d}f(\mu)}{\mathrm{d}\mu}\delta\mu$$

It is then possible to express the sensibility coefficient as a function of the local average Mach number.

$$\sin(\mu) = \frac{1}{M} \tag{4.10}$$

$$\frac{\mathrm{d}\sin(\mu)}{\mathrm{d}\mu} = \frac{\mathrm{d}M^{-1}}{\mathrm{d}M}$$

$$\cos(\mu)\frac{\mathrm{d}\mu}{\mathrm{d}M} = -M^{-2}$$

$$\frac{\mathrm{d}\mu}{\mathrm{d}M} = -\frac{1}{cos(\mu)M^2}$$

Expressing now the cosine as:

$$\cos(\mu) = \sqrt{1 - \sin^2(\mu)}$$

and recalling equation 4.10 one simply obtains:

$$\frac{\mathrm{d}\mu}{\mathrm{d}M} = \frac{1}{1 - 1/M^2}$$

Finally the sensitivity coefficient is expressed as:

$$|\frac{\mathrm{d}M}{\mathrm{d}\mu}| = M\sqrt{M^2 - 1}.$$

In conclusion, the extraction uncertainty on the Mach is

$$U_{M,ext} = M\sqrt{M^2 - 1}U_{\mu,ext}. \tag{4.11}$$

It is important to notice how the extraction uncertainty on the Mach number has a dilation-shrinkage effect depending on the value of the Mach number in that position: $U_{M,ext}$ has a quasi-square behaviour that tends to shrink the uncertainty to almost nothing when the mach number approaches one, while significantly dilating the uncertainty whenever the Mach number approaches two. For Mach numbers greater than two, it is extremely important to minimize the extraction uncertainty on the μ angle, for example by increasing the scale factor, in order to limit the uncertainty bands in the high speed region of the flow.

SRQ total expanded uncertainties

Now tht all the uncertainties playing a key role in the posty processing have been quantified, the total expanded uncertainties on the system response quantities can be calcuylated. The variable chosen for the accuracy assessment is the Mach number M, but in the post processing tools there are two system response quantities (SRQ): the Mach number and Mach angle. Both variables are very important for two different reasons: the Mach number is fundamentally important for the accuracy assessment because is the parameter that directly influences performance parameters of expanders or that characterizes expansions, while the μ angle is an optimal parameter to evaluate the quality of the experimental results since is a much more sensitive parameter to disturbances in the flow, furthermore its uncertainties do not depend on the flow field like for the Mach number. Finally, the total expanded uncertainties are:

$$U_M = \sqrt{(U_{data,M})^2 + (U_{M,ext})^2 + 2\rho_{data,ext}U_{data,M}U_{M,ext}}, \tag{4.12}$$

and

$$U_\mu = \sqrt{(U_{data,\mu})^2 + (U_{\mu,ext})^2 + 2\rho_{data,ext}U_{data,\mu}U_{\mu,ext}}. \tag{4.13}$$

4.4 Mach Lines Extraction and Post Processing Results

This section covers the results of the post processing of the Schlieren data for all the three process runs of the ORCHID presented in Sec. 2.5. The full capabilities of the tools are presented by analyzing how well the programs - with optimal input parameters - can extract lines depending on the Schlieren image quality and how this affects the averages over time of the system response quantities and their uncertainties.

When dealing with experimental results, the **acquisition frequency** can play a fundamental role in the validity of the results; the **Nyquist Shannon sampling Theorem** sets the value of minimum sampling frequency able to correctly capture all the information in a signal equal to twice the frequency of the signal itself. If the acquisition frequency is not greater of equal of this set minimum, one can incur in the aliasing phenomena which makes the definition of an unambiguous signal impossible.

As shown in table 2.3 the Schlieren data was taken at 2 different sampling rates: PR.022 data was acquired with the HS4M camera at $f_s = 60 \ Hz$ while PR.024 and PR.026 data were acquired with the Bobcat camera at $f_s = 24.75 \ Hz$. When dealing with photographed data, it is important to keep in mind that the sample is not taken instantaneously but in a certain amount of time, which is the exposure time. The HS4M camera exposure time was set to $600 \ \mu s$, while the bobcat was set up in the automatic configuration, so the exposure time is limited by the capabilities of the camera summarized in Tab. 2.2 and by the acquisition frequency (frame rate): thus the exposure time of the Bobcat can be considered to be maximum $1/24.75 \ Hz$. The characteristic time of the supersonic flow in the nozzle captured by the Schlieren images is extremely small:

$$T_{flow} = \frac{L_{nozzle}}{M(x)c(x)},$$

approximating in excess the time by estimating $M = 1.32$ and $c = 134 m/s$, which are the conditions right after the throat at $x/H_t = 2$ on design, and given that $L_{nozzle} \approx 0.1 \ m$ one can obtain

$$T_{flow} < 550 \ \mu s.$$

The time, approximated in excess, that it takes for a fluid particle to cross the entire field of view (FOV) of the Schlieren image is definetly smaller than the exposure time of the high speed camera: thus the image taken is not instantaneous, but is an averge over time of a period which is longer than the characteristic time of the nozzle.

In conclusion, the problem of the sampling frequency can be completely neglected as the Schlieren images are not instantaneous measures and the flow field is being already averaged over time when a single image is taken.

4.4.1 Flow Symmetry Assessment

Once it has been proven that the acquisition frequency in our case will not influence the dataset in any way, the flow symmetry hypothesis in the nozzle can be experimentally verified: this is a very important results since if the flow is symmetric in one of the process runs, it will also be symmetric in all the other runs as long as the nozzle is the exact same and that the steady state boundary conditions total uncertainties are similar. As a result, the flow symmetry assessment can be performed in just one dataset, possibly the one with the highest quality.

In the present case, the flow symmetry assessment is performed at two different axial coordinates in the nozzle: one closer to the throat and the second one closer to the exit where the Mach lines are almost completely extraight and the flow has almost completed the expansion. In order to be more accurate, the flow symmetry check closer to the throat is performed in the PR.026 zoomed-in dataset, while the one is performed in the PR.024.

It is important to mention that the flow symmetry assessment can be performed at any given axial coordinate keeping in mind that in the Kernel region the Mach lines are curved, so the line extracted is close enough to the curved Mach line only if the interrogation windows are small enough. Furthermore, to each point in a supersonic flow one can associate two characteristics, going in the flow direction but specular with respect to the flow velocity direction. These characteristics correspond to the Mach lines. When checking the flow symmetry, opposite (mirrored) Mach lines must be compared, thus the image must be good enough to be able to detect edges of opposite mach lines above and below the midplane otherwise no flow comparison can be made since the flow velocity direction is not known.

The angles of the Mach lines extracted can only be considered to be Mach angles μ if the velocity direction is subtracted from the Mach line angle and in order to do so the velocity inclination must be known. The flow symmetry program extract the angle between the Mach line and the horizontal axis, called symbolic Mach angle μ^* with whom a symbolic Mach number M^* is computed. If the flow symmetry assessment is performed in the fully expanded 1D flow where the nozzle's profiles become straight parallel lines, one can assume that $\mu^* = \mu$ and $M^* = M$.
The reason why the symbolic Mach number M^* is computed, is to give the user a sense of what could be the difference between the Mach fields above and below the midplane, while the angles μ^* are useful to better visualize the differences between the top and bottom Mach fields.

In conclusion, the flow symmetry tool will give as outputs the average over time of the Mach lines angles $\mu^*(y)$ at the choosen axial coordinate x_{ch}, the average extracted angles above and below the midplane and the corresponding Mach values. The user will then use these informaition to either confirm or reject the hypothesis of symmetric flow in the nozzle.
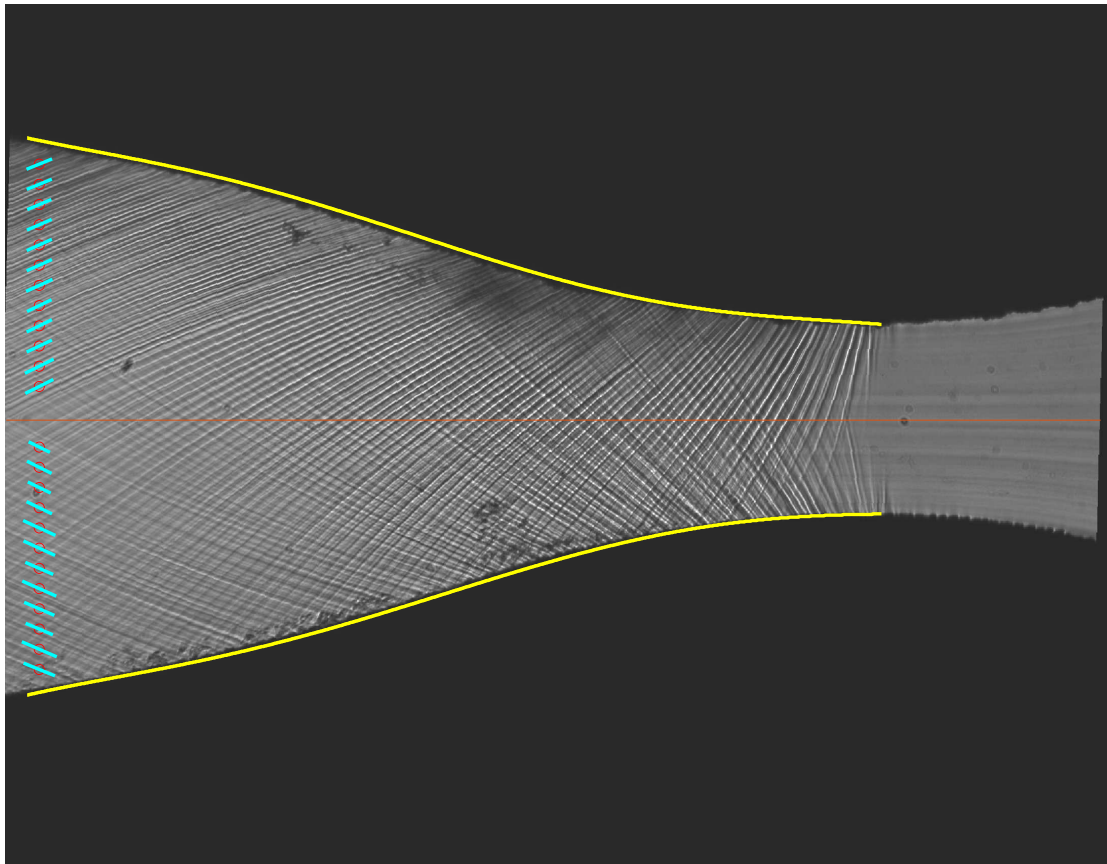

Figure 4.12: PR.026 flow symmetry assessment: average Mach lines superimposed on a zoomed-in dataset Schlieren image
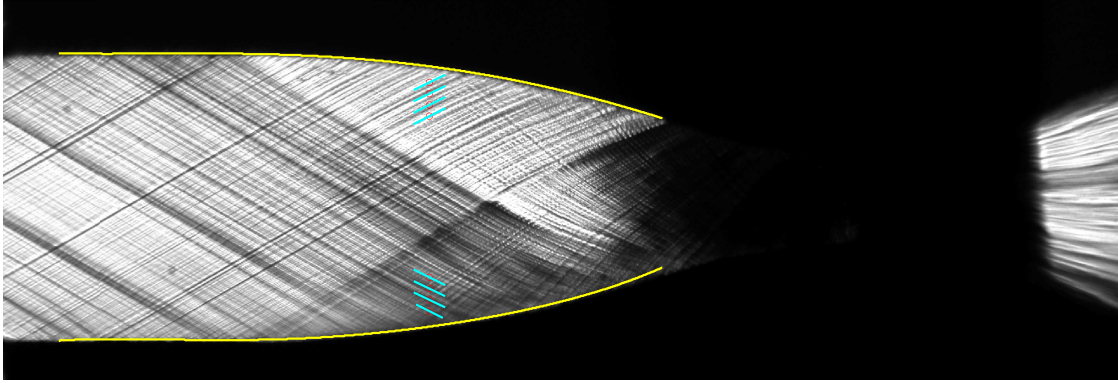
Figure 4.13: PR.024 flow symmetry assessment: average Mach lines superimposed on a zoomed-out dataset Schlieren image

In figures 4.13 and 4.12 the average detected lines over the chosen N_{img} frames are superimposed on the first Schlieren image of each dataset. The choice of the axial coordinates at which the symmetry check was performed is based on a compromise between the following factors:

- Presence of opposite Mach lines in the binarized image above and below the midplane;

- Quality of the image: the level of brightness and contrast must be optimal or close to optimal and as much constant as possible during the frames;

- The Mach lines must be as straight as possible, thus 1D or quasi 1D flows are prefered.

If an optimal dataset is available, one where opposite lines can be binarized in the fully expanded 1D flow, the average computed values $\mu^*(y)$ must be constant.

In the analyzed cases, on the contrary, this was not possible; since the windows move from the midplane to the walls it is expected of $\mu^*(y)$ to decrease. The expansion of the flow in the nozzle is not equal in each y coordinate: the flow will at expand faster on the walls until the inflection point of the nozzle's profile is reached, then the expansion on the midplane is a lot faster and will reach the fully expanded state a lot earlier than the flow closer to the walls as it is possible to see from the results of the method of characteristics presented in Chapter 2.

Observing the results summarized in figures 4.14 and 4.15, it is possible to prove that the steady state flow in the nozzle is symmetric. The the simbolic average angles above and below the midplane are always very similar and within each other's uncertainty in both the zoomed out and zoomed in results at two different axial coordinates. Furthermore, once the angles are proven to be extremely small, it is possible to compute the difference between the average M^* values above and below the midplane for the two axial coordinates in order to fully comprehend how small the differences in the Mach number actually are.

$$PR.026 \begin{cases} M^*{}_{up} = 2.420 \\ M^*{}_{down} = 2.423 \end{cases}$$

Figure 4.14: PR.026: Mach line angle distribution $\mu^*(y)$ along the adimensional height of the nozzle $y/H(x)$ and total expanded uncertainty bars above and below the midplane
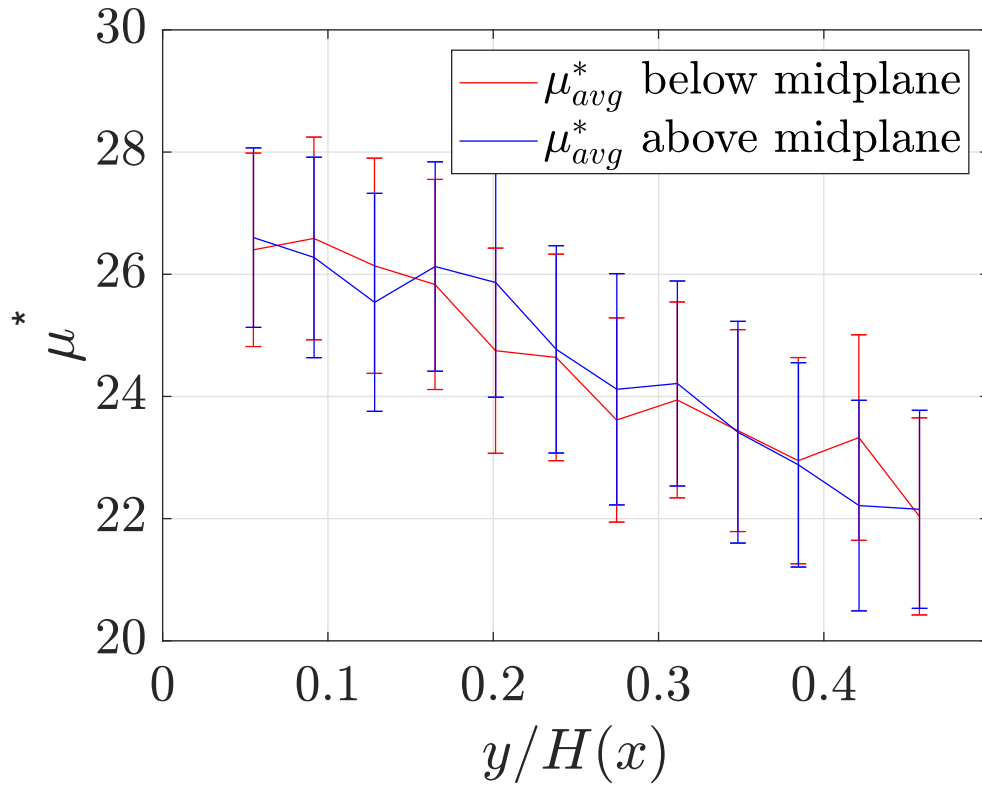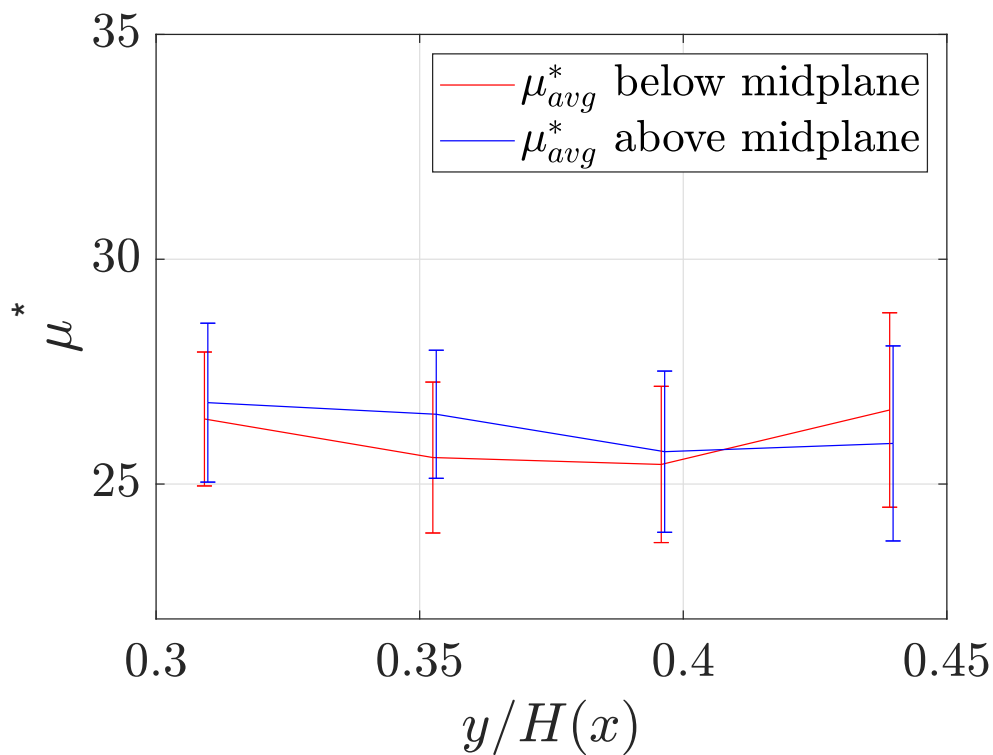

Figure 4.15: PR.024: Mach line angle distribution $\mu^*(y)$ along the adimensional height of the nozzle $y/H(x)$ and total expanded uncertainty bars above and below the midplane

4.4.2 Statistical Convergence of Data

After the flow symmetry assessment, the statystical convergence program has to be used in order to verify that the dataset is large enough to achieve negligible error on the accuracy of the statystical quantities considering also that the number of extracted lines can be, and usually is, lower than the total number of frames in the dataset because in some windows the peaks in the HPCS correspond to lines that are shorter than the minimum allowed length. Thus, once this analysis is complete, the considered Schleiren datasets will be large enough to ensure the validity of the extracted results.

The statystical convergence analysis is carried out by analyzing in various k-locations the standard deviations in the means of the μ angle and the Mach:

$$\overline{u_\mu(k)} = \frac{u_\mu(k)}{\sqrt{N}}$$

$$\overline{u_M(k)} = \frac{u_M(k)}{\sqrt{N}}$$

as well as the average values of the extracted angles and corresponding Mach when varying the total number of frames considered. The analysis has to be performed for each dataset unless the same camera set up, resolution, brightness and boundary condition steady state definition is used.

In the following graphs, the axial position of the interrogation windows is indicated with k, which is the index of the interrogation windows in the GpRS. As a result k spaces from 1, closer to the exit, to the total number of windows in the discretized domain n_{windows}, towards the throat of the nozzle. The variables that are presented in the following figures are the standard deviation of the mean of the Mach value and the average Mach since these are the SRQ of interest for the accuracy assessment.
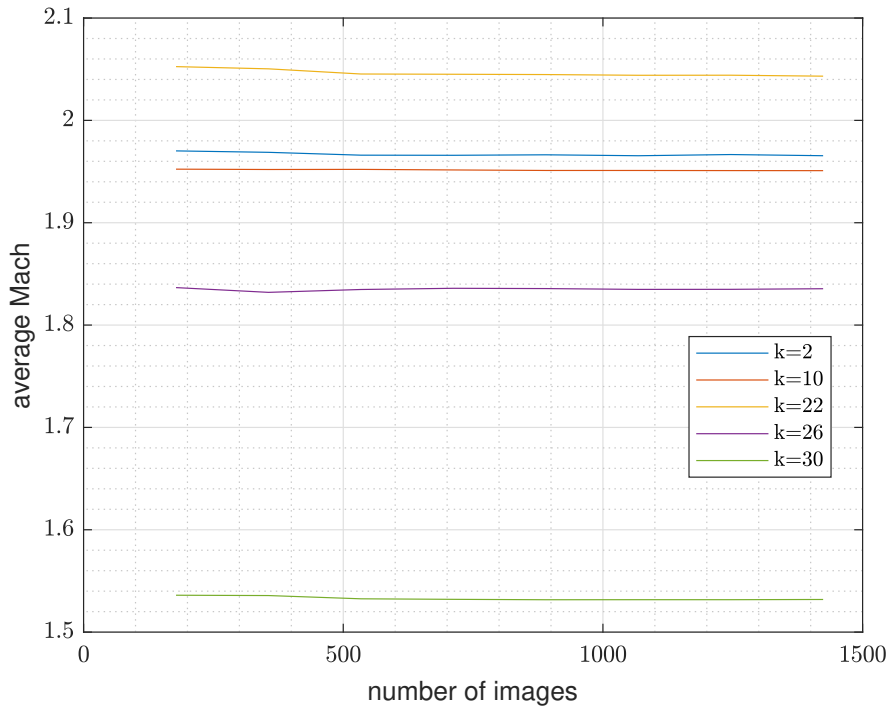
Figure 4.16: PR.022: Average M value over time in different k locations
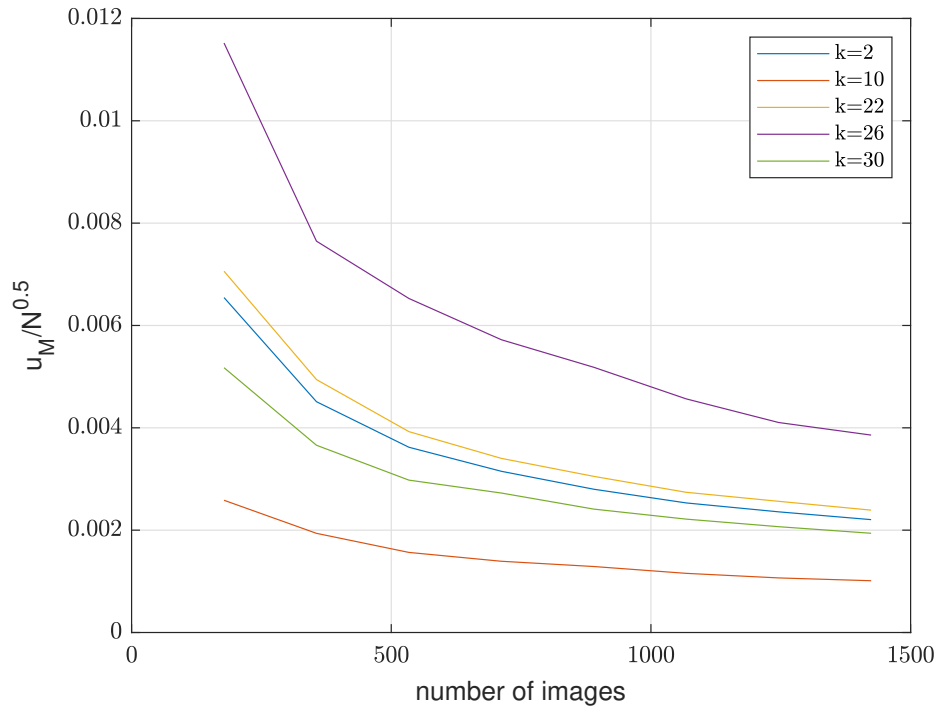
Figure 4.17: PR.022: Standard deviation of the mean $\overline{u_M}$ in different k locations
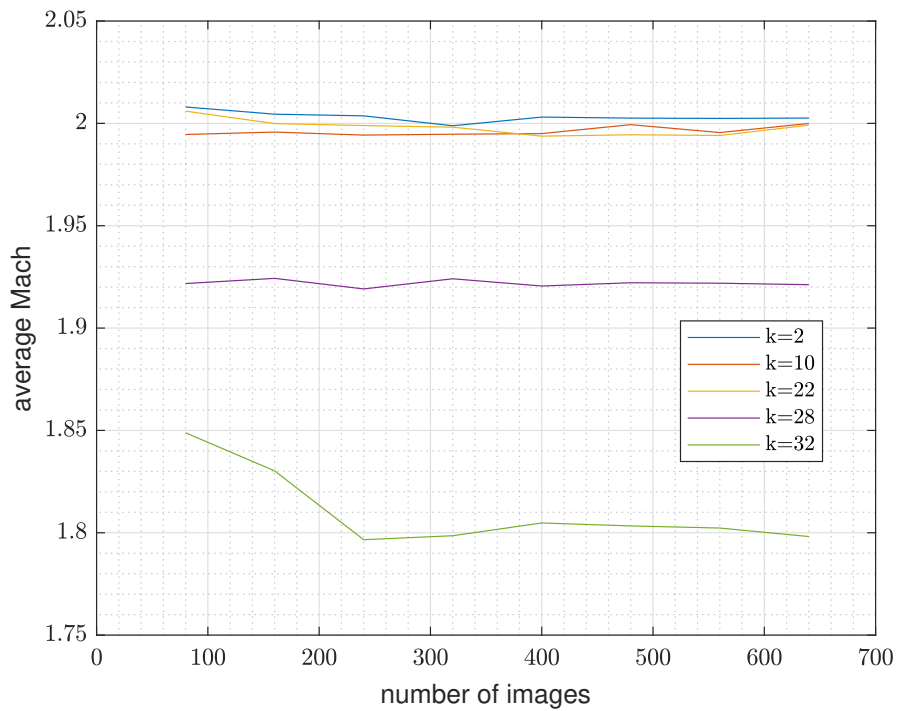
Figure 4.18: PR.024: Average M value over time in different k locations

Observing the results of the program it is possible to assess that for each process run the dataset is large enough to converge the means and standard deviations for the SRQs. The three dataset are quite different in number of images but it is important to keep in mind that the statistical convergence dipends on the quality of the dataset and the steady state condition of the flow, thus
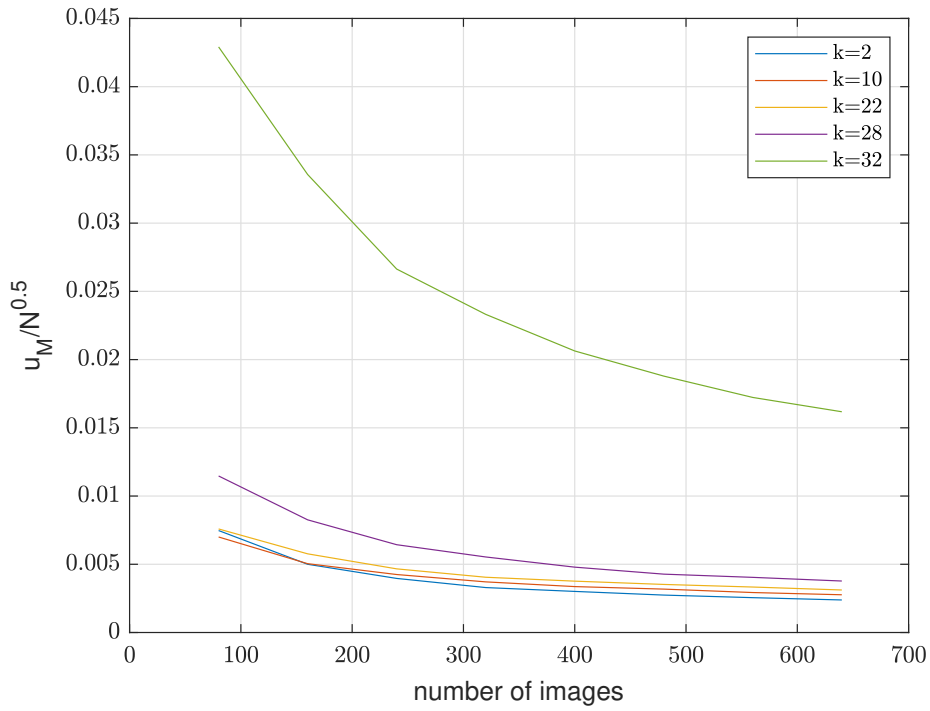
Figure 4.19: PR.024: Standard deviation of the mean $\overline{u_M}$ in different k locations
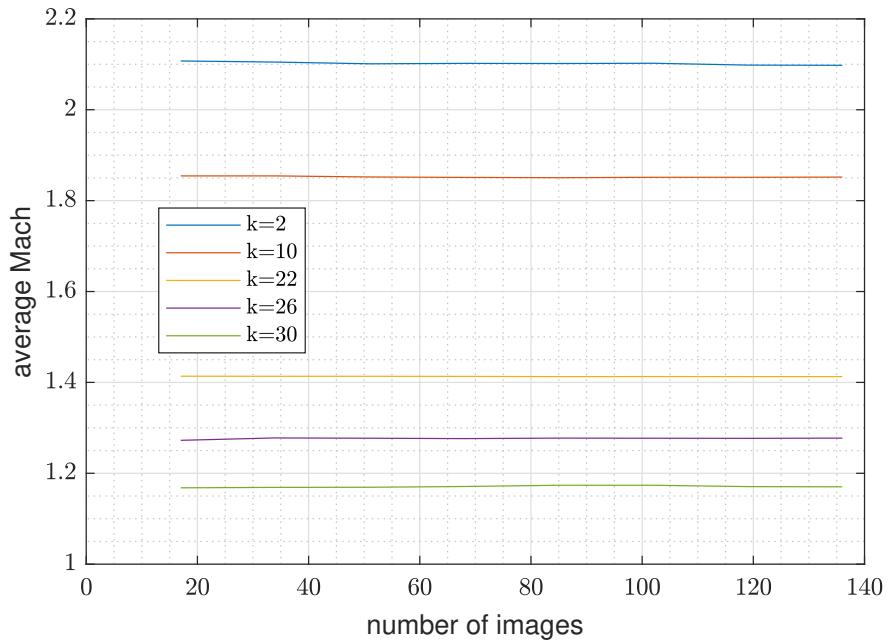
Figure 4.20: PR.026: Average M value over time in different k locations

camera which has a higher resolution and better overall quality of the picture.
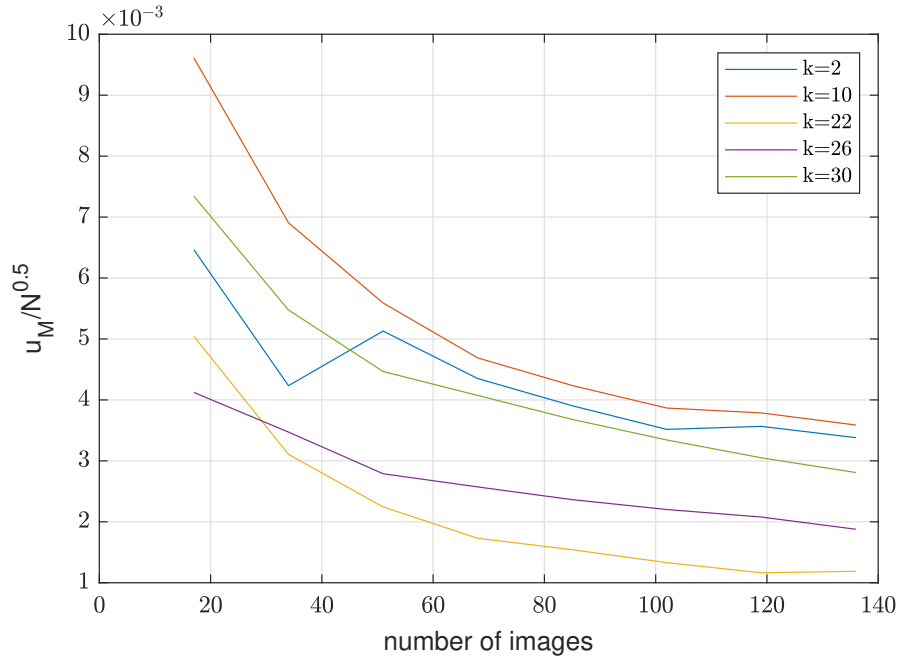
Figure 4.21: PR.026: Standard deviation of the mean $\overline{u_M}$ in different k locations

4.4.3   Midplane Mach Line Detection

Results of the midplane *Line Detection Program* for the three process runs PR.022, PR.024 and PR.026 are presented; the average extracted lines over time in each interrogation windows are superimposed on the first Schlieren image of the dataset. The SRQs values are presented in the following chapter since are used for the accuracy assessment.
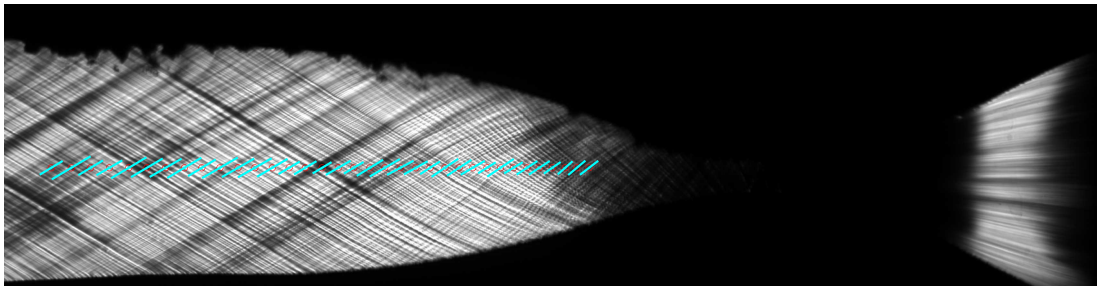
Figure 4.22:   PR.022: average extracted lines on the midplane superimposed on the first frame of the dataset

To each window results, a breakdown of the total expanded uncertainty is presented: the relative influence of each uncertainty varies with respect to the quality of the dataset. It must be kept in mind that the uncertainty distribution results are presented in the adimensional nozzle reference system, so the origin is in the nozzle's throat and the x-axis is flipped with respect to the Schlieren images.

The total uncertainties in figure 4.26, 4.27 and 4.28 are a direct measure of the quality of the dataset. The random uncertainty $U_{data,\mu}$ is directly proportional to the random uncertainty in the
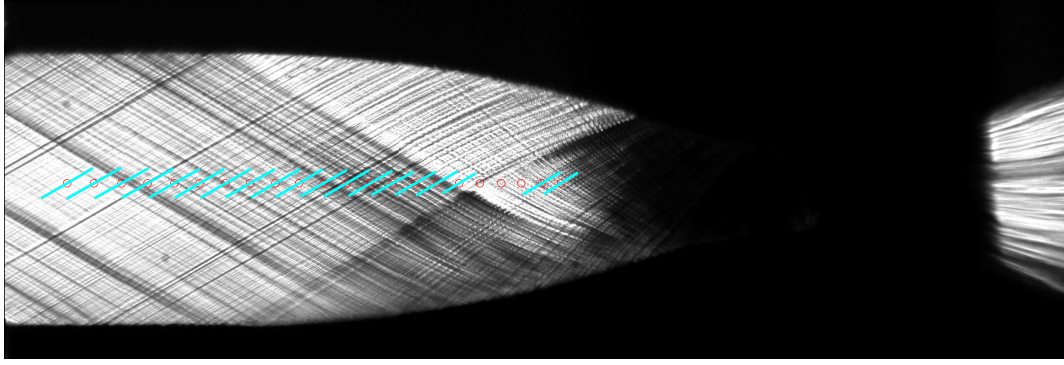
Figure 4.23: PR.024: average extracted lines on the midplane superimposed on the first frame of the dataset
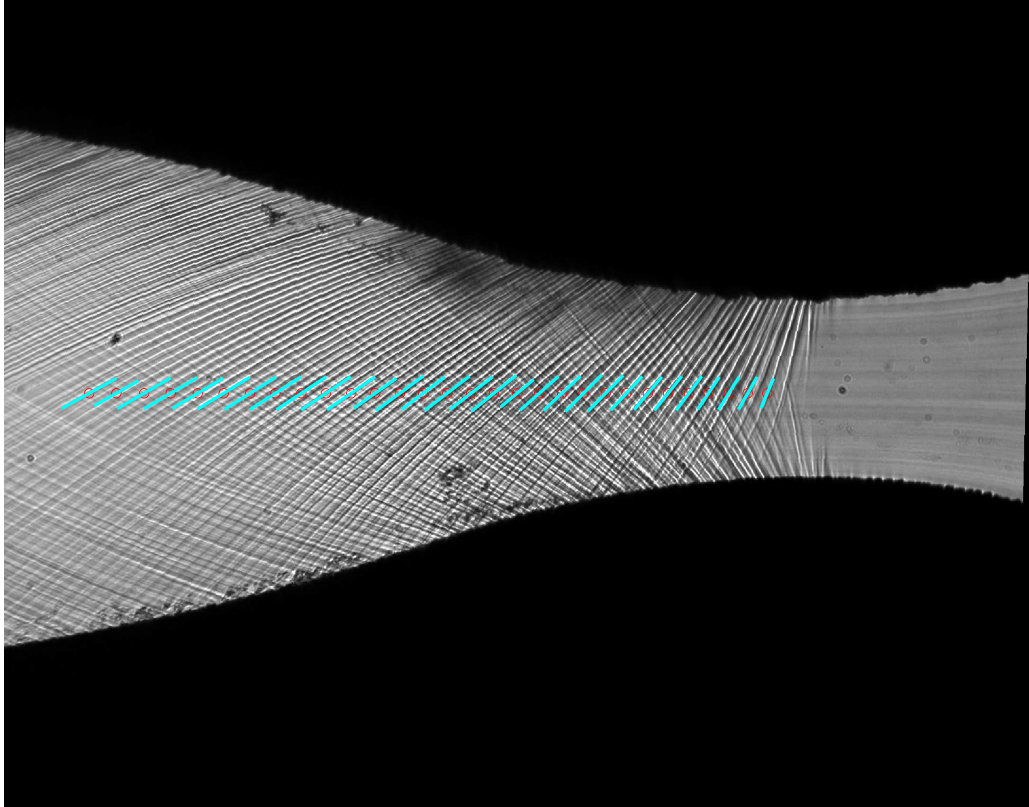
Figure 4.24: PR.026: average extracted lines on the midplane superimposed on the first frame of the dataset

Mach $U_{data,M}$, while the uncertainty in the Mach angle extraction in the midplane

$$U_{\mu,ext} = \sqrt{U_{\text{Hough,res}}^2 + AR_{95}^2}$$

has an influence on the Mach uncertainty which strongly depends on the Mach value: when Mach increases the uncertainty in the angle extraction gets dilated almost quadratically, while when Mach decreases the uncertainty gets shrinked according to equation 4.11. It is for this reason that the

uncertainty breakdown analysis on the μ angle is the best way to assess the quality of the results and to estimate where and if improvements can be made.

When comparing the uncertainty breakdown graphs, the axial coordinate of the results is a fundamental parameter: both PR.022 and PR.024 extracted results are at least 2 throat heights away from the NRS origin while in the case of PR.026 results are extracted stating from $X_{NRS} \approx 0.2$; this is obviously correlated to the fact that the first two mentioned runs are zoomed-out Schlieren and the last one is a zoomed-in, thus the physical dimensions of the windows is significantly smaller, the camera can be set up with a better brightness contrast and the field is overall better resolved. The zoom of the image is not the only factor that influences the axial position of the results: the brightness gradient along the image is extremely important. If the brightness level in the Schlieren photograph is almost constant throughout the entire nozzle just like for PR.026, the optimal binarization applies to the entire supersonic field thus the random uncertainty coming from the binarization problems in areas where the local gradient is close to the threshold can be minimized. For instance, the random uncertainties in PR.022 average on a 1.2 deg and rarely go below 0.5 deg, while in PR.026 averages on 0.8 deg and in some locations it reaches zero.

It is also very interesting to notice the influence of the scale factor combined with the quality of the walls of the Schlieren dataset on the position uncertainties. The total uncertainty in the adimensional position in which the value extracted in a window is assigned, depends mainly on two types of uncertainty: the discretization $U_{\Delta x}$, which cannot be removed, and the reference system change one, $U_{X,NRS}$ which depends on the scale factor uncertainty U_{SF} and throat position $U_{th,loc}$. The scale factor uncertainty is a function of the uncertainty of the throat height in the image plane and in the physical plane, while the uncertainty on the throat position is influenced by the polynomial fit of the Schlieren or calibration image walls. Comparing the three cases, it is obvious how the high scale factor and high quality dataset PR.026 has a neglegible NRS uncertainty throughout the entire analyzed expansion if compared to the discretization one, furthermore the two lines remain almost parallel. On the other hand, for the other two cases, the nozzle reference system position uncertainty grows significantly with the adimensional coordinate, reaching similar values to the discretization uncertainty. This effect is mainly caused by the higher relative uncertainty on the throat height due to the reduced scale factor.

Another importat observation on the results must be made by comparing PR.022 and PR.024: in both cases the zoom is practically the same but the results are quite different in quality. More in parricular, PR.022 has overall better field resolution and similar uncertainties and this is strictly correlated to the use of a better camera, the HS4M , with respect to the Bobcat.
The HS4M has a higher resolution and better overall image quality than the Bobcat, thus the scale factor is higher even though the nozzle is a little further away, the brightness gradients are better resolved and the binarization has much less noise.

Finally, in figure 4.27 one can notice the absence of results from $X_{NRS} = 2.5$ to $X_{NRS} = 3.5$. The explanation for this lies again in the poor image quality and brightness level: the window sizes in PR.024 are significantly larger than the windows in PR.022 because the optimal binarization has areas where no lines are present, thus the windows must be increased in size to increase chances of detecting decent lines. Furthermore, even with large windows sometimes too much information is lost in some windows since the lines detected are below the minimum length or require a pixel skip factor which is too high and could cause large "fake lines" problems in line-dense areas. By looking the *information_lost* vector, one can spot the locations where the results are just not enough to have decent statystical convergence: for this reason, those locations are discarded from the results.

(a) PR.022

(b) PR.024

(c) PR.026
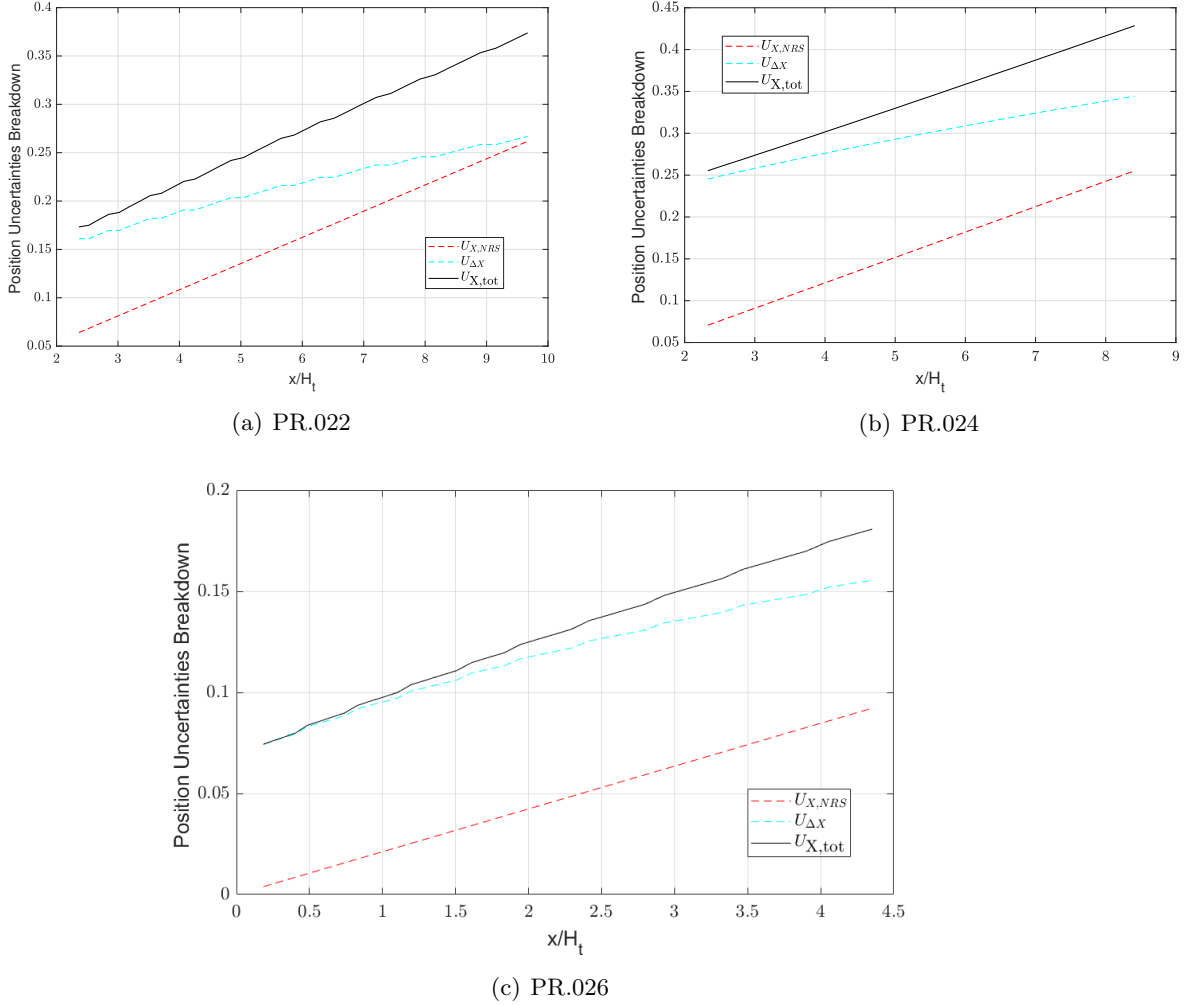
Figure 4.25: Comparison of position unecrtainty breakdowns for the three processed datasets.

4.4.4 Wall Mach Line detection

Results of the *Wall line detection program* for the three process runs are presented: the average extracted lines over time in each interrogation window are superimposed on the first Schlieren image together with the midplane average lines.

The first observation that must be made is that not always is it possible to extract results which are good enough for an accuracy assessment on both walls of the nozzle. In PR.022, for instance, the top wall is completely obscured by the melted polymer used to seal the top profile of the nozzle; the sealing mostly leaked outside the TS not compromising the flow in the nozzle but definetly compromising the extraction of information from the image. In PR.026 the results on the bottom wall are significantly worse than the top wall due to dark spots caused by impurities on the glass outside the test section, which strongly distupt the extraction of straight lines. In PR.024 it was possible to extract lines on both walls but the quality of the results is rarely equal: in most cases it is possible to clearly define a "better" wall simply by looking at the total uncertainty vectors. The wall with less uncertainty is then used for the accuracy assessment given that the flow has been proven to be symmetric.

Again, as mentioned for the midplane detection tool, the domain in which lines are extracted depends on the image quality, brightness gradient as well as the scale factor. Having larger scale factor it is possible to discretize the domain in physically smaller windows thus it is possible to
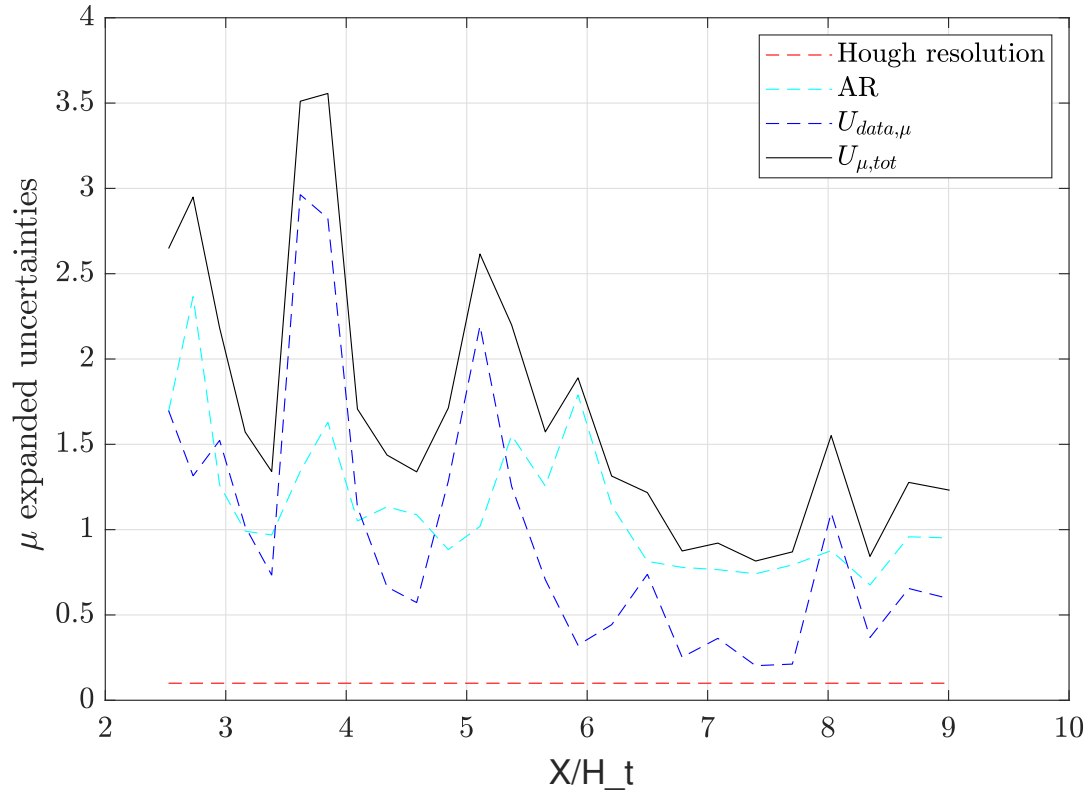
Figure 4.26:   PR.022: uncertainties breakdown for the extracted μ angle
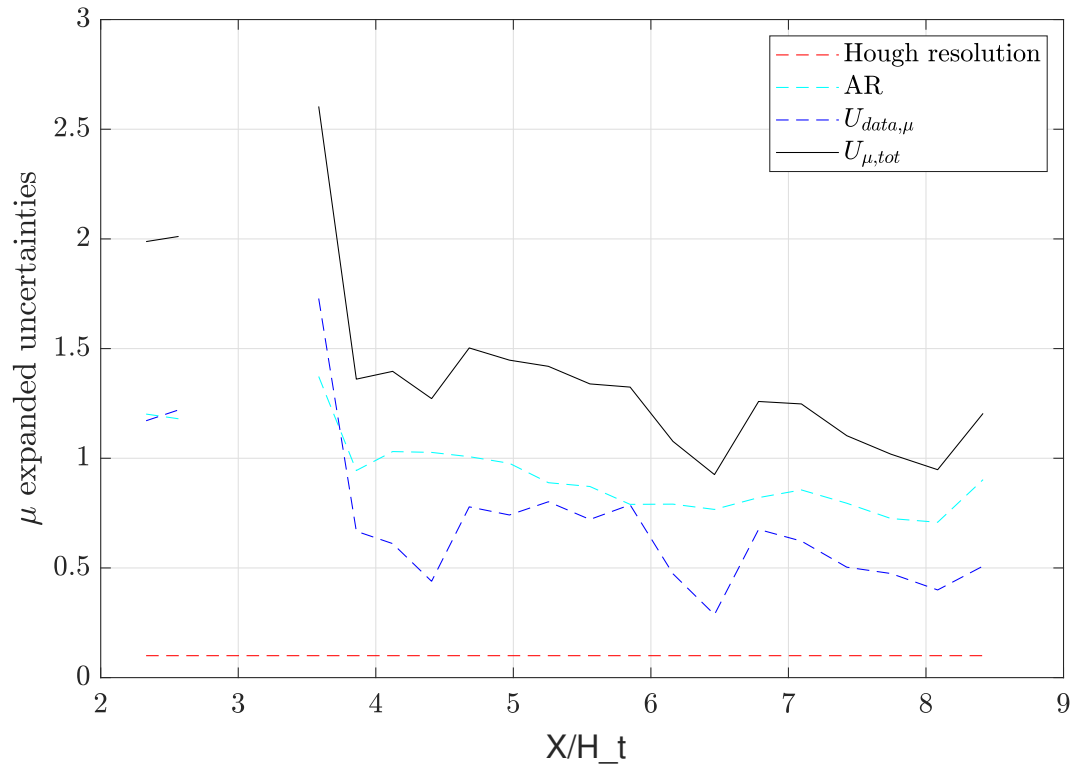
Figure 4.27:   PR.024: uncertainties breakdown for the extracted μ angle
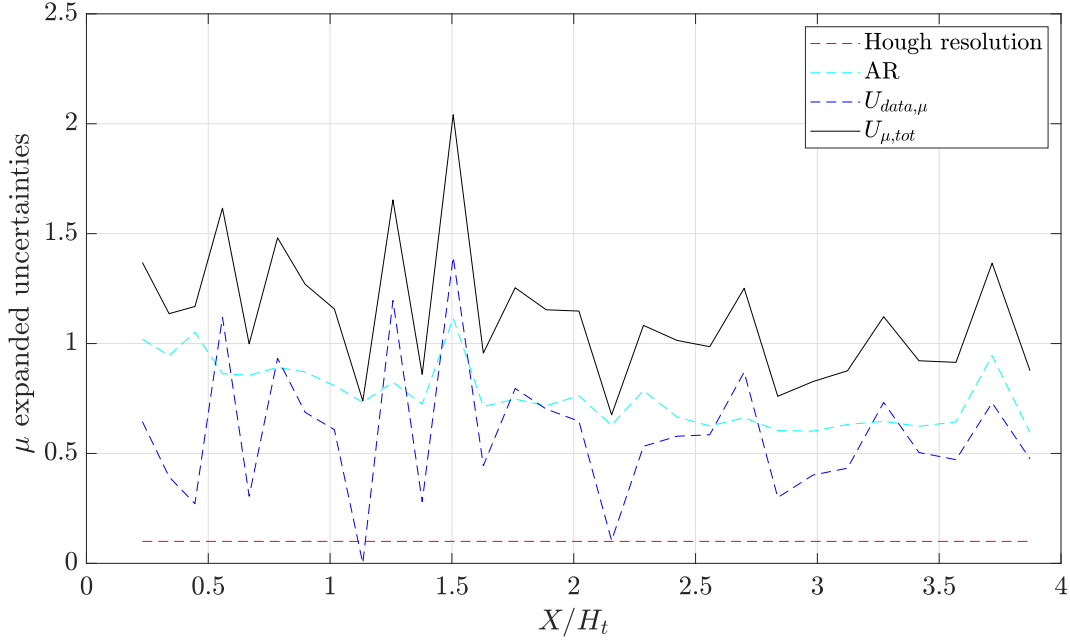
Figure 4.28: PR.026: uncertainties breakdown for the extracted μ angle

approach the throat, given that the brightness level is acceptable, keeping the height ratio r small enough to avoid considering misallignment errors.

The total expanded uncertainty in the μ angle

$$U_{\mu,\text{tot}} = \sqrt{U_{data,\mu}^2 + U_{ext}^2 + 2\rho_{data,ext}U_{data,\mu}U_{ext}}$$

for the wall line detection tool is significantly larger than the one in the midplane line detection tool because the extraction uncertainty has another important source of error: the wall angle.

The extraction uncertainty, which has been quantified in Sec. 4.3, in the *wall line detection program* is

$$U_{ext} = \sqrt{AR_{95}^2 + U_{\alpha,w}^2 + U_{\text{Hough,res}}^2}$$

in which the most significant source of error when is the uncertainty in the wall angle $U_{\alpha,w}$. The uncertainty in the wall angle directly influences the Mach according to equation 4.11 which dilates the effect as the Mach umber increases. For this reason, the results on the wall strongly depend o the quality of the dataset or the calibration image since the user can choose which walls are going to be used to evaluate the uncertainty in the wall angle. It is important to mention that the *wall line detection program* can receive as an input an external curve with zero uncertainty on the angle, coming from the geometry of the nozzle. If the user is able to feed to the program the equation of the exact curve of the nozzle's profiles, the uncertainties in the Mach along the walls will decrease significantly.

As already mentioned in the previous section, if too many lines are lost in a window, the statistical convergence of data is not verified thus the results on some widows are removed; this can be seen by looking at the lines on the wall in Fig. 4.31.
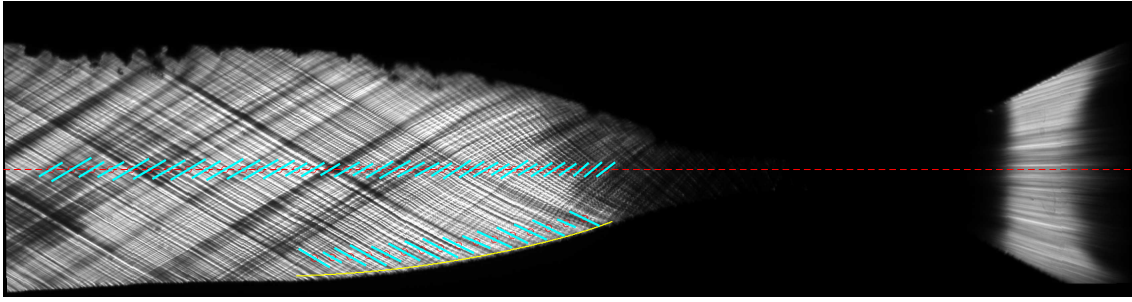
Figure 4.29: PR.022: all average extracted lines superimposed on the first frame of the dataset
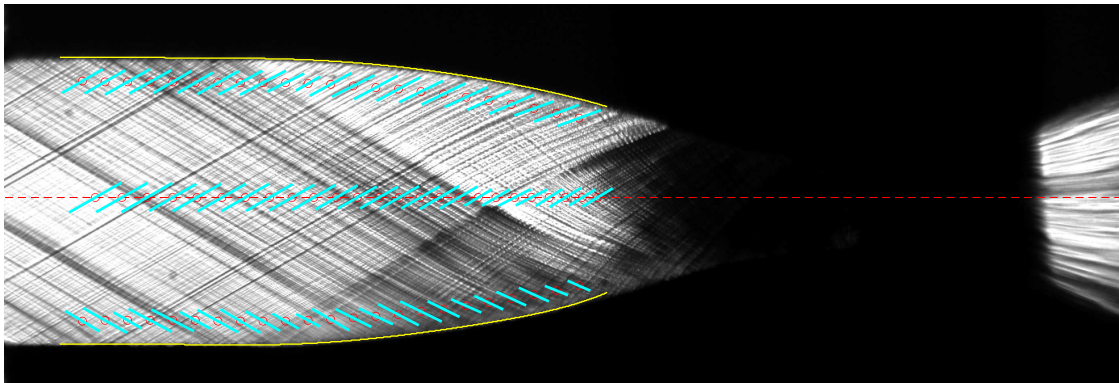
Figure 4.30: PR.024: all average extracted lines superimposed on the first frame of the dataset

4.5 Refractivity Index Analysis and Recommendations

The quality of the dataset plays a key role in the value of the total uncertainty resulting from the extraction of Mach lines from Schlieren images, and in the interval in which lines can be extracted. It is very clear how if the image is too dark or too bright, the extraction of lines becomes more and more difficult, the random uncertainty grows significantly due to the non-constant binarization of the images caused by the small brightness gradients in these areas. The differences between the three runs suggest that in order to obtain much better experimental results from the Schlieren, smaller fields of view need to be used: this limits the difference in brightness between the throat region and the end of the FOV towards the exit of the nozzle. By zooming in, it is possible to reduce the detected density change in the FOV, which is directly correlated to the refractive index, thus to the amount of light being scattered and not enering the camera lenses.

It is possible to deduce that the quality of the dataset is reduced if the refractive index changes too much during the expansion of the nozzle thus allowing too much light on one side (burned image), and too little on the other (dark image). Finding the refractive index change threshold could significantly improve future experimental data: by changing the FOV capturing only sections of the nozzle, the refractive index change Δn can be limited to a value below the maximum threshold, thus obtaining clear Mach lines throughout the entire photographed section of the nozzle. Furthermore, zoomed-in images have the advantage of increasing the scale factor which significantly improves the overall quality of the results by directly reducing angular uncertainty and allowing smaller height
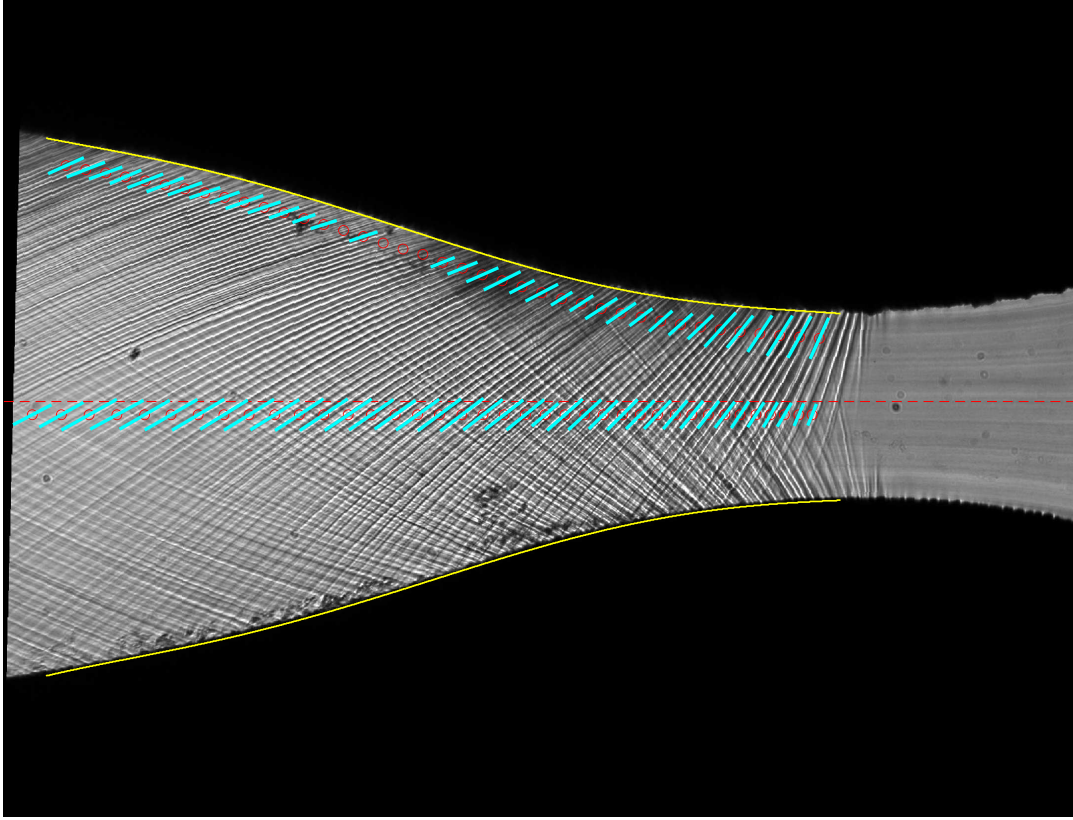
Figure 4.31: PR.026: all average extracted lines superimposed on the first frame of the dataset

ratios r thus increasing the spatial resolution. The level of optimal brighness in a Schlieren image as a function of the refractive index change is not known a priori, but having the PR.026 dataset that has an optimal brighness level throughout the entire image, the maximum refractive index change allowed to have good results will be greater or equal to the refractive index change of the optimal case of PR.026:

$$\Delta n_{\text{opt}} = \Delta n_{\text{PR.026}} = n_{\text{th}} - n_{\text{exit}} \leq \Delta n_{\text{max}}.$$

The refractive index is a function of the local density $\rho(x, y)$ of the fluid and the molar refractivity A according to equation 4.14:

$$n(x, y) = \sqrt{\frac{1 + 2A\rho(x, y)/M}{1 - A\rho(x, y)/M}} \tag{4.14}$$

An optimal brighness level was achieved experimentally in PR.026, which is a zoomed in dataset. The photographed domain of the nozzle is known thanks to the calibration sections and translation to the physical plane achieved with the developed tools. Furthermore, the end of the FOV for PR.026 coincides with the end of the Kernel region on the midplane, thus the midplane axial coordinate where the Mach has reaches its peak value (Fig. 4.32).

The refractive index field can be calculated for the optimal case PR.026 and is shown in figure 4.33. The variation of the n in this process run, which is an optimal value for Schlieren data extraction, is:

$$\Delta n_{\text{opt}} = 1.010999 - 1.001477 = 9.522(10^{-3}) \approx 0.01.$$

Figure 4.32:   Refractive index field in the diverging part of the nozzle (top half) and Mach number distribution (bottom) for PR.026

Now the constraint on the refractive index of any process run can be imposed by limiting the Δx that can be captured in the nozzle, thus limiting the FOV of the image:

$$\Delta x_{\mathrm{opt}} = \Delta n_{\mathrm{opt}} \frac{\mathrm{d}x}{\mathrm{d}n}, \tag{4.15}$$

where

$$\frac{\mathrm{d}n}{\mathrm{d}x} = \frac{\mathrm{d}n}{\mathrm{d}\rho}\frac{\mathrm{d}\rho}{\mathrm{d}x};$$

now, deriving the refractive index with the density, one can easily obtain the relation between the gradient of the density and the gradient of the refractive index:

$$\frac{\mathrm{d}n}{\mathrm{d}\rho} = \frac{1}{2}\left(\frac{1+2A\rho/M}{1-A\rho/M}\right)^{-1/2}\left[\frac{2A}{M(1-A\rho/M)} - \frac{A(1+2A\rho/M)}{M(1-A\rho/M)^2}\right]\frac{\mathrm{d}\rho}{\mathrm{d}x}. \tag{4.16}$$

Recalling Eqn. 4.15, one can express the maximum axial interval Δx_{opt} that can be captured by the camera to limit the change in the refractive index to an optimal value:

$$\Delta x_{\mathrm{opt}} = \frac{\Delta n_{\mathrm{opt}}}{\frac{\mathrm{d}\rho}{\mathrm{d}x}}\frac{2\sqrt{\frac{1+2A\rho/M}{1-A\rho/M}}}{\left[\frac{2A}{M(1-A\rho/M)} - \frac{A(1+2A\rho/M)}{M(1-A\rho/M)^2}\right]}. \tag{4.17}$$

The interval in Eqn. 4.17 depends on the fluid and the density distribution $\rho(x)$, given the assumption that the density variations along the y axis are smaller than the ones on the x axis.

Now that the optimal FOV is known depending on the density field, the optimal change in refractivity index can be imposed to another dataset, namely PR.022, deriving multiple intervals $\Delta x_{\mathrm{opt}}(i)$, with $i = [1, 2, 3]$ shown in figure 4.34. As one can notice, the refractivity index changes quite significantly when operating in higher densities and pressures conditions: it is possible to

Figure 4.33:   Refractive index field in the diverging part of the nozzle (top half) and Mach number distribution (bottom) for PR.026

conclude that the parameter that expresses the need for reducing the refractivity index gradient inside a Schlieren image is not the pressure ratio of the nozzle, but the difference in pressures between inlet and outlet of the nozzle. To be more precise, it should be the difference of the densities but when designing experiment, the inlet and outlet pressures can be directly controlled and measured, thus making this a much more useful parameter. Finding a connection between the difference in total pressures and the refractivity index change can convey useful information to predict how small the FOV has to be and/or what kind of filter must be applied to the camera to capture well the entire section of the expansion.

$$
\text{PR.026:} \quad
\begin{cases}
P_{\text{in}}^0 - P_{\text{out}}^0 = 8.8 - 0.7 = 8.1 \ bar \\
n_{\text{in}} - n_{\text{out}} = 1.01775 - 1.00148 = 0.01627
\end{cases}
$$

$$
\text{PR.022:} \quad
\begin{cases}
P_{\text{in}}^0 - P_{\text{out}}^0 = 18.65 - 2.1 = 16.55 \ bar \\
n_{\text{in}} - n_{\text{out}} = 1.06015 - 1.0042 = 0.05591
\end{cases}
$$

In order to quickly estimate the number of FOVs needed for an optimal Schlieren image, one could devide the total difference in the refractive index between inlet and exit of the nozzle by the optimal value of PR.026, which is 0.0163. If the refractive index are not known but the pressures are, the following emprirical relation can be helpful:

$$
N_{\text{intervals}} \approx \text{floor} \left(\frac{Z(P_{\text{in}}^0 - P_{\text{out}}^0)}{(P_{\text{in}}^0 - P_{\text{out}}^0)_{\text{opt}}} \right)^{3/2}, \tag{4.18}
$$

where Z is the estimation of the compressibility factor, floor() means that the lower integer value predicted by the formula is suggested. For the optimal pressure difference, 8.1 can be used. Eqn.4.18 has been proven effective in the ORCHID typical operating conditions using the measured flow fields of the three process runs as well as three other flow fields, obtained from SU2 CFD simulations with

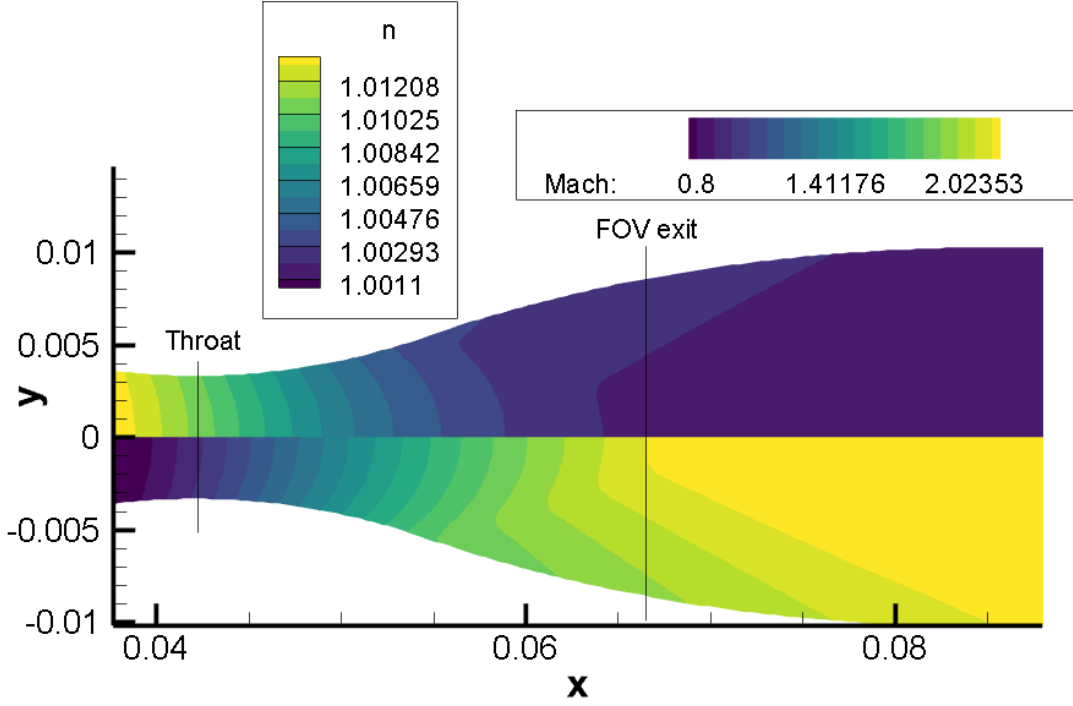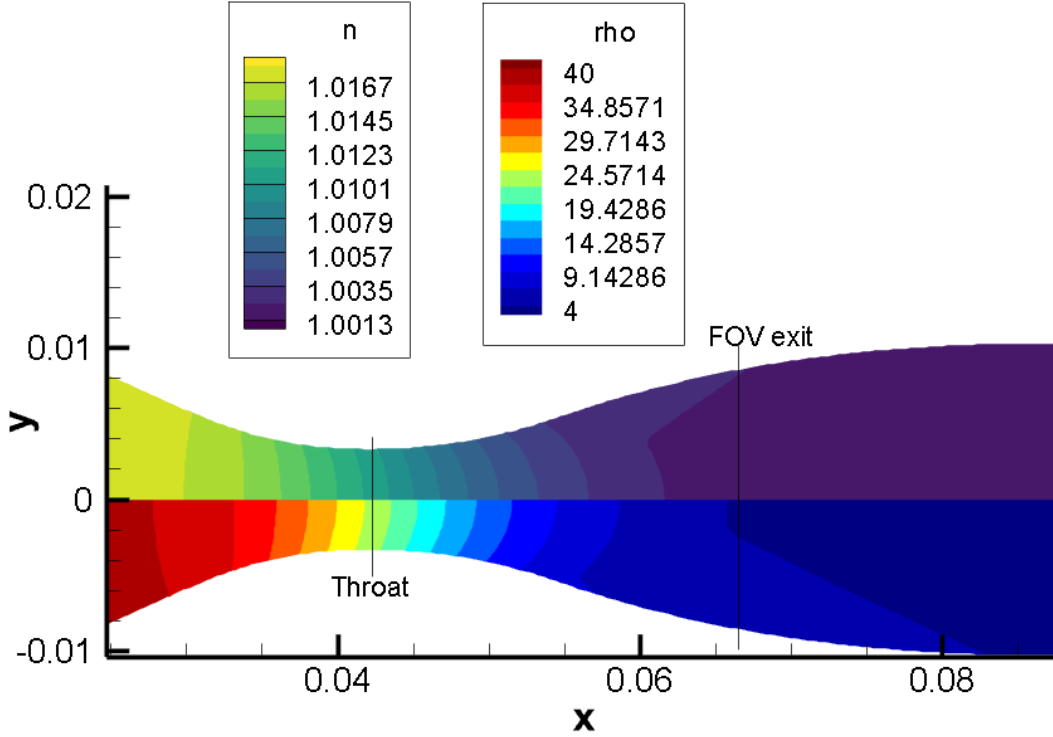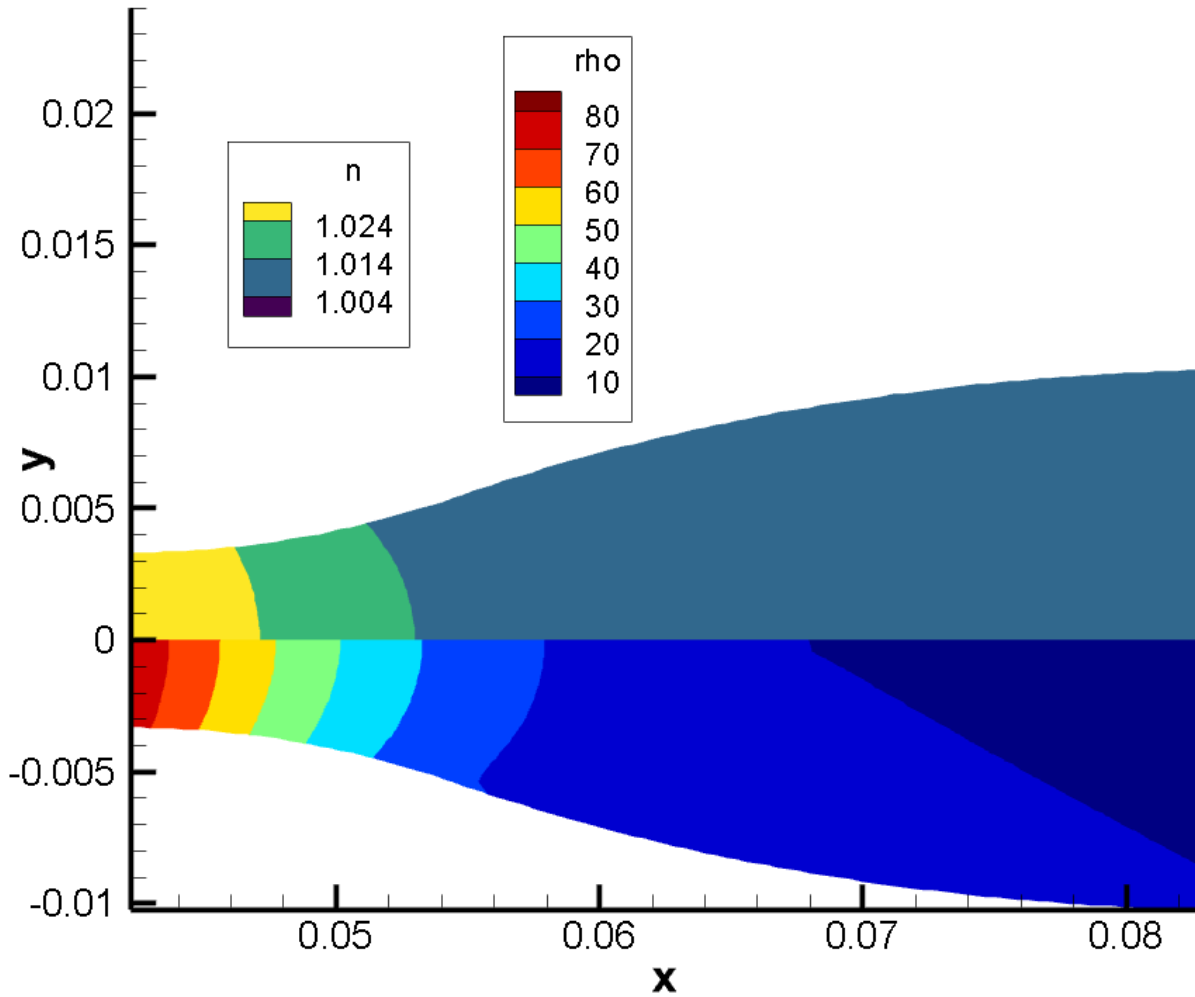Figure 4.34:   Refractive index field in the diverging part of the nozzle (top half) and Mach number distribution (bottom) for PR.026

Peng-Robinson EoS and variable specific heat model. From Fig. 4.34 one can notice how to be able to optimally acquire Mach lines in the kernel region close to the throat, two FOVs are necessary. This is obviously very impractical. Instead of acquiring Schlieren images for three different sections of the nozzle, it is recommended to apply a filter in front of the camera to reduce the amount of light in the low refractivity index region only, thus visualizing limited brighness levels on the sides of the image.

The recommended acquisition procedure for high pressure expansion such as PR.022 is the following: firstly capture with a single FOV the first two intervals $\Delta x_{\mathrm{opt}}(i = 1, 2)$ then the entire flow field with another FOV can be captured to have an overview of the flow and to possibly verify flow symmetry at the exit of the nozzle. For the first FOV, the camera settings can be tuned for the first section, closer to the throat. Then, applying a filter to limit the brightness of the second section will allow the correct capture of both intervals with an optimal contrast and brighness level, thus reducing to a minimum the uncertainties while maintaining a good scale factor and not wasting too much time to set up a three-FOV Schlieren acquisition campaign. The type of filter to use depends on the the amount of light that needs to be filtered, thus on the source light beam of the Schlieren measurement chain and the refractive index values in the FOV.

Chapter 5

Accuracy Assessment of the SU2 Flow Solver

5.1 Comprehensive Overview of the Uncertainties

Once the means and standard deviations of the steady state operating conditions of the ORCHID in the process runs have been calculated (Tab. 2.5), the nozzle boundary conditions for the various runs must be evaluated in order to obtain the necessary inputs for the CFD simulations. It is important to notice how the acquisition system Type B uncertainty, which is constant for all the runs, has an indirect effect on the Boundary conditions (BC) since the real fluctuations are not exactly the meassured ones. When the post processing is performed, the total expanded uncertainties on the boundary conditions must be associated to every mean value of the TS conditions.
For each variable of interest v_i the total expanded uncertainty has been computed by square root summing the expanded Type A uncertainty and the Type B acquisition system uncertainty:

$$U_{\text{tot,exp}} = \sqrt{(Ku_{\text{std,dev}})^2 + (U_{\text{acq,sys}})^2}$$

.

The inlet total pressure P^0_{in} of the nozzle was evaluated using the evaporator pressure PZA003. The total pressure at the evaporator is decreased the total pressure losses $\Delta P_{\text{loss.}}$ which takes into account the losses in the pipeline ΔP_2, the mechanically operated valve MOV002a ΔP_1 and the settling chamber ΔP_{sc}. The total inlet pressure, then, was expressed as

$$P^0{}_{in} = PZA003 - P_{\text{loss.}},$$

where

$$\Delta P_{\text{loss.}} = 0.7[\text{bar}].$$

The pressure at the exit of the nozzle P^0_{out} is assumed to be the backpressure $PT004$ measured in the receiver after the nozzle. This assumption, which is a standard procedure in nozzle experimental tests, has been proven valid considering that the flow velocity is extremely low and the losses from the exit of the nozzle to the receiver are neglegible; as a consequence it is reasonable to assume that the exit static pressure is the measured backpressure in the receiver. Since the SU2 CFD flow solver uses absolute pressure values and the measured pressures are in bar gauge, one bar is added to the total inlet and back pressures.

At this point, all the uncertainties in the BoP, Schlieren measurement chain, test section and post processing tools have been quantified. The accuracy of the SU2 CFD solutions is predicted by comparing the simulation to the experimental results with all the uncertainties on the extraction of the results from the Schlieren images. The total expanded uncetainties on the boundary conditions can be proagated through the simulations in order to estimate the simulation output uncertainty due to the inputs, necessary for a full validation u_{input}. In the present work, these uncertainties in

Table 5.1: Boundary conditions and their uncertainty for the process runs

Process Run	Nozzle Boundary conditions					
	P_{in}^0 [bar]	$U_{PT,in}$ [bar]	T_{in}^0[ºC]	$U_{TT,in}$	P_{out}^0 [bar]	$U_{P,out}$ [bar]
PR.022	18.65	0.147	252.6	1.986	2.09	0.048
PR.024	17.27	0.137	252.0	1.984	1.53	0.014
PR.026	8.8	0.07	257.3	2.02	0.692	0.0005

the boundary conditions of the nozzle are used to evaluate the steadiness of the flow.

The test section and Schlieren measurement chain uncertainties, on the other hand, directly influence the quality of the dataset and the symmetry of the flow; their effect is thus reflected on the post processing uncertainties. If the Schlieren measurement chain is not perfectly aligned, some areas of the dataset images could be slightly out of focus thus reducing the quality of the binarized image and, as a consequence, the extraction of the Mach lines has much higher values of uncertainty.

The effect of the test section sources of error are very subtle and hard to evaluate on the computed Mach value: the geometry of the nozzle used for the three Process Runs was designed with the method of characteristics in order to minmize the losses in On-Design conditions; this was done by evaluating the flow turning angle across each characteristic given a certain on design pressure ratio

$$(P_{in}^0/P_{out}^0)_{\text{design}} = 8.8$$

and flow conditions[1], then imposing that the nozzle's profiles have to follow the flow expansion. The MoC, in other words, is used to create an ideal profile such that it allows the cancellation of each reflection, creating an isentropic expansion. When considering the runs under evalaution, PR.022 can be considered on-design, PR.024 is close to the on-design conditions and PR.026 is off design. It is important to keep in mind that in non ideal flows, the on design conditions of the nozzle are not only given by the pressure ratio but also by the nozzle inlet conditions, since the thermophisical properties (e.g. γ, c) of these vapors strongly depend on the operating conditions. As a result, if the on-design pressure ratio is maintained in a nozzle but the inlet conditions change, the flow expansion will be different from the one predicted, thus the on-design conditions are not met entirely and the expansion will not be isentropic as for the on-design case.

As already explained, when the nozzle was assembled in the test section, the effective throat height has been measured to be 6.66 [mm] which is smaller than the on-design value of 8 [mm]. This assembly error slightly changes the area distribution $A(x)$ of the nozzle, thus the needed pressure ratio to keep the on design condition changes as well. The error is introduced since the inlet and back pressures imposed by the BoP are the original on-design pressure ratio which becomes slightly off-design. Since the effective throat height is smaller than the designed one, the flow expands more than the on design case so when the flow enters the receiver which has a higher pressure than the flow at the exit, recompression shocks form at the nozzle exit and can be seen in the zoomed out Schlieren images in PR.022 and PR.024. When the nozzle expands in slightly off-design conditions, the losses obviously become more important since the expansion moves further away from the ideal isentropic expansion in a perfectly smooth nozzle designed with the method of characteristics.

---

[1]On-design BC: $P_{in}^0 = 18.4$ bar, $P_{out}^0 = 2.1$ bar, $T_{in}^0 = 252º$ C

5.2 Deterministic CFD simulation

Steady 2D inviscid simulations of the flow-field in the ORCHID nozzle are obtained using the open-source flow solver SU2 for a half nozzle with symmetry conditions along the midplane. In order to model the properties of the hexamethyldisiloxane organic vapor, SU2 embedded thermodynamic libraries are used. The fluid models that have been used are the Ideal gas and Peng Robinson equation of state, both models have been tested in the polytropic form or non polytropic.

In the present work, the only simulation with the Ideal Gas model presented is the one with constant specific heat C_P (polytropic) since the non-polytropic version with $C_P(T)$ varying with the temperature does not change significantly the results of the simulations wich are substantially far away from the experimental result, as expected. On the other hand, results for both of the Peng-Robinson implementations, with constant and non constant C_P, are presented since both results are close to the experimental data. In conclusion, three different simulations for three process runs are presented in this thesis. The computational grid is an unstructured mesh where tetrahedrons
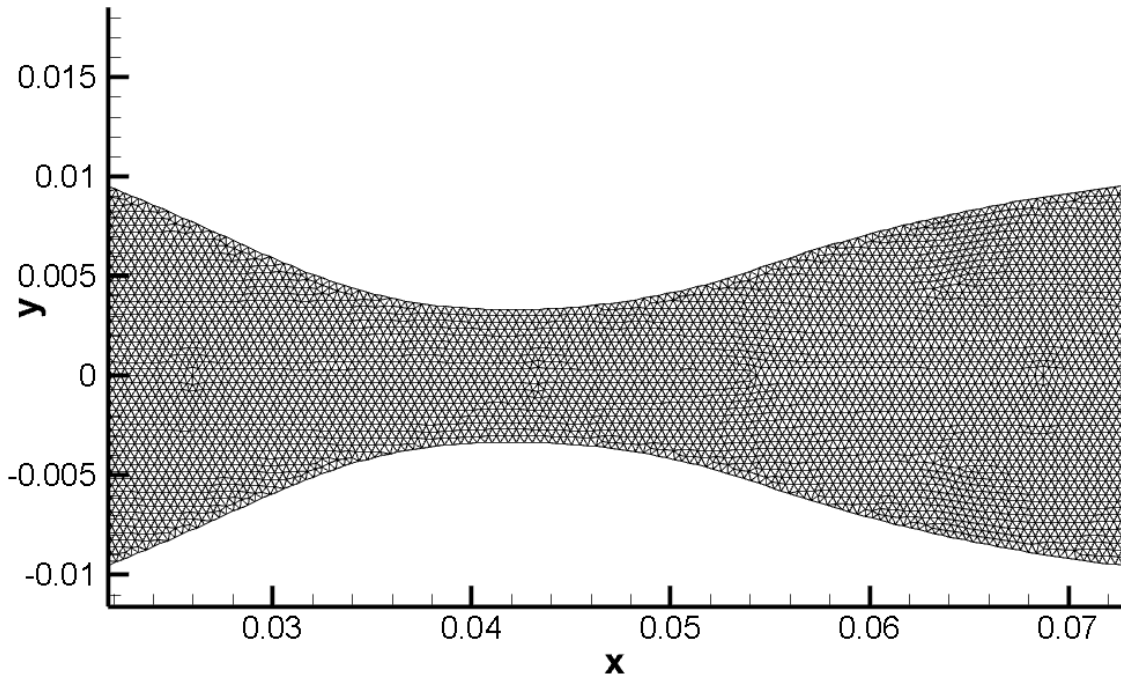
Figure 5.1: Zoom on the CD meshed section of the nozzle

are used to discretize the core region. To ensure the convergence of the results, the constant height channel after the diverging part of the nozzle has been increased in length from 10 to 30 $[mm]$; the added constant section channel helps convergence because of the coarser mesh used in this last section. Furthermore, the orignal design of the nozzle was modified since the effective throat height in the experiment was less than 8 $[mm]$: the top profile of the nozzle has been translated vertically towards the symmetry plane of $\delta y = 0.67$ $[mm]$ to ensure that the effective throat height is 6.66 $[mm]$, thus the the inlet and outlet heights are 23.1 $[mm]$ and 20.7 $[mm]$ respectively.

All the three inviscid simulations for each process runs have been converged to machine level accuracy ($\epsilon_{res} \leq -15$) using a second order accurate upwind flux-difference splitting scheme (ROE) with the Euler Implicit time discretization scheme. The convergence of the simulations has been achieved in about 3500 iterations: the first 1000 iterations are converged using a first order scheme with a Courant–Friedrichs–Lewy (CFL) condition equal to 16, then the solution has been restarted twice with CFL= 18 using this time the second order accurate scheme. The CFD simulations were performed with a workstation equipped with an Intel i7-8750H (4.10 Ghz boosted, 6 cores). A
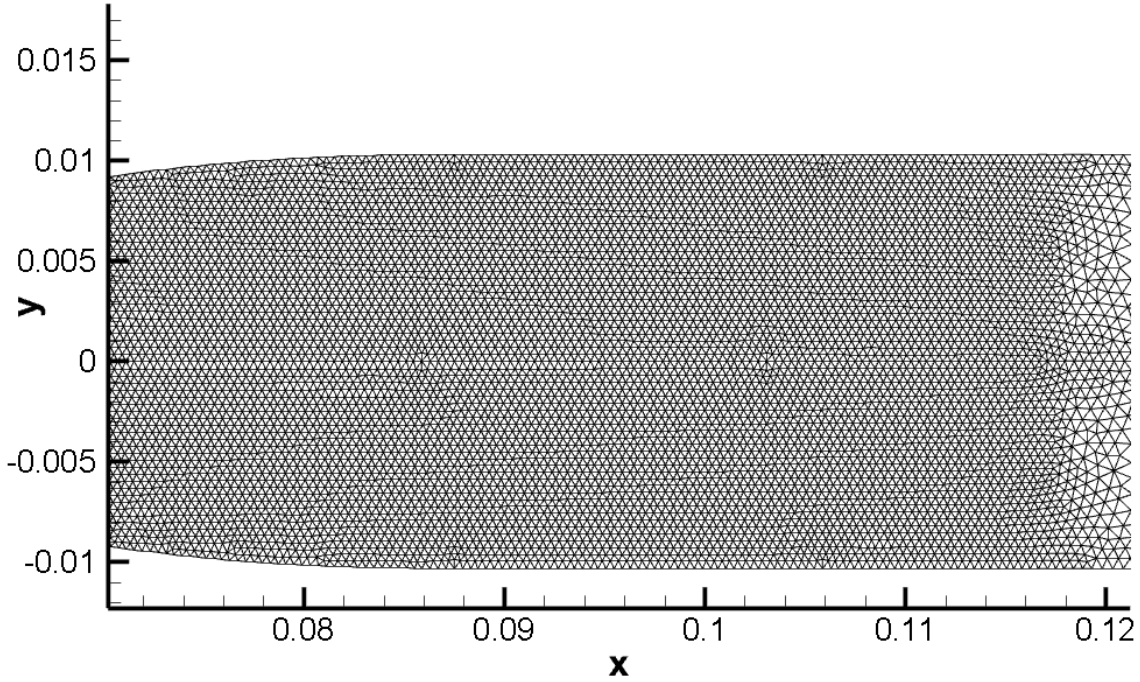
Figure 5.2: Zoom on the divering and constant section meshed nozzle

grid convergence study based on the methods given by Celik *et al.* (2008) and American Society of Mechanical Engineers (ASME) (2009) was performed. In particular, the Mach number was used to assess the influence of the grid size on the discretization error and the results. The outcomes showed that an unstructured mesh of $N_e = 15000$ elements provides mesh independent results and, as such, the numerical uncertainty can be deemed negligible.

The input boundary conditions used for the simulations are reported in Tab. 5.2. For the polytropic simulations, the constant value $\gamma_0 = 1.0214$ is used because C_P is kept constant, while for the non polytropic simulation γ_0 is used as the inital value and is then calculated by knowing the cubic polynomial equation of the constant pressure specific heat

$$C_P(T) = C_{P0} + C_{P1}T - C_{P2}T^2 + C_{P3}T^3,$$

where for the MM organic vapor the coefficients are

$$\begin{cases} C_{P0} = 51.89 \\ C_{P1} = 0.74134 \\ C_{P2} = -0.4161(10^{-3}) \\ C_{P3} = 0.7(10^{-7}) \end{cases}.$$

In Tab. 5.3 the properties necessary to succesfully configure the simulation of the non ideal vapor expansion are presented together with the properties of an ideal gas such as air.

Table 5.2: Boundary conditions for the Euler CFD simulations

Process Run	Nozzle BCs		
	$P_{in}^0 \; [KPa]$	$T_{in}^0 \; [K]$	$P_{ex}^0 [KPa]$
PR.022	18.897	525.75	2.118
PR.024	17.499	525.15	1.550
PR.026	8.917	530.45	0.975

Table 5.3: MM properties compared with an ideal gas (air)

	P_{cr} [kPa]	T_{cr} [K]	M_{mol} [g/mol]	ω(acentric factor)
MM	19.4	518.7	162.38	0.419
Air (dry)	37.85	132.63	28.96	0.0335

The solutions of the simulations are strongly influenced by the fluid model: in Fig. 5.3 and 5.5 the resolved flow fields using the non-polytropic implementation are presented for two equation of states: the ideal gas and the Peng-Robinson, respectively . It is possible to notice immediately how the Ideal Gas predicts an higher Mach number at the exit and an overall faster expansion compared to the Peng-Robinson model; furthermore the Ideal gas produces non physical soltions since at the exit of the nozzle, in the constant section channel, the Mach field is not constant while, on the contrary, the Peng-Robinson model predicts a constant Mach number at the exit, which is the physical solution. This can be appreciated in Fig. 5.5 where the top half of the nozzle is the PR expansion and the bottom half the Ideal Gas, both non polytropic, proving that the IG model is not suited for these non-ideal expansions.
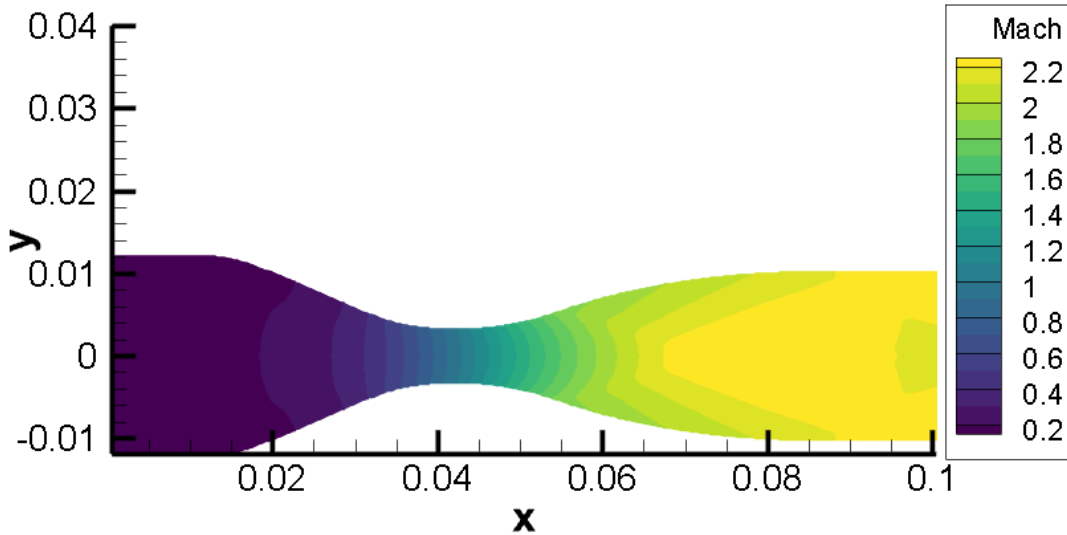

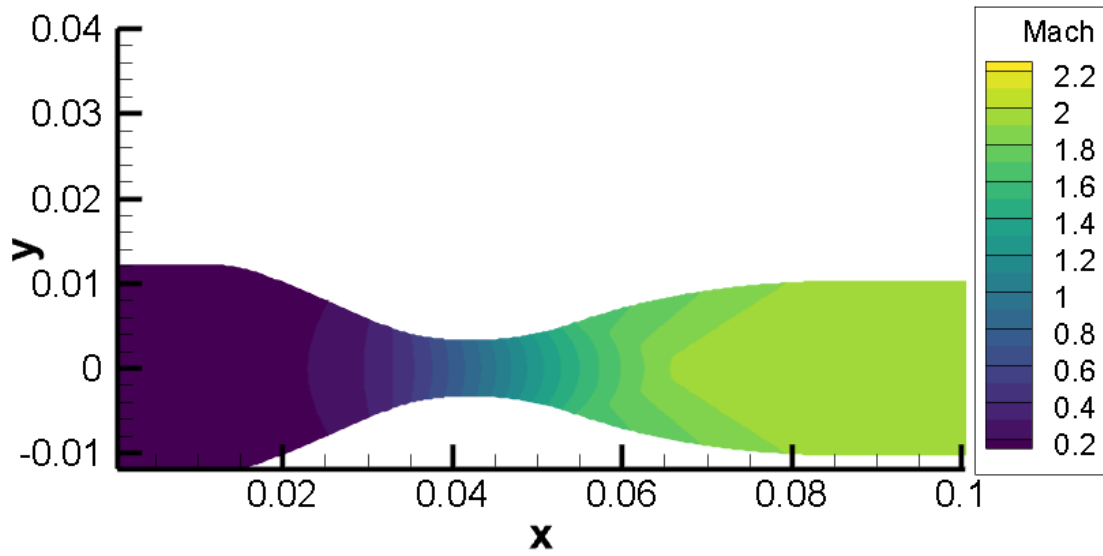Figure 5.3: Flow field solution for PR.022 expansion using the non-polytropic Ideal Gas model ($N_e = 15200$)

Figure 5.4: Flow field solution for PR.022 expansion using the non-polytropic Peng-Robinson model($N_e = 15200$)
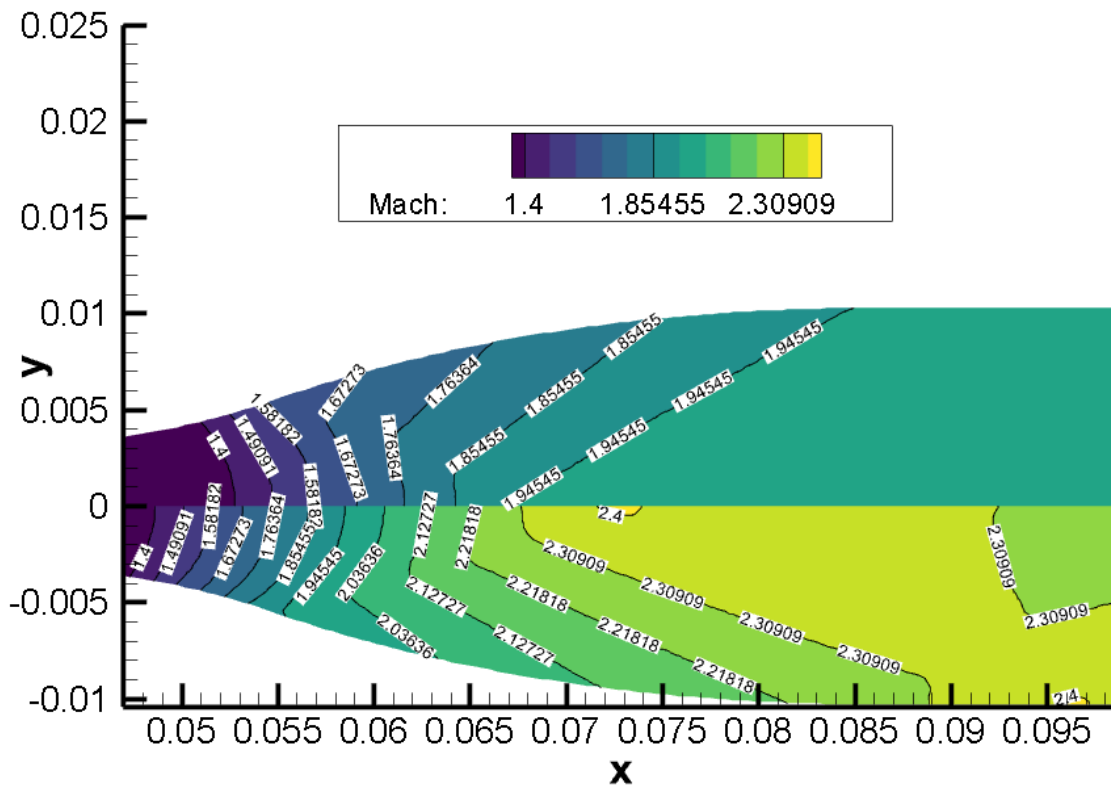

Figure 5.5: Comparison of flow field solutions for PR.022 using the non-polytropic Peng-Robinson model (top half) and the Ideal Gas mode (bottom half).

5.3 Accuracy Assessment of the SU2 CFD Solution Using the Extracted Experimental Results

Experimental results, extracted with the developed programs, can now be compared with the SU2 CFD Euler simulations to predict the accuracy of the fluid models in different regions of the T-S diagram for the MM in vapor state.

Simulation and experimental results are compared in terms of Mach umber with respect to the adimensional axial coodinate x/H_t for the three process runs, respectively PR.022, PR.024 and PR.026. Thanks to the symmetry of the flow, results of the CFD simulation are only obtained for half a nozzle and are compared experimental results on the midplane and on the wall with the lowest values of uncertainty on the Mach. It is important to keep in mind the zoom level of the images and resolution of the camera for the three process runs to better interpret the results. The scale factor SF gives an indication on how small can the interrogation windows be and thus, how refined the experimental data can be and how close PR.022 is a zoomed-out dataset but has a higher camera resolution, thus the scale factor of the Schlieren images is not the lowest. PR.024 has the lowest scale factor: the dataset has a slightly smaller field of view, but this beneficial effect on the scale factor is countered by the lower resolution of the camera (Bobcat). Finally, PR.026 has the highest scale factor because is a zoomed-in dataset even if it was taken with the Bobcat camera.

Nozzle Midplane

When the average extracted Mach, its uncertainty on the value and uncertainty in the position are compared to the output of the three Euler simulations on the midplane, two different situations are observed. As a result, in order to correctly draw conclusions from the accuracy assessment, the two zoomed out process runs PR.022 and PR.024 are analyzed first since the outcome of the assessment is the same, while for PR.026 a slightly different outcome is explained at last.

Euler simulations and experimental results for PR.022 and PR.024 are presented in figures 5.7 and 5.8. One can easily notice the rather large difference between the three CFD simulation results. The ideal gas simulation not only over predicts the Mach values on the midplane, it also predicts a non physical trend since after reaching the maximum value it decreases substantially before re accelerating around $x/H_t = 9$. This non-physical behaviour and the over prediction of the Mach value is clearly caused by the incapability of the Ideal gas model to solve flows where non ideal fluid effects are predominant; as a matter of fact, the compressibility factor Z for these two process runs is far from one (see Fig.2.9) especially in the converging part of the nozzle and the throat proximity, as a result, the error in the prediction of the fluid behaviour where Z is less than one is propagated and dilated all the way to the exit of the nozzle where Z is close to one. This can be observed in the simulation results: the shift between the IG results and the PR grows as the flow expands reaching large differences in the highly non ideal expansions (PR.022 and PR.024) and smaller ones for the almost ideal expansion of PR.026. Furthermore, in Fig. 5.6 a comparison of the same polytropic Ideal gas model between PR.022 and PR.026 shows that the irregularities in the Mach number predictions significantly decrease as the flow moves towards the more ideal region where Z is closer to one (PR.026).

On the other hand, both Peng-Robinson models for both PR.022 and PR.024 predict similar possible solutions where the Mach is constant once the flow is fully expanded. The only difference between the two implementations, polytropic and non-polytropic, is that the Mach values are smaller when when C_P is not constant, meaning that the model is capable of better representing the physics of the problem. As a matter of fact, the C_P in real flows is never constant with temperature, but in many applications assuming constant specific heat does not introduce significant errors, especially in flow with ideal gas behaviour. This can be clearly seen in the PR.026 case, where the two PR implementations are pedictin almost the same expansion.
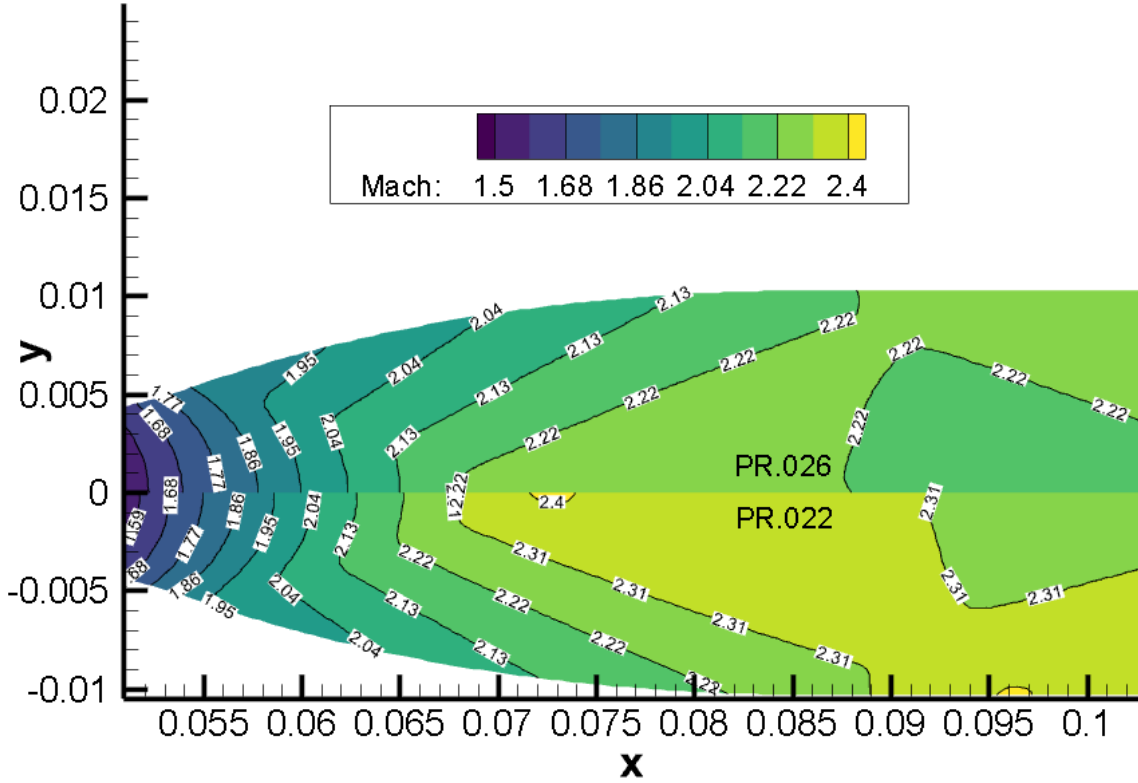
Figure 5.6: Comparison of the SU2 predictions using the polytropic Ideal Gas model for the highly non ideal expansion of PR.022 (bottom half) and the more ideal one of PR.026 (top half) proving that the Ideal Gas model solution is slghtly less incorrect if a more ideal region of the flow expansion is considered.

Table 5.4: Average differences between experimental values and simulation in four different intervals of the midplane of the nozzle and average uncertainties.

ProcessRun	PR.022		PR.024		PR.026	
x/H_t	$\overline{\Delta M}$	$\overline{U_M}$	$\overline{\Delta M}$	$\overline{U_M}$	$\overline{\Delta M}$	$\overline{U_M}$
0.23 to 1.88	-	-	-	-	0.01	0.022
1.99 to 3.0	0.07	0.11	-	-	0.085	0.048
3.0 to 4.2	0.06	0.12	0.05	0.1	0.098	0.060
4.2 to 8.8	0.03	0.10	0.02	0.07	-	-

From these results, it is clear that the most advanced fluid model considered, the PR non polytropic, is capable of predicting very well the expansion on the midplane in terms of Mach when

$$2.2 \leq \frac{x}{H_t} \leq \frac{x_{\text{exit}}}{H_t}$$

since not only all the uncertainty bands cross the simulation, but the average experimental values are very close to the deterministic simulation output. In Tab.5.4 the midplane of the nozzle where lines were extracted is divided into four sub-intervals in which the average Mach difference between the average Mach number of the experiment and the CFD predition using the PR non polytropic model

$$\overline{\Delta M} = \text{abs} \left(\frac{1}{N_{\text{intervals}}} \sum_{\text{intervals}} \overline{M(k)} - M_{\text{sim}} \right)$$

is calculated as well as the average uncertainty on the experimental value

$$\overline{U_M} = \frac{1}{N_{\text{intervals}}} \sum_{\text{intervals}} U_M(k).$$

The prediction accuracy is proportional to how small is the difference between the experimental average and the simulation compared to the experiment uncertainty.

A measure of the accuracy of the prediction, taking into account the value of the experimental uncertainty as well as the offset between the experiment and simulation prediction, can be defined using the accuracy parameter defined in Eqn. 5.1 where

$$0 < \text{acc} < 1$$

with accuracy being one meaning a perfect match with zero uncertainty. The accuracy equation is expressed as

$$\text{acc} = \frac{1}{\overline{U_M} + 1} e^{-\frac{\overline{\Delta M}^2}{\eta \overline{U_M}^2}} \tag{5.1}$$

where

$$0 < \eta < \infty$$

is a parameter which can be chosen by the user depending on how accurate the experimental results are. In other words, if η increases to values larger than one, more weight will be given to the precision of the measurements, which is $\overline{\Delta M}$. On the other hand, reducing η gradually increases the effect of $\overline{U_M}$ on the accuracy value.

When the uncertainties on the Mach number are always below 0.10, meaning that the datasets have high quality, $\eta = 0.5$ is recommended. In order to give equal weight to the two parameters, $\eta = 1$ is used here to calculate the accuracy of the simulation in a few different cases.

In conclusion, the accuracy parameter not only quantifies the overall accuracy of the solution using a weighted method considering both parameters, the average experimental uncertainty and the SRQ average difference, but can also be used to assess the capability of the numerical simulation to correctly predict the experimental values. As a matter of fact, the condition which verifies that the simulation always falls inside the uncertainty bands, given that they are reasonably accurate, with 100% confidence level can be derived from Eqn. 5.1 by imposing that the uncertainty has to be greater than the difference of the Mach numbers, and using Taylor expansion to express the fraction.

Finally one can simply obtain the constraint to assess that the numerical prediction falls in the uncertainty bands:

$$\text{acc} \geq e^{-1/\eta};$$

In the present case, $\eta = 1$ thus the value of the accuracy must be greater or equal than 0.368.

The first interval in Tab. 5.4 is very close to the throat, in the Kernel region, and only PR.026 was capable to resolve it with an extremely high degree of accuracy acc = 0.79.

The second interval is in the middle of the expansion of the nozzle in the kernel region: PR.022 has a couple of datapoints in this region but the predictions are fairly accurate, while PR.026 data starts to deviate from the simulation; the uncertainty bands are very small and clearly do not meet the numerical predictions, thus the accuracy tends to zero.

$$\begin{cases} \text{acc}(PR.022) = 0.60 \\ \text{acc}(PR.026) = 0.041 \end{cases}$$

The third interval shows a good level of accuracy for the close to on design conditions and still a very low accuracy for PR.026.

$$\begin{cases} \text{acc}(PR.022) = 0.69 \\ \text{acc}(PR.024) = 0.71 \\ \text{acc}(PR.024) = 0.06 \end{cases}$$

Finally the fourth interval once again confirms the accuracy of the Peng-Robinson model for the on design cases:

$$\begin{cases} acc(PR.022) = 0.86 \\ acc(PR.026) = 0.83 \end{cases}.$$

Figure 5.7: PR.022: comparison of the SU2 prediction and experimental results on the midplane. The domain has been discretized in 24 windows but 4 have been removed due to non convergence of data. The nozzle's throat height is 6.66 $[mm]$.

When considering the CFD simulation and experimental results comparison on the midplane for the PR.026 in figure 5.9, a few differences with the previous cases can be instantly noticed. Firstly, the results of the three simulations are much more similar to one another with respect to the previous cases: while a clear but small difference can be appreciated between the IG and the PR simulations, trying to distinguish the two Peng-Robinson implementations, polytropic and not, can be quite hard. The reason why the three outputs of the Euler simulations are much more similar to one another with respect to the previous cases, lies in the value of the compressibility factor Z, which for PR.026 is much closer to one and almost constant throughout the expansion (see Fig.2.9) . Again, as for the previous runs, the ideal gas model predicts larger Mach values than the Peng-Robinson. Secondly, the extracted experimental results can resolve the flow expansion with a much higher precision and resolution thanks to the significantly larger scale factor of the Schlieren images of the dataset. Thirdly, the uncertainty bands are much smaller than the other cases and results can be extracted almost at the throat of the nozzle: this is due to the better brightness level of the images as well as a larger scale factor. Lastly, the experimental results match the simulation predictions only when
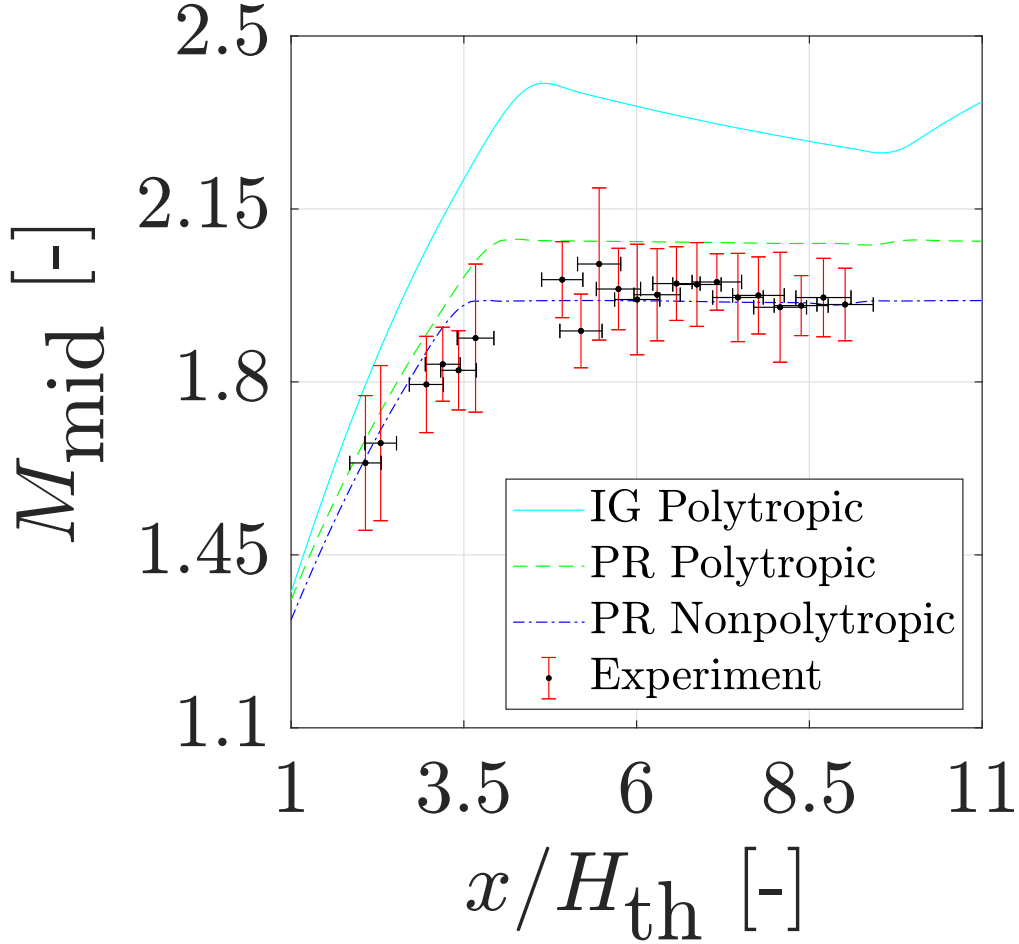
$$0.1 \leq \frac{x}{H_t} \leq 2.2,$$

Figure 5.8: PR.024: comparison of the SU2 prediction and experimental results on the midplane. The domain has been discretized in 22 windows but 3 have been rmoved due to non convergence of data. The nozzle's throat height is 6.66 [mm].

and slowly depart from the PR simulation output after what seems a slight change in slope of $M(x/H_t)$ around $x/H_t \approx 2.3$. It seems clear that the PR simulations are slightly better than the IG just because the Mach values are slightly smaller, thus closer to the experimental results. The uncertainty bands in the experiment, however, are very small and do not ever cross the Peng-Robinson CFD output indicating that the simulations are inadequate to predict the organic vapor expansion under the PR.026 boundary conditions for this given geometry. The identification of the specific problem causing inadequate results when an Euler CFD analysis with the non polytropic PR gas model is used for this specific case is not an easy task and, to the author's knowledge, it has not been done before .

The reason behind the difference between the experimental results and the Euler PR non polytropic, is not related to the post processing method or zoom level of the dataset: Head (2020), as a matter of fact, uses the developed tools presented in this thesis to extract the midplane Mach of a zoomed-in Schlieren dataset, with the same exact field of view of PR.026 but at a higher inlet pressure, similar to the PR.022. The results show that the Peng-Robinson non polytropic fluid model accurately predicts the Mach values on the midplane thoughout the entire diverging part of the nozzle, thus the problem must be elsewhere. The fluid model itself could also be excluded from the casuses of the down shift in the midplane Mach results: more complex and accurate fluid models such as the iPRSV and the Helmholtz energy equation of state have been used for SU2 simulations [2] in similar conditions and it was noticed that non of them predict a significant and immediate

---

[2]Steady simulations using the iPRSV model or the reference fluid model based on the Helmholtz EoS can be run

change in slope of the curve $M(x/H_t)$ like the one observed in the experimental results (Fig. 5.9). The differences in the predictions of these models are small but can be appreciated in non ideal conditions, where the compressibility factor is less than one; in PR.026, again all these equations of state do not differ too much from one another, therefore and no model predicts results that can be deemed accurate in the prediction of the flow for this specific case.

For these reasons, the cause of the difference between simulations and experimental results is believed to be the adjoint effect of the boundary layer and 3D corner vorices in the nozzle. The Euler assumption was introduced because the nozzle has been designed using the method of characteristics to obtain an area distribution $A(x)$ in such a way that the flow turning angle equals the turning angle of the nozzle's profiles, thus obtaining an (almost) ideal isentropic expansion. In on-design conditions, the viscous effects for these vapors are very small, but when the operating conditions are far off-design then this can change. Since the geometry was modified when the nozzle was sealed, viscous losses become more prominent, especially in PR.026 where the Mach number and the pressure ratio is higher than the other cases and the expansion is far away from the on design conditions. The inlet conditions of PR.026, as a matter of fact, are very different from all the other cases: all the fluid properties which depend on temperature and/or prssure, such as speed of sound c or γ, evolve in a different way thus the expansion itself is even further than the on design case, thus 3D effects in the corners where the flow is subsonic could increase losses even more. From preliminary 2D RANS simulations, it was possible to observe that the Mach prediction shifts downwards slightly when viscosity is considered; in order to verify that the difference between simulation and experiment in PR.026 is caused by the boundary layer, accurate RANS simulations with valid fluid models such as PR, iPRSV or Helmholts equation of state must be performed and converged to second order accuracy. The influence of 3D effects caused by the squared section of the nozzle must be assessed with 3D simulations using either Large Eddy Simulation (LES), RANS or even better Direct Navier-Stokes (DNS).
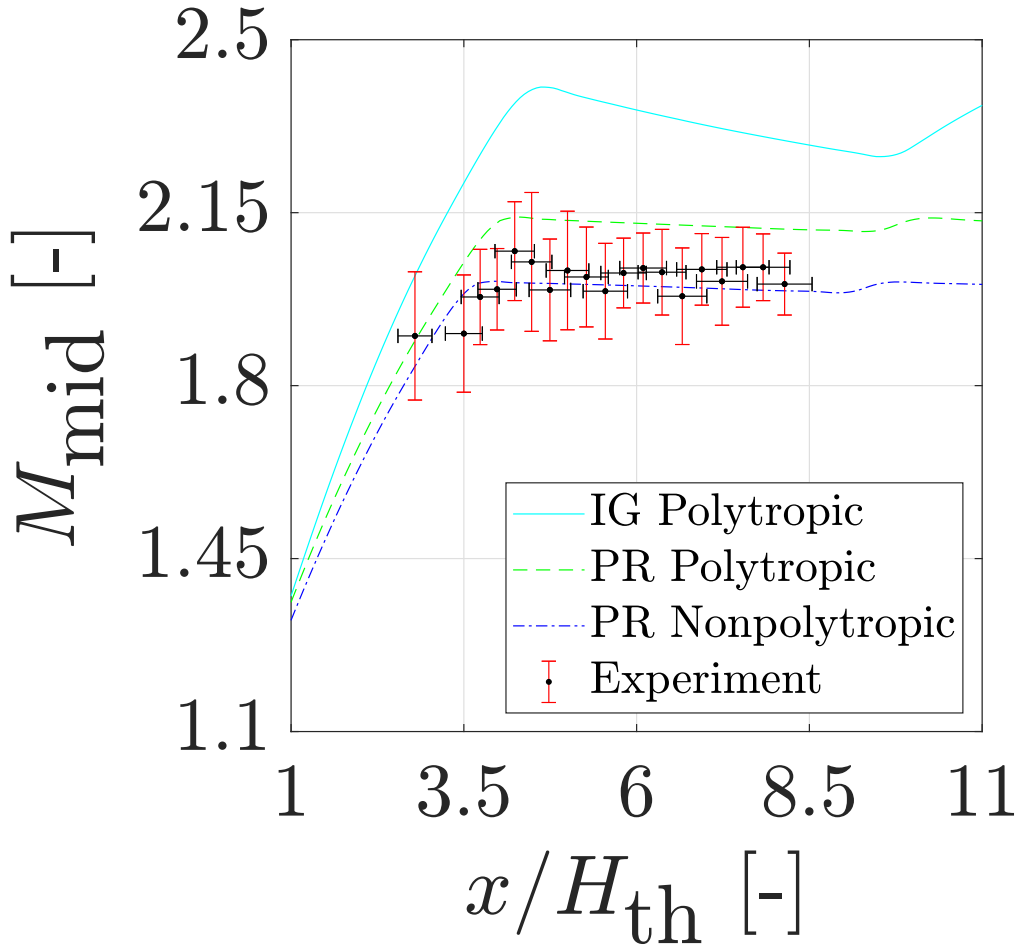
---

using FluidProp thermodynamic library in SU2.
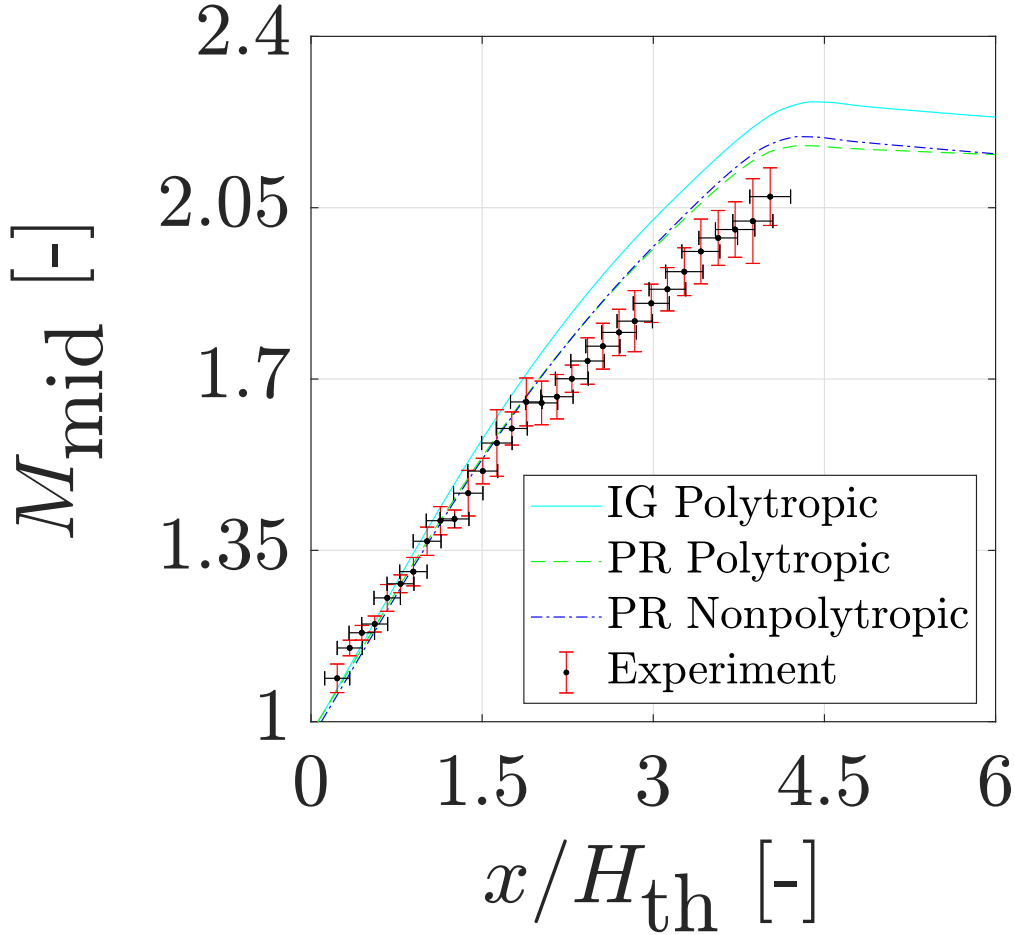
Figure 5.9: PR.026: comparison of the SU2 prediction and experimental results on the midplane. The domain has been discretized in 30 windows, the nozzle's throat height is 6.66 $[mm]$.

Nozzle walls

The comparison between simulation and experimental results on the nozzle's profiles has a different result than the midplane. All three cases show that the measured Mach number is lower than the results of the Euler simulations, with PR.026 showing results from which many more deductions can be made. The simulation outputs are consistent with what has been observed on the midplane: the distance between the different fluid models is proportional to the non ideality of the flow, thus proportional to $1 - Z$. Again, the ideal gas model results show a non physical expansion and a large over prediction in the Mach number. The PR models, on the other hand, seem to be able to approximate the trend of the Mach field on the walls when

$$\frac{x}{H_t} > 3,$$

but the values are higher than the experiment for the entire nozzle profile. From Fig.5.10 it is possible to confirm that the Peng-Robinson non polytropic simulation is able to predict with high precision the Mach number only when the curvature of the nozzle walls becomes very small

$$\frac{x}{H_t} > 6.2;$$

this is valid only for the PR.022 inlet conditions, which are the ones used to design the nozzle geometry. Comparing the Mach experimental results with the simulation in the common axial interval

$$3 \leq \frac{x}{H_t} \leq 4.5,$$
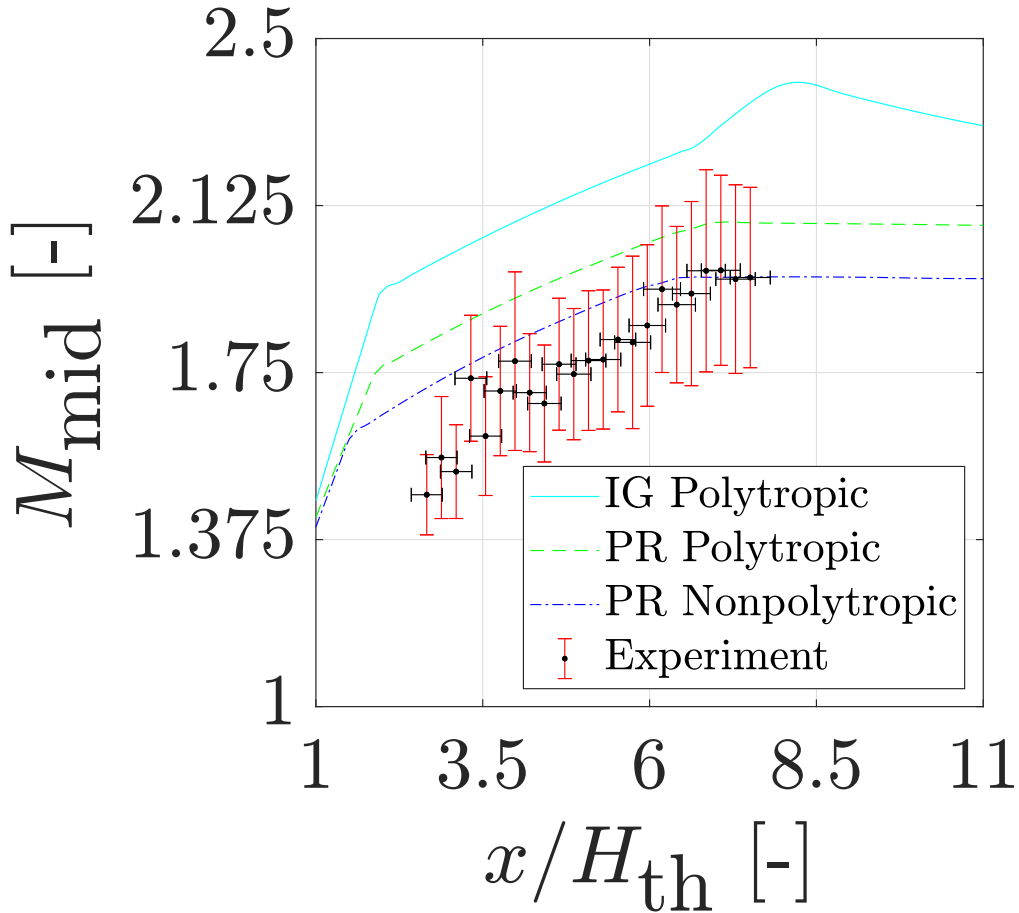
Figure 5.10:   PR22:comparison of the SU2 prediction and experimental results on the nozzle's walls

one can notice how all three accuracy assessments on the walls show that the extracted Mach numbers are significantly lower than the numerical predictions and it seems that the sharp change in slope in the simulation outputs around $x/H_t \approx 2$ is, in reality, much smoother and at lower Mach values. This behaviour is even more prominent in the PR.026 results, where experimental results can be compared to the simulation for the entire Kernel region, where the slope of the $M(x/H_t)$ is steeper since the expansion fan is being generated in the concave region, and part of the reflex region, where the slope is less steep and the flow has fully expanded on the midplane.

Thanks to the zoomed in dataset (PR.026), it is possible to investigate how accurate the SU2 simulations are compared to the experimental results in proximity of the throat $x_t/H_t = 0$. Observing Fig. 5.12 it is possible to notice that in the interval

$$0.1 \leq \frac{x}{H_t} \leq 1.4$$

all three simulations, predicting almost the same Mach values in this interval, are predicting the correct Mach number. Around $x/H_t \approx 1.5$ the experimental results deviate quickly from the numerical prediction following a smoother trend and a lower overall Mach number before approaching again the Peng-Robinson non polytropic simulation results around $x/H_t \approx 3.5$.

The reason for this downward shift of the Mach results on the walls in the last part of the Kernel region and the reflex region

$$1.4 \leq \frac{x}{H_t} \leq 6$$

can be related to two main factors: firstly the effects of the boundary layer and the viscosity of the real flow on the walls are more prominent than in the midplane, especially when the flow turning
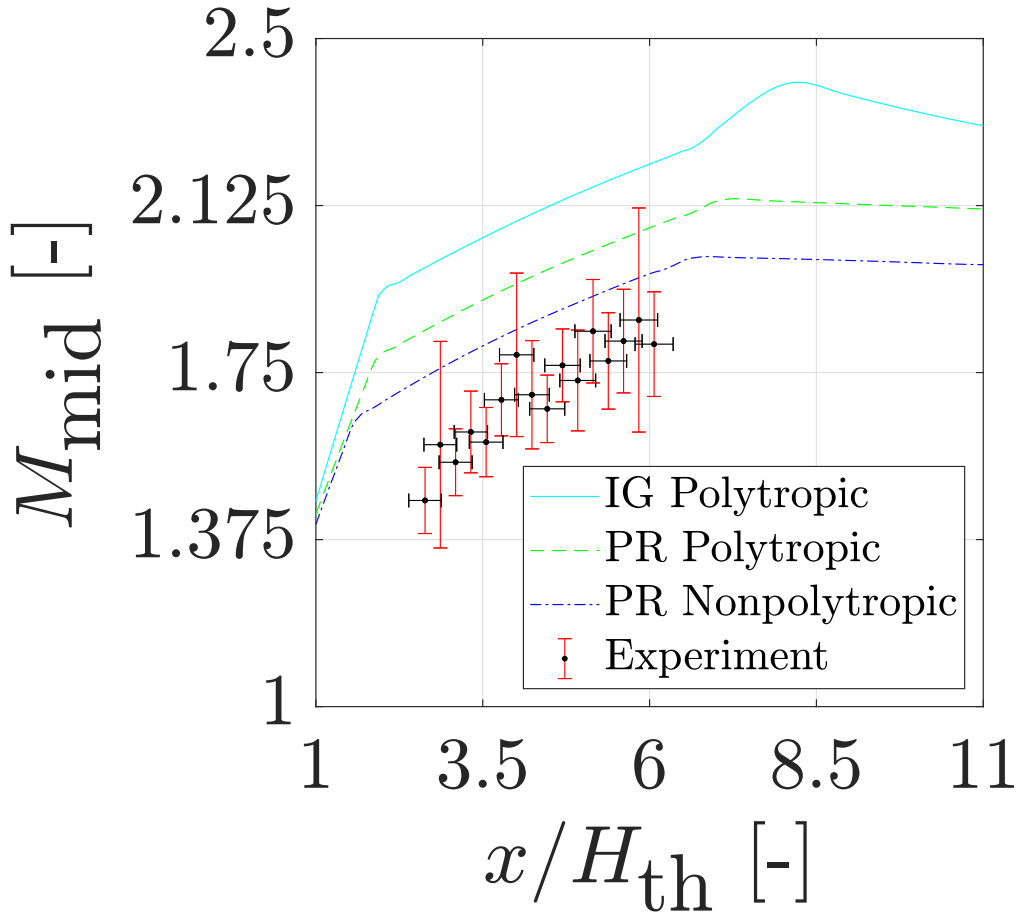
Figure 5.11: PR24: comparison of the SU2 prediction and experimental results on the nozzle's walls

angle is large, such as in the specified domain. On the contrary, at the exit of the nozzle, the PR non polytropic numerical prediction is in accordance with the simulations as shown in Fig. 5.10, as well as right after the throat (Fig. 5.12) before the nozzle curvature becomes more prominent. Secondly, 3D effects become more predominant when moving towards the borders of the test section: the gasket sealing the test section can introduce flow non uniformities in proximities of the walls due to the slow erosion caused by the high speed flow. Furthermore, in the corners of the squared section of the nozzle, vortices and 3D effects can locally modify the flow and, since the Schlieren photographs are taken from the side of the test section, these flow non uniformities and 3D effects in the corners, which dissipate energy, are captured in the image. As a result, the Mach number along the vertical coordinate $M(y)$ has the maximum value on the midplane, while decreases approaching the walls due to the losses above mentioned, as proven by Shen (2019).

One could argue that the Mach angle on the walls extracted from the Schlieren images does not exactly correspond to the Mach extracted from the the numerical solution, which is precisely at the walls thanks to the slip condition of the inviscid simulation; as a result, the comparison between the two is not performed in the same position. This effect, which is explained in 4.3, is a combination of both the slight difference in velocity (both module and direction) between the center pixel of the interrogation window where the Mach angle is extracted and the Mach number precisely on the wall deriving from the simulation output file. As shown in Sec. 4.3, if the r r of the interrogation windows is small enough this effect becomes very small; in PR.026 the height ratio is extremely small thanks to the very large scale factor of the images but the down shift of the results is still present, thus proving that this second cause for the difference of the results is neglegible with respect to the first one, related to the viscous and 3D effects.
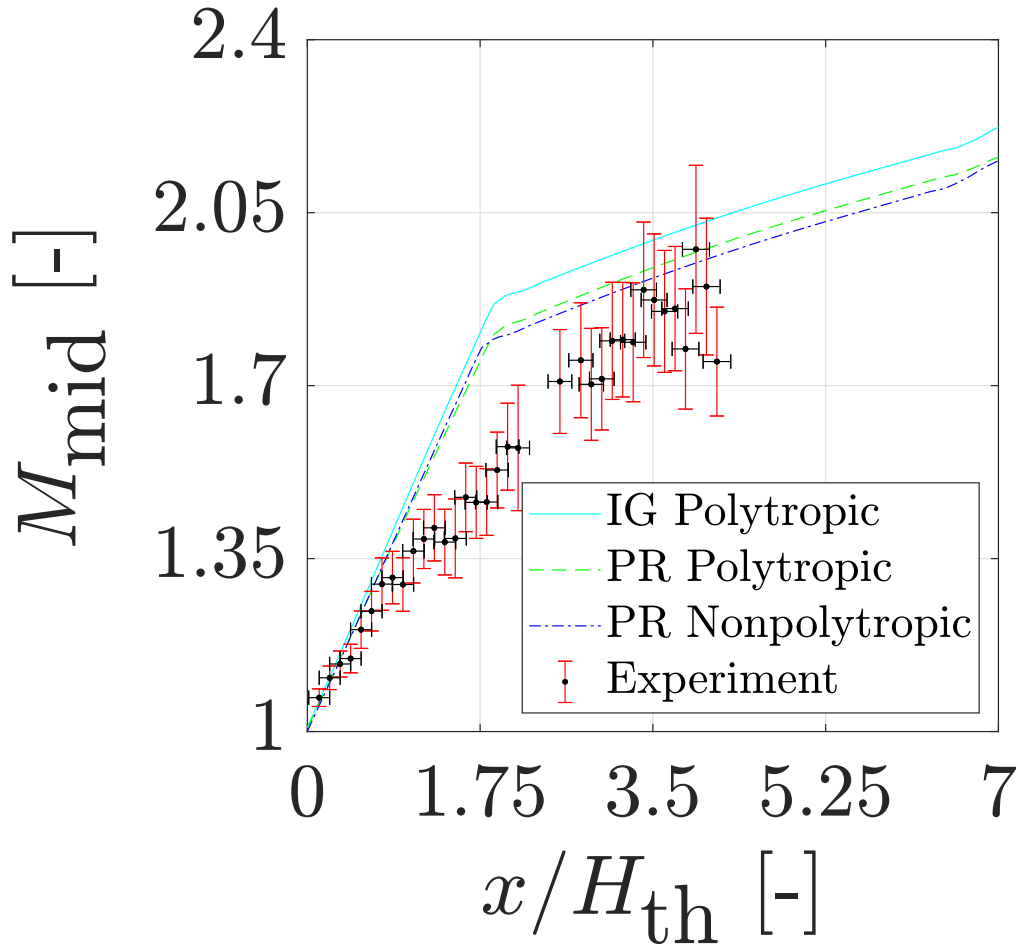
Figure 5.12:   PR26: comparison of the SU2 prediction and experimental results on the nozzle's walls

In conclusion, again 3D effects and viscous effects could be the main cause for this difference between experimental results and simulations: this effects become much more important when the flow in the proximity of the test section borders and corners is studied, this is the reason why in the midplane accuracy assessment this effect was much smaller. The verification of this hypothesis requires the user to run 3D viscous simulations on the nozzle and verify that that the numerical predictions capture the experimental results. In order to do so, a more complicated approach must be implemented in the extraction of the Mach number from the solution file of the CFD analysis since the Mach number on the walls of the nozzle will obviously be zero for the no-slip condition. Thus in order to compare simulation and experiment, the Mach number from the simulation output must be extracted at a certain distance from the wall, possibly the same adimensional distance from the center pixel of the windows to the wall of the Schlieren images. Implementing this approach for a viscous CFD analysis could show a much better match between the simulation and the experiment.
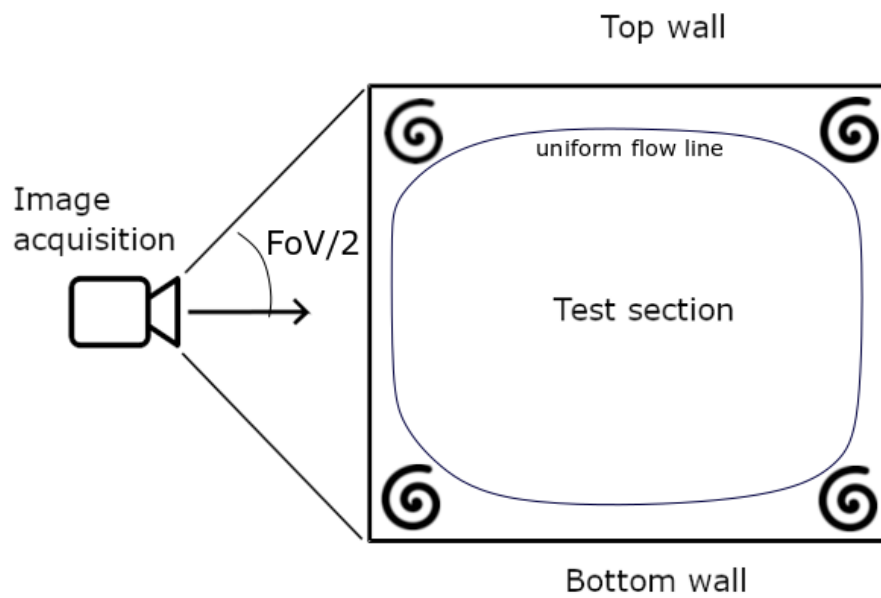
Figure 5.13: Simplified scheme showing how the Schlieren data on the top and bottom walls is influenced by the corner effects creating non uniform flow (not in scale)

Chapter 6

Conclusions

The need for a comprehensive validation of CFD software for NICFD is related to the realization of optimal designs for ORC expanders, which are efficient and cost-effective power generation systems from heat sources that can range from waste heat of combustion or renewable energies. In this thesis, the a first step towards a validatidation is taken by setting the basis for full validation procedures using experimental data.

The research questions of this work were:

- What are the predictive capabilities of the SU2 Fluid Dynamic Solver when simulating dense organic vapor flow expansions in highly non-ideal conditions?

- How can we determine the accuracy of a numerical prediction using experimental data? What experiment is more suited? Which SRQs can be used? How do we extract experimental data?

- What kind of simulations have to be performed? Can an Euler simulation be used for the UQ in the numerical framerwork or is viscosity influencing the results?

- Can we identify all of the error sources affecting the experimental results and quantify the uncertainties in the data extraction process and in the experimental campaign?

The research questions were answered by processing and using experimental data in order to achieve a number of key objectives throughout this Thesis:

- identification of all the error sources affecting measurements in superssonic organic vapor expansions in an empty nozzle;

- quantification of the total expanded uncertainties on the boundary conditions of the nozzle and the test section related variables;

- identification and analysis of flow features in the nozzle;

- development of a drift-proof steady state hybrid identification method which can be very useful when the conventional methods relying on very long testing times are not applicable;

- development of a Schlieren data extraction method and its tools for the correct extraction of the midplane and wall Mach fields, together with the evaluation of all the uncertainties in the post processing method and the total uncertainties on the extracted variables;

- proof of the flow symmetry in the ORCHID nozzle developing a tool capable of comparing opposite Mach lines in a nozzle with their relative uncertainties;

- evaluation the accuracy of the SU2 flow solver Euler simulation coupled with the Peng-Robinson equation of state together with variable specific heats in a supersonic expansion of the hexamethyldisiloxane in its non-ideal vapor state;

- identification of key parameters and effect that influence the accuracy of the numerical predictions, and

- analysis of the experimental campaign data acquisition procedures and optimization for better experimental results.

In particular, in Chapter 2, after analyzing the ORCHID facility set up and operation, steady state conditions of the flow in the test sections were identified for three different experiments. For the first two, a conventional approach was used while for the third process run a new hybrid approach was developed (presented in appendix A) and used to identify steady state conditions in smaller intervals of time. Once steady state conditions were known, all the error sources in the balance of plant, test section and Schlieren measurement chain were identified and the uncertainties, then, quantified.

It was then necessary to develop a method and the tools necessary to accurately extract data from the Schlieren images, more in particular the μ angle and, as a result, the Mach number in various axial coordinates of the nozzle. In Chapter 3 the Hough transform and its algorithm are explained in detail; furthermore the implemented line detection tools, using a classical discretized Hough transform together with a Canny edge detection algorithm, are introduced.

Chapter 4 proposes a Schlieren data processing method using 4 developed codes capable of verifying the flow symmetry in the nozzle, then evaluate the steady state condition of the flow and the minimum number of samples needed for the statistical convergence of the results, and finally extracting the Mach number on the midplane and on the nozzle's profiles. The developed tools are discussed in detail and represent an innovative way to apply the Hoguh transform for the extraction of Mach lines in a user-specified domain. Each extracted μ angle and Mach value has a total expanded uncertainty as well as a spatial uncertainty taking into account all the post processing uncertainties. It was shown how these uncertainty are strongly correlated to the quality of the Schlieren datasets and the scale factor. Furthermore, the uncertainty on the Mach number also depends on the local value of the Mach itself. When lines are detected on the nozzle walls, larger uncertainty values are found due to the uncertainty on the local wall angle of the nozzle. Typical values of Mach midplane uncertainties at the exit of the nozzle are approxmately 0.05 for zoomed-out good quality datasets, and 0.03 for datasets with smaller FOV (larger scale factor). In the Kernel region of the nozzle Mach number uncertainties are much smaller and range from 0.002 to 0.009.

Results on the nozzle profiles, on the other hand, have Mach number uncertainties ranging from 0.05 to 0.15 in the reflex and uniform flow regions of the nozzle. If large scale factor good quality Schlieren images are considered, the wall Mach number uncertainties inside the Kernel region, close to the throat, are very small: around 0.02 in average. This is due to the fact that at lower Mach numbers the uncertainties are shrinked significantly.

The Schlieren datasets are also analyzed to understand the flow feature that are visible from the Schlieren. At the end of the chapter, a refractive index analysis is used to evaluate the optimal FOV for Schlieren analysis.

Finally, in Chapter 5 the CFD analysis are presented and the experimental data extracted from the Schlieren images are used to assess the accuracy of the simulations. In order to better understand the accuracy of the SU2 Euler solutions, two different equations of state, namely the Ideal Gas and the Peng-Robinson, have been used for all the three process runs tested in the ORCHID. The Peng-Robinson model has been used in two different simulations, one with the assumption of constant specific heat (polytropic) and one with the specific heat function of the flow temperature (non polytropic). The outcome of the accuracy assessment shows that the most complicated model tested, the Peng-Robinson equation of state complemented with a 3rd order polynomial to estimate the specific heat is the most accurate model used in the analysis. It is capable of predicting the

thermophysical properties necessary for the flow solver to accurately predict the Mach number across the expansion for the two process runs close to the on design conditions of the nozzle. The other tested models are not capable of predicting the Mach field except for the PR.026 case, in the proximity of the throat, where all the simulations produce similar results. This result shows that when the compressibility factor of an expansion is close to one, the vapor behaves more like an ideal gas, thus more complex thermodynamic models tend to the IG solution.

The results presented in this work also show that the best simulation, the Peng-Robinson non polytropic, is not always capable of predicting correctly the Mach number in the nozzle. In particular, when the inlet conditions are close to the ones used to design the nozzle, the midplane Mach field is predicted with a high degree of accuracy, while when the inlet conditions are far away from the design one and the velocity of the flow is higher, a slight offset is present caused by small losses due to 3D effects and fluid viscosity. Furthermore, from the comparison of the Mach numbers between simulation and experiment on the wall it was possible to prove that Euler simulations may not be suitable to predict the Mach field on the nozzle's profiles due to the stronger effects of viscosity and vortices in proximity of the test section walls which cause a reduction in the local Mach number not captured by the 2D inviscid CFD analysis.

This work represents a fundamental first step towards an accurate validation of the main equations of state coupled with thermodynamic models that are or can be implemented in a CFD software such as SU2 for non ideal supersonic organic vapor flows. There are several different fluid models, some much more complicated than others, and assessing the validity of each model depending on the range of values of the compressibility factor Z or the fundamental derivative Γ in the expansion, allows CFD predictions with a known level of accuracy in order to optimize or design ORC expanders.

As mentioned in the introduction of this thesis, a full validation requires the numerical uncertainty analysis together with the experimental one. At the time of writing, Bills (2020) is working on the evaluation of the input uncertainty propagated through the numerical framework as well as the CFD grid uncertinty and numerical round-off error to finally proceed with the validation of SU2, thus completing the work presented in this thesis integrating the experimental and numerical uncertainties in a validation framework.

The numerical round off and CFD grid uncertainties are expected to be neglegible with respect to the uncertainty of the inputs in the simulations and the experiments, but a rigorus quantification is still required. The nozzle boundary condition expanded uncertainties are not the only input uncertainties in the simulations: the critical point parameters, the C_P equation and other fluid parameters also have an uncertainty associated to the determnistic value used in the simulations. All these input uncertainties must be propagated through the simulation to evaluate their uncertainty on the SRQ using random sampling methods, usually computationally intensive, in the input intervals such as the Latin hypercube sampling or the even faster Stochastic expansion methods for the numerical UQ.

6.1   Recommendations

In this section, a summary of different suggestions and future recommendations that been discussed throughout the thesis is presented for both the implemented line detection tools and the experimental campaign.

6.1.1   Line Detection Tools

At the time of writing, the line extraction tools results strongly depend on the level of experience that the user has with the codes. A document called **Schlieren Data Extraction Procedures** has been written, and is in constant update, with more suggestions and tutorials on how to use the codes to obtain otpimal extracted values from the Schlieren images. Many processes are already

automated in the codes, such as the optimization of the extracted lines length and quality, the identification of walls, the choices of using the throat or another point to identify the domain, the skip of black pixels if the image is not cut at the exit of the nozzle and other small details, but the process itself is not automated and each section must be run individually in order to correctly choose all the parameters. Once all the parameters are chosen, the whole code can be run. Automating a few key steps could improve the usability of the codes thus requiring less training on a new user.

Optimizing the entire codes is not hard, but it could require quite some time; for this reason, since the time of this thesis was limited, an automated parameter-choosing process was not implemented. In the following paragraph, suggestions on how to modify the codes are presented.
Considering the midplane line detection tool, the entire input sections, calibration, calculation, filtering and statistical quantities evaluation could be automated using a gradient based method in MATLAB called *fmincon*. The above mentioned sections are the ones that will give as an output the SRQ needed, which are the μ angle and/or the Mach number. It is recommended to choose one of these SRQs keeping in mind that the μ angle has a higher sensibility to changes in the expansion and its uncertainties are not influenced by the velocity of the flow. It must be kept in mind that the choice between the most appropriate SRQ does not only depend on which variable is more accurate, but also on which variable is more important on the final application of a validation: the Mach number plays an important role in the evaluation of the performance of an expander, thus even though the uncertainties are dilated by the value of the SRQ itself, using the Mach number as the main SRQ could still be the best choice. Once the SRQ is defined, the above mentioned sections of the program will become the non linear constraints of *fmincon*, the main body of the program will be the same one as it is now without the sections that will go in the constraint of the optimization. The objective function of the optimization could be

$$X = \sum \left(U_{SRQ} + U_{x,NRS} \right),$$

where U_{SRQ} is the total expanded uncertainty on the chosen SRQ. The output of the program gives optimal binarization parameters; it must be reminded that some fundamental steps such as image rotation, alignment between the Schlieren dataset and the calibration image, choice of walls, choice of throat detection method and so on must always be left to the user.

6.1.2 Experimental Campaign Set Up and Procedures for Non-Ideal Vapor Expansions Studies

There are many recommendations reguarding the experimental campaign set up and procedure that can significantly increase the quality of the experimental results; in the following list, a summary of what has been noticed to be important in the experiments is presented. It is important to point out that the experiments presented in this thesis as well as in Head (2020), are the very first of its kind since they are the first experimental campaigns performed on the ORCHID. Regarding the Schlieren acquisition:

- Marking the exact throat location in the nozzle TC with a light sensitive paint could significantly decrease the uncertainties in the NRS to almost zero. In the dataset used, the throat position had to be evaluated by the program since its position in pixels was unknown; marking the position of the throat in the Schlieren, on the other hand, makes the identification of the GpRS coordinate of the throat very easy and reduces the uncertainty significantly.

- Applying a filter in front of the camera can significantly increase the quality of the results: when large density gradients are captured in a Schlieren image, the camera set up can be optimized to either capture the Mach lines in the lower density section or the higher density section. Using a filter which reduces the amount of light entering the camera in the lower density regions, the camera can be set up to the new brighness gradient which is now significantly smaller if the filter is designed properly. When the brighness gradient is smaller, the camera can capture well the entire FOV reducing all Type A uncertainties in the Mach line extraction process as well as allowing the extraction of lines all the way to the throat.

Reguarding the balance of plant:

- When the nozzle test section is opened, it is recommended to wait at least 20 minutes to stabilize the temperatures and pressures when the WF loop is modified. The acquisition frequency of 1 Hz for all the key process variables of the ORCHID throughout the entire process run produced a sufficiently accurate description of the behaviour of the balance of plant, but when it comes to flow measurements in the TS this acquisition frequency has to be increased. In particular, when the test section is opened and the key variables have reached steady conditions (10 to 20 minutes after the opening of the valve), a higher frequency of acquisition for at least the nozzle boundary conditions is recommended. The acquisition frequency of the nozzle boundary conditions should be similar or slightly lower than the acquisition frequency of the TS measurements. Considering Schlieren data acquisition, it has been shown that acquisition frequencies between 25 and 60 Hz are optimal; the boundary conditions, as a consequence, should be acquired at a frequency about half of the Schlieren acquired frames per seconds

$$f_{acq} \approx \frac{1}{2} fps_{\text{Schlieren}}.$$

This way, the hybrid implemented steady state identification method can be applied in small intervals of time having still plenty of datapoints such that the statistical quantities have a low enough standard deviation of the mean. Furthermore, if the acquisition frequency of the BC is much lower than the Schlieren measurement chain's, the steady state (SS) acquisition time is increased unnecessarily since the SSI method needs a certain amount of points to calculate averages and standard deviations. As a result, in the time that is needed to obtain a minimum required dataset of BC values, the Schlieren dataset became much larger than it should be thus increasing the time of the post processing without a reason. Adopting similar acquisition frequencies between nozzle BCs and Schlieren images, the post processing of unnecessary data can be avoided .

  In conclusion, during the operating conditions of the nozzle, higher acquisition frequencies of the BCs allows a more accurate identification of the steady state intervals;

- It has been noticed, in the pre processing stage, that the nozzle moves quite a lot especially when high inlet pressures are used. The vibrations, as well as an overall upward shift, can cause difficulties in the alignment of the dataset. It is recommended to verify that the nozzle housing is capable of keeping the nozzle as still as possible during high speed expansion tests.

Appendix A

Steady State Analysis

A.1 Overview of the Hybrid Steady State Identification Method

The off-line SS identification method developed in this Thesis derives from the concepts of SSI presented by Cao & Rhinehart (1995), Flehmig & Marquardt (2006) and Crow *et al.* (1955). The method identifies a SS interval I_w by firstly finding an interval where the least squares second order polynomial fit $p_v(x)$ of the filtered data has a negligible slope in the considered interval (approximately smaller than the standard deviation σ_v of the data in the interval) and curvature for all the process variables under consideration

$$|\frac{\mathrm{d}p_v(x)}{\mathrm{d}x}|_{SS} \leq (\sigma_v) \quad ; \quad \frac{\mathrm{d}^2 p_v(x)}{\mathrm{d}x^2} \to 0. \tag{A.1}$$

Then an average of the ratio $\overline{G_v}$ of variances between a datapoint $v(x_i)$ and the mean in a window $\overline{v(w)}$, and two consecutive values in that window, is evaluated in forward moving windows.

$$G_1(i) = \frac{1}{N_s(w)} \sum_{i=1}^{N_s(w)} \left(v(x_i) - \overline{v(w)} \right)$$

$$G_2(i) = \frac{1}{N_s(w) - 1} \sum_{i=1}^{N_s(w)} \left(v(x_i) - v(x_i + 1) \right)$$

The interval where this mean ratio $\overline{G_v}$ is smaller or equal to one plus three times the standard deviation is selected:

$$\overline{G_v(w)} = \frac{1}{N_s(w)} \sum_{i=1}^{N_s(w)} \left(\frac{G_1(i)}{G_2(i)} \right) - 3(\sigma_v). \tag{A.2}$$

$$\overline{G_v(w)} \leq 1. \tag{A.3}$$

At this point the the identified interval I_w should verify steady state, but another verification to ensure that the variance of the results is not too large. The identified interval is split into two sub-intervals

$$I(w) = I_{w-1/2} + I_{w+1/2}$$

where means and standard deviations are computed for each process variable v under evaluation:

$$\overline{v_{w-1/2}} = \frac{1}{N_s(w)/2} \sum_{i=1}^{N_s(w)/2} v(x_i)$$

$$\sigma_{vw-1/2} = \sqrt{\frac{1}{N_s(w)/2 - 1} \sum_{i=1}^{N_s(w)/2} \left(v(x_i) - \overline{v_{w-1/2}} \right)}$$

$$\overline{v_{w+1/2}} = \frac{1}{N_s(w)/2} \sum_{i=N_s/2}^{N_s(w)} v(x_i)$$

$$\sigma_{vw+1/2} = \sqrt{\frac{1}{N_s(w)/2 - 1} \sum_{i=N_s(w)/2}^{N_s(w)} \left(v(x_i) - \overline{v_{w+1/2}}\right)}.$$

Finally the constraint in equation A.4 proves that the variance of the results is sufficiently constant in the steady state interval

$$\max[\overline{v_{w-1/2}} + \sigma_{vw-1/2}, \overline{v_{w+1/2}} + \sigma_{vw+1/2}] - \min[\overline{v_{w-1/2}} - \sigma_{vw-1/2}, \overline{v_{w+1/2}} - \sigma_{vw+1/2}] \leq 3(\sigma_v) \quad \text{(A.4)}$$

An interval verifying all the constraints of this analysis can be considered to be in steady state conditions; furthermore this developed method ensures that no drift is present in the steady state interval.

A.2   Application of the SSI Method to PR.026

The developed off-line SSI method has been applied to the experiment PR.026-NT001 to find a SS state interval in the small amount of time in which the nozzle test section was opened. The number of points used for the evaluation of the statistical quantities such as variances and means in each step is not ideal, meaning that a larger number of points is recommended. The present analysis is performed on a lower than recommended number of points because of the low sampling frequency of the boundary conditions (1 Hz) was coupled with a much higher frequency of acquisition of the Schlieren images (24 Hz), thus only a few seconds of steady state is sufficient for the convergence of the statistical quantities in the Schlieren post processing tools. The problem arises when, even if a few seconds are sufficient for the Schlieren data convergence, they are not sufficient for the convergence of the BCs acquisitions. Thus, it is recommended to acquire the nozzle's test section parameters at a similar samplig rate than the Schlieren measurement chain.

In Fig. A.1 the interval conidered for the SSI is shown. After filtering the outliers, the polynomial fit of the data is performed in three sub-intervals as shown in Fig. A.2. It is clear how the second interval I_2 is the one containing the steady state since the constraints in Eqn. A.1 are verified for all the considered variables; all the second derivative values are neglegible:

$$|\frac{\mathrm{d}^2 p_v(x)}{\mathrm{d}x^2}| < 5 \times 10^{-5}.$$

The first derivative coefficients range from 0.0023 to 0.0066 in the chosen interval, and are always about one order of magnitude smaller than the standard deviation of the data:

$$|\frac{\mathrm{d}p_v(x)}{\mathrm{d}x}|_{I_2} \approx 0.1\sigma_v.$$

The analysis interval is then reduced to more or less the second sub-interval which verified the constraints in Eqn. A.1. In this interval the parameter G_v is evaluated according to Eqn. A.2 and the results are presented in Fig. A.3 where it is possible to identify which sub-intervals verify the constraint in Eqn. A.3. At this point, the sub-intervals chosen are the ones from 3 to 6 and knowing the spacing between the intervals and the exact time in which the original interval started, it is possible to derive the steady state final interval:

$$13:36:28 \quad - \quad 13:36:48.$$

In this interval, the final constraint in Eqn. A.4 is then verified for the evaporator pressure, back pressure, inlet temperature and flow rate. The result of this analysis is shown in Fig. A.4, while the averages and standard deviations have been already shown in Tab. 2.5.
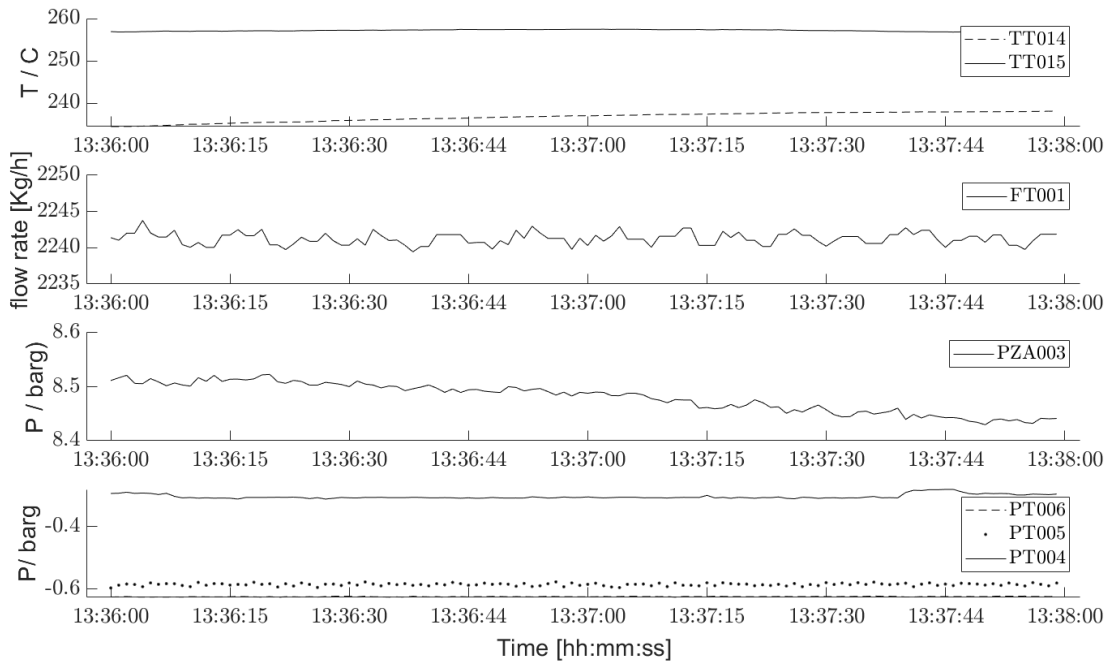
Figure A.1: Overview of the considered interval where the steady state could be identified
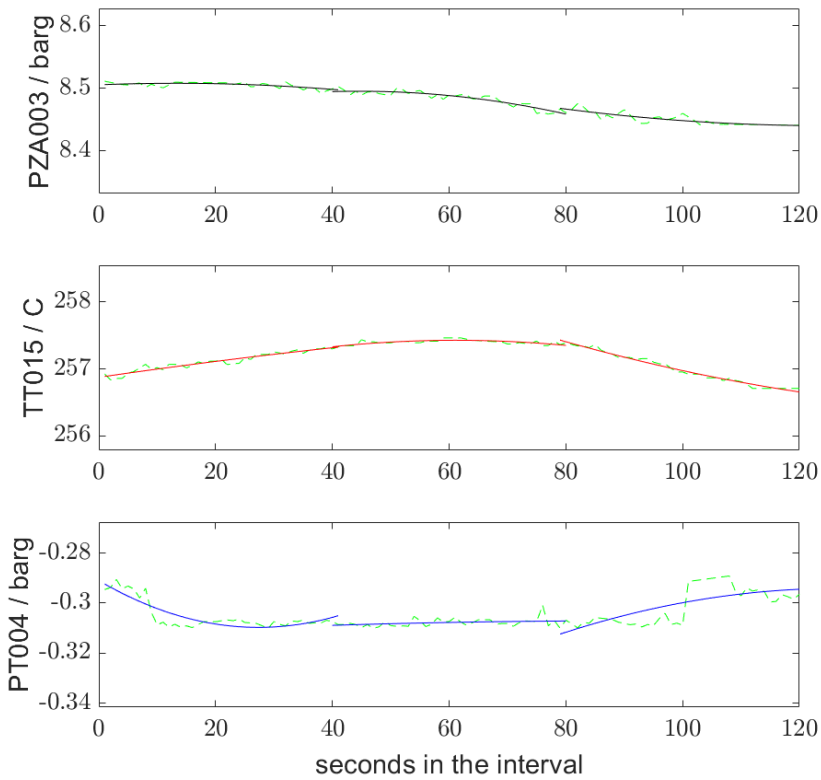

Figure A.2: Fit of the filtered data for the nozzle's boundary conditions. The flow rate is constant throughout the entire intreval, as a consequence it is not shown here.
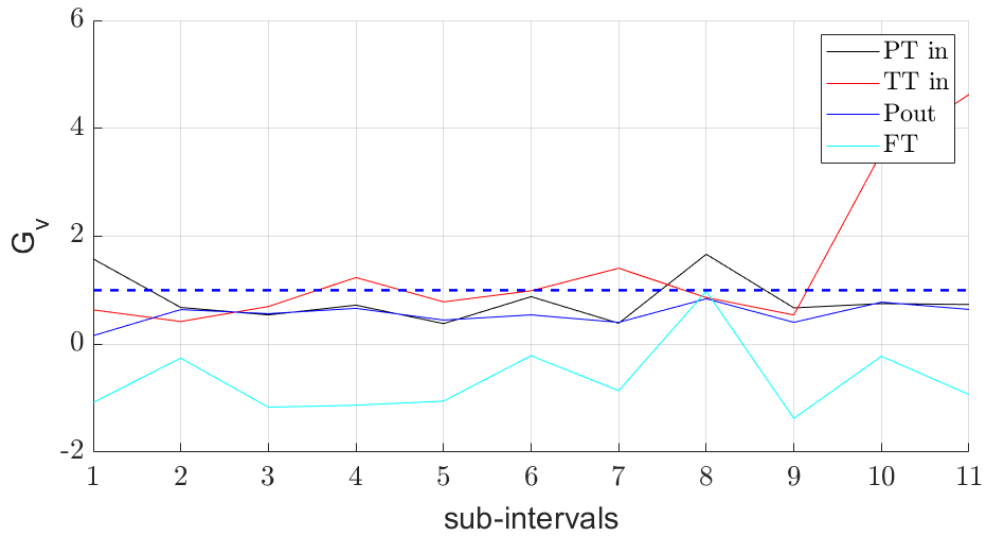
Figure A.3: G_v ratio as a function of the intervals considered in the reduced domain. The sub-intervals from two to six are steady state with zero drift.
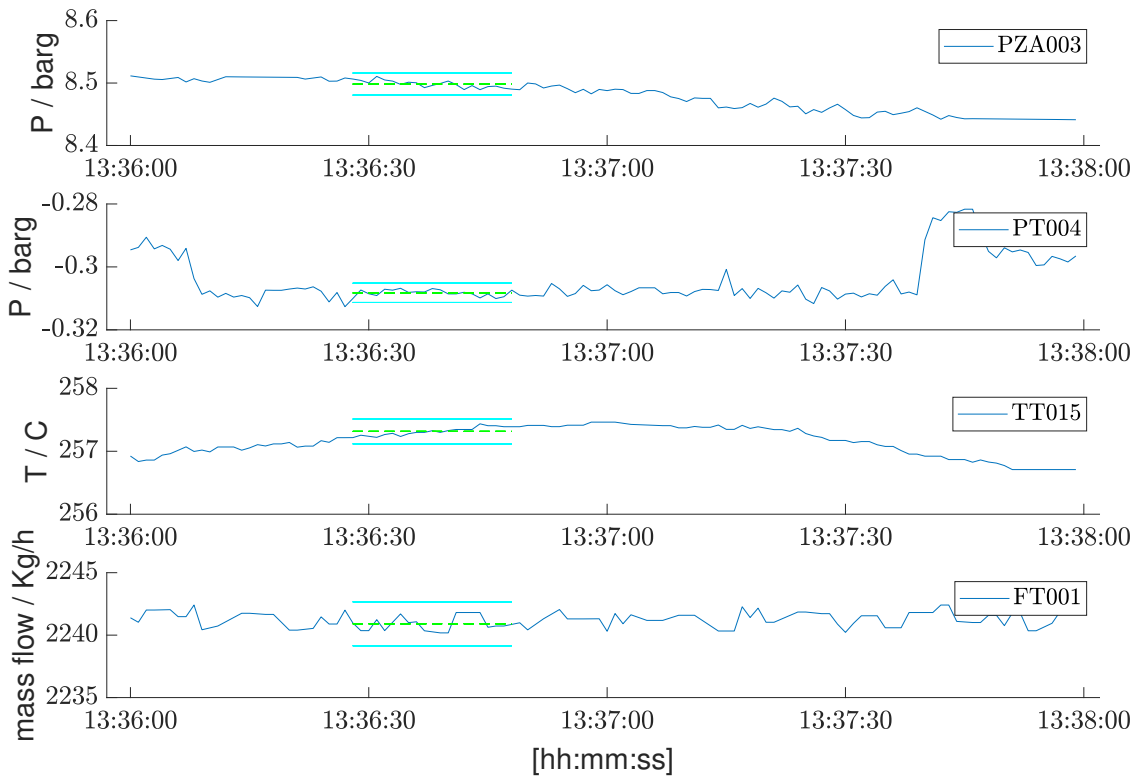

Figure A.4: Identified steady state interval for PR.026 nozzle boundary conditions: the solid cyan lines represent the three sigma limits of the average in the steady state interval, while the green dashed lines are the average values.

Appendix B

Line Detection Tool Steps and Code Nuances

A step by step tutorial on how to correctly use the line extraction tool is presented in this Appendix. Let us consider a zoomed-in Schlieren image of the nozzle since this configuration is the overall best one to validate a CFD software for non ideal applications since it is possible to resolve the domain closer to the throat, where the non ideal effects of the fluid are much more significant. In the following sections, PR26 is considered: it goes without saying that the values assigned to the input parameters are related to the considered dataset but having numerical examples close to the parameter explanation can be extremely useful to quickly use the developed tools in an optimal way.

B.1   Midplane Line Detection Tool

PROCEDURE:

Define the expansion: estimate the angles that are expected at the beginning, middle and end of the line extraction domain.

- estimated_machangle_start = 29;

- estimated_machangle_middle = 50;

- estimated_machangle_end = 75;

- xx_f = [0 , 0.5 , 1]';

First run to set up the binarization parameters[INPUT 1]: assume there is no rotation in the data, take just a few dataset images at first and assume a threshold. Those values are already optimal for PR26.

- rotation_adjustment = 0 ;

- Nimg = (first frame):1:10;

- threshold = [0.01, 0.09];   [low,high]: increase low to avoid detecting small gradients, decrease high value to detect smaller gradients;

- gauss_noise_filter = 2.55;   increase to reduce noise: if the binarization and edged image has too many wobbly lines, increase this value;

- brightness_data = 70;   used to increase brightness if the image is too dark;

- threshold_imgad = NaN;   [low, high]: adjust contrast: increase higher threshold to get white out of light grey area. Use NaN to use the automatic adjustment - Recommended;

Working space parameters [INPUT 2]:

- offset = 18;   [pixels] increment offset to move the midplane up, decrement to move the midplane down in the image. If the offset is larger than 10 or 20 pixels, an automatic translation of the images is performed to center the nozzle in the image;

- C_end = 0.76;   percentage of the image where the program has to stop acquiring lines;
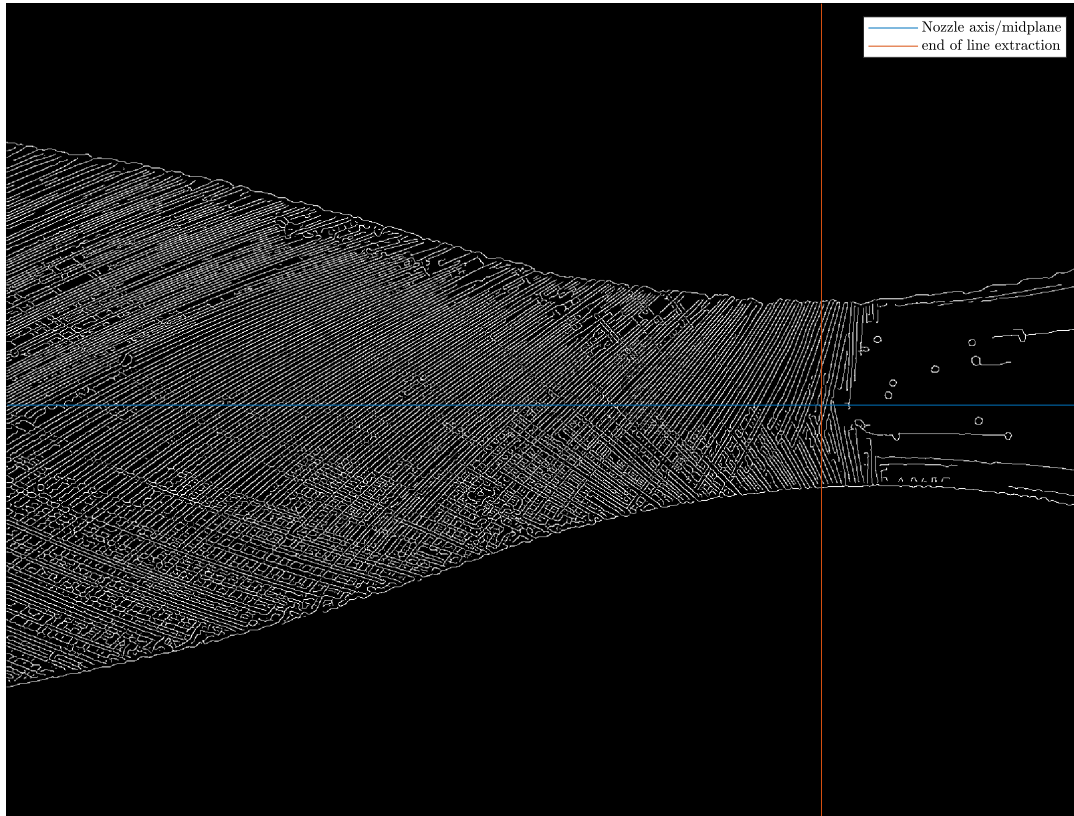
Figure B.1:   Binarized image (PR26)

Calibration 1: in this section, the throat will be used so the procedure applies to the method which uses the throat to calculate the scale factor and define the NRS.

- USE_THROAT = 1;

- throat_mm = 6.66 ;   nozzle's throat dimensions in millimeters;

- U_throatmm = 0.5*0.1;   uncertainty in the throat height in millimeters;

- Calibr_start_domain = 0.03 ;   percentage of the image where the wall will start being acquired;

- Calibr_end_domain = 0.95;

- threshold_imbinarize = 0.1;   is the relative brightness level under which grey becomes white. Lower threshold values correspond to less details in B& W image. If the image is all white the value must be increased;

Figure B.2: Extracted walls in the calibration image (PR26)

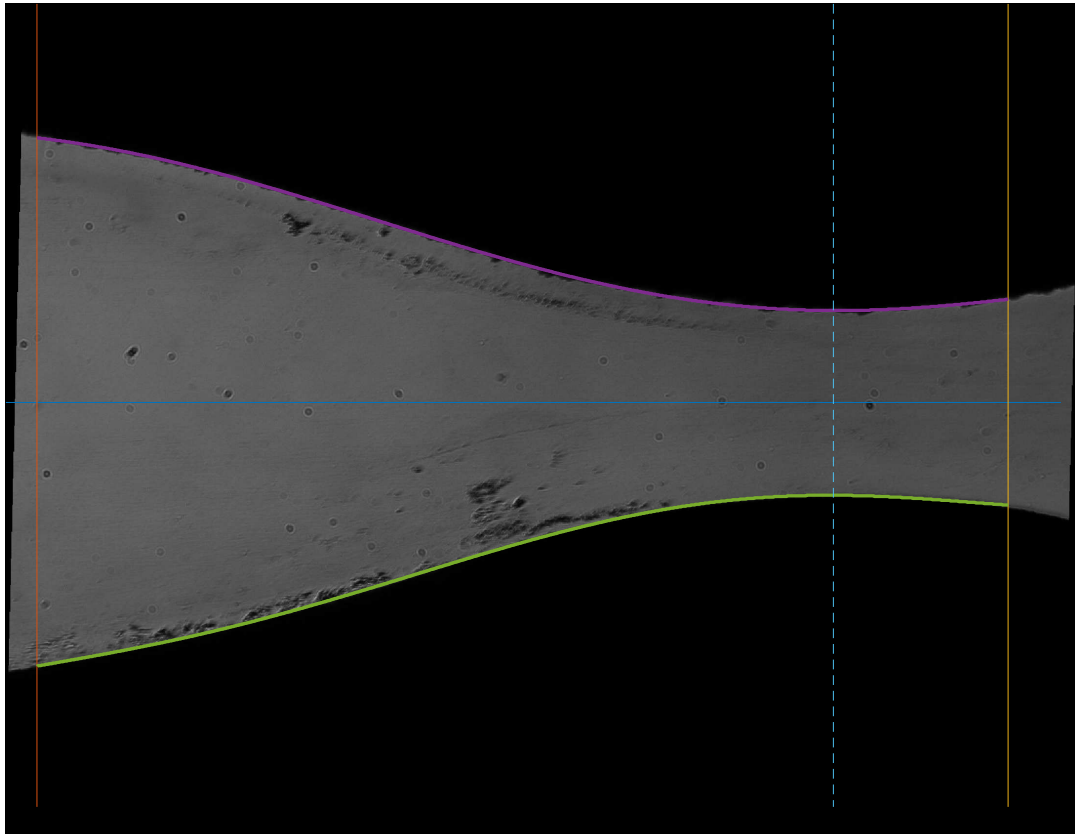- poly_order_walls = 5;   order of the polynomial fit of the walls. Usually between 3 and 6;

Calibration 2:

- threshold_schlieren = 0.04;   is the same binarization parameter as the threshold_imbinarize but for the Schlieren dataset instead of the calibration image;

- C_schlieren_end_domain = 0.88;   percentage of the image where the acquisition of the walls in the Schlieren data will stop ;

- poly_order_walls_schlieren = 5;

Verifications and adjustments: verify that the quality of the acquired walls is optimal, that the calibration and Schlieren walls match and that the binarization parameters are optimal.

re-run: the program will output the rotation of the Schlieren images in the dataset: that value must be used to update the rotation adjustment parameter. Furthermore, further rotation adjustments can be made to both the calibration and the dataset to make the extracted walls match perfectly. Since the working space parameters have been already optimized in the INPUT 2 section, now the user has to go back and acquire the entire dataset:
Nimg = (first frame):1:total;
rotation_adjustment = 1.4 ;   [degrees];

re-run: run again Input 2 and the two calibration phases.
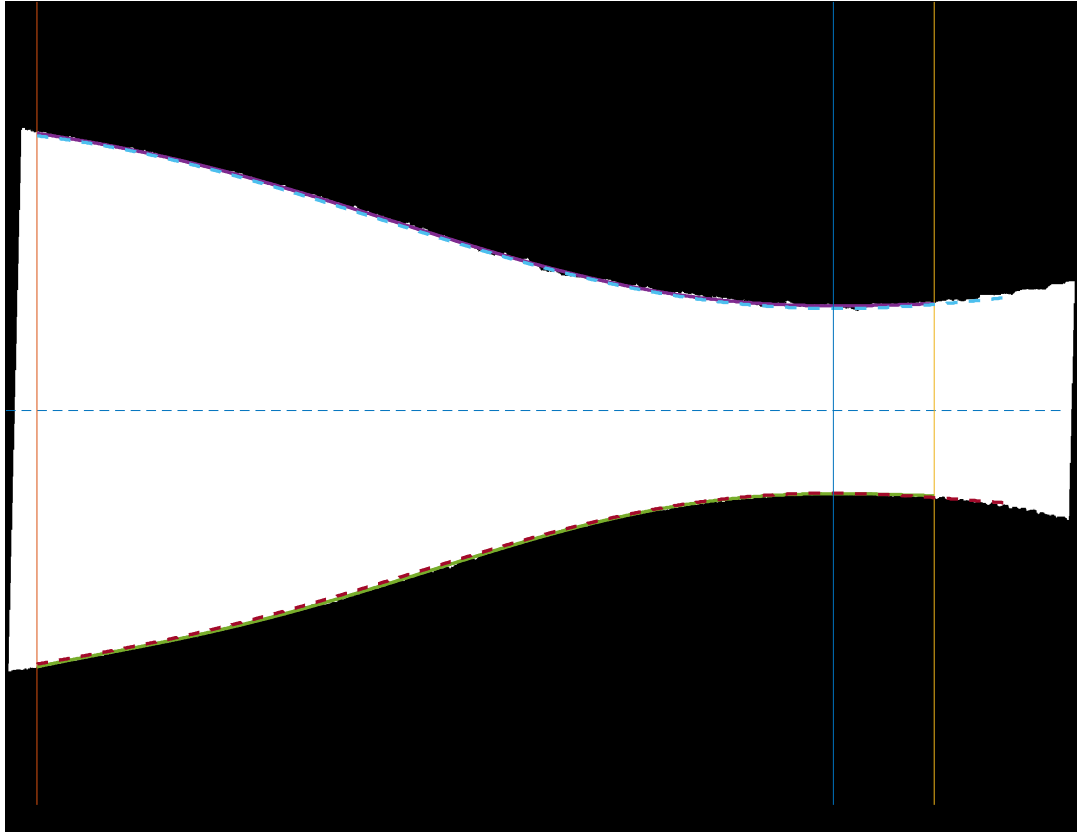
Figure B.3:   Optimal results from the calibration phases (PR.026)
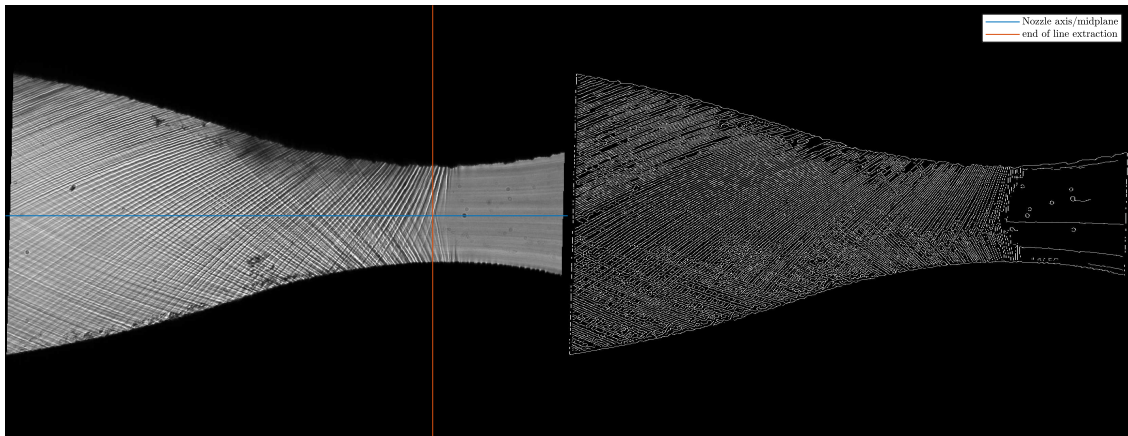
Figure B.4:   Correctly binarized and rotated Schlieren image (PR26)

Input 3: Discretize the domain by choosing an appropriate number of intervals. It is fundamental to try to keep the windows as square as possible, possibly with the base slightly larger than the height and not the opposite.

- Initial_dx_offset = 0;   number of pixels to skip from the beginning of the image before starting to mesh the domain;

- intervals = 38;

- window_start = 1;   first interrogation window in which lines are saved;

- window_finish = intervals;   last interrogation window in which lines are saved;

- upp_max = 38;   indication of the maximum semi-height of the windows along the midplane, above the axis;

- low_max = 38;   symmetric windows along the chosen axis are recommended, thus upp_max == low_max ;

- dx_min = 42;   minimum width of the interrogation windows. lowering this value keeping all the others constant will increase the difference in size between the larger windows and the smaller closer to the throat. It is recommended to not go below 35-40 pixels of minimum width;

- Hough_theta_step = 0.2 ;   hough transform resolution [degrees];

- estimated_min_mu = 30 ;   [deg] current simulation minimum estimated angle (do NOT be conservative);

- C0 = sqrt(2) ;   initial factor for max length lines to be identified;

- fill_gap_lines = 1;   initial pixel skip factor;

- max_pixel_skip = 3;   maximum accepted pixel skip factor;

Calculation: it is important to check the command window for errors. There are three types of errors: fatal, serious and minor. If a <u>fatal error</u> is encountered either the program did not find any line in the first window and first frame or the program does not find lines in two or more consecutive windows. The result is a full stop of the program. All the previous steps must be optimized; likely solutions for this include:

- optimize binarization parameters to increase lines quality;

- change discretization if possible: increase window size and verify that the base of the window is always larger than the height;

- increase initial_dx_offset if the first window is not good due to absence of lines;

- increase maximum pixel skip factor considering that higher values can increase chances of detecting casual collinear points which do not correspond to lines (fake lines);

- consider skipping the first frame changing the Nimg vector.

If a <u>serious error</u> is encountered, the program will keep working but warns that in the first frame, a lines has not been found in an interrogation window which is not the first one. It is possible to encounter more than one serious error if the empty windows are not adjacent. If more than one or two serious error are encountered, it is strongly recommended to restart the program following the checklist previously presented for the fatal error. A good simulation should not have any serious error, which will only occur on the first frame. To fully understand the cause of these errors, the local check section <u>Checking data in a frame</u> can be very helpful: in order to use this, simply select the first frame $x = 1$ and plot the windows with the succesfully extracted lines inside.

<u>Minor errors</u> warn the user that in a specific window k and frame f the Mach line verifying the constraints imposed was not detected. Minor errors will be present most of the times: it is important to verify that the number of minor errors is not too large that could affect the statystical quantities

and thus the results. This can be easily done by checking the information_lost vector which contains the number of data missing from every window in the domain. When locations with a large number of information lost are found, it is recommended to use the Checking data in a location section to understand why lines are rarely found in that position. To solve the absence of lines, the only options available are the modification of the mesh and the dataset binarization parameters. If some windows have problems that cannot be solved, it is possible to remove them manually later on from the results.

Results and statystics: this section, after filtering outliers, calculates all the uncertainties and average values on the μ angle and M number in all the k- locations of the domain.

Results 1: translating results from the GpRS to the NRS is a fundamental step in the line extraction process. It is recommended to check the value of the total uncertainty coming from the NRS identification by verifying that this uncertainty is much smaller than the discretization one. An example is presented in figure B.5, where it is clear that the uncertainty coming from the scale factor and the throat position has a very low influence on the total position uncertainty, which derives mostly from the discretization of the domain in windows .
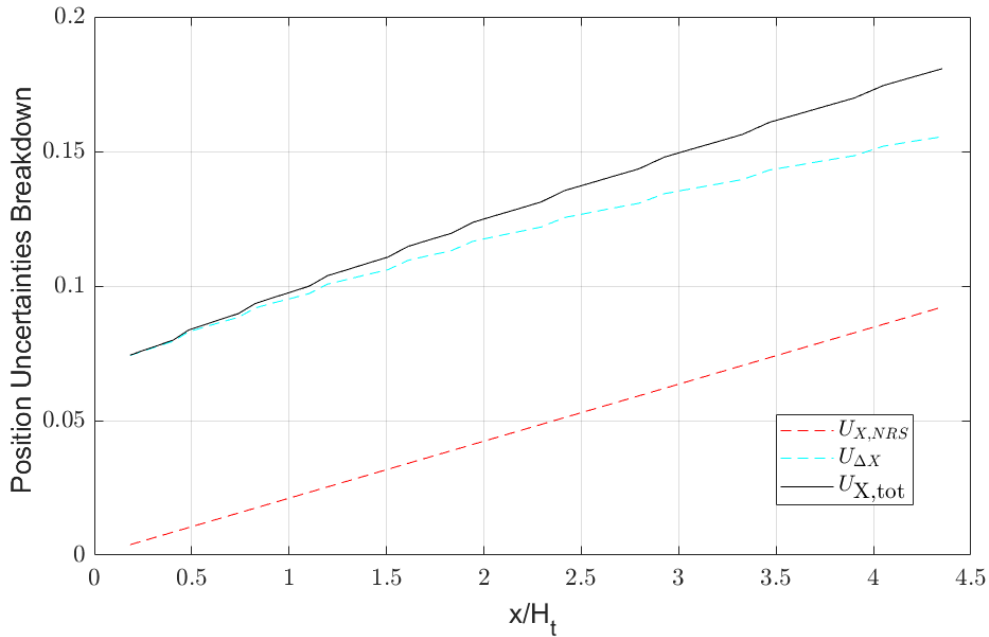
Figure B.5:   Adimensional position uncertainties with respect to the center pixel adimensional location $x_{cp}(k)/H_t$ (PR.026)

Save / Load: the variables are saved only if simulation_save_results is equal to 1, and previous results are loaded only if LOAD_PREVIOUS_RESULTS is 1. It is important to check the name of the mat file that will be saved and/or loaded.

Final plots: superimposition of the average detected lines on a Schlieren image, Mach number and Mach angle plotted in the adimensional domain x/H_t, uncertainties breakdown and more.

B.2 General Tips for the Line Detection Programs

Flow Symmetry Assessment

The program will compare opposite Mach lines at increasing distances from the midplane, at a specified adimensional axial coordinate. When a Schlieren image is binarized, not always it is possible to recognize both Mach lines: more frequently, some areas will have only one predominant type of lines. It is extemely important to evaluate the flow symmetry in positions where opposite lines, above and below the midplane, are present. The program, by default, tries to detect the predominant lines on top and bottom half of the nozzle but it is possible to switch the orientation of the angles, detecting the complementary Mach angle, if the uncommon condition of being able to detect the complementary Mach lines is presented. To switch angles, change the value of the flag to one: Switch_angles = 1.

If lines are not found, consider increasing the pixel skip factor, but an accurate visual check of the matrix mi_angle_UP(time, locations) and mi_angle_DOWN(time, locations) must be done to understand if "fake" lines are detected by verifying that the angles in those matrices are close to the expected value.

Line detection tool - Statistical convergence

It goes without saying that this program is the most computationally intensive tool developed. Before the complete analysis, it is recommended to set the correct binarization and discretization parameters considering only just a few images and looking at the results of the first few input sections without running the analysis. Once the parameters are all set, the complete analysis can be done on the entire dataset. If a dataset has more than 2000 images, the program could require a very large amount of RAM; furthermore, out of experience, even datasets which are poor in quality achieve statistical convergence after a bit over 1000 images: a dataset that requires more than this many images to achieve convergence is probably too poor in quality to be used for a comparison with a simulation or is probaly not in steady state. Good dataset achieve statistical convergence in less than 500 images; if the brightness levels in the dataset are very constant, then about a few hundred images is the threshold to ensure a very good level of accuracy in the statistical quantities evaluation. It is important to point out that if oscillations are present in the final plots of the program after 1000 images and convergence seems that it has not been achieved yet due to these oscillations, the dataset is probably not in steady state. In conclusion, the program is able to capture the drift of the boundary conditions. In Fig. B.6 it is possible to notice that the standard deviation on the μ angle for PR.026 considering a much larger interval than the identified steady state one oscillates strongly: these changes in the standard deviation after one thousand images does not happen when a steady state dataset is analyzed.

Wall Line Detection Program

Most of the recommendations and constraints have already been discussed in the main body of the thesis. This section presents solution to problems that can occur when running the *Wall line detection program*. When, usally the first times running the program on a new dataset, lines are extracted on both walls or on a user-chosen wal which is not ideal, the program could slow down in the extraction process to the point that it is best to stop the program while running the CALCU-LATION section and change the input parameters. This situation is very easy to recognize: when running the programs, it is always stongly recommended to check the command window constantly to gather informations reguarding the program status. When the CALCULATION sections are running, it is extremely common to receive now and then some minor error messages, informing the user that a specific line was not extracted because it did not meet the requirements imposed by the user. If no message appears after a minute of calculation, it is likely that the "slow calcu-lation" condition has been encountered. After stopping the program, it is recommended to check the structure LINES1(time, location) and LINES2(time, location) in order to understand where
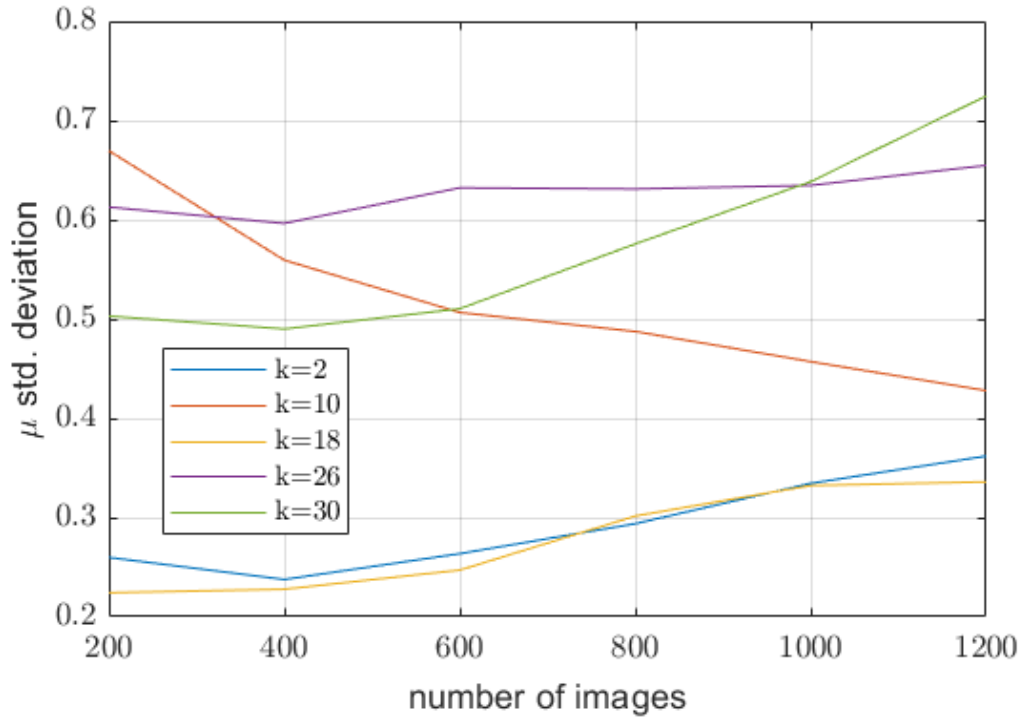
Figure B.6:   Statystical convergence analysis on a non-steady state dataset: standard deviation on the μ angle - (PR.026)

the program stopped and how many calculation it performed. An average calculation time for the wall line extraction using an Intel i7 8750H (2.21GHz nominal) is about 15-20 lines every second, which correspond to 15-20 cells in the LINES structures. If checking the LINES structures one finds many empty cells (showing 1x0) then again the input parameters need to be changed. It is usually recommended to check both LINES structures in order to identify which ones is containing many empty cells and then select the best wall in order to perform calculations only on that one, selecting, for example, BEST_WALL = 'lower'.

Bibliography

AGARD 1994 Quality assessment for wind tunnel testing. *Tech. Rep.*.

AIAA 1999 Assessment of experimental uncertainty with application to wind tunnel testing. *Tech. Rep.*.

AMERICAN SOCIETY OF MECHANICAL ENGINEERS (ASME) 2009 Standard for Verification and Validation in Computational Fluid Dynamics and Heat Transfer. *Tech. Rep.* V&V20-2009. ASME.

ANAND, NITISH 2016 Supersonic turbine design using method of characteristics. Master's thesis.

BECKER, R. 1922 Impact Waves and Detonation. *Zeitschrift für Physik* **8**, 381.

BILLS, L. 2020 Validation of the SU2 flow solver for classical NICFD. Master's thesis.

BORN, M. & WOLF, E. 2003 *Principles of Optics*, seventh extended edn. Cambridge University Press.

CAO, S. & RHINEHART, R. R. 1995 An efficient method for on-line identification of steady-state. *J. Proc. Cont.* **5** (6), 363–374.

CASATI, E., VITALE, S., PINI, M., PERSICO, G. & COLONNA, P. 2014 Centrifugal turbines for mini-Organic Rankine cycle power systems. *Journal of Engineering Gas Turbines and Power* **136** (12), 122607.

CELIK, I. B., GHIA, U., ROACHE, P. J., FREITAS, C. J., COLEMAN, H. & RAAD, P. E. 2008 Procedure for estimation and reporting of uncertainty due to discretization in CFD applications. *Journal of Fluids Engineering* **130** (7).

COLEMAN, H.W. & STEELE, W.G. 2009 *Experimentation, Validation, and Uncertainty Analysis for Engineers*.

COLEMAN, H. W. & STERN, F. 1997 Uncertainties and CFD Code Validation. *Journal of Fluids Engineering* **119** (4), 795 – 803, (Also "Discussion and Authors' Closure," Vol. 120, Sept. 1998, pp. 635–636.).

CROW, E. L., DAVIS, F. A. & MAXFIELD, M. W. 1955 *Statistics Manual*. Dover Publications.

DIJKSHOORN 2020 Simulation of two dimensional steady state boundary layer effects applied to non-ideal gas flows. Master's thesis.

DUDA, R. O. & HART, P. E. 1972 Use of the hough transformation to detect lines and curves in pictures. *Graph image process* .

DUHEM, P. 1909 On the propagation of shock waves in fluids. *Z. Phys. Chem* **69**, 169–186.

EÇA, L., VAZ, G. & HOEKSTRA, M. 2010 Code Verification, Solution Verification and Validation in RANS Solvers. In *ASME 2010 29th International Conference on Ocean, Offshore and Arctic Engineering*, pp. 597–605.

ECONOMON, T. D., PALACIOS, F., COPELAND, S. R., LUKACZYK, T. W. & ALONSO, J. J. 2015 SU2: An open-source suite for multiphysics simulation and design. *AIAA Journal* **54** (3), 828–846.

EKLUND, D. R., ROMERO, V.J., MEHTA, U. B., PEARCE, J.A. & KEIM, NICHOLAS S. 2016 Simulation credibility advances in verification, validation, and uncertainty quantification. *Tech. Rep.*. Ames Research Center Moffett Field, California.

ERCOFTAC 2016 Special interest groupls.

FLEHMIG, F. & MARQUARDT, W. 2006 Detection of multivariable trends in measured process quantities. *Journal of process control* .

GOLDSTEIN, R. & KUEHN, T. H. 1983 *Optical systems for flow measurement - shadowgraph, schlieren , and interferometric techniques. Chap. 8 of Fluid Mechanics Measurements*. Springer-Verlag, Berlin.

GORI, G., ZOCCA, M., CAMMI, G., SPINELLI, A., CONGEDO, P. M. & GUARDONE, A. 2020 Accuracy assessment of the non-ideal computational fluid dynamics model for siloxane MDM from the open-source SU2 suite. *European Journal of Mechanics - B/Fluids* **79**, 109–120.

GORI, G., ZOCCA, M., CAMMI, G., SPINELLI, A. & GUARDONE, A. 2017 Experimental assessment of the open-source su2 cfd suite for orc applications. *Energy Procedia* **129**, 256 – 263, 4th International Seminar on ORC Power Systems September 13-15th 2017.

GUARDONE, ALBERTO, COLONNA, PIERO, CASATI, EMILIANO & RINALDI, ENRICO 2014 Non-classical gas dynamics of vapour mixtures. *Journal of Fluid Mechanics* **741**, 681–701.

GUARDONE, A., SPINELLI, A. & DOSSENA, V. 2013 Influence of molecular complexity on nozzle design for an organic vapor wind tunnel. *J. Eng. Gas Turb. Power* **135** (4), 042307.

HASSELMANN, K., REINKER, F., WIESCHE, S., KENIG, E. Y., DUBBERKE, F. & VRABEC, J. 2014 Performance Predictions of Axial Turbines for Organic Rankine Cycle (ORC) Applications Based on Measurements of the Flow Through Two-Dimensional Cascades of Blades. In *Proceedings of the ASME 2014 Power Conference*.

HAYES, W. D. 1958 The basic theory of gasdynamic discontinuities. In *Fundamentals of gasdynamics. Vol. 2*. Princeton University Press.

HEAD, A., DE SERVI, C., CASATI, E., PINI, M. & COLONNA, P. 2016 Preliminary design of the ORCHID: A facility for studying non-ideal compressible fluid dynamics and testing ORC expanders. In *ASME Turbo Expo*, - GT2016-56103, p. 14.

HEAD, A. J. 2020 Novel experiments for the investigation of non-ideal compressible fluid dynamics: The ORCHID and first results of optical measurements. PhD thesis.

HEAD, A. J., IYER, S., DE SERVI, C. & PINI, M. 2017 Towards the validation of a CFD solver for non-ideal compressible flows. *Energy Procedia* **129** (Supplement C), 240 – 247, 4th International Seminar on ORC Power Systems September 13-15th 2017. Pg.

INSTRUMENTS, TEXAS 2013 *ADC Performance Parameters*.

ISO 1993 *Guide to the Expression of Uncertainty in Measurement*. ISO, Geneva, 1993. Corrected and reprinted, 1995.

JIANG, T., CHEN, B., HE, X. & STUART, P. 2003 Application of steady-state detection method based on wavelet transform. *Computers and Chemical Engineering* **27** (4), 569 – 578.

KIM, M., YOON, SEOK H., DOMANSKI, PIOTR A. & PAYNE, WILLIAM V. 2008 Design of a steady-state detector for fault detection and diagnosis of a residential air conditioner. *International journal of refrigeration* pp. 790–799.

LANDAU, L.D. 1942 On shock waves. *J. Phys. USSR* **6**, 229–230.

LIU, YANG, LU, YUTONG, WANG, YUEQING, SUN, DONG, DENG, LIANG, WANG, FANG & LEI, YAN 2019 A cnn-based shock detection method in flow visualization. *Computers & Fluids* **184**, 1 − 9.

LO, R. & TSAI, W. 1995 Gray-scale hough transform for thick line detection in gray-scale images. *Pattern Recognition Vol 28 n.5* .

MAINI, R. & AGGARWAL, H. 2009 Study and comparison of various image edge detection techniques. *International Journal of Image Processing (IJIP)* .

MERZKIRCH, W. 1987 *Flow Visualization*. Academic Press.

OBERKAMPF, W. L & ROY, C. J. 2010 *Verification and Validation in Scientific Computing*. Cambridge University Press.

OBERKAMPF, W. L. & TRUCANO, T. G. 2002 Verification and Validation in Computational Fluid Dynamics. *Prog. in Aerosp. Sciences* **38** (3), 209–272.

PENG, D.Y. & ROBINSON, D.B. 1976 A new two constant equation of state. In *Ind. Eng. Chem. Fundam.*.

JOURNAL OF PHYSICS: CONFERENCE SERIES, IOP PUBLISHING, ed. 2017 *Proceedings of the NICFD 2016 Seminar, 1st International Seminar on Non-Ideal Compressible-Fluid Dynamics for Propulsion & Power, vol. 821*.

PINI, M., VITALE, S., COLONNA, P., GORI, G., GUARDONE, A., ECONOMON, T., ALONSO, J.J. & PALACIOS, E. 2017 SU2: the open-source software for non-ideal compressible flows. In *International Seminar on Non-Ideal Compressible-Fluid Dynamics for Propulsion & Power*.

POPE, A. 1961 Wind Tunnel Calibration Techniques. *Tech. Rep.*. NATO.

REINKER, F., KENIG, E. Y., PASSMAN, M. & AUS DER WIESCHE, S. 2017 Closed loop organic wind tunnel (clowt): Design, components and control system. In *ASME ORC2017 - 4ᵗʰ International Seminar on ORC Power Systems - Milan 13 -15 september*, pp. 200–207.

RHINEHART, R. 2013 Automated steady and transient state identification in noisy processes. *Proceedings of the American Control Conference* .

ROACHE, P. J 2009 *Fundamentals of verification and validation*. Hermosa publ.

ROMERO, V. 2011 Comparison of a pragmatic and versatile real space model validation framework against several other frameworks. In *Proceedings of ASME*.

ROMERO, V. 2015 The real space model validation approach as a unifying extended hybrid of the ASME vv10 and vv20 approaches. In *Proceedings of ASME 2015*.

ROMERO, V., LUKETA, A. & SHERMAN, M. 2010 Application of a versatile real space validation methodology to a fire model. *Journal of Thermodynamics and Heat Transfer* .

ROY, C. & OBERKAMPF, W. 2010 A complete framework for verification, validation, and uncertainty quantification in scientific computing (invited). In *Aerospace Sciences Meetings*, p. 124. AIAA.

SETTLES, G. S. 2001 *Schlieren and Shadowgraph Techniques: Visualizing Phenomena in Transparent Media*. Springer-Verlag Berlin Heidelberg.

SHEN, J. 2019 Integrated supersonic wind tunnel nozzle. *Chinese Journal of Aeronautics* .

SOAVE, G. 1972 Equilibrium constants from a modified redlich–kwong equation of state. *Chem. Eng. Sci.* .

SPINELLI, A., CAMMI, G., GALLARINI, S., ZOCCA, M., COZZI, F., GAETANI, P., DOSSENA, V. & GUARDONE, A. 2018 Experimental evidence of non-ideal compressible effects in expanding flow of a high molecular complexity vapor. *Experiments in Fluids* **59** (8), 126.

SPINELLI, A., COZZI, F., DOSSENA, V., GAETANI, P., ZOCCA, M. & GUARDONE, A. 2016 Experimental investigation of a non-ideal expansion flow of siloxane vapor MDM. In *ASME Turbo Expo 2016* .

SPINELLI, A., DOSSENA, V., GAETANI, P., OSNAGHI, C. & COLOMBO, D. 2010 Design of a Test Rig for Organic Vapours. In *Proceedings of ASME Turbo Expo 2010* . ASME, Glasgow, UK.

SPINELLI, A., PINI, M., DOSSENA, V., GAETANI, P. & CASELLA, F. 2013 Design, Simulation, and Construction of a Test Rig for Organic Vapors. *J. Eng. Gas Turb. Power - T. ASME* **135** (4), 10.

VAN DER STELT, T.P, NANNAN, N. R & COLONNA, P 2012 The iPRSV equation of state. *Fluid Phase Equilibria* **330**, 24–35.

THOMPSON, P. A. 1988 *Compressible Fluid Dynamics*. McGraw-Hill.

VITALE, S., GORI, G., PINI, M., GUARDONE, A., ECONOMON, T. D., PALACIOS, F., ALONSO, J. J. & COLONNA, P. 2015 Extension of the SU2 open source CFD code to the simulation of turbulent flows of fuids modelled with complex thermophysical laws. In *Proceedings of the 22nd AIAA computational fluid dynamics conference*, pp. 1–12. American Institute of Aeronautics and Astronautics.

WARRICK, E. L. 1946 The application of bond refractions to organo-silicon chemistry. *Journal of the American Chemical Society* **68** (12), 2455–2459.

WHITE, M. T. & SAYMA, A. I. 2018 Design of a closed-loop optical access supersonic test facility for organic vapors. In *ASME Turbo Expo 2016 - Oslo June 11 - 15* .

WOODLAND, B. J., BRAUN, J. E., GROLL, E. A. & HORTON, W. T. 2012 Experimental testing of an organic rankine cycle with scroll-type expander. *Publications of the Ray W. Herrick Laboratories.* Paper 52.

ZEL'DOVICH, Y.B. 1946 On the possibility of rarefaction shock waves. *Zh. Eksp. Teor. Fiz.* **10** (4), 363–364.

ZUCROW, M. J. & HOFFMAN, J. D. 1976 *Gas dynamics, Vol I*.